Cardiff University

School of Chemistry

TIME RESOLVED SPECTROSCOPY OF 21^{ST} CENTURY MATERIALS

A thesis submitted in partial fulfilment of the requirements for the award of Doctor of Philosophy

April 2023

By

Haleema Yahya Otaif

Acknowledgements

First of all, I would like to express my sincere gratitude to my supervisor, Dr. Joseph Beames, for his kind and endless guidance, support, inspiration and encouragement throughout my thesis work. His exceptional mentorship, expertise, and patience have been invaluable in shaping my research and pushing me to achieve my best. I am truly fortunate to have had him as my supervisor, and I express my deepest appreciation for his contributions to my academic journey. I would also like to extend my sincere thanks to my second supervisor, Prof. Simon Pope, for his generous support and invaluable contributions to my thesis.

Next, I want to express my gratitude to my family for being an integral part of my journey. To my dear parents, I am eternally thankful for their sacrifices and dedication in providing me with the best possible education. I am also deeply grateful to my husband, Yasir, for his efforts in taking care of our home, ensuring a smooth flow of life. His unwavering belief in me, constant encouragement, and pride in my achievements have been a driving force behind my motivation. To my dear children, Rawan, Mohammed, and Rahaf, you are my pride and joy. Thank you for being a constant source of inspiration and for reminding me of the beauty of life beyond the sciences.

Additionally, I would like to thank the Pope group, the Ben Ward group, Dr. Manon Pritchard, and Anna Wright, at Cardiff University for supplying the compounds discussed in this work.

Finally, I would like to thank Jazan University and the Ministry of Education in Saudia Arabia for funding my degree program.

Preface

Chapter 3 consists of my contributions to work that has been published previously in three papers: 'Polysubstituted ligand framework for color tuning phosphorescent iridium(III) complexes' by Fitzgerald et al, published in Inorganic Chemistry Journal, DOI: 10.1021/acs.inorgchem.1c02121

'Spectroscopic and theoretical investigation of color tuning in deep-red luminescent iridium(III) complexes' by Stonelake, T. M. et al, published in Inorganic Chemistry Journal, DOI: 10.1021/acs.inorgchem.9b02991

'Bis-cyclometalated iridium(III) complexes with terpyridine analogues: syntheses, structures, spectroscopy and computational studies' published in RSC Advances, DOI: 10.1039/D1RA07213G for which I am first author.

Chapter 4 contains my contributions to work that has been published previously in two papers: 'Iridium(III) sensitizers and energy upconversion: the influence of ligand structure upon TTA-UC performance' by Elgar et al, published in Chemistry- A European Journal, DOI: 10.1002/chem.202004146.

'Deep red emitting heteroleptic Ir(III) complexes that incorporate unsymmetrical 4-quinoline carboxylic acid derived ligands' by Elgar et al, published in European Journal of Inorganic Chemistry, DOI: 10.1002/ejic.202300102

Another manuscript including data from chapter 6 titled 'Nanoscale interaction of colistin and antimicrobial therapy with the mcr positive bacterial cell membrane' is ready for publication and will soon be submitted to Nature Nanotechnology.

It is anticipated that this work will form the basis of at least two further publications, one consisting of data from Chapter 4, and the second consisting of the data from Chapter 5. Both papers are in preparation and will be submitted soon to PCCP.

Abbreviations

B3LYP (Becke, 3-parameter,Lee–Yang–Parr) exchange-correlation functional

CT – Charge Transfer excited state

DFT – Density Functional Theory

DMC – Dichloromethane

DNA – Deoxyribosenucleic acid

EDG – Electron Donating Groups

ESA – Excited State Absorption

EWG – Electron Withdrawing Groups

FA – Fluorescence Anisotropy

FP – Fluorescence Polarization

GSB – Ground State Bleach

HOMO – Highest Occupied Molecular Orbital

ICCD – Intensified Charge-Coupled Device

ILCT – Intraligand Charge Transfer

IQE – Internal Quantum Efficiency

ISC – Intersystem crossing

k_{nr} – Rate of nonradiative decay

k_r – Rate of radiative decay

LC – Ligand Centred transition

LE – Locally Excited state

LLCT – Ligand to Ligand Charge Transfer

LMCT – Ligand to Metal Charge Transfer

LUMO – Lowest Unoccupied Molecular Orbital

MLCT – Metal to Ligand Charge Transfer

NIR – Near infrared

ns – Nanosecond

OLED – Organic Light Emitting Diode

PMT – Photomultiplier Tube Detector

$\boldsymbol{p}$ – polarization

$\boldsymbol{r}$ – anisotropy

rISC – reverse intersystem crossing

RP-ISC – Radical-Pair Intersystem Crossing

S_0 – Singlet electronic ground state

S_n – Singlet electronic excited state

SOC – Spin-orbit Coupling

SOCT-ISC – Spin–Orbit Charge-Transfer ISC

TA – Nanosecond time-resolved Transient Absorption

TADF – Thermally Activated Delayed Fluorescence

TD – TDF Time Dependent - Density Functional Theory

T_n – Triplet electronic excited state

TTA – Triplet-Triplet Annihilation

UV-Vis – Ultraviolet – Visible

XRD – X-ray Diffraction

μs – Microsecond

τ - Lifetime

Table of Contents

List of Figures

List of Tables

Abstract

Spectroscopy is an important tool for chemists, that is widely used for characterizing novel materials and determining their physical and chemical properties through the analysis of their interactions with electromagnetic radiation. Conventional optical spectroscopic techniques, such as steady-state absorption and emission, can provide useful information about the electronic structure, molecular geometry, and functional groups of molecules in a sample, and allow chemists to identify the chemical composition and properties of many photostable compounds. However, these techniques are limited in providing information on reaction intermediates, excited states, and reaction dynamics. Therefore, transient spectroscopic techniques can be used to monitor the dynamics of excited states and observe how they decay back to the ground state, making it possible to obtain information on the energy, lifetime and nature of the excited states, and how external factors, such as temperature, influence their behaviour. In this thesis, a combination of steady-state and transient spectroscopic techniques, along with computational chemistry methods, are used to investigate and characterize a variety of novel luminescent organic and inorganic compounds. Firstly, I analyze the spectroscopic properties of a range of new cyclometalated Ir^{III} complexes, varying in main ligand structure, ancillary ligands, or attached substitution groups, synthesized by the Pope group at Cardiff University. It was found that the photophysical properties of the complexes were highly tunable through modifications to their molecular structure. Using the combination of spectroscopy and computational methodologies this thesis highlights the development of a photocharacterisation library of over 30 heteroleptic iridium complexes, that displays relationships between photophysical properties and ligand design, ultimately used to design new iridium complexes that emit in the deep-red and near-IR regions. Secondly, the same analysis methodology was used to study photophysical properties of an N-substituted naphthalimide dyad and its thionated variants, supplied by Anna Wright from the Yi-Lin group at Cardiff University. These compounds demonstrate different types of emission, such as fluorescence, phosphorescence and thermally activated delayed fluorescence (TADF). Thionation of the carbonyl groups in these dyads has a significant effect on the singlet excited states responsible for the photochemical properties of these species which exhibit quenching of the prompt fluorescence, but the thionation does not appear to significantly change the triplet state. The analysis techniques provide a good insight into the effect of structure geometry, temperature, and solvent on the electronic character of these organic compounds. Finally, I describe the development of the transient absorption spectrofluorometer for highly sensitive fluorescence polarization measurements. The instrument was used to investigate the emission polarization of new dye-doped polymers and to examine the binding interactions between colistin and two strains of E. coli. The results show that the modifications of the spectrofluorometer is a cost-effective, and accurate tool for exploring fluorescence polarization and binding interactions in both biological and chemical systems.

1. Introduction

1.1 Introduction and Background

Research in spectroscopy of organic and inorganic compounds has expanded enormously in scope and importance over the last 100 years and continues to be a hot topic in instrument development and application because of its importance in understanding the fundamental electronic structure and energy flow in novel materials. We see the results of these careful spectroscopic studies every day, in a wide range of technologies that have revolutionized the way we live and work. This includes, but is not limited to, OLED/LED displays in smartphones, TV screens, computer monitors, and other electronic devices (Hong et al. 2021); light harvesting materials in solar cells which convert sunlight into electricity (Sinopoli et al. 2017), making renewable energy sources more accessible and affordable; as well as light sources and lighting materials such as fluorescent and LED lamps which have replaced traditional incandescent bulbs, reducing energy consumption and improving the lifespan of lighting systems (Fu et al. 2017).

Spectroscopy is an analytical technique that studies the interaction between matter and electromagnetic radiation. The sample’s response to exposure to electromagnetic radiation allows a careful observer to gain valuable information about the atoms and molecules in the sample, such as information on their electronic structure, chemical states, and physical properties, and how they may change with varying conditions like solvent, temperature or pressure. (Burgess and Jones 1995; Pavia et al. 2009; Balzani et al. 2014) In the following sections, the properties of light, its interaction with molecular systems, the nature of the generated excited states, and their chemical and physical reactions will be introduced briefly to provide a background to this thesis which discusses the electronic spectroscopy of organic and inorganic novel materials. The fundamental principles described here will be discussed primarily in the context of the electronic spectroscopy of solution phase chemical samples which forms the body of this work.

1.1.1 Nature of light

The dual nature of light is highly important to molecular spectroscopy and photochemistry, namely that light can be treated as both a wave and a particle. (Porter 1983; Vandergriff and McLean 2008) The ‘colour’ of light is a property determined by its wavelength, whereas the energy imparted by light is typically considered as the energy of a photon (a particle of light): an important property from the standpoint of photochemistry/ spectroscopy. These two fundamental properties are correlated by the fundamental equation called Bohr's frequency condition (Bohr 1913):

$$E = h\nu = hc/\lambda = hc\tilde{\nu} \qquad \textbf{(Equation 1.1)}$$

where ***E*** is the energy per photon, ***h*** is Planck's constant (6.62 X 10^{-34} J. Hz^{-1}), v is the frequency, c is the velocity of light (3.00 x 10^{8} ms^{-1}), ***λ*** is the wavelength, and **ṽ** is the wavenumber. (Vandergriff and McLean 2008)

The visible part of the electromagnetic spectrum, for example, extends from 400 to over 700 nm and hence one mole of photons is equivalent to approximately 3.26 to 1.65 eV, respectively. (Day 1955) Light can be considered polychromatic or monochromatic. Polychromatic light has a distribution of photons of different wavelengths, while for monochromatic light photons are limited to one wavelength or more realistically to a narrow range of wavelengths. Similarly light may be incoherent as from ordinary light sources such as a lamp or most traditional LEDs, or alternatively the light may be coherent, such as laser light where all the light is in phase and collimated. Traditionally lasers have also been considered monochromatic, however, more recent developments in laser technologies can supply more broadband polychromatic light (e.g. frequency comb lasers). (Svelto 2009; Picqué and Hänsch 2019) Lasers are widely used in spectroscopy as a light source due to their many advantages over traditional light sources. As mentioned above, the light emitted by a laser is monochromatic, coherent and tunable which leads to better resolution and accuracy in measurements. Additionally, the high intensity of laser light makes it easier to detect weak signals (high signal-to-noise ratio), making analysis more sensitive and reliable. Another key advantage of lasers is their ability to produce pulses of light, allowing time-resolved measurements of fast reactions. This can be particularly useful in fields such as chemistry and biology, where understanding the dynamics of chemical reactions is crucial. (Haken 1986; Svelto 2009)

1.1.2 Quantum mechanical model of atoms and molecules

To gain a better understanding of the interaction between light and matter, it is essential to have a grasp of the quantum mechanical model of atoms and molecules that explains the behaviour of electrons and electronic structure. According to quantum mechanics, particles like electrons can exhibit wave-like properties, which means that their exact location or other characteristics cannot be known with certainty. Consequently, the behaviour of electrons is described using a set of mathematical equations known as wavefunctions. A wavefunction is a mathematical function that describes the quantum state of a particle (an electron) as a function of position, momentum, time, or spin. The wavefunction is usually denoted by the symbol $\boldsymbol{\psi}$. The wavefunction is a complex-valued function, that includes an imaginary number, but its absolute square is always a real quantity that gives the probability density of finding an electron in a particular location (normally identified by Cartesian x, y, and z coordinates) or with a particular energy. This means that wavefunctions can be used to determine the distribution of the electron's density with respect to the nucleus in an atom. (Nielsen and Martin 1985; Cotton et al. 1995; Silberberg et al. 2006; Heine 2007; Housecroft and Sharpe 2008) The wavefunction satisfies the Schrödinger equation, which is a fundamental principle of quantum mechanics, first formulated by Erwin Schrödinger in 1926. (Schrödinger 1926) It explains how the wavefunction evolves over time and has a general form known as the Schrödinger equation:

$$H\psi = E\psi \qquad \textbf{(Equation 1.2)}$$

H is the Hamiltonian operator, a set of mathematical operations representing the total energy of the quantum particle (such as an electron in an atom), $\boldsymbol{\psi}$ is the wavefunction of this particle that can be used to find the special distribution of the probability of finding the particle, and E represents the total energy (kinetic and potential) of the quantum particle within the atom. The wavefunctions are complicated mathematical functions, and the Schrödinger equation has been exactly solved only for hydrogen (contains one electron). The solution of the Schrödinger equation for a hydrogen atom yields a set of wavefunctions with a corresponding energy (eigenfunctions and eigenvectors). The wavefunctions of hydrogen atom are called atomic orbitals where an atomic orbital is a function that describes one electron in an atom. (Nielsen and Martin 1985; Cotton et al. 1995; Silberberg et al. 2006; Heine 2007; Housecroft and Sharpe 2008)

In an atom or molecule, each orbital is described by three interrelated quantum numbers: the principal quantum number ($\boldsymbol{n}$), the angular momentum quantum number (azimuthal quantum number ($\boldsymbol{l}$), and the magnetic quantum number ($\boldsymbol{m_l}$). The principal quantum number determines the energy level of the electron (principal electron shell) and the size of the orbital. It can take on positive integer values ($\boldsymbol{n}$ =1,2,3…..) and cannot be zero or negative. As the value of $\boldsymbol{n}$ increases, the energy of the electron also increases, the orbital size becomes larger, and the electron spends more time farther away from the nucleus. The relation between $\boldsymbol{n}$ and the energy level and orbital size can be illustrated by the Bohr model of atoms, seen in figure 1.1. (Nielsen and Martin 1985; Cotton et al. 1995; Silberberg et al. 2006; Heine 2007; Housecroft and Sharpe 2008)

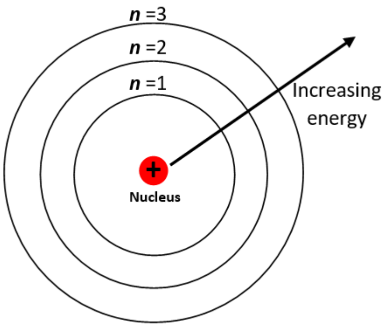

Figure 1.1 Bohr model of atoms representing energy levels characterized by the principal quantum numbers.

In the case of the hydrogen atom, the electron typically resides in the first energy level (principal shell) of the atom and is referred to as the ground state or lowest energy state. In the case of an electron gaining energy or being in an excited state, it can be promoted to the second (or higher) energy level, where $\boldsymbol{n}$=2, as seen in figure 1.2. This process is known as absorption since the atom "absorbs" energy or photons and that energy is utilised in the electron promotion. Conversely, when electrons move to lower principal shells, the value of n decreases by whole numbers, and energy is released. This process is often radiative and this is known as emission and will be discussed later in more detail. (Cotton et al. 1995; Silberberg et al. 2006; Heine 2007)

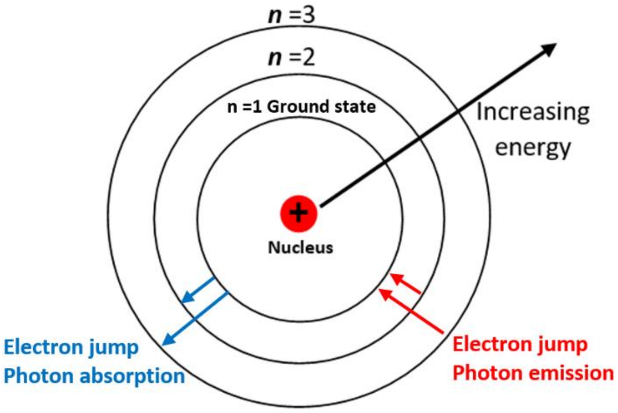

Figure 1.2 Schematic representation of electron transitions between the energy levels of the atom.

The angular momentum quantum number (l) describes the shape of the orbital and can take on values from 0 to n-1 (l =0,1,2...n -1). For example, if n = 1, then the only possible value of l is 0; if n= 2, the possible values of l are 0 and 1. The values of l are usually assigned by letters as follows:

l = 0 ***s*** *(or the s subshells)*
l = 1 ***p*** *(or the p subshells)*
l = 2 ***d*** *(or the d subshells)*
l = 3 ***f*** *(or the f subshells)*

Orbitals are named according to their principal and angular momentum quantum numbers, such as, *1s, 2s , 2p* and so forth. For *1s*, 1 is the energy level (principal shell) of the orbital and *s* is a representation of its shape, or more precisely the electron distribution.

The magnetic quantum number (m_l) determines the orientation of the orbital in space and can take integer values (including zero) ranging from -l to +l. The total number of possible orbitals with the same value of l is 2l + 1. For example, if l = 0, then the only possible value of m_l is 0; if l = 1, the possible values of m_l are -1, 0, and +1; and if l = 2, m_l can be −2, −1, 0, +1, or +2. Therefore, there is one *s*-orbital, and there are three *p*-orbitals, five *d*-orbitals, and seven *f*-orbitals, each corresponding to a specific value of m_l. Orbitals with the same principal quantum number and same subshell have the same energy, and are called degenerate energy levels, (Cotton et al. 1995; Silberberg et al. 2006; Heine 2007) as shown in figure 1.3.

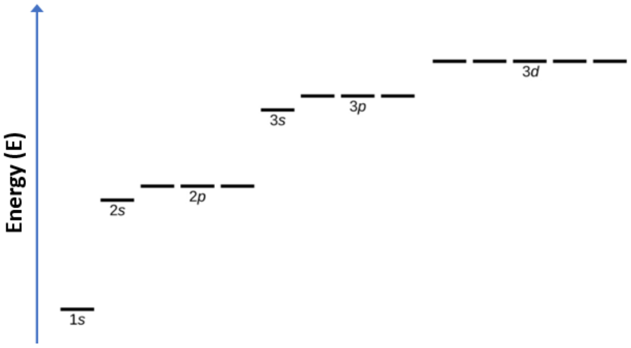

Figure 1.3 The energies of electron orbitals in a multi-electron atom.

In a multi-electron atom, the distribution of electrons within orbitals is governed by the fundamental principle known as the Aufbau principle. This principle states that electrons must occupy the subshells' orbitals with the lowest energy levels before they can occupy higher energy subshells. For example, the *1s* subshell is filled with electrons first, followed by higher energy subshells such as *2s, 2p, 3s,* and so on. Within a subshell, every orbital must be singly occupied with one electron before any one orbital is doubly occupied, which is referred to as Hund's rule. (Warner and Berry 1985)

There is a fourth quantum number called the spin quantum number (m_s) which describes the orientation of the spin of the electron and can take on values of +1/2 (spin up ↑) or -1/2 (spin down ↓). Any electron, regardless of the atomic orbital in which it is located, can only have one of those two values of the spin quantum number. The Pauli exclusion principle states that within an atom, it is impossible for two electrons to have the same set of these four quantum numbers. When two electrons are present in the same orbital, they must have opposite spin states ↑↓, and they are known as paired electrons. The total spin, denoted by S, is the sum of the spin quantum numbers of all the electrons in the system. The possible values of S depend on the number of electrons and their arrangement in the system. For example, if there are two electrons in the system with opposite spins, the total spin is zero ($S=0$). If there are two electrons with the same spin, the total spin is 1 ($S=1$). The total spin S of a system is important to calculate its spin multiplicity. Spin multiplicity, denoted by $2S+1$, refers to the number of possible degenerate spin states that the system can have. If $S=0$, then the spin multiplicity of the system is 1, or a singlet state; whilst a system with $S=1$ has a multiplicity of 3, a triplet, which means there are three possible states corresponding to the three possible combinations of electron spins that produce a total spin of 1. (Warner and Berry 1985)

The spin multiplicity is an important property of a system that affects its magnetic properties, chemical reactivity, and spectroscopic behaviour. For example, a molecule with an odd number of electrons has a non-zero total spin and therefore exhibits paramagnetic behaviour, while a molecule with an even number of electrons, for example most ground state polyatomic systems, may have a zero total spin and exhibit diamagnetic behaviour. Spin multiplicity also plays a crucial role in determining the allowed transitions in electronic spectroscopy, as will be explained in the next section. (Nielsen and Martin 1985; Cotton et al. 1995; Silberberg et al. 2006; Heine 2007; Housecroft and Sharpe 2008)

The behaviour of electrons in a molecule can be described in much the same way that the distribution of electrons in atoms is described using atomic orbitals. The region of space in which an electron in a molecule is likely to be found is defined as a molecular orbital (MO), which can be mathematically described through the use of wavefunctions ($\boldsymbol{\psi}$) because they are solutions to the Schrödinger equation for the molecule. (Cotton et al. 1995; Silberberg et al. 2006; Heine 2007). When two or more atoms come close to each other, their atomic orbitals (wavefunctions) can combine and overlap to generate molecular orbitals. This process is called the linear combination of atomic orbitals (LCAO). The overlapping atomic orbitals must have similar symmetry and energy levels to form a stable molecular orbital. The formed bonds are named according to the type of overlap between atomic orbitals. Sigma, σ, bonds are a result of the head-to-head overlapping of atomic orbitals whereas pi, π, bonds are formed by the lateral overlap of two atomic orbitals. This can also be thought of with respect to the bond axis – a sigma bond is formed on the bond axis, whereas a pi bonding interaction lies above and below the bond axis.

Two types of molecular orbitals can result from the combination of atomic orbitals, each with its own unique characteristics, namely bonding and antibonding orbitals, (Warner and Berry 1985) figure 1.4.

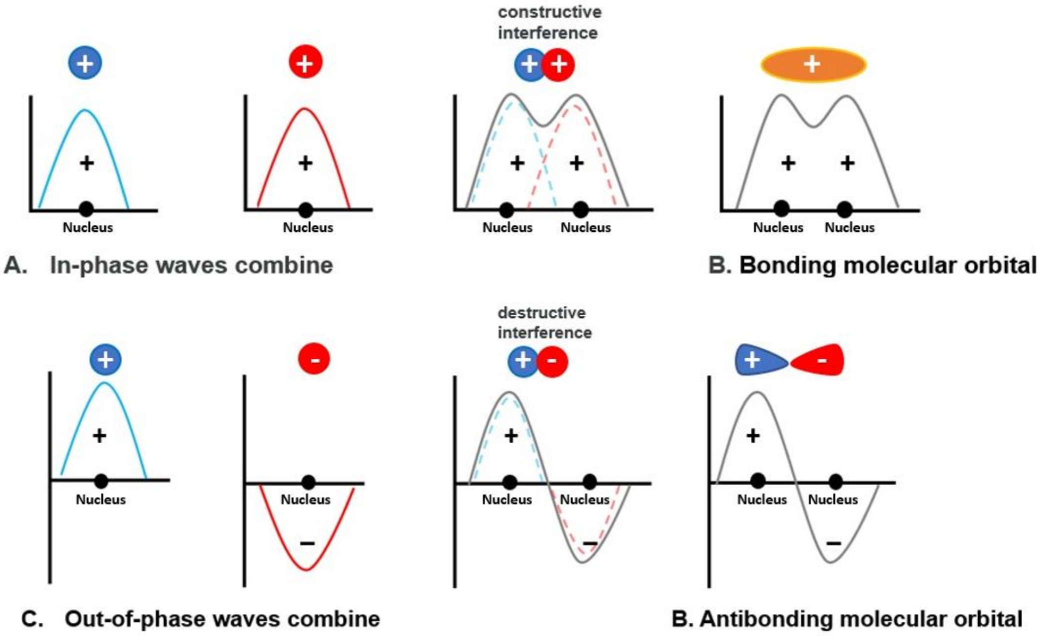

Figure 1.4 Schematic representation of the linear combination of atomic orbitals to generate bonding and antibonding molecular orbitals.

Bonding molecular orbitals, denoted as σ or π, are formed when atomic orbitals combine in-phase, resulting in constructive interference that increases the electron density between the nuclei of the two atoms. Bonding orbitals promote the formation of stable chemical bonds between atoms. In a bonding molecular orbital, the electrons are ‘shared’ by both atoms, and the energy level of the molecular orbital is lower than that of the parent atomic orbitals. Antibonding molecular orbitals, denoted as σ^* or π^*, on the other hand, are formed when atomic orbitals combine out-of-phase, resulting in destructive interference that creates a node or a region of zero electron density between the two nuclei. This reduces the electron density between the two atoms and is destabilizing with respect to the bond (of course this is only true if the orbital is occupied) and the energy level of the molecular orbital is higher than that of the parent atomic orbitals. The molecular orbital diagram of molecular hydrogen H_2 is shown in figure 1.5 as an illustrative example of a molecular orbital diagram. (Warner and Berry 1985;Ramsden 1994)

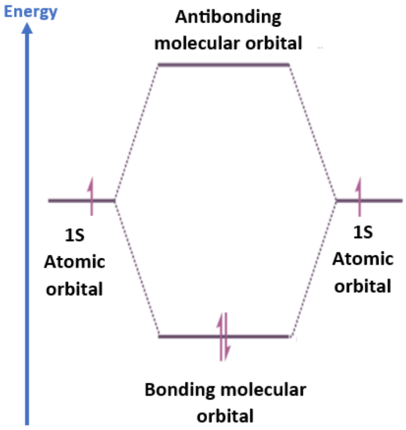

Figure 1.5 Molecular orbital diagram of molecular hydrogen H_2

Given the requirements for a bonding or antibonding interaction between atomic orbitals it should also be clear that there are scenarios in which two atoms approach each other but the atomic orbitals do not interact because of lack of compatible symmetries or wavefunction overlap. These are considered nonbonding molecular orbitals, denoted as n, Nonbonding orbitals can play an important role in chemical reactions, as they can participate in interactions with other molecules and are frequently involved in spectroscopic parameters of a molecular system. (Warner and Berry 1985;Ramsden 1994)

Similar to atomic orbitals, each molecular orbital has an associated energy, and the lowest energy MOs are filled ‘first’ by electrons when constructing a bonding picture of a molecular system. For example, if a molecule has electrons to fill 10 orbitals, the 10 MOs with the lowest energies will be filled. The 10th MO would be called the "highest occupied molecular orbital" (HOMO) and the 11th MO which is unfilled would be the "lowest unoccupied molecular orbital" (LUMO). The energy difference between the HOMO and LUMO is often referred to as the energy gap. The energy gap plays an important role in determining the spectroscopy properties of a molecule.

When a molecule absorbs photons with energy matching the energetic gap between molecular orbitals, it can cause electrons to transition between orbitals, for example from bonding molecular orbitals to antibonding orbitals. This results in the creation of an electronic absorption spectrum which demonstrates the energy gap between these orbitals. However, unlike atoms, the spectrum of molecules is more complex. This is because vibration and rotational motions of the nuclei are also involved in governing the spectral profile. For example, when electrons transfer from bonding to antibonding orbitals the bond associated with this ‘antibonding’ character becomes weaker and the bond length increases. This leads to coupling of the electronic excitation with vibrational motion (figure 1.6). The concept of spin multiplicity is applied to molecular orbitals in a similar way as to atomic orbitals and also impacts transition intensities. These concepts are discussed in more detail later in this chapter. (Warner and Berry 1985;Ramsden 1994)

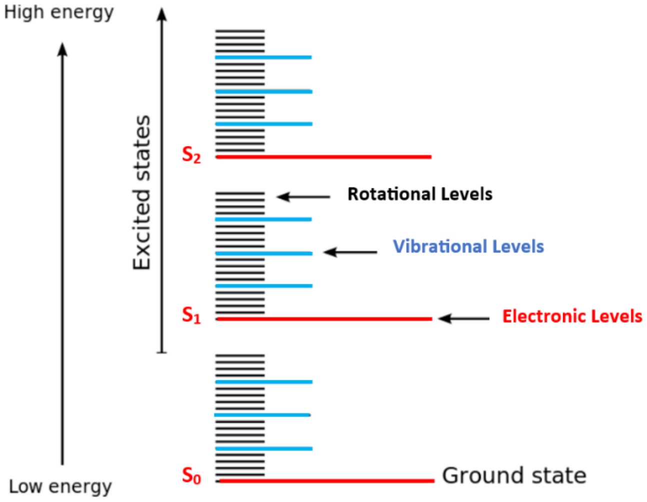

Figure 1.6 Schematic representation of electronic, vibrational, and rotational energy levels of a molecule

1.1.3 Beer-Lambert Law

The Beer-Lambert Law describing light absorption is of fundamental importance to furthering the discussion of the interaction of light with matter (Kafle 2020; Shinde et al. 2020). The law relates the absorbance (*A*) of a material to a light path length through the sample (ℓ) and the concentration of the absorbant (*c*)

$$A = \log_{10} (I_o/I_t) = \varepsilon \ell c \qquad \textbf{(Equation 1.3)}$$

Where I_o is the incident light intensity, I_t is the transmitted intensity, and ε is the molar extinction coefficient (molar absorptivity) which is a function of wavelength of the incident light. If there are more than one absorbing species present, the total absorbance, is simply the sum of the absorbances of the individual components. The fraction of light (f_1) absorbed by one of these species is given by

$$f_1 = \varepsilon_1 c_1 / (\varepsilon_1 c_1 + \varepsilon_2 c_2 + \ldots . + \varepsilon_n c_n) \qquad \textbf{(Equation 1.4)}$$

The Beer-Lambert law is not valid, or at least requires more careful application, if the incident light is polychromatic over a range of wavelengths where the molar extinction coefficient (ε) is not constant. It is also worth considering that in many cases the intensity of the absorbed light is not simply the difference between the intensities of incident (I_o) and transmitted light (I_t). For example, for a solution phase system held in a quartz cuvette in a traditional UV-Vis spectrometer, reflection and absorption of the cell and absorption by non-active components or the solvent must be also taken in consideration. Light scattering by undissolved particulates, aggregates or bubbles is also commonplace and must be considered at all times. (Kafle 2020; Shinde et al. 2020)

As mentioned above, absorption of visible and/or ultraviolet light typically causes the absorbing species to move between electronic states. Radiative transitions between a ground state (with energy E1) and an excited state (with energy E2), form absorption and emission spectra, respectively. The energy difference between the two energy levels determines the energy and wavelength of the emitted or absorbed photon.

$$E = E2 - E1 = hc/\lambda = hc\tilde{\nu} \qquad \textbf{(equation 1.5)}$$

The probability of absorption or emission of a photon by an atom or molecule is described by Einstein coefficients. (Einstein 1916) Einstein proposed that there are three processes occurring in the formation of atom/molecular spectra: absorption, spontaneous emission, and stimulated emission. The Einstein **A** coefficient is related to the rate of spontaneous emission of light ($\mathbf{A_{21}}$), and the Einstein **B** coefficients are related to the absorption ($\mathbf{B_{12}}$) and stimulated emission of light ($\mathbf{B_{21}}$). The difference between spontaneous and stimulated emissions is that spontaneous emission occurs when an electron spontaneously decays from a higher energy level to a lower energy level without any external influence. On the other hand, stimulated emission, also known as induced emission, is the process in which an electron is stimulated to decay from a higher energy level to a lower one by an incoming photon of the same (or near) frequency or energy, causing it to release a second photon that is identical in frequency, phase, polarization, and direction of travel to the incoming photon, shown in figure 1.7. Stimulated emission is the basic principle behind the creation of lasers. In a laser, photons emitted by stimulated emission stimulate more atoms or molecules to emit photons in the same direction. This process is repeated many times (called laser amplification), creating a coherent beam of light with a single frequency and phase. (Herd et al. 1997)

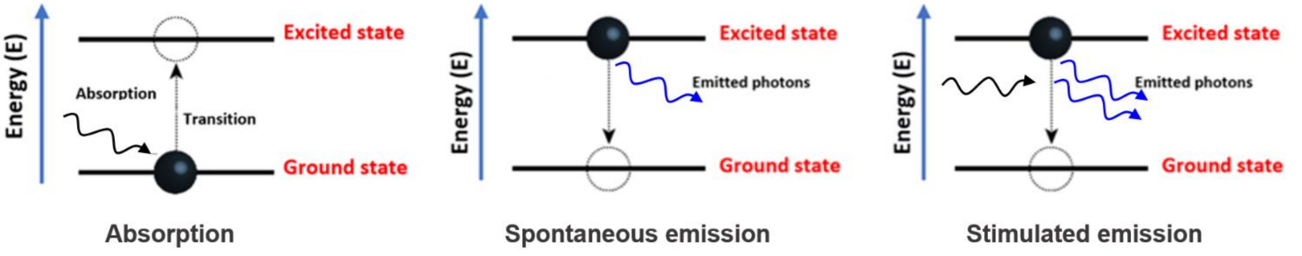

Figure 1.7 Schematic representation of the absorption, spontaneous emission, and stimulated emission.

The rate of absorption of photons depends on two factors: the number of molecular systems in the ground state (N_1) and the energy density of incident photons $\rho(v)$. The energy density $\rho(v)$ in this case is specific: it represents the number of photons that have the exact energy for the transition between energy E1 and E2. The more photons there are to absorb, the higher the absorption rate. The rate of absorption can be mathematically expressed:

$$r_{\text{absorption}} = \frac{dN_1}{dt} = B_{12}N_1\rho(v) \qquad \textbf{(Equation 1.6)}$$

The rate of spontaneous emission is independent of the incident energy density, ρ(υ). Instead, it is determined by the number of electrons present in the higher energy orbital that can spontaneously decay to the lower energy orbital and emit photons.

$$r_{\text{spontaneous emission}} = \frac{dN_2}{dt} = A_{21}N_2 \qquad \textbf{(Equation 1.7)}$$

Where A_{21} is Einstein’s coefficient for spontaneous emission, N_2 is the number of electrons or systems in the excited state.

The rate of stimulated emission depends on the number of electrons in the excited state *and* the energy density of the incoming photons can be written as:

$$r_{\text{stimulated emission}} = \frac{dN_2}{dt} = B_{21}N_2\rho(v) \qquad \textbf{(Equation 1.8)}$$

Where B_{21} is Einstein’s coefficient for stimulated emission.

In molecules, rotations and vibrations of atoms are also associated with discrete energy levels, which are supported within each electronic state (figure 1.6). Therefore, many transitions with different energies can occur in molecules leading to a broadening of the absorption bands, for example transitions from a ground electronic state to a higher electronic state but with various degrees of vibrational excitation. To better understand this, it can be helpful to look at a schematic of the relevant energy levels and their properties, as shown in figure 1.8.

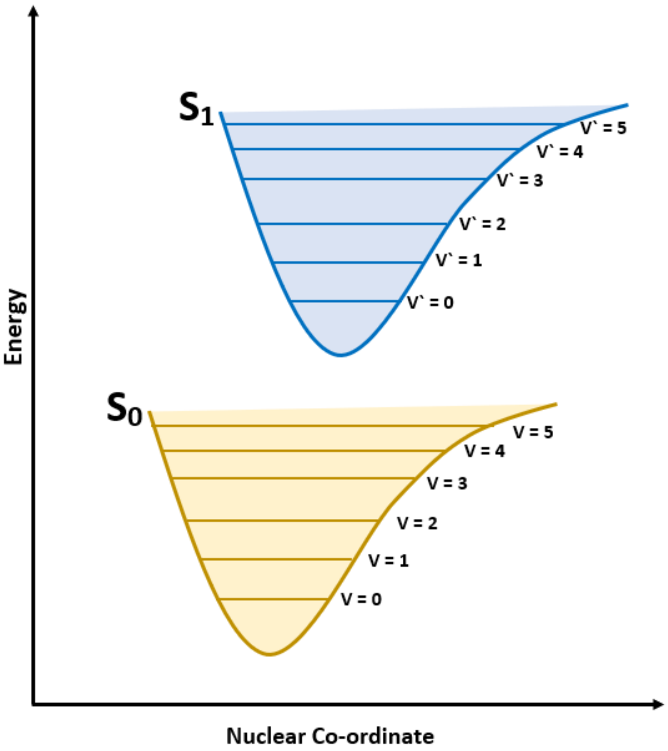

*Figure 1.8 Schematic representation of Morse-like potential wells of the electronic ground state (**S_0**) and first excited state (**S_1**). The vibrational states within each potential are shown, from the lowest energy, υ = 0, upwards.*

Each bound excited state in a molecular system consists of a Morse-like potential well, with energy levels that correspond to vibrational states (υ = 0 … υ = n) due to the vibrational motion of the molecule and its interaction with the environment. When the system is electronically excited, it moves from the electronic ground state (**S_0**) to an excited state (**S_n**) which in this explanatory case we treat as **S_1**. The **S_1** state is offset in the nuclear coordinates with respect to **S_0** due to the change in the geometry of the molecule between the two states as described on page 9. This is because when an electron moves to a higher energy level, the electron distribution changes around the nuclei, leading to changing the forces between the nuclei. This in turn can change the effective molecular bond order and hence bond lengths causing the excited state to adopt a different geometry. Electronic transitions occur much faster than the motion of the nucleus, according to the Born-Oppenheimer approximation (Born and Oppenheimer 1927; Baer and Englman 1997). Therefore, electronic transitions are treated as being vertical in the picture above because the electronic transitions take place instantaneously with respect to the nuclear coordinate shown on the x-axis. The figure shows a single nuclear coordinate in the x-axis but there are in fact 3N-6 vibrational coordinates for each non-linear polyatomic molecule and therefore this potential energy surface slice exists in each of these dimensions. This leads to the formulation of the Franck-Condon principle, (Condon 1926; Franck and Dymond 1926; Condon 1928; Frank 2022; Yamanaka et al. 2023) which states that the overlap between the ground and excited state wavefunctions determines the probability (the Franck-Condon factor) of such a transition occurring, as shown in figure 1.9.

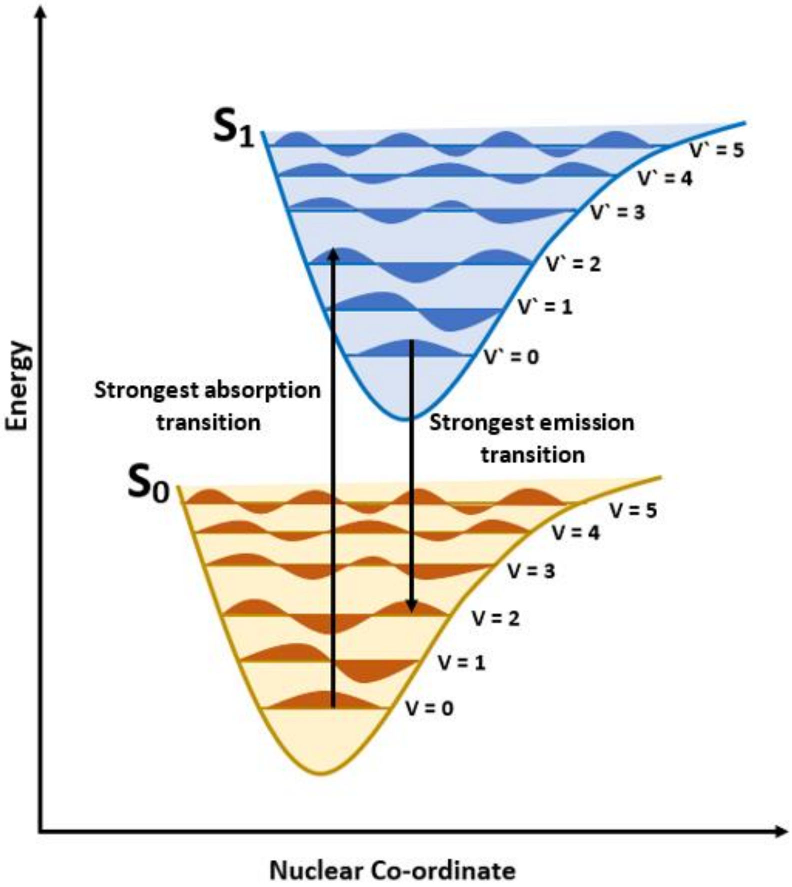

Figure 1.9 Representation of the Franck-Condon principle. The overlap of vibrational wavefunctions between the two states defines the probabilities of absorption and emission. Therefore, the strongest absorption and emission transitions are shown.

Transitions to lower and higher vibrational levels within the $\mathbf{S_1}$ state can occur as a result of optical absorption transitions of lower probabilities, leading to a characteristic Franck-Condon intensity pattern in the absorption spectrum. The emission process is the reverse of this, with transitions occurring from the $\mathbf{S_1}$ state back to the $\mathbf{S_0}$ state, with probabilities of emission at a given frequency related to the overlap of the vibrational wavefunctions. One would expect the emission spectrum to be the same as the absorption spectrum, but for a molecule in solution solvent-collision induced relaxation (called vibrational relaxation) within the $\mathbf{S_1}$ state happens very quickly, on the order of $\sim 10^{-12}$ seconds or faster. This is much faster than the time required for radiative decay, which occurs on the order of $\sim 10^{-9}$ seconds. (Jaffé and Miller 1966; Priestley and Haug 1968) As a result, the population of the $\mathbf{S_1}$ state will typically reach the lowest vibrational level of $\mathbf{S_1}$ ($\upsilon = 0$) before emission. Therefore, the overlap between the wavefunction of the lowest vibrational of the $\mathbf{S_1}$ state ($\upsilon = 0$) and the vibrational levels of the $\mathbf{S_0}$ state determines the shape of the emission spectrum. When comparing the peak intensity absorption wavelengths with those of an emission band there is a loss of energy, known as the Stokes Shift (Stokes 1852; Gispert 2008; Ghosh et al. 2023). This loss of energy reflects the overlap between the initial and final states during the absorption and emission process, changes in molecular geometry and collisional relaxation. Characteristic absorption and emission spectra, which show the energy levels involved in the absorption and emission process, are shown in figure 1.10.

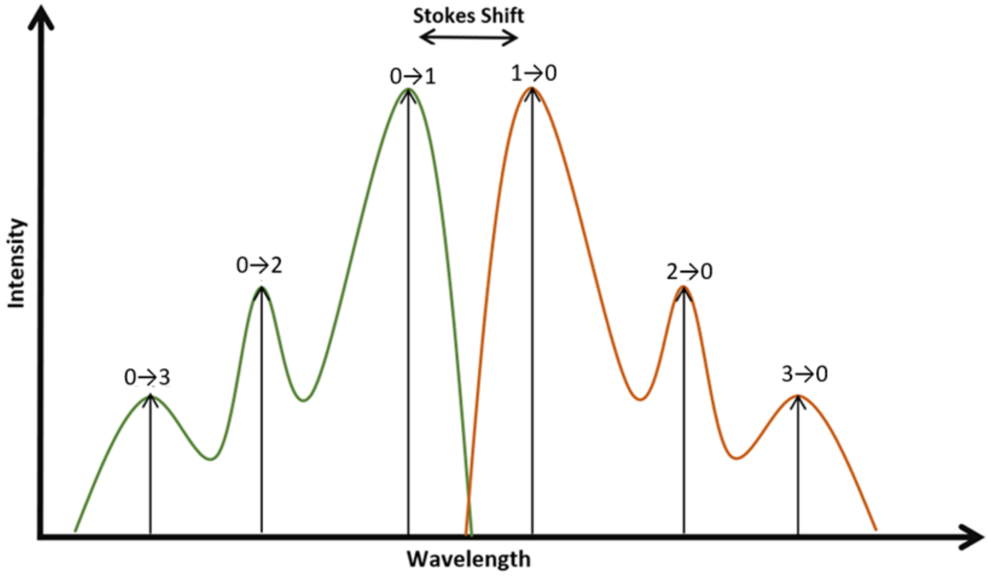

Figure 1.10 Typical absorption and emission spectra for a conjugated organic material, showing vibronic features and the Stokes shift between absorption and emission.

1.1.4 Excited states and spin multiplicities

The terms "singlet state" and "triplet state" refer to different types of electronic states that are characterized by the number and spin of electrons. Singlet and triplet excited states are different in nature, and each possesses completely distinct properties, including bond length and molecular geometry, among others. These states are important in understanding the electronic and optical properties of atoms, molecules, and materials (Roundhill 1994; Balzani et al. 2014).

When an electron is excited to a higher energy level, it can form either a singlet or a triplet state (figure 1.11). In a singlet state, the excited electron has the same spin orientation as it did in the ground state, meaning the electrons in the ground and excited state have an opposite spin. In a triplet state, the excited electron has the same spin orientation as that in the ground state, meaning they are parallel to each other.

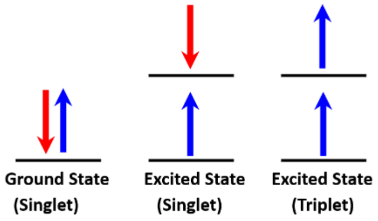

Figure 1.11 Schematic representation of electron spins for a singlet and triplet state.

Electronic transitions between the ground state and different excited states are governed by a set of rules called selections rules which describes the allowed transitions. (Roundhill 1994; Balzani et al. 2014). For example, the LaPorte selection rule, which applies to centrosymmetric systems, states that electronic transitions between different orbitals with the same symmetry are forbidden. The other rule guiding electronic transitions is called the spin selection rule, and states that the spin multiplicity value cannot change during a transition from one electronic state to another. Transitions that follow this rule are known as 'spin-allowed', while transitions that do not obey this rule are described as 'spin-forbidden. However, spin-forbidden transitions can occur in some cases due to spin orbit coupling (SOC), which is a relativistic effect that occurs when an electron's spin is coupled to its orbital motion, causing formally spin-forbidden transitions to become allowed (albeit normally weakly allowed). According to spin selection rule, transitions between singlet and singlet states and between triplet and triplet states are spin-allowed, as they do not involve a change in multiplicity. Singlet-singlet transitions are particularly common, as the ground state of most molecules is a singlet. These transitions are responsible for most of the absorption bands observed in molecules. Triplet-triplet transitions are also formally allowed but are not normally observed in traditional absorption spectroscopy due to the rarity of species with triplets ground states. However, these transitions are important in transient spectroscopy, which involves the study of excited states using absorption spectroscopy before they decay. These transitions can be generated using a pulse of light and can provide valuable information about the properties of triplet states. An example of a spin-forbidden transition is the transition from a singlet state to a triplet state. These transitions are typically slower and less intense than spin-allowed transitions, and thus can be observed as very weak bands at longer wavelengths in absorption spectra (Roundhill 1994; Balzani et al. 2014).

Selection rules are also applied to radiative emission. Emission processes can be distinguished as phosphorescence or fluorescence (Figure 1.12) depending on if the transition is associated with a spin quantum number change or not. When emission occurs from a high lying level in the singlet manifold back to the singlet ground state, it is termed fluorescence and is fully spin-allowed, leading to typically intense emission. In contrast, phosphorescence emission involves a transition from a triplet excited state to the singlet ground state, which is spin-forbidden and therefore is weak and normally considerably slower than fluorescence. (Kasha 1947; Roundhill 1994; Balzani et al. 2014).

To better understand the excited state processes that occur within a molecular system it is useful to consider many of these processes in terms of the time and nature of the transitions through a Jablonski diagram,(Jablonski 1933; Jabłoński 1935) as shown in figure 1.12.

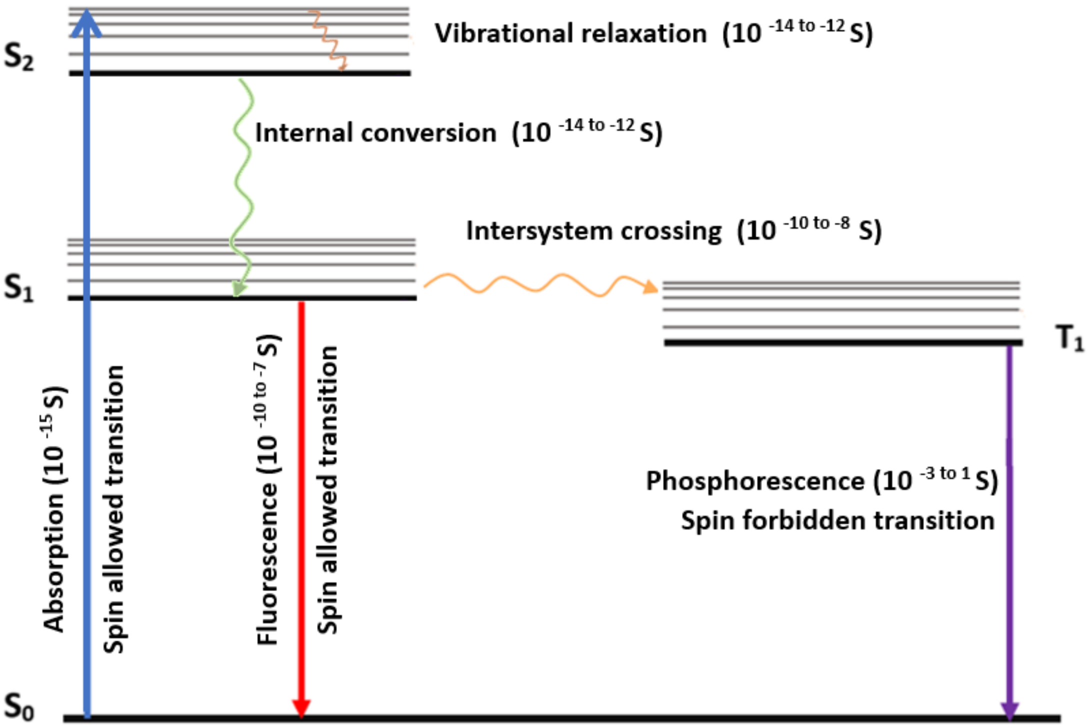

Figure 1.12 A Jablonski diagram illustrating the transitions between energy levels and the processes that take place within the excited state manifolds.

Following photoexcitation from a singlet ground state, a molecule can readily access a higher excited singlet state $\mathbf{S_n}$ (n>1). From this state, the material can undergo an ultrafast process called internal conversion (IC), which is non-radiative relaxation to lower electronic states that happens very quickly, on the order of 10^{-12} to 10^{-15} seconds (Bixon and Jortner 1968; Englman and Jortner 1970; Avouris et al. 1977). In an IC process, the energy difference between upper and lower excited states is converted to vibrational energy or transferred to the solvent. As a result of this fast internal conversion, emission is generally observed from the lowest singlet state, $\mathbf{S_1}$, a phenomenon known as Kasha's rule (Kasha 1950; Braslavsky 2007). Once in the $\mathbf{S_1}$ state, the molecule can undergo vibrational relaxation, which involves transitions between vibrational levels and occurs on the order of 10^{-12} to 10^{-15} seconds. This brings the material to the lowest vibrational level in the $\mathbf{S_1}$ state (Bondybey 1984; Elsaesser and Kaiser 1991). It is also possible for the excited state population to undergo intersystem crossing (ISC), a process that involves a spin-flip of an electron and has a low probability in traditional small molecules. Intersystem crossing (ISC) is responsible for populating the triplet state following photoexcitation within the singlet manifold. Radiative decay, or the emission of light, can occur from either the $\mathbf{S_1}$ or $\mathbf{T_1}$ state, as fluorescence or phosphorescence, respectively. (Kasha 1947) As phosphorescence is a spin-forbidden transition, the triplet state has a longer lifetime than the singlet state. (Lower and El-Sayed 1966) Both fluorescence and phosphorescence recorded in solutions are affected by the surrounding environments, such as the polarity of the solvent, temperature, pH and presence of molecular oxygen.

- **Solvent polarity:**

The polarity of a molecule, which refers to the separation of electric charge within it, can be quantified by its dipole moment. In general, the dipole moment of a molecule depends on the arrangement of its atoms and the distribution of electrons in its orbitals. (Sun and Song 1977; Wilde and Watts 1991) In solutions, when a molecule is in its ground state, the dipole moment of the molecule interacts with dipole moments of the surrounding solvent molecules (the solvent cage). As the molecule is photoexcited it is rapidly promoted to an excited state (normally to an excited vibronic level within the singlet manifold) and then it relaxes through IC and/or ISC to a state in which it adopts a new electronic configuration, leading to a change in its dipole moment. Therefore, the solvent molecules rearrange themselves around the dipole moment of the excited molecule, which leads to a lowering of the energy of the excited state and subsequently reducing the energy gap between excited and ground electronic states thereby shifting the emission to a longer wavelength than the initial instantaneous excitation process which happens faster than the solvent can re-arrange. This effect is called solvent relaxation and occurs in a timescale of 10-100 picoseconds. (Middelhoek et al. 1995) The shift of an emission or absorption band with varying solvent systems is commonly referred to as solvatochromic shift and it is evident in emission spectra. (Suppan 1990; Renger et al. 2008; Marini et al. 2010).

Of course, the solvent effect is more or less pronounced according to the nature of the solvent and the solute properties. Different types of transition are affected differently by changes in polarity. For example, in a $\pi\pi^*$ transition, the antibonding molecular orbital is typically more polar than the bonding molecular orbitals, due to the separation of charge. As a result, increasing the solvent polarity stabilizes the antibonding molecular orbital, leading to a reduction in the energy gap between π and π^* and causing the emission to shift to longer wavelengths (positive solvatochromism), shown in figure 1.13. Similarly, in a charge transfer (CT) transition, where there is a transfer of electron density from a donor orbital to an acceptor orbital, then the excited state is more polar due to the significant separation of charge and creation of a dipole moment between the donor and acceptor parts of the molecule. Therefore, in polar solvents, there is a considerable reduction in the energy gap and a significant red shift in the emission band. (Rezende et al. 2011)

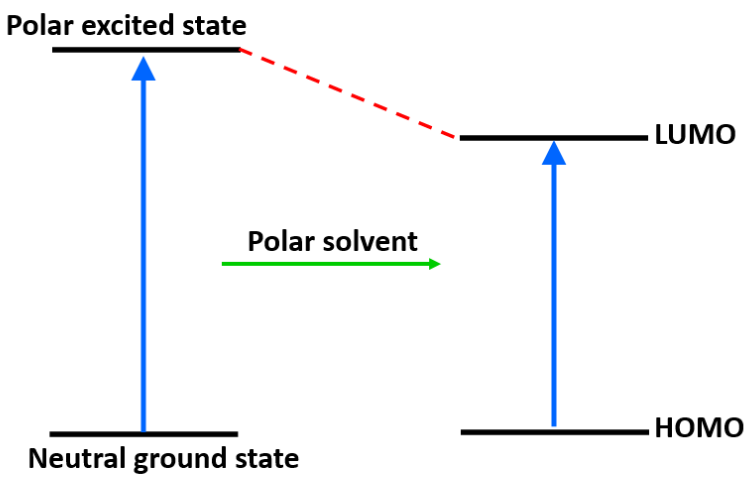

Figure 1.13 Schematic representation of positive solvatochromism.

For *nπ** transitions, the electrons within the non-bonding orbital (*n*) are responsible for creating a hydrogen bond with the polar solvent, making the HOMO more polar. However, if the electrons are excited to *π**, this hydrogen bonding interaction is reduced. As a result, the polar solvent will stabilize the HOMO more than the LUMO, increasing the energy gap and shifting the emission to shorter wavelengths (negative solvatochromism), (Rezende et al. 2011) as shown in figure 1.14 below.

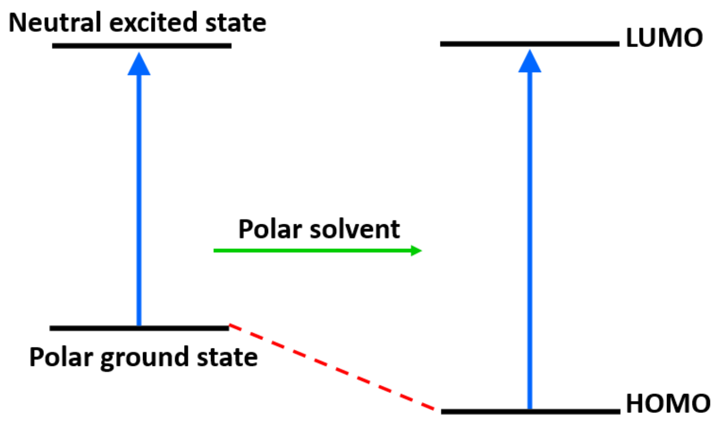

Figure 1.14 Schematic representation of negative solvatochromism.

- **Oxygen quenching**

Another factor that affects the intensity and lifetime of emission is the presence of molecular oxygen dissolved in the solvent. Oxygen can act as a collisional quencher for photoluminescence, an effect that is once again more pronounced in triplet-state phosphorescence. When a molecular system is in the triplet excited state it can interact with the oxygen in its triplet ground state leading to quenching the emission. When oxygen quenches the electronically excited states, the excitation energy is transferred to the oxygen molecule to enable the generation of the singlet excited states, $^1O_2^*(^1\Delta_g)$ of the oxygen molecule, as shown in figure 1.15. (Kautsky 1939; Lee et al. 1987)

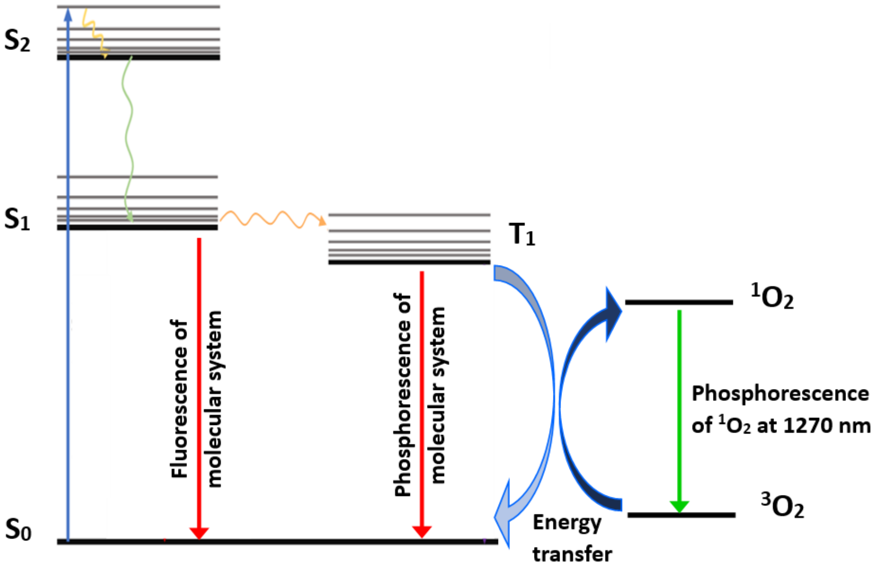

Figure 1.15 Jablonski diagram showing the production of singlet oxygen via energy transfer to ground state oxygen from the excited triplet state of a molecular system.

The quenching is effective because the excited triplet state of the molecular system (i.e. not oxygen) can convert to a singlet ground state through interaction with dissolved oxygen, a process that is normally spin forbidden in the molecular system alone. This is due to the electronic structure of molecular oxygen, which contrary to most molecules has a triplet ground state and singlet excited states. Therefore, if the molecule and oxygen are in close proximity, the deactivation of the molecule and activation of the oxygen are both individually spin-forbidden but become overall spin allowed when they happen in conjunction through collisional energy transfer. The quenching is particularly effective when the molecular energy level is similar to the oxygen excited state energy. The production of singlet oxygen can also be used as a measure of the population of triplet states. The sensitivity of triplet excited states towards the oxygen molecules has been used to develop optical oxygen-sensing systems (Kautsky 1939; Lee et al. 1987;Shi et al. 2022).

- **Temperature**

Generally, the intensity of the emission decreases at higher temperatures. This is because increasing the temperature increases the kinetic energy of the molecules, leading to increased numbers of collisions between molecules, which in turn increases the likelihood of internal conversion deactivation (direct IC to $\mathbf{S_0}$). For example, Lowering the temperature reduces the collisions between excited molecules and dissolved oxygen, resulting in a reduction of emission intensity. The effect of temperature is more prominent in phosphorescence where changes in population of the longer-lived triplet excited states are more pronounced through this temperature quenching, leading to reduced phosphorescence lifetimes and quantum yield. In contrast, at lower temperatures the quantum yield and lifetime of phosphorescence can increase significantly. Therefore, emission measurements at low temperatures can be used to determine phosphorescence vs. fluorescence. (Bowen and Sahu 1959; Ware and Baldwin 1965; Parikh et al. 2023).

Triplet excited states in molecules play a key role in determining their optical characteristics and form the basis for a wide range of applications, owing to their comparatively long lifetime. Chromophores with triplet excited states are necessary for a variety of applications, such as triplet photosensitizers and photodynamic therapy (which relies on the oxygen process described above), photocatalysis, triplet–triplet annihilation up-conversion and organic light-emitting diodes (OLEDs). Indeed, triplet phosphors are vital for electrically driven light-emitting devices, such as OLEDs and LEDs, to produce highly efficient electroluminescence. (Hussain et al. 2021) This is because under electrical excitation as opposed to the optical excitations I've discussed so far, the injected electrons and holes from opposite electrodes recombine to form multiple spin states with populations governed by the molecular spin statistics. In most OLEDs, singlet and triplet states are populated, with the excited singlet state with total spin $\boldsymbol{S} = 0$ (spin multiplicity is 1) generated with a probability of 25%, while the excited triplet states with $\boldsymbol{S} = 1$ (spin multiplicity is 3) are generated with a probability of 75%, (figure 1.16). (Kitai 2016) Notably, the triplet excited state can be formed directly under electrical excitation because electrical excitation, unlike photo-excitation, does not require the total spin change to be equal to zero. (Slonczewski 1999) In the case of fluorescent materials, only the singlet state can be utilized for light emission, limiting the internal quantum efficiency (IQE) of fluorescent light-emitting devices to 25%. Conversely, phosphorescent materials can harvest both directly prepared triplet states and indirect triplet states formed through ISC from the initially prepared excited singlet manifold, providing a theoretical IQE of 100% for phosphorescent light-emitting devices. The triplet excited state can alternatively be harvested through thermally activated delayed fluorescence (TADF) mechanism into the singlet manifold which is normally considered a reverse ISC process. In TADF materials, both electrically generated singlet and triplet excited states contribute to prompt and delayed emissions within the same wavelength region, theoretically leading to 100% emission from the singlet state, as in figure 1.17. (Bui et al. 2018; Kitai 2018; Zeng et al. 2019; Adachi and Sandanayaka 2020; Ward et al. 2020; Nakanotani et al. 2021; Li et al. 2022)

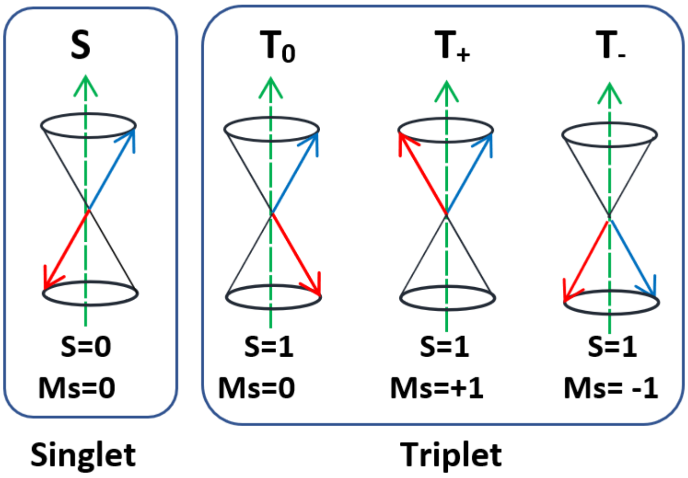

Figure 1.16 Conceptual diagram of the four spin states generated under electrical excitation. Statistically, electrons and holes recombine to form 25% excited singlet states and 75% excited triplet states.

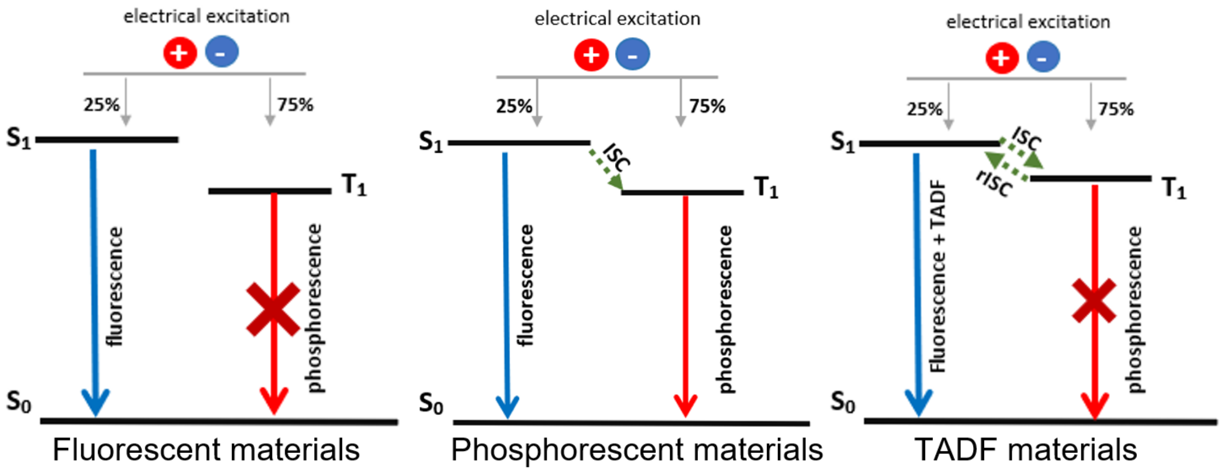

Figure 1.17 Radiative deactivation pathways existing in fluorescent, phosphorescent and TADF materials under electrical excitation.

Transition metal complexes are attractive for light-emitting applications, owing to their brightly coloured emission resulting from the intense metal-ligand interactions. (Roundhill 1994; Balzani et al. 2014). Third-row transition metal complexes, such as those based on Iridium , have been extensively used due to their very strong spin-orbit coupling induced by the heavy Ir^{III} atom, which promotes transitions between singlet and triplet manifolds. Organometallic iridium complexes, on which this thesis focuses, can support a broad range of molecular scaffolds and have been extensively explored as triplet emitters in organic light emitting diodes, photo-redox catalysts, chemosensors, electroluminescent devices and bioimaging applications. (Duan et al. 2003; Li et al. 2018; Ma et al. 2018; Tritton et al. 2022) This is thanks to their impressive luminescent properties such as high luminescence efficiencies, high thermal and chemical stabilities, large Stokes shifts, high phosphorescence quantum yield, as well as the versatility of tuning excited state properties which can be achieved through synthetic modification of ligand's structures. The high efficiency luminescence exhibited by Ir^{III} complexes is ascribed to their high capacity to access both singlet and triplet excited states via inter-system crossing (Jacko et al. 2010), commonly considered to be near unitary following excitation, (Ladouceur et al. 2013) resulting in potentially 100% efficient emission in response to electroluminescent excitation. (Kawamura et al. 2005)

Tuning the energy of the excited states Ir^{III} complexes can be achieved in different ways, such as binding different types of ligands to the metal centre. Selecting the appropriate ligands allows tuning the emission of the complexes across the visible spectrum from red at low energies to blue at high energies. Another approach for modifying the energy of the triplet excited states can be approached by altering the degree of π conjugation in main ligands or the ancillary ligand. Increasing π-conjugation stabilizes the energy of the triplet excited state and bathochromically shifts the emission band as well as increases the emission lifetime. Introducing substituents (electron donating or withdrawing groups) either on the main ligands or the ancillary ligand also enables to control the energy of the excited state and thus emission maximum. Due to the large number of possible ligand structures that can be bound to the iridium core, these complexes offer superb fine-tuning of luminescence through ligand adjustment. (Reddy and Bejoymohandas 2016; Caporale and Massi 2018; Stonelake et al. 2020; Elgar et al. 2021; Cheng et al. 2022). The dependency of emission bands on the ligand's structure has attracted many research groups to design novel Ir complexes with required properties to fit specific applications. In this thesis, I employed a spectroscopic analysis and computational calculation to identify the commonalities between the behaviours of groups of Ir^{III} complexes, and based on these observations, it is possible to use rational design for the effective engineering of a variety of these complexes with the desired emission and absorption qualities.

Organic dyads, which are made up of two or more chromophores, are another type of chromophore that possess accessible triplet states that can be populated and harnessed for commercial applications. Organic dyads have emerged as promising chromophores for application in optoelectronic devices as a low-cost and non-toxic alternative for transition metal complexes. (Guo et al. 2021) Similar to iridium complexes, the modification in the geometry of the dyad’s structure, altering the nature of the attached substituents or changing the degree of π-conjugation lead to a dramatic change in the dyad properties. (Bhosale et al. 2021) Therefore, naphthalimide dyads have been employed in a wide range of applications. For example, naphthalimides have been used in antimicrobial pharmaceutical applications due to the possibility of the interaction between their π-conjugated backbone and different active targets in biological systems. (Zhang and Zhou 2011) Other applications include fluorescence switches, laser active media, fluorescent markers in biology, ion probes and photoinduced electron transfer sensors (Kagatikar and Sunil 2022). Naphthalimide-based dyads are known to possess both singlet and triplet excited states with small energy differences (Δ_{ST}), which make them highly efficient in emitting strong and long-lived thermally activated delayed fluorescence (TADF) and/or phosphorescence. (Tang et al. 2019; Ye et al. 2022) Naphthalimide derivatives that display different emission colours (blue, yellow, orang and red) for organic light-emitting diode (OLED) applications have been widely reported. (Wang et al. 2010; Reineke et al. 2013; Arunchai et al. 2015; Luo et al. 2015)

Investigating the triplet excited states of a molecule can be challenging because it is not certain that the triplet excited state, unlike the singlet excited state, will be significantly populated after photoexcitation. This is particularly important for non-phosphorescent compounds or compounds with very little evidence of phosphorescence. Therefore, the use of an appropriate spectroscopic techniques are crucial. One such technique is nanosecond time-resolved transient absorption (TA) spectroscopy, which is commonly employed to study triplet excited states.

1.1.5 Transient/Flash Photolysis Spectroscopy

Steady state spectroscopic techniques, such as UV-Vis or infrared absorption and emission spectroscopies, are vital tools in chemical research. In steady state UV-vis absorption spectroscopy, a sample is typically probed with polychromatic ‘white’ light with a range of wavelengths ~200 < λ < 800 nm. One would then observe the characteristic interaction of the light with the studied sample manifested in the difference between the incident and transmitted intensities through the Beer-Lambert law. The steady state absorption spectrum of a sample in the solution phase is readily generated *via* continuous irradiation of the sample and simultaneously measuring the intensity of light transmitted through the sample. By comparison of the transmitted intensity with that of an adequate reference (a ‘blank’, normally consisting of just the solvent), the wavelength dependent absorption of the sample can be obtained. (Porter 1983).

The photophysical and photochemical processes, after light absorption by a sample molecule, are among the fastest events in chemical and biological systems. These processes take place on the femtosecond – nanosecond time domain (Figure 1.12). Therefore, if spectroscopists wish to probe these processes, one must develop tools to operate on these timescales. The advent of fast and ultrafast laser systems that produce pulses with nanosecond and femtosecond durations have enabled the investigation of short-lived transition states and transient species and opened the door to observing photophysical and photochemical process in real time (Berera et al. 2009; Farr et al. 2018).

Transient spectroscopy is an analytical technique applied in studying the excited states and observing their changes over the time. In contrast to steady state spectroscopy, the species studied by transient spectroscopy have an extremely short lifetime and are changing with time, hence the naming ‘transient’. Studying these transient species is achieved by inducing a photophysical or photochemical change in the sample under examination and observing the occurring changes using fast time resolved spectroscopy, transient absorption, or emission. Ideally these studies are performed not just with time resolution but also with wavelength resolution, thus maximizing the characteristic information gleaned from these measurements.

The flash photolysis/transient absorption (Stasicka and Marchaj 1977; Ferraudi 2010) technique was developed and introduced by Norrish and Porter in the late 1940s and the beginning of the 1950s. It is a powerful technique used to study the initial physicochemical impacts of light on the matter. The technique relies on irradiating a sample with a flash (a pulse) of light of extremely high-intensity and a very short duration (the pump). This results in generating high concentrations of excited states and/or intermediates, that can be identified and monitored by normal spectroscopic techniques, due to their high concentration. Therefore, a wealth of information about the structures and reactions of such transient species can be obtained. To detect the transient species generated by the pump, through monitoring the changes of their UV, Vis, or IR spectra, another light beam (the probe) is passed through the irradiated sample after a delay time, t, with respect to the pump pulse. The transient absorption spectrum (TA) is obtained by calculating the difference between the absorption spectra of the sample in ground and excited states. This can be better understood by looking at the diagram in figure 1.18.

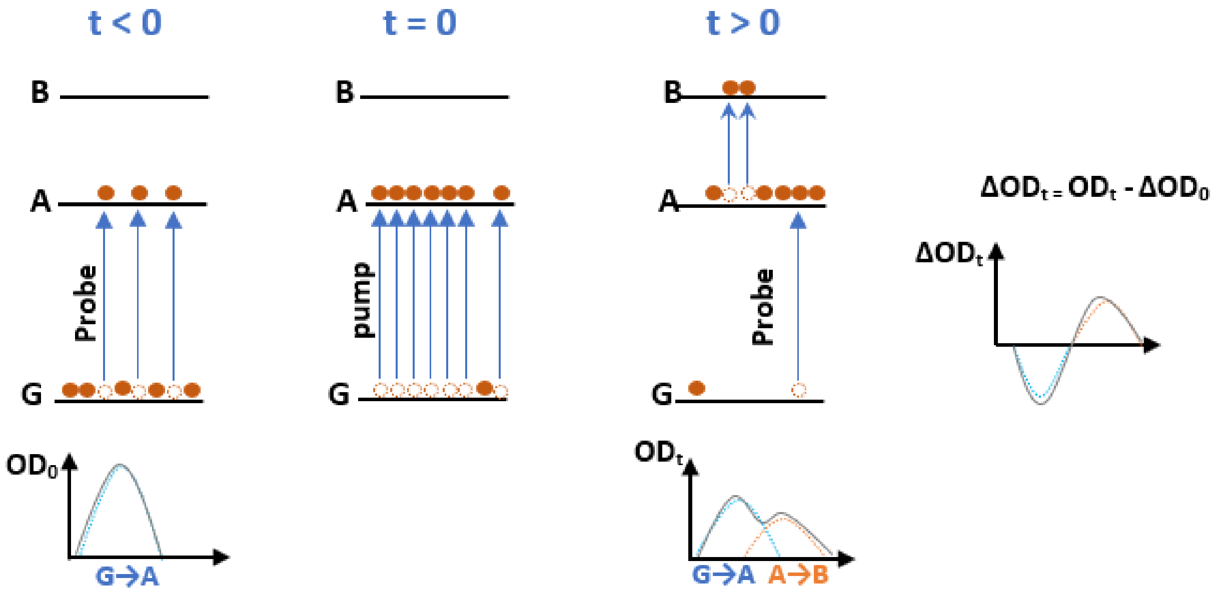

Figure 1.18 Schematic of a transient absorption experiment

Before the pump laser excites the sample (at t < 0), a reference spectrum is recorded using the probe beam, providing information about the absorption of the ground state of the molecular system under investigation, OD_0. The high-powered pump pulse then reaches the sample at t = 0, generating an excited state in the molecule. At t > 0, the probe is used to detect absorption from both A → B and G

→ A transitions, OD_t. The change in absorption between OD_t and OD_0 represents the transient absorption spectrum: $\Delta OD_t = OD_t – OD_0$. New features, +ΔOD, can be observed in TA spectrum due to excited state absorption, as well as a reduction in the ground state absorption -ΔOD. The decrease in G → A results from the depletion of the ground state by the pump pulse; which is known as ground state bleach GSB. By altering the time delay τ between the pump and the probe and recording the TA spectrum at each time delay, the TA spectra can be displayed as a function of time or a function of wavelength. TA spectrum can provide valuable information about the dynamic processes that occur in the sample under study, such as electron and/or proton transfer processes, excited-state energy migration, isomerization, and intersystem crossing. (Berera et al. 2009)

The lifetimes of the features observed in transient spectra can provide valuable information about the dynamics of the system being studied. By examining the lifetimes of various processes, we can learn about the nature of the states involved. For example, the duration of emission features can be used to distinguish between fluorescence and phosphorescence, as fluorescence typically has a shorter lifetime that coincides with the pump pulse. If an emission feature persists for hundreds of nanoseconds, it is likely to originate from a triplet state. By comparing the lifetimes of GSB, ESA, and emission features, we can assign different spectroscopic features to different states or species, as the differences in dynamics suggest they have different origins. On the other hand, if the lifetimes of features are correlated, they can be attributed to the same spectroscopic process. For example, if bleach and a transient absorption feature have similar lifetimes, they may be due to the same process: the depletion of a ground state absorption band by promoting the molecule to an excited state, creating a GSB feature, and the subsequent absorption band of the excited state creating an ESA. Both features will decay at the same time, indicating that the induced excited state decays back to the ground state, restoring the ground state absorption feature and decreasing the magnitude of the ESA.

Finally, recording spectra with the pump pulse alone, without the probe, and examining the light emitted by the sample provides time resolved luminescence measurements, which complement the transient absorption spectra.

1.1.6 Computational Chemistry Background

Computational chemistry (Cramer 2004) is cornerstone in chemical research. Computational chemistry calculations provide chemists with exceedingly useful tools for analysis of chemical phenomena, through the simulation of electronic properties and molecular interactions. They can also provide explanations of experimental findings that may be hard to explain in view of the collected experimental data only, and can provide insights into phenomena that are beyond current experimental methods. Therefore, computational chemistry methods can offer a powerful tool for deriving, testing, and validating mechanisms of chemical reactions.

Various computational methods are available for computing molecular properties, ranging from methods relying only on classical mechanics to more advanced methods based on quantum mechanics that deal with both static and dynamic electron correlation and provide an outstanding quantum mechanical description of molecular systems (e.g. MRCI). Density functional theory (DFT) (Burke and Wagner 2013) is somewhere between these two: DFT calculations are based upon the direct relationship between the energy of a system and the electron density of that system and provide a quantum mechanical prediction of molecular properties with comparatively low computational cost. DFT relies on spatially dependent electron density functionals to define the properties of multi-electron systems. DFT approach is an alternative to *ab initio* methods, such as Hartree-Fock theory for example that relies on construction of molecular orbitals from linear combinations of atomic orbitals using approximate solutions to the Schrodinger equation.

Utilization of DFT also allows time dependent DFT (TD-DFT) calculations to be performed, which enables the calculation of excited state properties. Time dependent DFT is a response method, where computation of electron density of the ground state in the original DFT ansatz forms the basis for TD-DFT calculations. TD-DFT is a very efficient computational tool for the calculation of excited state energies and vibrational frequencies. Additionally, TD-DFT calculations give access to information about transition energies and properties such as the contributions of molecular orbitals to electronic transitions, and oscillator strengths for electronic transitions.

In a DFT calculation a functional is required to approximate the electron correlation and exchange energies. A range of such functionals is available, each functional is designed for varying purposes. One hybrid functional, B3LYP (Becke, 3 parameter, Lee-Yang-Parr), is the most commonly used. (Yanai et al. 2004) This functional provides reasonable accuracy and relatively low computational expense over a very broad range of chemical problems. Hybrid DFT functionals use a combination of the electron exchange-correlation energy, that is either determined experimentally or estimated using another *ab initio* method, and the exact Hartree-Fock value. Below is the B3LYP equation (equation 1.9) employed for the electron exchange-correlation energy:

$$E_{xc}^{B3LYP} = E_c^{LDA} + E_x^{LDA} + a_c(E_c^{GGA} - E_c^{LDA}) + a_x(E_x^{GGA} - E_x^{LDA}) + a_0(E_x^{HF} - E_x^{LDA}) \quad \textbf{(Equation 1.9)}$$

Where a_0, a_c and a_x are fitting coefficients and have values of 0.2, 0.81 and 0.72 respectively, and were derived from the fitting of formation energies of small molecules. (Hansen 2010) The E_x^{HF} term is the Hartree-Fock exact exchange functional. The terms E_x^{GGA} and E_c^{GGA} are both generalised gradient approximations; the exchange functional Becke 1988 (B-88) and correlation functional of Lee, Yang and Parr, respectively (Becke 1988; Lee et al. 1988). The terms E_c^{LDA} and E_x^{LDA} are the local density approximation functionals for the correlation and exchange, respectively. This functional is used throughout this thesis.

For excited state calculations a Coulomb attenuating method or CAM-B3LYP is used, which is an augmented version of B3LYP. CAM-B3LYP incorporates additional terms for modelling long-distance interactions in a more accurate way. CAM-B3LYP comprises of 0.19 Hartree-Fock and 0.81 B-88 exchange interaction at short range and then 0.65 Hartree-Fock to 0.35 B-88 at long range (Yanai et al. 2004).

In most quantum computational methods, atomic orbitals are modelled using basis sets. Basis sets are made up of a set of mathematical functions that approximately describe the shape of the atomic orbitals and provide a representation of the orbitals that comprise the electronic structure of atoms. The best description of atoms is provided by basis sets that utilize Slater-type orbital functions, that rely on hydrogen-like orbital approximations where these basis sets can accurately describe the electron probabilities, with exponential decay at long distance from the nucleus but also satisfy Kato's cusp condition at short distance. However, the computational expense of Slater-type orbitals is normally considered too high to work with, as integral calculations are challenging to carry out with their linear combinations. Consequently, Gaussian functions (commonly called Gaussian-type orbitals, or GTOs) are the most used basis sets to describe orbitals. Compared to Slater-type orbitals, Gaussian-type orbitals decrease computational workload by 4-5 orders of magnitude and offer a much easier mathematical description of linear combinations of orbitals within a molecule. Although more Gaussian functions are needed in a basis set to get a similar representation of an orbital as obtained by Slater-type functions, this requirement does not diminish the efficiency gained from the ease of computation. Figure 1.19 depicts examples of the two functions.

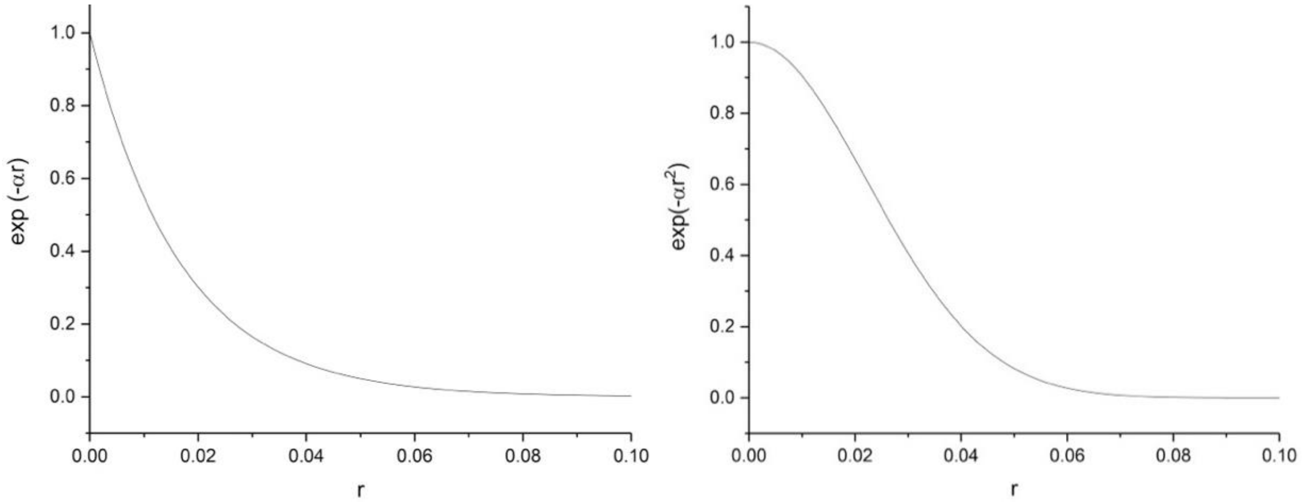

Figure 1.19 Typical Slater (left) and Gaussian (right) profile curves, as a function of an arbitrary radial distance variable r. These plots are indicative of functions used to model electronic orbitals. Slater functions are a better representation of electronic expectation values away from a nucleus but are more computationally costly to use.

Diverse basis sets that differ in the amount and type of functions used to describe the orbitals enable different levels of complexity and accuracy of calculations: a minimal basis set includes the minimum number of functions to describe an atom, and each orbital is described by a single function. More complete basis sets contain additional functions to add flexibility and account for polarisation, which enables modelling of *d* and *f* type orbitals in a more complete way. Various basis sets also contain 'diffuse' functions, that improve the accuracy of modelling the non-zero electron interaction 'tail' existing at long distances from the nucleus, which would be hard to emulate using a purely Gaussian description. Larger basis sets are required to describe the transition metal core electrons of transition metal complexes containing larger atoms, while the lighter atoms constituting the ligand structure can be described by smaller basis sets.

Due to the continuous improvements in the computational power of computers and the relatively computationally cheap nature of DFT calculations, density functional theory is becoming increasingly more popular among chemists and is widely used for the analysis of even very large chemical systems. Furthermore, the continuous improvements of easy-to-use software packages also contribute to the popularity and widespread use of DFT methods. Despite the unsuitability of DFT for producing quantitatively exact results, its ability to produce excellent qualitative analysis with a computationally cheap cost makes it a robust tool assist chemists to achieve reliable chemical analysis and useful predictions of chemical and spectroscopic properties. Utilization of DFT in the assignment of observed spectroscopic properties of transition metal complexes is a good example of such applications of DFT calculations, where these methods can produce simulations of the absorption and emission spectra of these transition metal complexes with high levels of accuracy, as well as providing a reliable assessment of the molecular orbitals taking part in those transitions.

1.1.7 Fluorescence Polarization and Anisotropy

Fluorescence anisotropy (FA) /polarization (FP) is an attractive and versatile technique that enables studying molecular orientation, rotational mobility, and interaction processes in solutions. FA/FP measurements have become prevalent particularly in biological chemistry and are applied extensively over a range of application fields such as disease diagnosis, detection of pollutants and contaminants in environmental screening and food safety studies in addition to the abuse of drugs in clinical chemistry and monitoring therapeutic drug levels in body fluids. (Jameson and Ross 2010; Zhang et al. 2019; Xiao and Zhen 2022)

General concept

Light can be described as oscillations of electromagnetic fields composed of electric and magnetic components perpendicular to the direction of propagation of light (Figure 1.20). In natural light, the electric field vector can assume any direction of oscillation normal to the light propagation direction. By using optically active devices, called polarizers, one direction of the electric vector can be isolated, generating plane polarized light (Figure 1.21). (Jameson and Ross 2010)

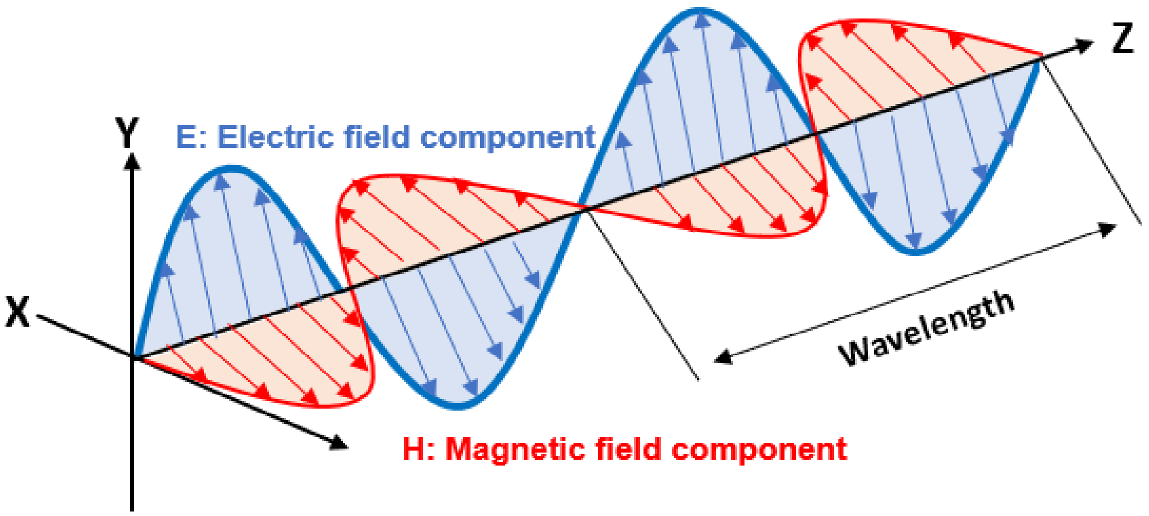

Figure 1.20 Oscillations of the electric and magnetic fields for a propagating electromagnetic wave.

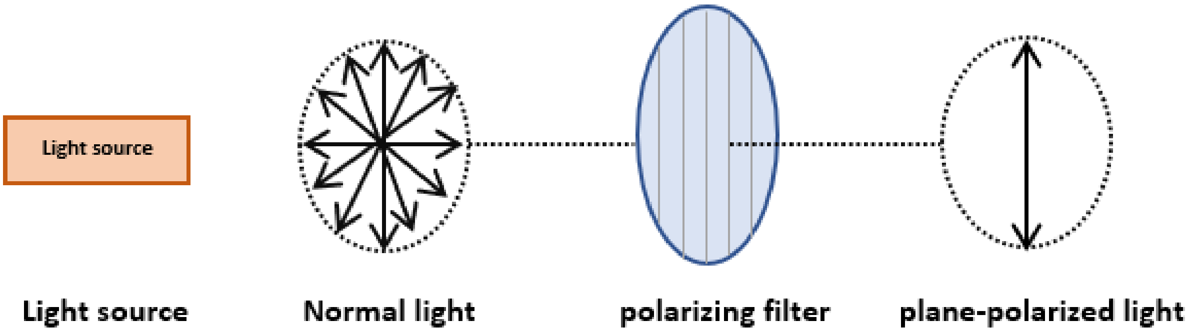

Figure 1.21 Generation of plane-polarized light from an unpolarized source.

By using polarized light for the excitation of a molecular sample under investigation, the resulting emission is also polarized in many cases. Samples displaying nonzero anisotropies are said to exhibit polarized emission, and the extent of polarization of the resulting emission is expressed in terms of polarization (***p***) or anisotropy (***r***).

These polarization properties are derived from an underpinning quantum chemical property that absorption or emission of a photon leads to a change in molecular dipole moment. The transition dipole moment that couples the initial and final state lies along specific vector direction within the molecule. Fluorophore molecules are randomly oriented in homogeneous solutions in the ground state, however upon excitation with polarized light, those fluorophore molecules that have their transition dipole moments oriented along the electric vector of the incident polarized light are preferentially excited, a process also known as photoselection. Therefore, the population of the excited state is partially oriented (Jameson and Ross 2010). If the photoexcited molecules were to promptly emit after photoexcitation, prior to molecular rotation, the emission of the oriented systems would primarily align with the vector of the transition dipole moment between excited and ground states, resulting in polarized emission.

The emission can become depolarized through several processes, the relative impact of which varies depending on the nature of sample under investigation. All chromophores have transition moments lying along specific directions within their molecular structures, and one common cause of depolarization is changing the direction of the transition moments as a result of rotational diffusion. Anisotropy measurements manifest the average angular displacement of the fluorophore taking place between light absorption and the resulting emission. The extent of rotational diffusion over the excited state lifetime governs this angular displacement. The rate of rotational diffusion is dependent on the shape and size of the rotating molecule in addition to viscosity of the solvent system. In solution, the rotational rate of fluorophores depends on the viscous drag exerted by the solvent. Therefore, changes in solvent viscosity are reflected in changes in fluorescence anisotropy. Hence, low-viscosity solutions of small fluorophores feature rotational diffusion rates that are is usually faster than the rate of emission. As a result, the emission is depolarized and the anisotropy becomes close to zero (Jameson and Ross 2010; Zhang et al. 2019; Xiao and Zhen 2022). Temperature also affects the polarization and anisotropy values since increasing the temperature increases the rate of molecular rotation and thus decreases the fluorescence polarization.(Kumke et al. 1997) With this in mind, the degree of polarization/ anisotropy of a fluorophore, at constant temperature and solution viscosity, is directly related to its molecular weight and shape, which changes upon binding with a macromolecule, such as a protein, and this change can be monitored as a function of solution make-up and time. In this example, monitoring fluorescence anisotropy can provide quantitative insights into molecular changes of the fluorophore such as efficacy of fluorophore-protein binding. This method has become widely used in clinical and biomedical fields, such as in bioimaging systems, immunoassays, ligand binding and drug discovery including G-protein coupled receptors and enzymes and protein-protein interactions.(Jones et al. 2008; Smith and Eremin 2008; Jameson and Ross 2010; Choi et al. 2012).

1.2 Aims and objectives

1.2.1 Iridium Complexes

The first aim of this thesis is to analyse the spectroscopic characteristics of a range of iridium complexes differing in main ligand structures, ancillary ligands and/or attached substituents. A combination of spectroscopic and computational methodology is used to gain a deep insight into the change in the spectroscopic properties due to the modification in ligand structures relative to prior work from the Beames group. This is performed with the purpose of developing a spectral database to create relationships between photophysical properties and ligand design. In this way, it would be possible to predict the photophysical properties of novel Ir^{III} complexes, and rational design used to design iridium complexes with desirable spectroscopic properties that fit potential academic or commercial applications.

1.2.2 Naphthalimide dyads

The second objective of this thesis is to apply the methodology developed for the analysis of iridium complexes to studying an N-substituted naphthalimide dyad and its thionated variants to investigate the formation of triplet states in these purely organic compounds. This class of materials has shown promise as OLED-like systems, harvesting the optical emission from both singlet and triplet manifolds, and may represent a non-toxic and cost-effective alternative to organometallic complexes for triplet sensitizers and medical applications. This assumes that the systems can be modified to enhance spin-forbidden processes. Therefore, studying the spectroscopic properties of naphthalimide dyads may provide valuable insights into the structure and function of these compounds relating to triplet harvesting activity, and thereby may lead to the design of new commercially relevant materials.

1.2.3 Fluorescence polarization measurements

The last aim of the thesis is to develop the current transient absorption spectrometer into a fluorospectrometer that can accurately detect and measure changes in the polarization of fluorescent molecules. The development of the instrument involves various stages, such as choosing suitable mechanical and optical components, which may include a light source, polarizers, a detector, and half-wave plates. The next step will be to assemble the components and calibrate the system by measuring its response to known polarization references. The sensitivity of the spectrometer will be tested using a variety of fluorescent molecules in solvents of different viscosities. Ultimately, the spectrometer will be used to study the emission polarization in two different applications: investigate how emission polarization changes by altering the fluorescent dye in novel dye-doped polymers, as well as study the binding between the antibiotic colistin and the outer membrane of the E. coli bacteria. If this fluorescence spectrometer can be successfully developed, it could provide an efficient, reliable, and cost-effective alternative to commercial instruments within the research group for examining binding interactions in chemical and biological systems.

2. Experimental

2.1 Transient/Flash Photolysis Spectrometer

The nanosecond transient measurements for all compounds analysed in this thesis were performed using an Edinburgh Instruments LP920 spectrometer that adapts a perpendicular pump-probe arrangement. All measurements were made in 3.5 ml cuvettes and have a path length of 1 cm. The sample is loaded in the cuvette and placed in the centre of the instrument before being irradiated by a pulsed xenon lamp, positioned on-axis to the detector system. Spectra can be obtained between $300 < \lambda < 800$ nm and a stable pulse time of approximately 2.5 ms. The pump excitation source was a laser (Continuum Surelite Nd:YAG, 1064, 532, 355 and 266 nm, 10 Hz) with a pulse width of approximately 8 ns. The laser input is at 90° to the detector and probe input, enabling the sample to be simultaneously stimulated by both sources and preventing any interference or damage to the detector caused by the laser and reducing scattering interference. This positioning also gives the advantage of being able to obtain emission data by using the pump laser only. This instrument has two distinct detection methods: an intensified charge-coupled device (ICCD) ($200 < \lambda < 750$ nm) and a second detector unit that uses a monochromator grating with a photomultiplier tube (PMT) detector ($200 < \lambda < 900$ nm): these are discussed below relating to the measurements to which they are best suited.

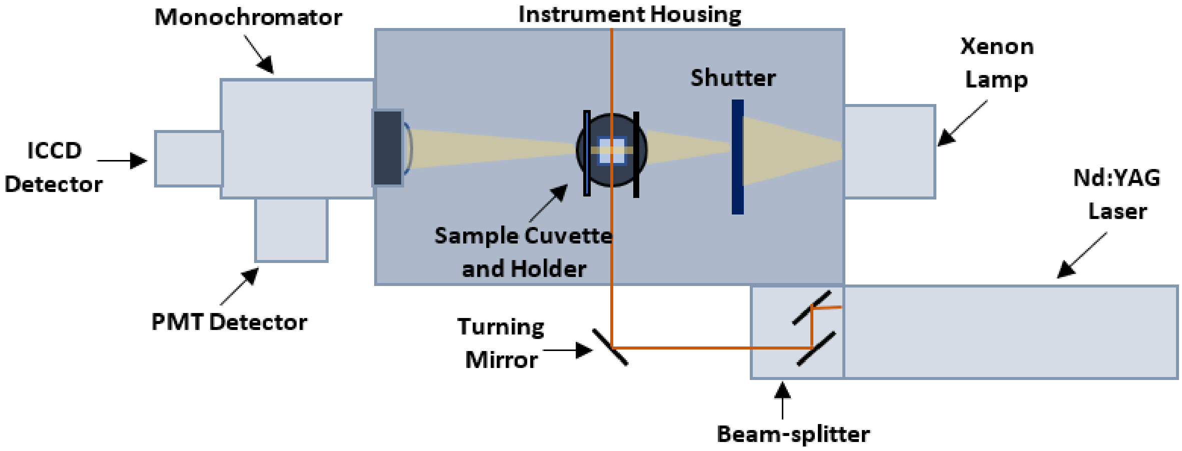

Figure 2. 1 Diagram of the transient absorption/flash photolysis spectrometer used in this work (Edinburgh Instruments LP920).

The flashlamp emits sufficiently spectrally stable light for most of the pulse duration, except for a short stabilization on period at the beginning of the pulse when the voltage is overdriven in order to initiate radiation. The early part of the stable lamp pulse (with respect to both intensity and emission spectrum) is used as a baseline (spectral background). To create transient absorption spectra, the excitation laser is triggered at a set interval after the lamp has stabilized. The excitation laser is triggered to create the transient species under investigation. To record transient absorption spectra, three measurements must be taken for each mode of operation (for kinetic or spectral measurements): one measurement performed with just the flash lamp, one with both the lamp and the laser pulse, and one with just the laser. The measurement with just the lamp serves as a probe background, and the measurement with just the laser provides an emission background. The difference between all these measurements is used to measure the change in the optical density (ΔOD) of the sample as a result of the laser pulse excitation. The equation used by the L900 spectrometer software to derive the emission subtracted ΔOD spectra is shown below in equation 2.1.

$$\Delta OD\ (\lambda) = \frac{I_p\ (\lambda)}{I_T(\lambda) - I_F\ (\lambda)} \qquad \textbf{(equation 2.1)}$$

Where $I_p(\lambda)$ = probe background intensity, $I_T(\lambda)$ = measurement intensity, $I_F(\lambda)$ = fluorescence background intensity.

A ΔOD spectrum measures the difference between the absorption of the excited state or photo-product and the absorption of the ground state, and it typically contains negative and positive features. As discussed in the theoretical background of transient absorption spectroscopy on page 24, negative features represent a decrease in optical opacity, and can be observed due to the depletion of the ground state, indicating that the excited state or photo-product absorbs less light at the corresponding wavelength than the ground state did prior to excitation. Emission of the sample following excitation could also contribute to ΔOD spectrum as a decrease in optical opacity; however, such decreases are usually subtracted from the emission background. Positive peaks indicate an increase in optical opacity, meaning that the excited state or photo-product absorbs more light at that wavelength than the ground state.

2.1.1 Transient Absorption Spectra

All transient absorption spectra (ie. Data displayed as ΔOD vs. wavelength) displayed in this work were obtained using ICCD detector which affords recording an entire TA spectrum from a single laser shot, over the range $200 < \lambda < 750$ nm. However, TA spectra were typically only recorded between $350 < \lambda < 700$ nm due to the low output of the probe lamp beyond these wavelengths (figure 2.2) which greatly decreases the signal-to-noise ratio. In order to obtain a spectrum, the ICCD camera is opened, or begins imaging, shortly after the laser pulse. The camera then captures the horizontally wavelength-dispersed lamp light for a specific time gate equivalent to a shutter time on a conventional camera. A single measurement does not provide a time-resolved spectrum; however, the delay time between the laser pulse and the flashlamp can be frequently changed and a TA spectrum recorded each time. A combination of these spectra can be used to assess the evolution of the transient over time.

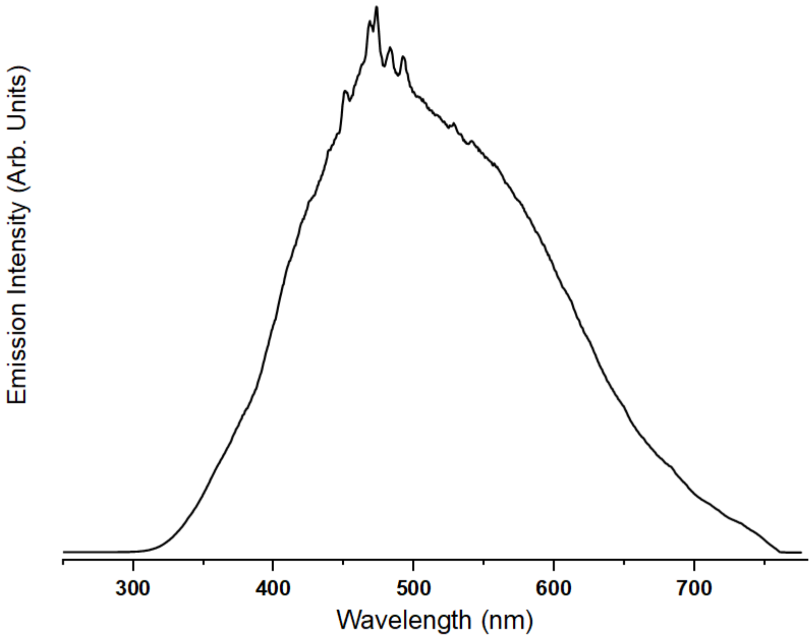

Figure 2.2 ICCD spectrum of the Xe flash lamp emission spectrum. This lamp is used as the probe in the LP920 spectrometer, which limits the wavelengths over which transient features can be observed. At the edges of this spectrum, as the intensity decreases, there is increased noise in the transient spectra.

2.1.2 Transient Kinetics

A photomultiplier tube (PMT) detector can be used in combination with a monochromator to conduct kinetic studies of a transient signal. This setup allows time-resolved monitoring of the changes in the absorption and emission of the sample following laser excitation over a certain time period, providing data that can be used to generate state lifetimes. This is used in conjunction with the ICCD approach: features observed in the transient absorption and emission traces from the ICCD can be identified for kinetic measurements, and the wavelengths of these features are selected in the monochromator. Time-resolved ΔOD spectra can be obtained using a PMT with good responsivity in the range of $200 < \lambda < 900$ nm by scanning narrow bands of wavelengths.

PMT (PhotoMultiplier Tube) detectors are devices used to detect and measure light. PMT detectors work by using an electron multiplier to convert the incoming light into an electrical signal. When the light strikes the photocathode, electrons are emitted and accelerated through a series of dynodes, creating an intrinsically amplified electrical signal. This signal can then be measured, allowing highly sensitive and precise measurements of light intensity. This method, therefore, is appropriate for use when detecting even weak output signals. The PMT is unable to differentiate between incident wavelengths, so a monochromator is used to choose the desired wavelength and block out all others.

The monochromator employed in this work is set to a bandwidth of 2.05 nm, as it provides a satisfactory signal to noise ratio without affecting the accuracy of the results, as most of the features studied here have a broad wavelength range. Crucially this bandwidth matches the spectral resolution of the ICCD camera, thereby matching resolutions of both detection methods.

The oscilloscope used to convert the detector's output to digital form has a temporal resolution of approximately 4 ns, which is shorter than the laser pulse duration of around 10 ns. However, although some of the compounds studied in this work have transient features with lifetimes that are 3-5 orders of magnitude larger than the oscilloscope resolution, the kinetic lifetimes can still be accurately determined from the data obtained without needing any additional processing. The PMT can be also used to construct a wavelength map, repeatedly stepping the wavelength being analysed and essentially constructing a 3D dataset in intensity, time and wavelength. Although accurate, each measurement in this mode typically requires hundreds of lasers shots, and can therefore suffer from long term instabilities. It is also worth noting that this mode of measurement is challenging for light-sensitive compounds, as repeated measurements can cause damage to the sample, resulting in inconsistent spectra, and this is where the ICCD approaches are essential. This PMT based method however is incredibly helpful in measuring the early-time response of a compound, as the laser intensity is too high for the ICCD detector to safely measure close to the onset of the pulse. It can also be used to provide an alternative measurement to corroborate the ICCD measurements at later timescales.

2.2 Computational Calculations

The optimization of the iridium complex structures (both the lowest singlet and triplet spin states) were carried out in the Gaussian 09 software package using the B3LYP functional with the 6-31G* basis set for the lighter atoms, and the Stuttgart-Dresden core potential and basis set for iridium. The complexes were computed as cationic where applicable and without the PF_6^-/BF_4^- counterion. The photophysical properties were calculated in an implicit solvent (matching that used in experiments) using a self-consistent reaction field model, which simulates the solvent effects by treating the complex within a dielectric continuum. Very tight convergence criteria and an ultrafine integration grid were used for all optimizations. All optimizations were confirmed as minima through harmonic vibrational frequency calculations. For each optimized geometry, single-point energy calculations were performed for the opposing spin state to the optimization process, by freezing the geometry but evaluating the energy. This yielded the triplet energy at the singlet geometry and the singlet energy at the triplet geometry for each of the complexes. By combining the results of single-point calculations with geometry optimizations, the vertical transitions between the ground states of the singlet and triplet states (spin forbidden transitions) can be determined. The energy difference between singlet optimized geometry and the single-point triplet state energy calculation performed using this geometry is corresponding to the spin forbidden absorption transitions $\mathbf{S_0 \rightarrow T_n}$. Similarly, the vertical emission transitions $\mathbf{T_1} \rightarrow \mathbf{S_0}$ can be calculated from the energy difference between triplet optimized geometry and the single-point singlet state energy calculation. The adiabatic emission energy is calculated from the difference between the lowest optimized singlet and triplet geometries, as shown in figure 2.3.

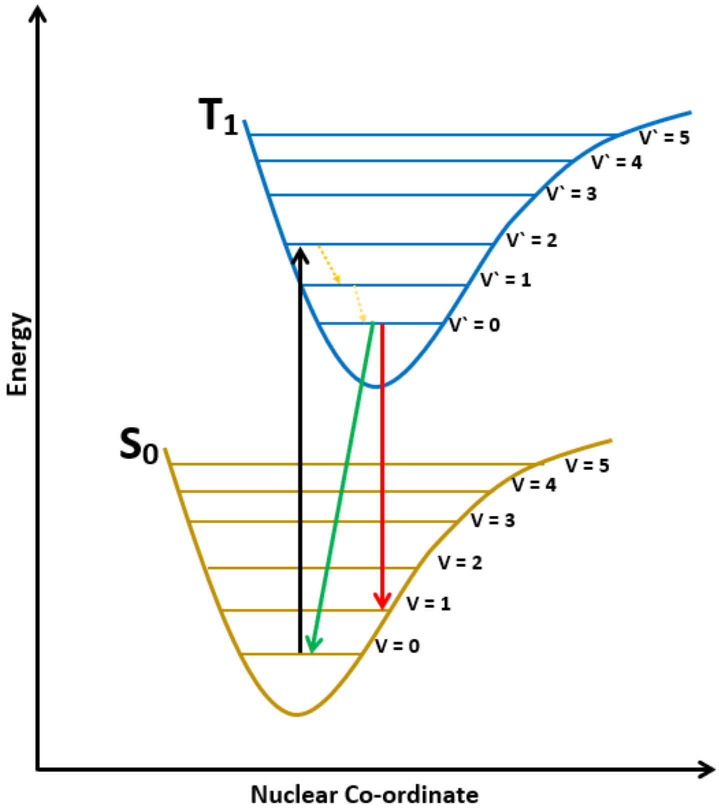

Figure 2.3 Morse potential diagram showing an example of the Franck-Condon vertical transitions for spin-forbidden absorption $S_0 \rightarrow T_1$ (black arrow) and phosphorescent emission $S_0 \rightarrow T_1$ (red arow) to and from a triplet state, beginning and ending at the singlet ground state. The Franck-Condon adiabatic transition for spin-forbidden phosphorescent emission is also shown (green arrow).

Simulations of spin-allowed absorption features were conducted using time-dependent density functional theory (TD-DFT) calculations, employing the CAM-B3LYP functional. Molecular orbital decomposition were conducted with the GaussSum software package. The calculated Kohn-Sham molecular orbitals were visualized by the Avogadro software package.

2.3 Sample Preparation

All iridium complexes analyzed in this work were synthesized by the Pope group at Cardiff University, and subsequently purified by silica gel column chromatography. Their synthesis was confirmed by the Pope group using ^{1}H and ^{13}C NMR as well as high resolution mass spectrometry. Naphthalimide compounds were synthesized by Anna Wright at Cardiff University in the Yi-Lin group. These compounds were also purified through column chromatography and characterised using ^{1}H and ^{13}C NMR and mass spectrometry. Each sample was dissolved in HPLC-grade solvent and placed in a quartz cuvette for spectroscopic measurements.

Based on recorded absorption spectra, the transient absorption measurements for iridium complexes and naphthalimide compounds were performed using 355 nm as the pump excitation wavelength. This wavelength was chosen because it was the lowest energy available pump wavelength with strong absorption that enabled access to the full visible emission/TA spectra of each compound. The spectroscopic experiments were typically carried out at ambient temperature (approx. 20 °C), although some spectra and lifetime measurements were performed at 77 K using an Oxford Instruments Optistat DN2 variable temperature liquid nitrogen cryostat.

The degassing procedure for oxygen-free measurements (emission and transient absorption) involved the use of a custom cuvette with a Youngs tap for sealing the vessel and allowing the inlet and outlet of gases, as well as a bulb for freezing the sample. The cuvette apparatus was connected to a Schlenk line equipped with a vacuum pump and a nitrogen output line. The custom cuvette was filled with 3.5 ml of the aqueous sample, which was kept in the bulb compartment and submerged in liquid nitrogen to freeze the sample. Once the sample had frozen, the cuvette was opened to the vacuum to extract the air, and kept under vacuum for 3-5 minutes while still immersed in liquid nitrogen. The cuvette tap was then closed to seal the cuvette under a vacuum, while allowing the sample to thaw. This procedure was repeated eight times, and on the last time, the nitrogen line was used to refill the apparatus with dry N_2. The cuvette apparatus was then sealed to maintain the nitrogen atmosphere and removed from the Schlenk line.

3. Transient Spectroscopic and Computational Analysis of Poly-substituted Iridium (III) Quinoxaline Complexes

3.1 Introduction

Transition metal organometallic compounds consist of transition metal ions (iridium in this study), complexed with organic ligands. This chapter focuses on iridium complexes, with a single metal core. The electronic structure of Ir is [Xe] $5d^7 6s^2$, and its complexes can exist in a variety of oxidation states between -2 to +6. Here we consider primarily the +3 oxidation state, with electron configuration [Xe] $5d^6$. The geometrical arrangement of donor atoms around an Ir^{III} metal centre is normally octahedral (Greenwood and Earnshaw 1997).

For free Ir^{+3} in the gas phase with no ligand field, the five *d*-orbitals are degenerate, in which the electrons have equal energy. In an octahedral crystal field, six ligands approach the transition metal ion along the *x, y*, and *z* axes. Therefore, the $d_{x^2-y^2}$ and d_{z^2} orbitals (which lay along these axes) overlap with the ligands' orbitals and form two bonding orbitals, σ_{z^2} and $\sigma_{x^2-y^2}$, and two antibonding orbitals, $\sigma_{z^2}^*$ and $\sigma_{x^2-y^2}^*$; whereas the d_{xz}, d_{yz}, and d_{xy} orbitals, which are directed between the ligands, are not used in the construction of σ molecular orbitals, and thus are considered nonbonding or, with appropriate ligands, may be involved in a *π* molecular-orbital system. Consequently, the originally degenerate d orbitals are split into two different levels. The energies of the d_{z^2} and $d_{x^2-y^2}$ orbitals (referred to as $\boldsymbol{e_g}$) are destabilized due to greater interactions with the ligands, while *the* d_{xy}, d_{xz}, and d_{yz} orbitals (referred to as $\boldsymbol{t_{2g}}$) decrease with respect to the free energy level and become more stable, shown in figure 3.1. This is known as crystal field splitting and is denoted by Δ_o (or Δ_{oct}) for octahedral complexes. The magnitude of the splitting Δ_o is affected by both the nature of the ligands, and the nature of the metal ion and its oxidation state. (Demas and DeGraff 1991; Crabtree 2009). The Δ_o value increases with increasing oxidation state and the radii of the metal ions due to increasing repulsion between *d*-electrons and the ligands.

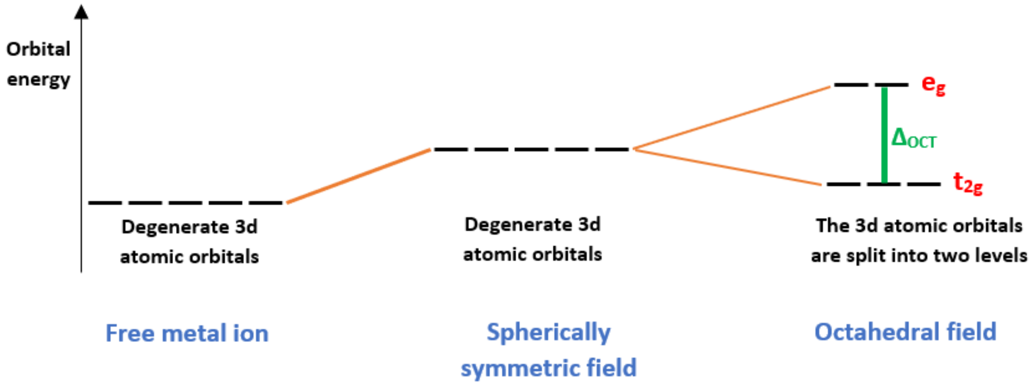

Figure 3.1 Diagram of changing degeneracies of metal d-orbitals upon complexation with an octahedral arrangement of ligands.

The metal $\boldsymbol{t_{2g}}$ orbitals may be used for π bonding to certain types of ligands in octahedral complexes. Ligands with empty *p* or *π* symmetry orbitals, that are close in energy to the metal d orbitals, can accept electrons from filled metal orbitals. This is commonly called back bonding because the direction of electron donation is opposite to that found in sigma bonding. These ligands are called *π* acceptor ligands, also known as 'strong field' ligands, and induce a large value of Δ_O. If ligands have filled *p* or *π* symmetry orbitals with suitable energy, they are able to donate electrons to an empty metal orbital. These ligands are called *π* donor ligands or 'low-field ligands' and decrease the value of Δ_O, shown in figure 3.2 below. Based on the nature of this *π*-interaction between the ligand orbitals and the *d*-orbitals on the central atom, and thus the size of the splitting Δ that they produce, ligands can be ordered in a list called the spectrochemical series. (Sathyanarayana 2001)

In octahedral complexes, a d^6 electronic configuration can be low or high spin, with a configuration of $\boldsymbol{t_{2g}^6\ e_g^0}$ or $\boldsymbol{t_{2g}^4\ e_g^2}$ respectively. The distribution of electrons between the $\boldsymbol{t_{2g}}$ and $\boldsymbol{e_g}$ levels is profoundly affected by Δ_o. If Δ_o is large (i.e., strong field ligand), it is energetically more favourable to pair electrons in the $\boldsymbol{t_{2g}}$ level than to keep them unpaired by distributing them throughout the $\boldsymbol{t_{2g}}$ and $\boldsymbol{e_g}$ levels (Hund's rule). Heavier metals, such as 3rd row metals, have a larger splitting of the $\boldsymbol{t_{2g}}$ and $\boldsymbol{e_g}$ levels (large Δo value) than 1st row metals. Therefore, Ir^{III} complexes are invariably low spin, regardless of ligand field strength, due to the position of iridium in the transition metal series and the charge on the ion itself. (Demas and DeGraff 1991; Schneider 2013) Although inorganic chemists typically use the terminology of $\boldsymbol{t_{2g}}$ and $\boldsymbol{e_g}$ orbitals, it is also convenient to re-label these in a fashion more commonly considered in physical chemistry, where in octahedral complexes they are termed HOMO (highest occupied molecular orbital) and LUMO (lowest unoccupied molecular orbital) respectively. It is worth noting here that the terminology 'octahedral' is commonly used in organometallic chemistry to define metal complexes coordinated with six ligands, even if the complexes do not formally have an O_h point group geometry.

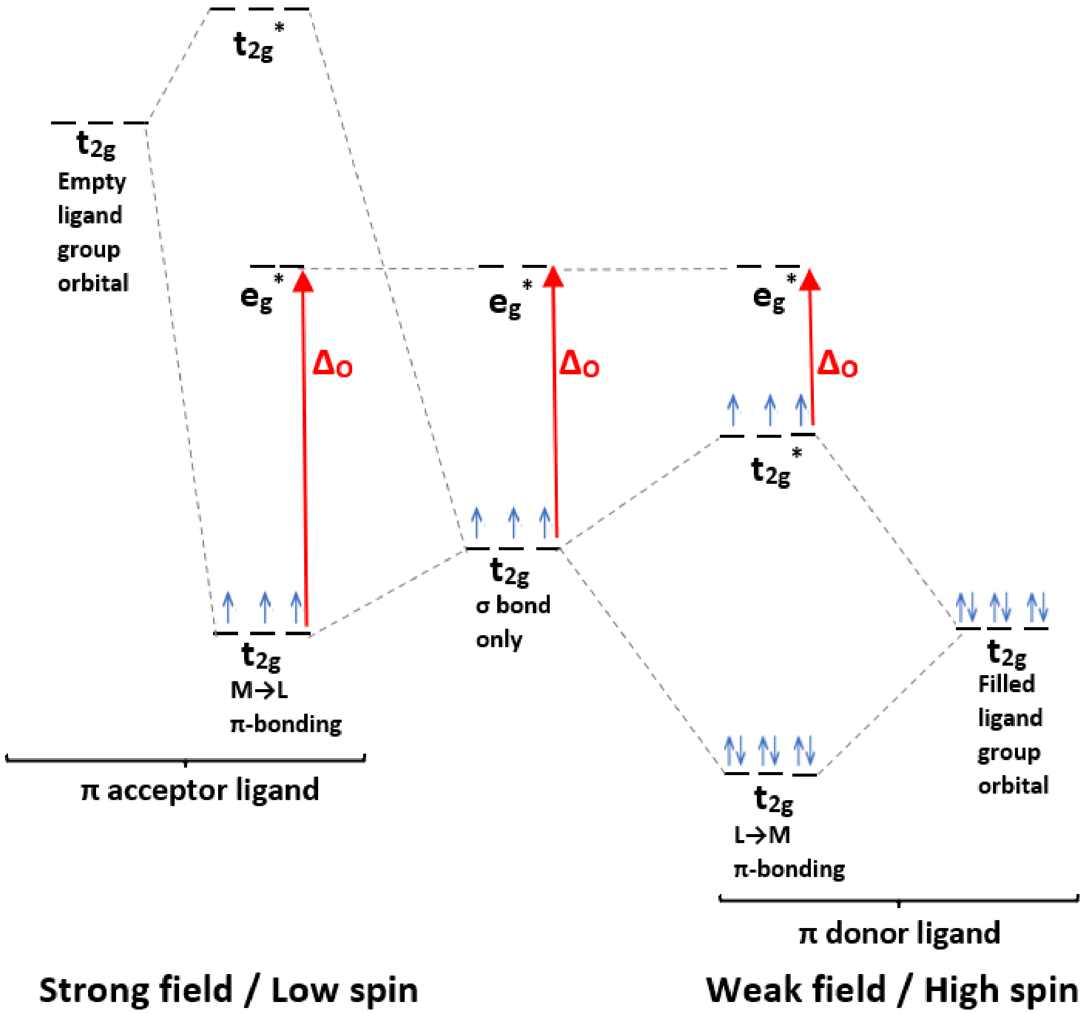

Figure 3.2 The molecular orbital energy levels in an octahedral complex with π-donor ligands and π-acceptor ligands.

Ligands that have more than one donor atom can bond to the same central metal ion through multiple sites to form stable ring-like compounds. Complexes with such ligands are called chelates, and ligands that perform this type of bonding are described as polydentate ligands. The most common polydentate ligands are bidentate and tridentate ligands, which coordinate with 2 and 3 bonds respectively. The stability of chelating complexes is generally attributed to the increase in total entropy when a multidentate ligand displaces more than one monodentate ligand. Generally, in the octahedral complexes, three bidentate ligands, or two tridentate ligands are bound to a metal centre. The complex is described as 'homoleptic' if all of the ligands are identical, and 'heteroleptic' if this is not the case. (Martell et al. 1994)

All synthesized Ir^{III} complexes involved in this work are heteroleptic, and consist of either bidentate or tridentate ligands; with general structures $[Ir(C\text{^}N)_2(X\text{^}Y)]^{n+}$ or $[Ir(N\text{^}N\text{^}C)_2]^{n+}$, respectively. These C^N ligands are called cyclometallating ligands and bonded to the iridium core via C and N atoms, where C has a formal negative charge to balance positive charges on Ir^{III}. The other ligand with a different structure (X^Y) is known as the ancillary ligand.

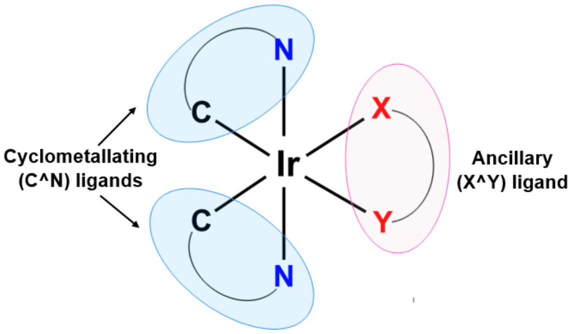

Figure 3.3 An illustration of the general structure of Ir^{III} complexes with bidentate C^N ligands and an ancillary (X^Y) ligand.

Cyclometallating ligands form strong covalent Ir-C and Ir-N bonds to the Ir^{III} core because the carbon atom in these ligands is a relatively strong σ-donor while the nitrogen atom is a good π-acceptor. This increases electronic interactions between the ligand π-orbitals and the *d*-orbitals of the Ir^{III}. Thus, incorporation of these ligands results in increased Δ_o splitting, higher-lying metal-centered excited states (MC) of the complex and as a consequence higher thermal stability at room temperature. Together with a large spin-orbit coupling induced by the heavy Ir^{III} ion, these complexes typically exhibit intense phosphorescence at room temperature, and through synthetic ligand modification high colour tunability of emission across the entire visible spectrum. (Chi and Chou 2010) By synthetic modifications of the cyclometallating *and* ancillary ligands, it is possible to alter the photophysical and electrochemical properties of Ir^{III} complexes to suit specific applications in diverse areas such as organic light-emitting diodes (OLEDs), photocatalysis, and luminescence-based sensors.

The optical properties and related applications of the organometallic complexes are strongly dependent on the characteristics of their emissive excited states, typically the lowest excited state, which can be described based on the different orbital types that lead to their formation. In principle, the excited states can be divided into four general types:

- Metal centred (MC), also known as *d*-*d*, excited states derive from the excitation of a bonding electron from the $\boldsymbol{t_{2g}}$ level to the $\boldsymbol{e_g}^*$ level and lead to weak absorption bands. These transitions are formally forbidden due to the LaPorte selection rule.
- Ligand centred (LC) $\pi\pi^*$ states arise from the promotion of a bonding π-electron or non-bonding orbital of the ligand to an antibonding π^* orbital of the same. These transitions are very intense and are localised on the ligands.
- Ligand to metal charge transfer (LMCT) which involves the transition of an electron from a ligand to a metal orbital.
- Metal to ligand charge transfer (MLCT) states which involves the movement of an electron from a metal-based orbital to a ligand orbital (e.g., π^*). These transitions occur in complexes with π acceptor ligands. MLCT and LMCT transitions often have absorption bands in the visible region of the electromagnetic spectrum with high extinction coefficients.

The two primary transitions that dominate the lowest excited states of Ir^{III} complexes are metal to ligand charge transfer (MLCT) and ligand-centered (LC) transitions. (Demas and DeGraff 1991; Demas and DeGraff 1997; Crabtree 2009)

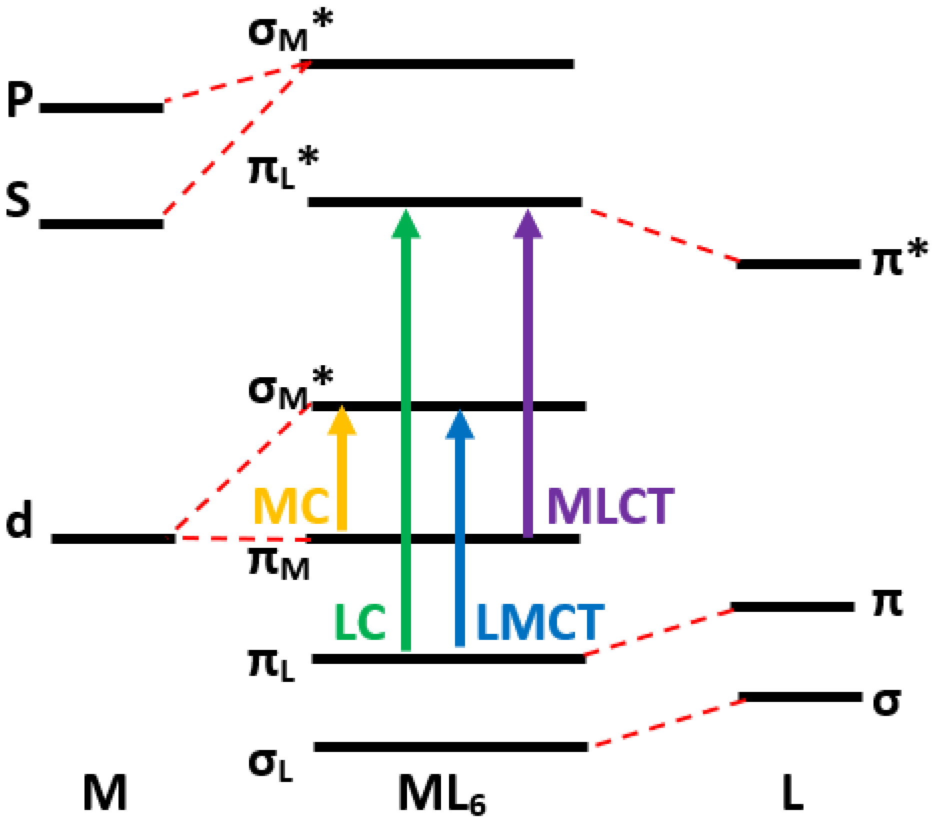

Figure 3.4 Schematic and simplified molecular orbital diagram for Ir^{III} complex in octahedral coordination geometry. The labelled arrows represent, (1) metal centered ligand field transition (dπ → dσ), (2) metal to ligand charge transfer (MLCT), (3) intraligand charge transfer (ILCT) or ligand to ligand charge transfer (LLCT) (4) ligand to metal charge transfer (LMCT) transitions.*

Strong spin-orbit coupling, induced by mixing contributions of the *5d* orbitals of the Ir^{III} centre into the excited states electronic character, facilitates intersystem crossing from any initially populated singlet manifold excited states to energetically accessible triplet states. Spin orbit coupling is a relativistic effect that occurs when an electron's spin is coupled to its orbital motion, causing formally spin forbidden transitions to become allowed. The triplet states populated during these ISC processes are always below their analogous singlet states and are responsible for phosphorescence. The ability of iridium complexes to access both singlet and triplet excited states is the reason for their high quantum efficiency luminescence, which theoretically approaches 100%. (Chou and Chi 2007; Tao et al. 2017; Wang et al. 2017)

The emissive excited states of phosphorescent cyclometallating Ir^{III} complexes mainly arise from triplet metal to ligand charge transfer (^{3}MLCT) or the mixture of ^{3}MLCT and ligand-centered (^{3}LC) transitions. (Lamansky et al. 2001; Lowry and Bernhard 2006; Zhou et al. 2008; Chou et al. 2011; Reddy and Bejoymohandas 2016; Han et al. 2016; Ma et al. 2017; Haghighatbin et al. 2018; Na et al. 2019; Kim et al. 2022) Furthermore, ligand–to–ligand charge transfer (^{3}LLCT) transitions are also possible in some Ir^{III} complexes. (You et al. 2008; Zhao et al. 2008; Reddy and Bejoymohandas 2016) Given the localization of non-negligible electron density within both HOMO and LUMO orbitals on the organic ligands, this once again demonstrates that it is possible to tune the electronic properties through ligand alteration. The lowest excited states in both singlet and triplet manifolds can be modified (leading to. for example, modified emission colour and luminescence lifetime) in a desirable way by deliberately adjusting the energy of metal and ligand orbitals. This can be achieved through inserting substituent groups into the cyclometalating or ancillary ligand systems, changing the level of aromaticity present on the ligands themselves (extended conjugation systems), or replacing the ligand parent structure entirely (altering ligand field strength). (Lamansky et al. 2001; Lowry and Bernhard 2006; Flamigni et al. 2007; Reddy and Bejoymohandas 2016)

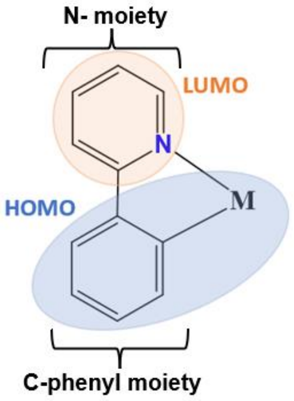

Figure 3.5 An illustration of the localisation of the HOMO and LUMO on the general structure of a cyclometallated metal complex in which 2-phenylpyridine is the ligand. The same localisation of the HOMO and LUMO occurs with complexes of other cyclometallating ligands. Generally, the HOMO is localised on the metal centre and the cyclometallated aryl ring of the ligand. The LUMO is localised on the heterocycle, the pyridyl moiety in this case.

Incorporating electron-withdrawing (EWG) and electron-donating (EDG) groups onto the organic framework of cyclometallating ligands is one of the most effective approaches for tuning, and fine-tuning, the lowest excited state energy. It is found that the introduction of an electron-withdrawing group (such as F, CF_3 and CHO) into the C-phenyl moieties gives rise to an increase in the HOMO–LUMO energy gap by stabilizing the HOMO level, ‘pulling’ electron density from the metal centre, whereas donating groups (such as –$C(CH_3)$ or –OCH_3) have an opposite effect. In contrast, introducing EWGs onto the N-moieties lowers the LUMO level by increasing the electron affinity of the cyclometallating ligand. Another strategy used to stabilize the HOMO involves increasing the electron deficiency of the Ir-C bond through incorporating electronegative atoms such as nitrogen into the phenyl ring of the C^N ligand. The presence of a nitrogen atom changes the distribution of electron density and creates a partial positive charge at carbon atoms in *ortho* and *para* positions to the nitrogen atom. This increases the electron-withdrawing ability of the aryl ring and hence stabilizes the HOMO. Likewise changing the degree of conjugation in the structure of cyclometallating or ancillary ligands is a further method exploited for modifying the lowest excited state. Increasing the *π*-conjugation by the attachment of an additional aromatic ring leads to a decrease in the energy levels of the LUMOs and hence the HOMO–LUMO gap. (Bejoymohandas et al. 2015; Lee et al. 2015; Xu et al. 2015)

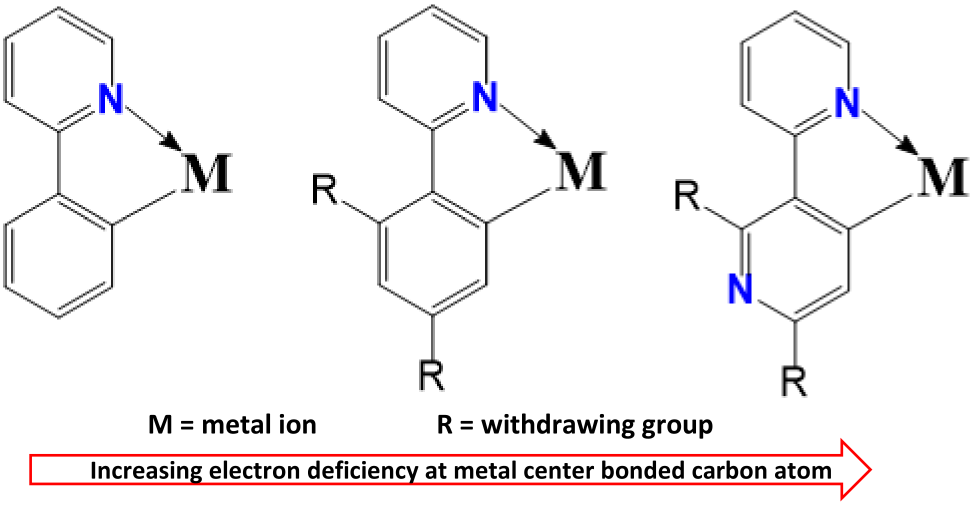

Figure 3.6 Comparison of electron deficiency at Ir^{III} *bonded carbon atoms in cyclometallating ligands.*

Although the ancillary ligand may not directly contribute to the excited state, it can also influence the excited state energy via altering the electron density at the metal center. (Dedeian et al. 1991; Colombo et al. 1994; Tamayo et al. 2005; Lowry and Bernhard 2006).

Cyclometalated Ir^{III} complexes have attracted the attention of research groups around the world due to their tunability of photophysical properties as described above. Through diligent synthetic choices, one can create complexes with a wide range of excited state lifetimes, high quantum efficiencies, flexible colour tuning, and good thermal stability. Therefore, they have been extensively explored as triplet emitters in organic light emitting diodes, photo-redox catalysts, photosensitizers, light–emitting electrochemical cells, metallo–pharmaceuticals, photodynamic therapy, bioimaging, and chemosensors.(You et al. 2014; Reddy and Bejoymohandas 2016; Caporale and Massi 2018; Hu et al. 2019; Zeng et al. 2019; Abbas et al. 2020) The efforts to design and develop new 'generations' of iridium complexes with improved photophysical properties is continuous and ongoing. With this in mind, the Beames group in collaboration with the Pope group at Cardiff University have studied a variety of novel luminescent Ir^{III} complexes with cyclometallating ligands, with the aim of tuning the emissive properties of iridium complexes through the adjustment of the ligand structure. The electronic properties of a series of Ir^{III} complexes with poly-substituted phenyl-quinoxaline ligands (scheme 3.1) have been experimentally studied using time-resolved luminescence and transient absorption spectroscopy and the results are supported by DFT calculations. (Phillips et al. 2018)

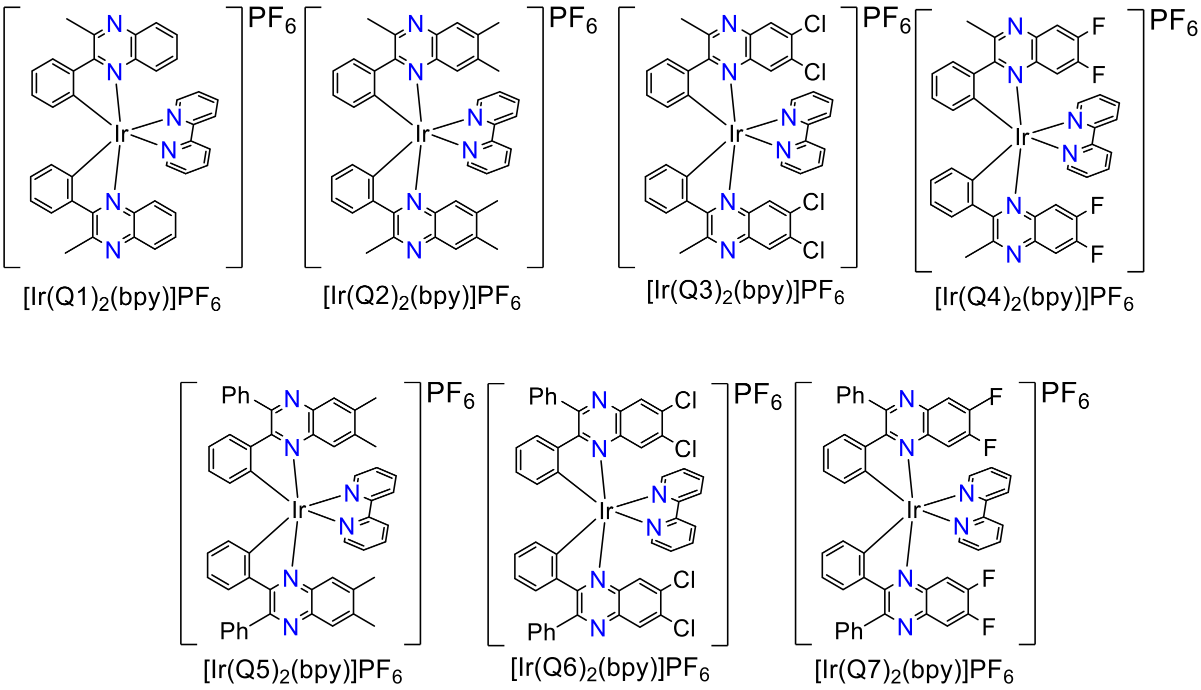
$[Ir(Q1)_2(bpy)]PF_6$ $[Ir(Q2)_2(bpy)]PF_6$ $[Ir(Q3)_2(bpy)]PF_6$ $[Ir(Q4)_2(bpy)]PF_6$

$[Ir(Q5)_2(bpy)]PF_6$ $[Ir(Q6)_2(bpy)]PF_6$ $[Ir(Q7)_2(bpy)]PF_6$

Scheme 3.1 Structures of the synthesized heteroleptic Ir^{III} complexes published previously by our research group.

As can be observed in the above figure, the seven complexes are formed of two phenyl quinoxaline ligands and a bipyridine ancillary ligand. The complexes were divided into two sets, distinguished by substitution with either a methyl group or a phenyl ring. Each set of complexes features Me, Cl and F groups as the substituents. Firstly, UV/Vis and emission spectra show that all the above complexes feature absorption and phosphorescent emissions in the visible region pertaining to metal to ligand charge-transfer (MLCT) transitions. The emission energy of these complexes were found to be finely tunable as a function of the nature of substituents on cyclometallating ligands. Time-dependent DFT calculations suggest a strong contribution of spin-forbidden MLCT transitions to the absorption bands in the visible region. The potential application of these complexes as sensitisers in TTA upconversion was evaluated using 9,10-diphenylanthracene as the acceptor. The experimental data revealed impressive upconversion quantum yields of up to 39.3 % in the case of methylated derivatives. (Phillips et al. 2018)

In a later study, the same base ligands were utilized to develop a new series of ten heteroleptic, neutral Ir^{III} complexes of the form $[Ir(L)_2(N\hat{}O)]$ where the ancillary ligand is picolinate or pyrazinoate (Scheme 3.2). (Stonelake et al. 2020)

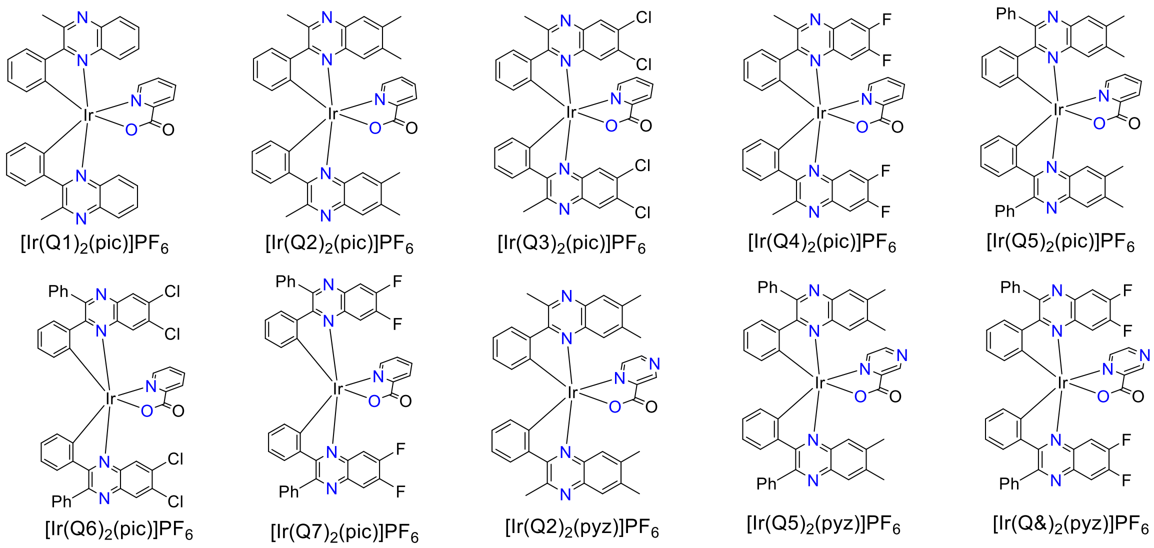

[Ir(Q1)$_2$(pic)]PF$_6$ [Ir(Q2)$_2$(pic)]PF$_6$ [Ir(Q3)$_2$(pic)]PF$_6$ [Ir(Q4)$_2$(pic)]PF$_6$ [Ir(Q5)$_2$(pic)]PF$_6$

[Ir(Q6)$_2$(pic)]PF$_6$ [Ir(Q7)$_2$(pic)]PF$_6$ [Ir(Q2)$_2$(pyz)]PF$_6$ [Ir(Q5)$_2$(pyz)]PF$_6$ [Ir(Q&)$_2$(pyz)]PF$_6$

Scheme 3.2 Structures of the mixed-ligand Ir^{III} picolinate and Ir^{III} pyrazinoate complexes published previously by our research group.

Again, their electronic characteristics were studied using UV−vis, time-resolved luminescence, and transient absorption spectroscopies in addition to cyclic voltammetry for evaluating their redox properties. The experimental data revealed that all the prepared complexes are phosphorescent in the red region of the visible light spectrum ($633 < \lambda_{em} < 680$ nm). Computational and spectroscopic studies suggest that the emission of these complexes in the visible light region are due to a combination of spin-forbidden MLCT and quinoxaline-centered transitions. Therefore, the emission wavelength of these complexes can be modulated via the substitution pattern of the cyclometallating quinoxaline ligand or by changing the ancillary ligand. It is noteworthy that the adjustment on the quinoxaline ligands results in fine tuning of emission bands whereas careful selection of the ancillary ligand allows broad or fine tuning of the band positions.

3.2 Bis-Quinoxaline Iridium (III) Complexes with Bipyridine Ancillary ligand

3.2.1 Complex Structures

Carrying on the aforementioned work and seeking to further understand the relationship between spectral properties and ligand design, the optical properties of a new set of Ir^{III} complexes are investigated here. These compounds feature the same base cyclometallating quinoxaline ligands that were used in previous work, but with different substitution patterns (shown in Scheme 3.3) and are investigated using a combination of spectroscopic techniques and computational chemistry approaches. The complexes were synthesised by the Pope group at Cardiff University, and consist of two phenyl-quinoxaline ligands (as main cyclometallating ligands) and an ancillary ligand coordinated to the iridium core. The substituent groups on C^N ligands are attached to either phenyl moiety or quinoxaline part in order to examine the effect that the position of substituents has on the absorptive and emissive properties of the complex. All the complexes are monocationic and paired to PF_6 counterions.

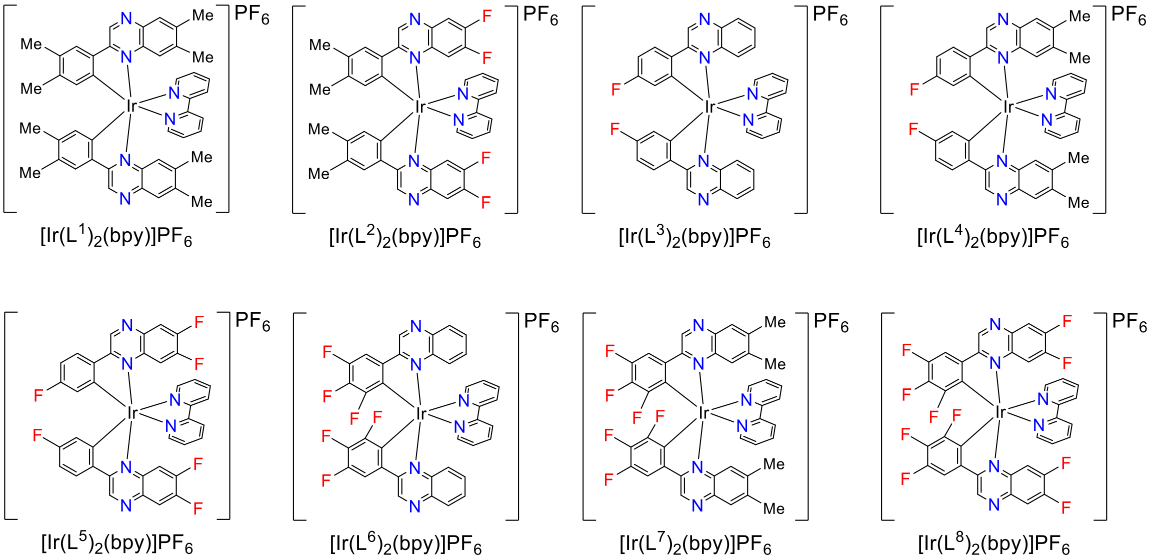

$[Ir(L^1)_2(bpy)]PF_6$ $[Ir(L^2)_2(bpy)]PF_6$ $[Ir(L^3)_2(bpy)]PF_6$ $[Ir(L^4)_2(bpy)]PF_6$

$[Ir(L^5)_2(bpy)]PF_6$ $[Ir(L^6)_2(bpy)]PF_6$ $[Ir(L^7)_2(bpy)]PF_6$ $[Ir(L^8)_2(bpy)]PF_6$

Scheme 3.3 The eight quinoxaline-based complexes with bipyridine ancillary ligand $[Ir(L^{1-8})_2(bipy)]^+$*.analyzed in this chapter.*

3.2.2 Steady State Absorption Spectra

The steady state UV-Vis absorption spectra of all complexes were recorded as solutions in acetonitrile at a concentration of 10^{-5} M, shown in figure 3.7. The complexes all exhibit similar spectra with three distinct absorption features: firstly, a higher energy band at $230 < \lambda < 320$ nm with a high molar absorption coefficient, secondly a moderately intense band at $320 < \lambda < 400$ nm, and finally a weaker broad band $\lambda > 400$ nm. A comparison of the absorption spectra of complexes with the free ligand data (figure 3.8) suggests that the short wavelength bands are associated with ligand centered $\pi\pi^*$ transitions, as similar features can be observed in the absorption spectrum of the free diquinoxalinepyridinyl ligand, which is bathochromically shifted upon coordination to Ir^{III} . Across the series of complexes, variations in the position of these bands are dictated by the nature and the position of the substituents on the quinoxaline ligands; with the longest wavelength band being the most sensitive to the variation in ligand structure. The difference in the spectroscopic features' responses to changes in the complex structure indicates that these features arise from different origin states. Previous studies on related Ir^{III} complexes have defined these lower energy features as singlet metal to ligand charge and spin-forbidden singlet-to-triplet MLCT transitions, where the latter is facilitated by the heavy Ir atom. Therefore, at this point, the high intensity absorption bands at $\lambda < 300$ nm are assigned as singlet-to-singlet spin-allowed ligand-centred (^{1}LC), and the features between $300 < \lambda < 400$ nm are attributed to both ligand-centred (^{1}LC) and metal to ligand (^{1}MLCT) transitions, considering their strong intensity and high energy. The broad bands at $\lambda > 420$ nm are assigned as a triplet spin-forbidden metal to ligand (^{3}MLCT) charge transfer, given the small energy gap typically found between the **S_0** and **T_1** states in Ir^{III} complexes and the reduced probability of this spin-forbidden process.

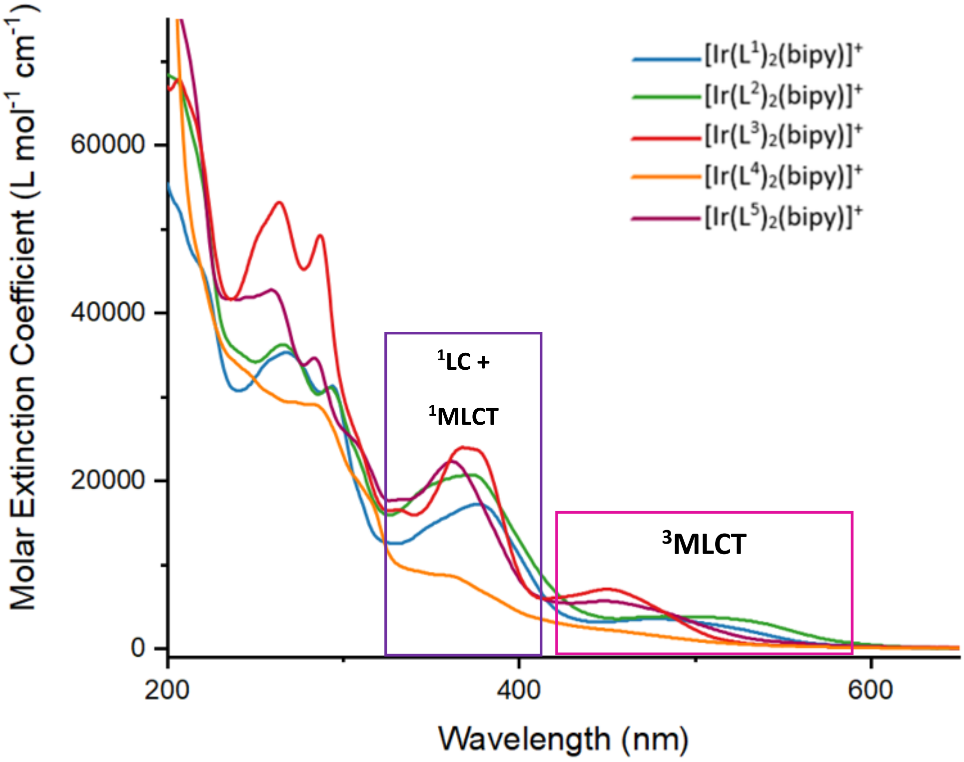

Figure 3.7 Normalised UV-Vis absorption spectra of [Ir(L$^{1\text{-}5}$)$_2$(bipy)]$^+$complexes in acetonitrile (1x10^{-5} M).

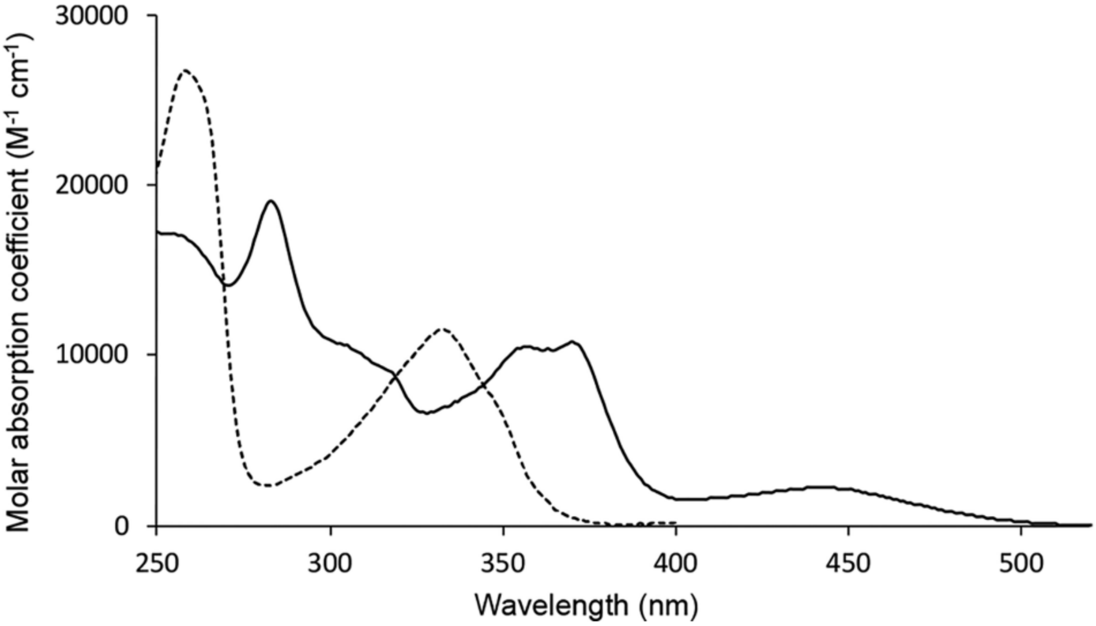

Figure 3.8 Example UV-vis. Absorption spectra comparing L^8 (dashed line) and [Ir(L^8)$_2$(bipy)]PF$_6$ (solid line) in acetonitrile.

In general, incorporating withdrawing fluorine substituents on the phenyl ring results in a significant hypsochromic shift of the MLCT features relative to the methylated variants. This blue shift is increased further by increasing the number of fluorine atoms on the phenyl ring. For example, polyfluorinated $[Ir(L^{6-8})_2(bipy)]PF_6$ complexes show more-blue shifted MLCT features compared with mono-fluorinated or methylated counterparts. Conversely, the addition of fluorine substituents to the quinoxaline ring leads to a bathochromic shift of absorption bands. Thus, the most red-shifted absorption is represented by $[Ir(L^2)_2(bipy)]PF_6$, which combines the methylated phenyl electron donor and the difluorinated quinoxaline. These observations are in agreement with the TD-DFT calculations discussed later in this chapter.

3.2.3 Emission Spectra

One of the key objectives of this study was to investigate the tunabilty of the emission bands by varying substituents on the ligands. The room temperature emission spectra of the complexes were obtained in aerated acetonitrile using a 355 nm excitation wavelength and collected using the ICCD camera. The complexes all display broad and typically featureless bands, with only the blue-shifted variants showing subtle vibronic spectra, suggesting that the emitting state of the complexes could be a mixture of both MLCT and LC excited states. The spectra are displayed in figure 3.9 below and normalised for comparison purposes.

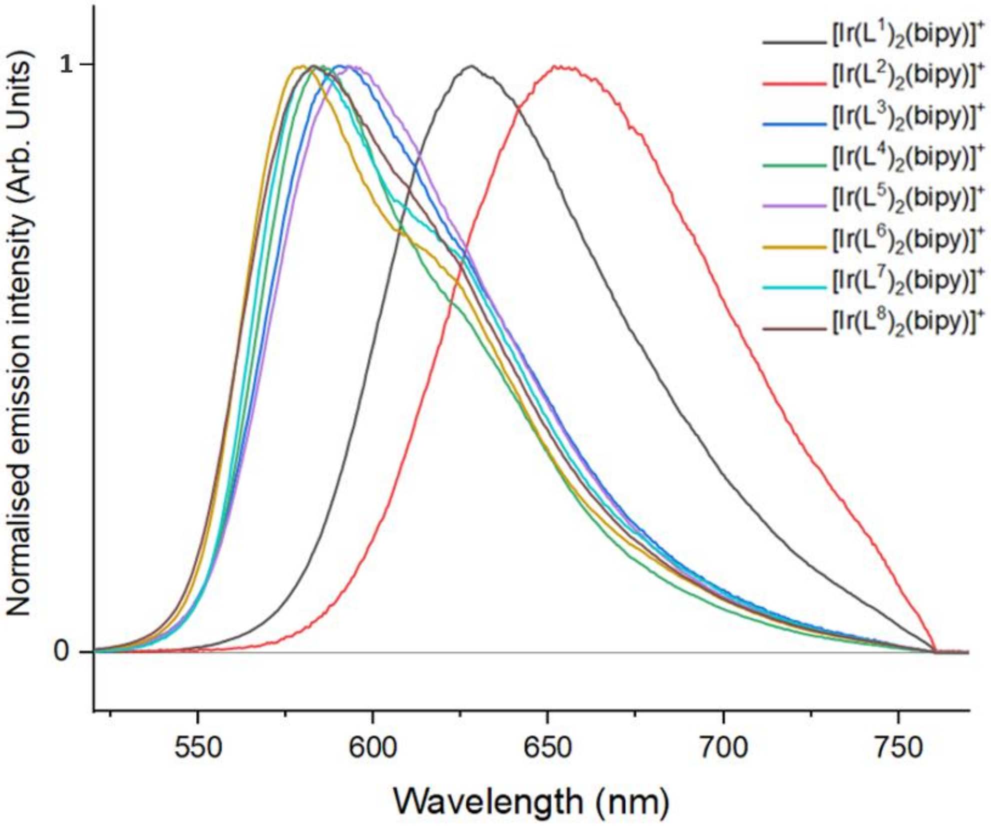

Figure 3.9 Normalised emission spectra recorded for all $[Ir(L^{1-8})_2(bipy)]^+$complexes (293 K, acetonitrile, $1x10^{-5}$ M).

As seen in the spectra above, the onset and emission peak maxima vary depending upon both the nature and the position of substituents located on the cyclometalated ligands, with peak tuning between $579 < \lambda_{em} < 655$ nm. The ordering of the band maxima is similar to the trend found in the UV-Vis. absorption data, with complexes that are fluorinated on the phenyl moiety, $[Ir(L^{3\text{-}8})_2(bipy)]PF_6$, displaying a blue shift compared to their methyl-substituted partners, $[Ir(L^1)_2(bipy)]PF_6$ and $[Ir(L^2)_2(bipy)]PF_6$. These experimental data are well matched by DFT calculations, correctly simulating the order of spin-forbidden $\mathbf{T_1} \rightarrow \mathbf{S_0}$ emission energies. It is noteworthy that the substitution on the phenyl ring in cyclometalated ligand results in a much broader shift in the emission bands while the substitution on the quinoxaline moiety allows a much finer tuning of emission. Thus, using this polysubstituted ligand backbone provides a significant tunability of the emission of Ir^{III} complexes. This allows precise control over the emission wavelengths (or colors) of the complexes, which can be advantageous for tailoring the ligand design to specific optoelectronic applications, such as OLEDs, sensors, and photovoltaics.

Excited state lifetimes were obtained from time-resolved data fit to a monoexponential function. The lifetime values range between $215 \text{ ns} < \tau < 747$ ns, which is typical of phosphorescent complexes in oxygenated solutions. It is noteworthy that the peak emission wavelength is strongly correlated with lifetime, ie., the most red-shifted methylated-phenyl complexes $[Ir(L^1)_2(bipy)]PF_6$ and $[Ir(L^2)_2(bipy)]PF_6$ exhibit the shortest phosphorescence lifetimes, consistent with the energy gap law. (Ramasamy and Hurtubise 1996) Under deoxygenated conditions, the luminescence lifetimes show moderate to significant increases, reaching several microseconds in some complexes, shown in table 3.1. These elongated lifetimes correlate well with the reduced quenching in the absence of $^3O_2$, emphasizing the triplet nature of the emissive state. Low temperature (77 K) luminescence measurements for the complexes were also obtained using frozen acetonitrile glass. The emission spectra closely resemble the room temperature spectra in terms of band onset and trends in emission maxima within the series (Figure 3.10). The emission lifetimes observed at 77 K for the complexes all extend into the microsecond regime, which is consistent with measurements under nitrogenated (deoxygenated) conditions. These observations, again, afford a definitive assignment of the emissive state as being triplet in character.

Table 3. 1 Emission lifetime for all complexes at 77K and under deoxygenated conditions

Complex	λ_{em} / nm	τ / ns At 77K	τ / ns Deoxygenated
$[Ir(L^1)_2(bipy)]PF_6$	628	2691±19	1886 ±1
$[Ir(L^2)_2(bipy)]PF_6$	655	2362 ± 20	1659 ± 5
$[Ir(L^3)_2(bipy)]PF_6$	590	1795 ± 132	3416 ± 16
$[Ir(L^4)_2(bipy)]PF_6$	585	3636 ± 32	4872 ± 15
$[Ir(L^5)_2(bipy)]PF_6$	596	4210 ± 51	1387 ± 1
$[Ir(L^6)_2(bipy)]PF_6$	580	4818 ± 275	5322 ± 20
$[Ir(L^7)_2(bipy)]PF_6$	583	5184 ± 66	6518 ± 45
$[Ir(L^8)_2(bipy)]PF_6$	583	4306 ± 63	1446 ± 1

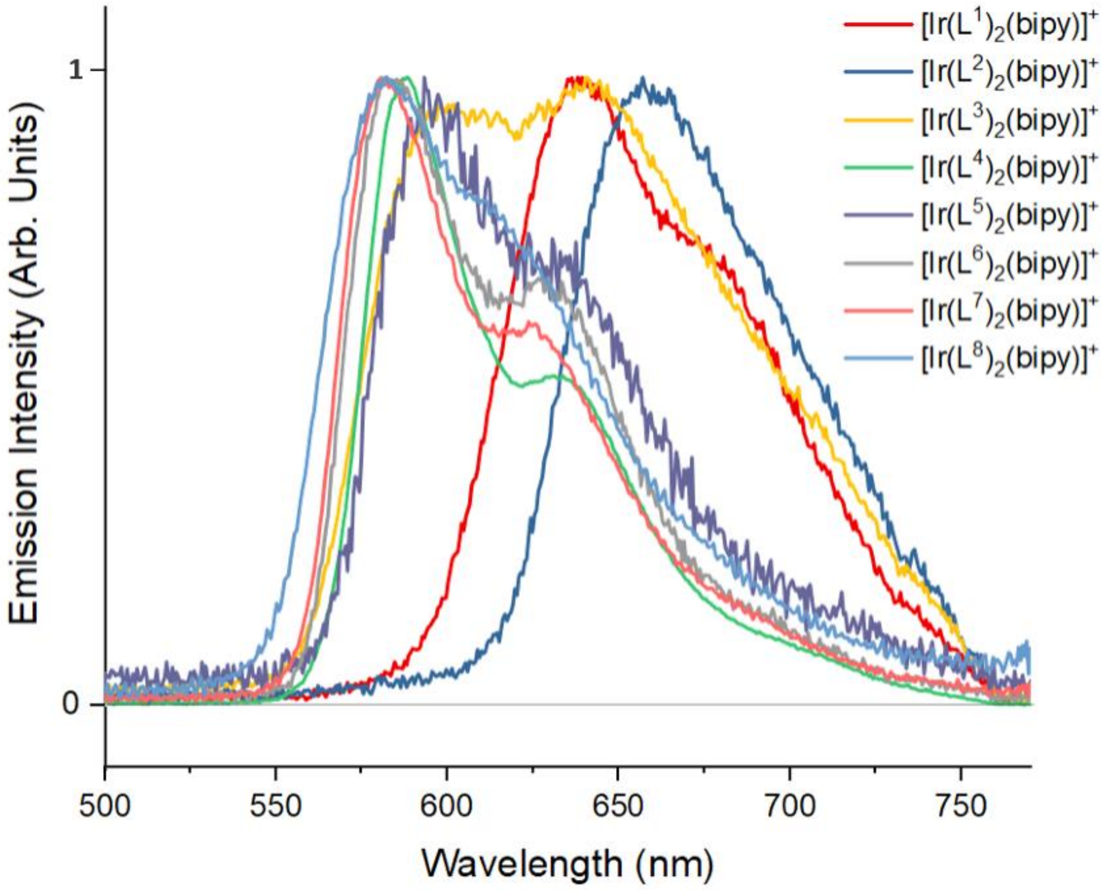

Figure 3.10 Normalised emission spectra recorded for all $[Ir(L^{1-8})_2(bipy)]^+$ complexes (77 K, acetonitrile, $1x10^{-5}$ M).

3.2.4 TA Spectra

Nanosecond transient absorption (TA) spectra of all Ir^{III} complexes were again obtained in aerated acetonitrile upon excitation at 355nm, and using the ICCD as the mode of detection. The TA spectrum of the $[Ir(L1)_2(bipy)]^+$ complex is shown below in figure 3.11 as an example spectrum.

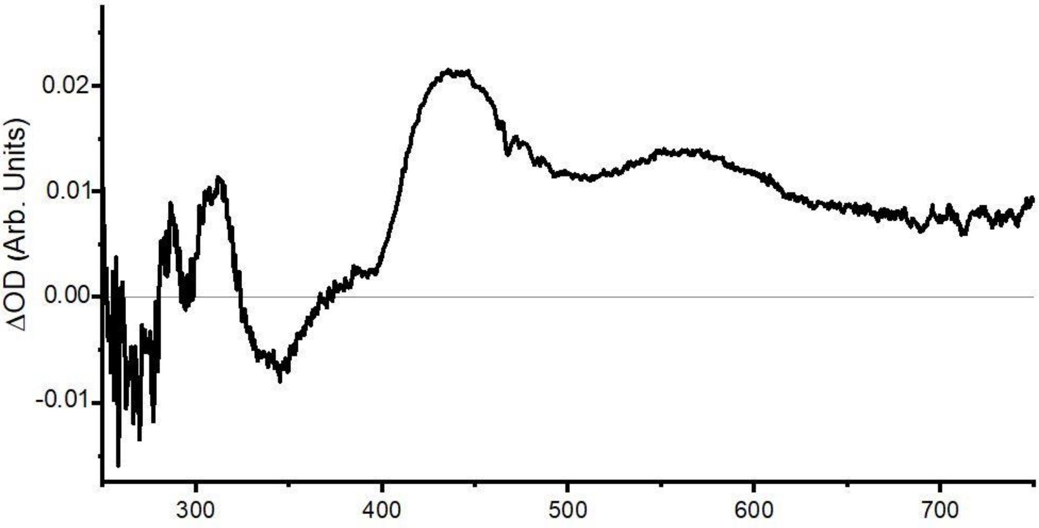

Figure 3.11 Transient absorption spectrum of the $[Ir(L^1)_2(bipy)]^+$ complex in acetonitrile in acetonitrile ($1x10^{-5}$M), λ_{ex} = 355 nm, delay time = 50 ns . The grey line represents ΔOD = 0

In general, the eight complexes all produce nearly identical spectral profiles, and are quite similar to that of the related Ir^{III} complexes previously reported. (Phillips et al. 2018) The TA spectra all possess three major features in the visible spectral region. The negative feature, ca. $350 < \lambda < 400$ nm, is assigned as a ground-state bleach: arising from the depletion of the ground-state ^{1}MLCT absorption band. This ground-state bleaching is split into a doublet in the fluorinated-phenyl complexes, but does not seem to form this doublet structure in their methylated analogues. The strong positive features in the regions $410 < \lambda < 435$ nm and $550 < \lambda < 670$ nm, are ascribed to triplet-to-triplet excited state absorption transitions, with the lower energy triplet absorption feature being noticeably more intense and better resolved in the fluorinated-phenyl complexes (figure 3.12).

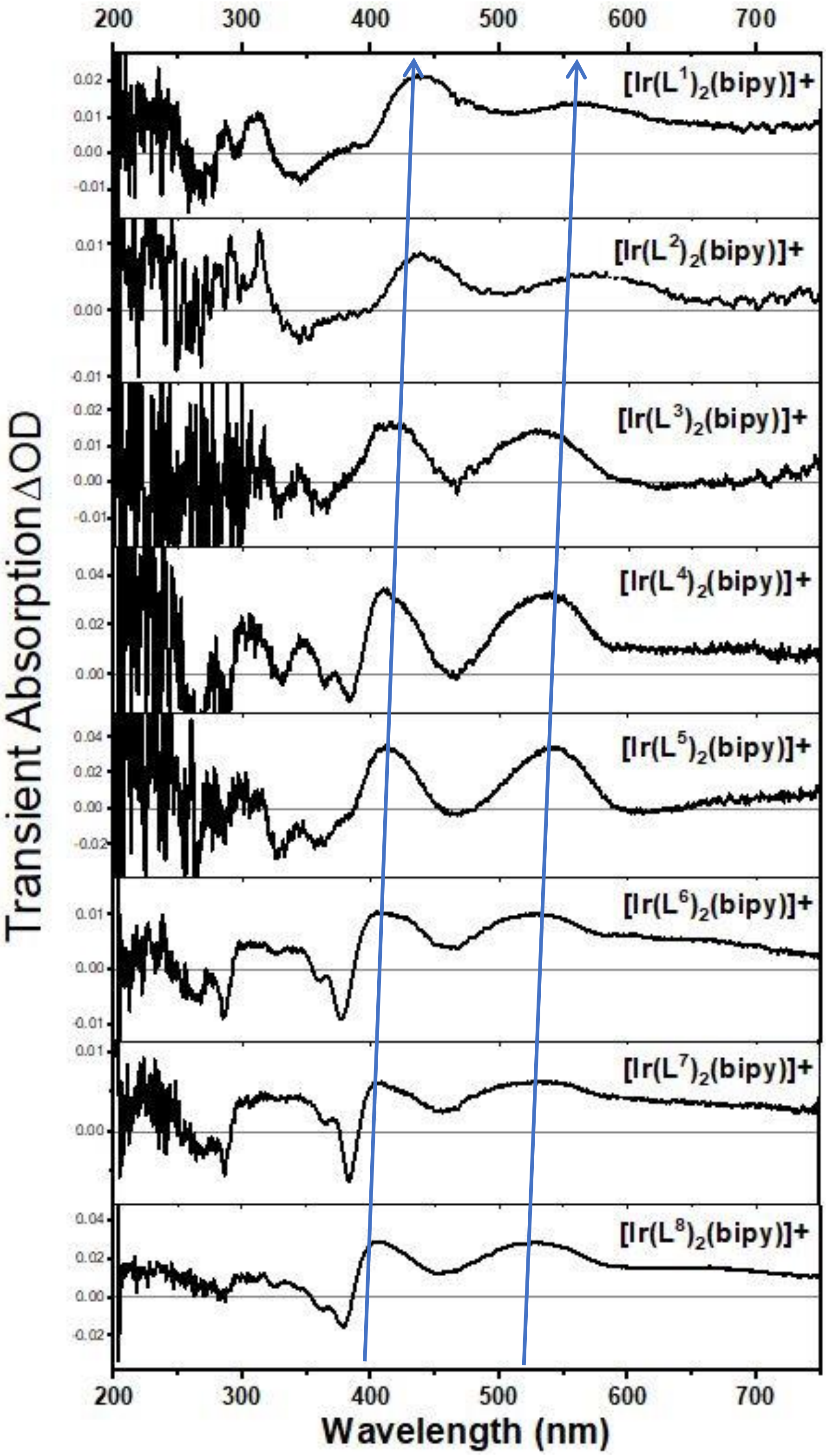

Figure 3.12 Background and fluorescence subtracted transient absorption spectra of [Ir($L^{1\text{-}8}$)$_2$(bpy)]PF$_6$ complexes in acetonitrile, λ_{ex} = 355 nm, delay time = 50 ns. The grey line represents ΔOD = 0 in all cases. Blue lines show the shift in the major TA features induced by substituents on the quinoxaline.

Figure 3.12 presents a comparison of the transient spectra of all complexes. The spectral features in the TA spectra noticeably shift depending on the substituted cyclometalated ligand used, following the same ordering as the emission spectra with respect to their band positions. For example, $[Ir(L^2)_2(bipy)]PF_6$ complex shows triplet state features at longer wavelengths versus $[Ir(L^{3–8})_2(bipy)]PF_6$ at shorter wavelengths. The lifetimes of the features are strongly correlated to those of the $\mathbf{T_1 \rightarrow S_0}$ emission decay kinetics of the complexes, supporting the assignment of these features as originating from triplet states. The tunable triplet excited states in these complexes make them potentially suitable as a general molecular framework for electrical diode applications. (Tamayo et al. 2005; Baranoff et al. 2009; Wong and Ho 2009)

3.2.5 Kinetics Studies

The kinetics of the main transient absorption features observed using the ICCD were further investigated using the photomultiplier tube (PMT) detector in conjunction with the monochromator. This allows us to isolate and examine narrow wavelength bands within the spectra (i.e. individual TA features) with respect to time. The transient kinetics of the major features of the $[Ir(L^1)_2(bpy)]PF_6$ and $[Ir(L^6)_2(bpy)]PF_6$ complexes in aerated acetonitrile at ambient temperature can be seen in figure 3.13.

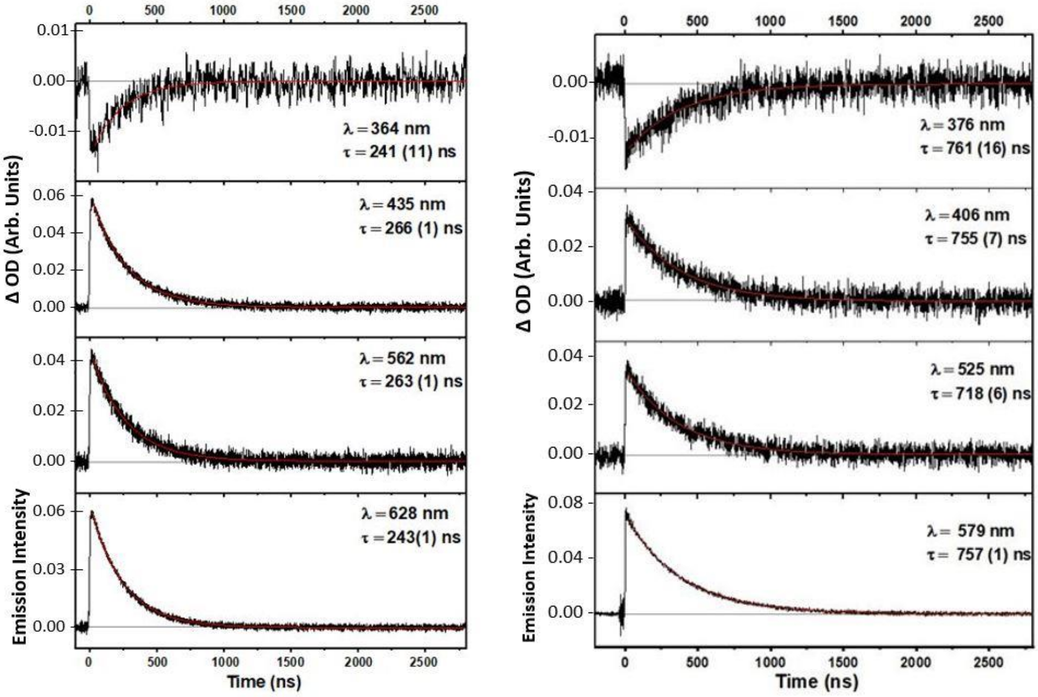

Figure 3.13 Transient kinetic measurements of the $[Ir(L^1)_2(bpy)]$ complex left and the $[Ir(L^6)_2(bpy)]$ complexes in acetonitrile at room temperature, aerated. The wavelengths and lifetimes of each trace are inset. The bottom trace is an emission trace, the top three are difference in optical density traces. All are fitted to mono-exponential decay functions (red line)

All kinetic traces decay monoexponentially and exhibit a complete return to baseline, suggesting that each observed feature is attributed to a singular and reversible process, specifically the relaxation of photoexcited species to their original state. This indicates that the photoexcitation process has not induced any permanent chemical change, e.g. photodegradation, clearly demonstrating the photostability of these complexes. For all the compounds investigated here the kinetic data demonstrate that all the features identified for a complex display similar decay lifetimes, providing evidence that the features all originate from the same excitation and intersystem crossing processes that produce an emissive ^{3}MLCT state. There is no evidence of any features that could correspond to an additional singlet-to-singlet emissive process, e.g. delayed fluorescence, within these spectra, and no evidence of multiple emissive states.

The average lifetime of the complexes shows a clear dependency on the nature and position of the substituents, shown in table 3.2. The fluorinated-phenyl complexes in aerated solutions show a remarkable increase in the lifetimes comparing with their methylated counterparts with trifluorinated-phenyl complexes further prolonging the lifetime of the excited state. This could increase the potential applications of these complexes. Complexes with relatively long-lived excited states are of interest for photosensitizer applications, (Gao et al. 2018) for example, in luminescent imaging applications to increase signal-to-noise ratios (by competing with autofluorescence from biological samples), (Finikova et al. 2008; Yoshihara et al. 2015) and in photoredox catalysis and upconversion to enable efficient diffusion-based quenching of a sensor. (Goldsmith et al. 2005; Zeitler 2009; Singh-Rachford and Castellano 2010)

Table 3. 2 Average lifetimes of the $[Ir(L^{1-8})_2(bpy)]^+$ complexes, shown alongside the substituents of the complexes.

Complex	Average lifetime (ns)	substituent on Phenyl ring	Substituent on Quinoxaline
$[Ir(L^1)_2(bipy)]PF_6$	253	2 x Me	2 x Me
$[Ir(L^2)_2(bipy)]PF_6$	215	2 x Me	2 x F
$[Ir(L^3)_2(bipy)]PF_6$	430	F	H
$[Ir(L^4)_2(bipy)]PF_6$	446	F	2 x Me
$[Ir(L^5)_2(bipy)]PF_6$	571	F	2 x F
$[Ir(L^6)_2(bipy)]PF_6$	747	3 xF	H
$[Ir(L^7)_2(bipy)]PF_6$	586	3 xF	2 x Me
$[Ir(L^8)_2(bipy)]PF_6$	535	3 x F	2 x F

As mentioned earlier, the emission lifetimes increased under deoxygenated or low-temperature conditions due to the reduced collisional quenching rate between triplet oxygen and the triplet excited state, shown in figure 3.14 and table 3.1.

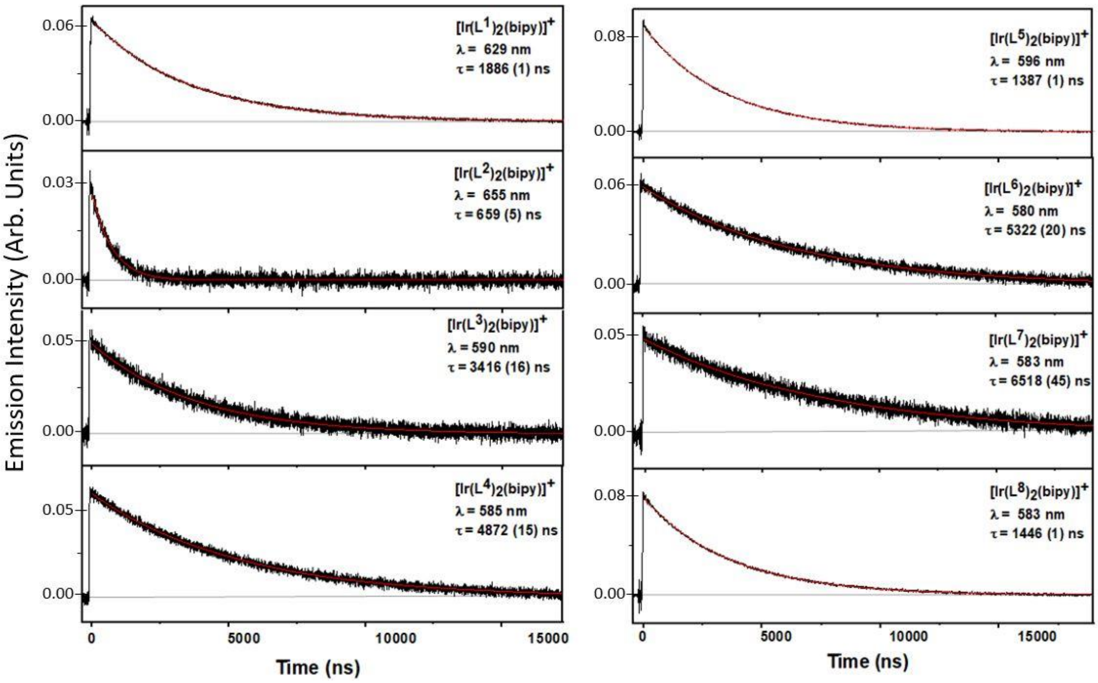

Figure 3.14 Kinetic emission measurements of [Ir($L^{1\text{-}8}$)$_2$(bpy)] complexes in degassed acetonitrile (1x10^{-5}M). All are fit to mono-exponential decay functions (red line)

The qualitative similarity of observable features of all eight complexes indicates that the identical or similar processes are occurring for each complex; with the quantitative variability in absorption and emission wavelengths and lifetimes attributed to the different effects of the quinoxaline substituents on these processes.

3.2.6 DFT analysis

Density functional theory (DFT) calculations were performed on each of complexes with the aim of investigating the impact of the position and the type of substituents on cyclometalated ligand upon the electronic structure and the optical properties of [Ir(L^n)$_2$(bipy)]$^+$. All calculations were conducted using the B3LYP functional with a 6-31G* basis set and an SDD (Stuttgart-Dresden basis set) for the central iridium atom. Calculations were performed within an implicit acetonitrile solvent, consistent with the spectroscopic measurements.

The optimized geometries of all complexes obtained by DFT were confirmed through harmonic vibrational frequency calculations and are shown in figure 3.15. The computationally derived structures exhibit near C_2 symmetry, with a distorted octahedral geometry around the iridium metal center. In order to verify this methodological approach, the DFT optimized minimum energy structures were compared against those obtained from x-ray diffraction crystallography. The computationally modelled structures of Ir^{III} complexes are in superb agreement with crystallographic data. As an example of this, figure 3.15 shows the singlet ground state geometry calculated for the

$[Ir(L^1)_2(bipy)]PF_6$ and $[Ir(L^2)_2(bipy)]PF_6$ complexes overlayed on the experimentally X-ray (crystal) structures.

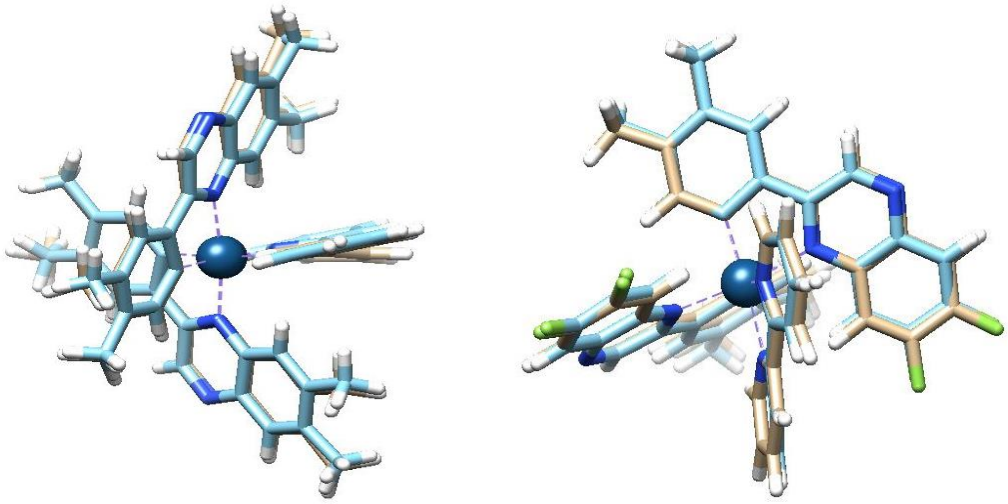

Figure 3.15 Overlay of the crystal structure (blue) and DF-DFT//B3LYP/6-31G(SDD) optimized structures (brown)* ***Left*** *for $[Ir(L^1)_2(bipy)]^+$, and* ***Right*** *for $[Ir(L^2)_2(bipy)]^+$*

Decomposition analysis was performed on the orbitals of each complex in order to help understand the nature of the excited state as well as the type of charge transfer within the complexes induced by excitation, i.e. the degree of MLCT character vs intraligand character. This is achieved through calculating the percentage contributions to each of the molecular orbitals from each various moieties within the complex, using the GaussSum software package. Visualization of the frontier molecular orbitals and decomposition analysis for the $[Ir(L^1)_2(bipy)]PF_6$ complex are shown in figure 3.16 and table 3.3.

Table 3. 3 A summary of the major contributions to each MO from each subset of the complex. Q1 and Q2 are the quinoxaline ligands.

Complex	**Ir *5d***		**Q1**		**Q2**		**bipy**
	HOMO-1	HOMO	LUMO	LUMO+1	LUMO	LUMO+1	LUMO+2
$[Ir(L^1)_2(bipy)]^+$	4	32	50	44	44	50	95
$[Ir(L^2)_2(bipy)]^+$	4	32	63	31	31	64	96
$[Ir(L^3)_2(bipy)]^+$	8	35	48	48	47	48	96
$[Ir(L^4)_2(bipy)]^+$	5	32	50	45	45	50	96
$[Ir(L^5)_2(bipy)]^+$	6	33	41	54	54	41	96
$[Ir(L^6)_2(bipy)]^+$	4	34	48	47	47	48	97
$[Ir(L^7)_2(bipy)]^+$	2	32	48	47	46	47	97
$[Ir(L^8)_2(bipy)]^+$	2	33	47	48	48	48	96

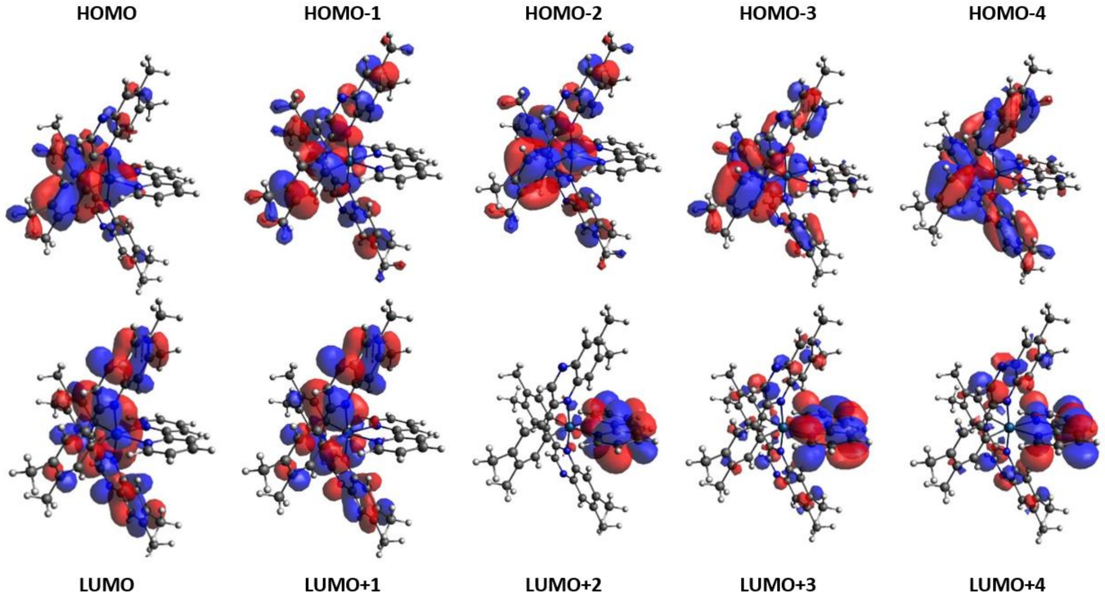

Figure 3.16 Calculated Kohn-Sham frontier molecular orbitals for $[Ir(L^1)_2(bipy)]^+$.

The MO analysis (table 3.4) predicts that the occupied molecular orbitals in this set of Ir complexes possess a considerable metallic *d*-orbital character while the unoccupied molecular orbitals are mainly ligand-centered. In all cases, the HOMO is made of almost equal contributions from the Ir metal center (32–35%) and from each quinoxaline ligand (Q1/Q2), with negligible contribution from bipy (2%). For the LUMOs, the two quinoxaline ligands demonstrate a near degenerate character, with molecular orbitals delocalized over both quinoxaline ligands with similar contributions from each, given the symmetry structure of the complexes. This is displayed in the percentage contributions in table 3.3. However, in some cases, the two quinoxalines create pairs of pseudodegenerate orbitals with alternating contributions from each of the of the quinoxalines. As an example of this, the LUMO of the $[Ir(L^1)_2(bipy)]^+$ is comprised of contributions of 50% and 44% from the quinoxalines, Q1 and Q2, respectively, whilst the LUMO+1 shows the reverse (Q1 = 44%; Q2 = 50%). This effect is due to the near C_2 symmetry of the system, with subtle geometrical distortions leading to a lowering of the total symmetry and thus a splitting in the orbitals. The metal contribution to the unoccupied orbitals is negligible, suggesting that the lowest excited state has a significant degree of MLCT character. The bipy ligand contribution is also predicted to be negligible to the LUMO or LUMO+1, the orbitals to which we ascribed the majority of the longer wavelength photoexcitation bands, although it is the dominant contributor to the LUMO+2 orbital (96%) and will likely be important in the short wavelength absorption spectra structure.

Table 3.4 A description of the calculated MO contributions, excited state descriptions and associated transitions for the $[Ir(L^1)_2(bipy)]^+$ complex (L1 and L2 are the different quinoxaline ligands; bipy = bipyridine). Molecular orbital contributions less than 10% have been omitted for clarity.

	Moiety Contribution to Orbital (%)				**Orbital Contribution to Excited State**	
Orbital	**Ir (*5d*)**	**bipy**	**L1**	**L2**	**Excited State**	**Contributing Transitions (> 10 %)**
LUMO +4	1	76	11	11	1 (409 nm f=0.2089)	HOMO-1 → LUMO (10%)
LUMO +3	2	80	9	9		HOMO → LUMO+1 (83%)
LUMO +2	2	95	1	1	2 (403 nm f=0.0588)	HOMO-1 → LUMO+1 (11%)
LUMO +1	4	2	44	50		HOMO → LUMO (83%)
LUMO	4	2	50	44		
HOMO	32	2	33	33	3 (348 nm f=0183)	HOMO → LUMO+2 (88%)
HOMO -1	4	1	47	47		
HOMO -2	10	1	45	45	4 (331 nm f=0.1855)	HOMO -2 → LUMO (26%)
HOMO -3	20	3	39	39		HOMO -1 → LUMO +1(55%)
HOMO -4	22	4	39	35	5 (330nm f=0.2751)	HOMO-2→ LUMO+1 (25%)
						HOMO -1 → LUMO (53%)

TD-DFT calculations in conjunction with the long-range corrected CAM-B3LYP functional were also performed on the optimized singlet ground-state geometries with the aim of estimating the vertical transitions energies of the low-lying singlet and triplet excited states of the complexes. This method supports the analysis and assignments of the experimentally observed absorption features, as well as allowing us to better understand the fine band shifts observed in the steady state UV-Vis absorption spectra. For each complex, the lowest 30 singlet-to-singlet spin-allowed and 30 singlet-to-triplet spin-forbidden transitions were calculated and compared with the absorption spectra. The lowest predicted singlet and triplet transitions for each of the complexes are presented in table 3.5. In all cases, the computed transition energies are in reasonable qualitative agreement with the experimental UV/Vis absorption spectra discussed earlier. Table 3.4 above reports the results of the singlet TD-DFT calculations for the first five singlet excited states, using the $[Ir(L^1)_2(bipy)]PF_6$ complex as an archetype. Notably, these singlet transitions typically originate from the high-lying occupied orbitals and are mainly into the LUMO and LUMO+1, indicating that the absorption bands of this complex are mostly MLCT and ILCT in character, which can explain the observed band shift in the absorption spectra induced by the adjustment of the substituents of these ligands.

The calculated wavelengths of triplet absorption bands are significantly red-shifted in comparison with singlet absorption bands (table 3.5). Although the triplet TD-DFT calculations do not provide oscillator strengths for spin-forbidden transitions, it can be assumed they would be substantially lower in intensity than their spin allowed singlet counterparts. Thus, these calculations further support the assignment of the longer wavelength ($\lambda > 420$ nm) steady state absorption bands as singlet-to-triplet spin-forbidden transitions.

Table 3.5 Computed values for the vertical spin allowed and spin-forbidden absorption wavelengths for the $[Ir(L^{1-8})_2(bipy)]^+$ complexes.

Complex	**$S_0 \rightarrow S_1$ Abs. (nm)**	**$S_0 \rightarrow T_n$ Abs. (nm)**
$[Ir(L^1)_2(bipy)]^+$	409	544
$[Ir(L^2)_2(bipy)]^+$	419	563
$[Ir(L^3)_2(bipy)]^+$	385	502
$[Ir(L^4)_2(bipy)]^+$	383	496
$[Ir(L^5)_2(bipy)]^+$	390	510
$[Ir(L^6)_2(bipy)]^+$	377	493
$[Ir(L^7)_2(bipy)]^+$	375	486
$[Ir(L^8)_2(bipy)]^+$	381	501

From table 3.5, it can be seen that the lowest spin-forbidden singlet-triplet transition is predicted to occur at 544 nm for $[Ir(L^1)_2(bipy)]^+$, ascribed to a mixed ^{3}MLCT/^{3}ILCT transitions which may become weakly allowed due to spin–orbit coupling effects. This transition correlates well with structureless and low intensity absorption band seen at 550 nm in the experimental absorption spectrum. The longest wavelength singlet excitation is predicted to be an intense HOMO to LUMO+1 transition at 409 nm ($f = 0.2089$), followed at higher energy by an intense HOMO to LUMO transition at 403 nm, both of which are comprised of a combination of ^{1}MLCT and ^{1}ILCT excited states of the two C^N ligands. Both transitions correspond well with the structured absorption features at around $350 < \lambda < 400$ nm in the experimental spectrum. These two excited state transitions provide a good illustration of the influence of pseudo-degenerate splitting of the orbitals upon the absorption spectra, given that the contributing transitions arise from the same occupied orbitals (HOMO) and proceed to either the LUMO or the LUMO+1 with alternating percentages. In addition, intense transitions are expected to lie between $350 < \lambda < 300$ nm, including transitions with much more mixed ^{1}ILCT/^{1}LLCT/^{1}MLCT character. In the high-energy region ($\lambda < 300$ nm), the calculations indicate that in addition to ligand centered ^{1}LC transition, ^{1}ILCT/^{1}LLCT/^{1}MLCT have some contributions.

Vertical and adiabatic spin-forbidden $\mathbf{T_1 \rightarrow S_0}$ emission energies were calculated from the optimized lowest triplet state stationary point, and the results are shown in table 3.6.

Table 3.6 Computed values for the vertical and adiabatic emission wavelengths for the [Ir(L^{1-8})$_2$(bipy)]$^+$ complex along with experimental values

Complex	$T_1 \rightarrow S_o$ Em. (nm) Vertical	$T_1 \rightarrow S_o$ Em. (nm) Adiabatic	$T_1 \rightarrow S_o$ Em. (nm) Exp.
[Ir(L^1)$_2$(bipy)]$^+$	694	622	628
[Ir(L^2)$_2$(bipy)]$^+$	712	640	655
[Ir(L^3)$_2$(bipy)]$^+$	664	586	590
[Ir(L^4)$_2$(bipy)]$^+$	662	585	585
[Ir(L^5)$_2$(bipy)]$^+$	670	589	593
[Ir(L^6)$_2$(bipy)]$^+$	668	582	579
[Ir(L^7)$_2$(bipy)]$^+$	672	583	583
[Ir(L^8)$_2$(bipy)]$^+$	663	585	583

The above table clearly shows that the predicted $T_1 \rightarrow S_0$ wavelengths, both vertical and adiabatic, nicely match the experimentally observed trend; showing the correct order of the complex emission centers. Although vertical emission energies tend to be systematically underestimated, the calculated adiabatic energy values are remarkably well matched to experimental data. Therefore, this method can afford a good insight into the effect that ligand structure modifications will have on the spectral properties of the complexes.

The assignment of $T_1 \rightarrow S_0$ emission is strongly supported by the spin-density distribution for the lowest triplet T_1 states of these Ir^{III} complexes determined by Mulliken spin-density analysis. From figure 3.17, the spin density distributions of Ir^{III} complexes at T_1 are mainly localized on the C^N ligand and Ir metal center, proving that the emissions in these iridium complexes are ascribed to the metal to ligand charge transfer transition (^{3}MLCT) and the intraligand charge-transfer transition (^{3}ILCT) in the CN ligands.

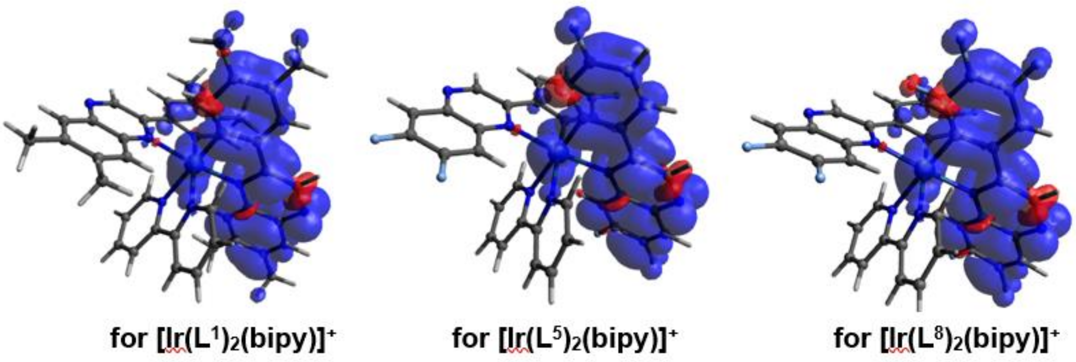
for [Ir(L^1)$_2$(bipy)]$^+$ for [Ir(L^5)$_2$(bipy)]$^+$ for [Ir(L^8)$_2$(bipy)]$^+$

Figure 3.17 Calculated spin densities of the [Ir(L^1)$_2$(bipy)]$^+$, the [Ir(L^3)$_2$(bipy)]$^+$and the [Ir(L^8)$_2$(bipy)]$^+$

The effects of quinoxaline ligand substitution was investigated by examining the energy values of the HOMO and LUMO orbitals of each of the complexes (Table 3.7). TD-DFT calculations predict that substitution on either phenyl or quinoxaline moieties can alter the energy levels of both HOMO and LUMO, with the phenyl moiety predicted to have a greater impact on the energy levels and thus optical properties. For example, $[Ir(L^2)_2(bipy)]^+$ is expected to possess the smallest band gap due to destabilization of the HOMO (through methylating the phenyl donor) and stabilization of the LUMO (achieved through fluorination of the quinoxaline). This is clearly reflected in the largest bathochromic shift observed in the emission wavelength and the shortest lifetime. In contrast, sequential fluorination of the phenyl donor is predicted to lead to a progressive stabilization of the HOMO level and thus a hypsochromic shift in the position of emission peak maxima. Thus, trifluorinated-phenyl complexes are predicted to possess the lowest HOMO energy levels and shortest wavelength emission, which is consistent with experimental measurements.

Table 3.7 Calculated energies of the frontier orbitals of the Ir^{III} complexes and their differences.

Complex	HOMO energy (eV)	LUMO energy (eV)	∆E
$[Ir(L^1)_2(bipy)]^+$	-5.62	-2.54	3.08
$[Ir(L^2)_2(bipy)]^+$	-5.76	-2.77	2.99
$[Ir(L^3)_2(bipy)]^+$	-6.03	-2.74	3.29
$[Ir(L^4)_2(bipy)]^+$	-5.95	-2.64	3.31
$[Ir(L^5)_2(bipy)]^+$	-6.1	-2.86	3.24
$[Ir(L^6)_2(bipy)]^+$	-6.15	-2.88	3.27
$[Ir(L^7)_2(bipy)]^+$	-6.08	-2.77	3.31
$[Ir(L^8)_2(bipy)]^+$	-6.22	-3.00	3.22

3.3 Bis-Tridentate Quinoxaline Iridium (III) Complexes

In order to investigate the effect of modifying the backbone structure of the cyclometallating ligand on the luminescence properties, the analysis methodology used above was again applied to examine a new set of complexes in which the Ir metal was instead bound with two diquinoxaline ligands, adopting a tridentate coordination mode, meaning that an ancillary ligand is not involved in the complexes' structures.

3.3.1 Complex Structures

The tridentate ligand used in this set of complexes is comprised of two quinoxaline moieties connected by a pyridine ring, providing an extended *π*-conjugation to the ligand backbone. The ligand chelates to the iridium core through three sites: one quinoxaline bonds via a nitrogen atom and the other quinoxaline bonds via a carbon atom while the pyridine ring bonds through the nitrogen heteroatom. Two ligand variations were synthesised, featuring H and Me groups as the substituents. The general structure of the resulted tridentate complexes is $[Ir(N\hat{}N\hat{}C)_2]^+$. X-ray analysis confirms that both ligands adopt a N^N^C coordination which is different from their analogues $[Ir(terpy)_2]^{3+}$ (where terpy = 2,2′:6′,2″-terpyridine) that possesses a N^N^N binding mode. Both complexes are monocationic and paired to PF_6 counterions, shown in scheme 3.4.

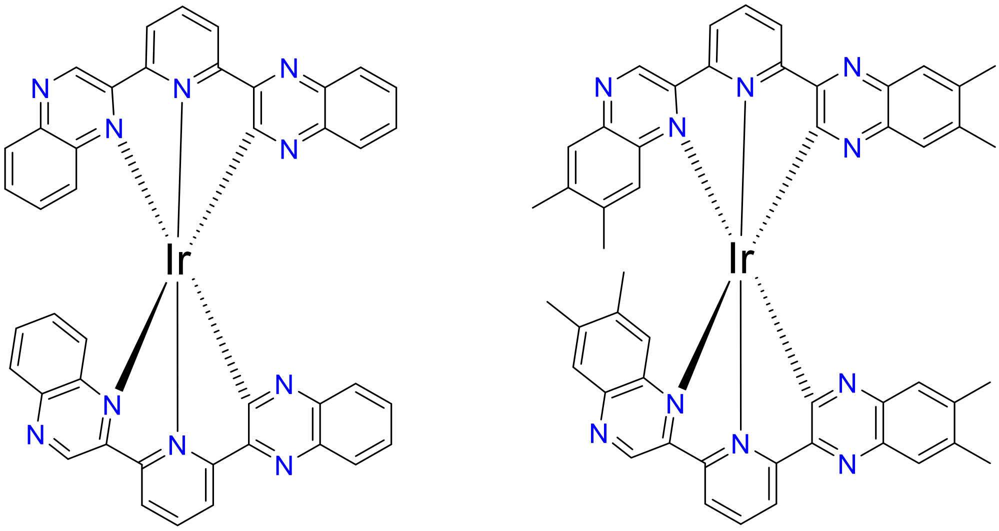

$[Ir\,(L^9)_2]\,PF_6$ $[Ir\,(L^{10})_2]\,PF_6$

Scheme 3.4 The tridentate quinoxaline complexes

3.3.2 Steady State Absorption Spectra

The steady state UV-Vis absorption spectra of two tridentate complexes were recorded as solutions in chloroform at a concentration of 10^{-5} M, shown in figure 3.18.

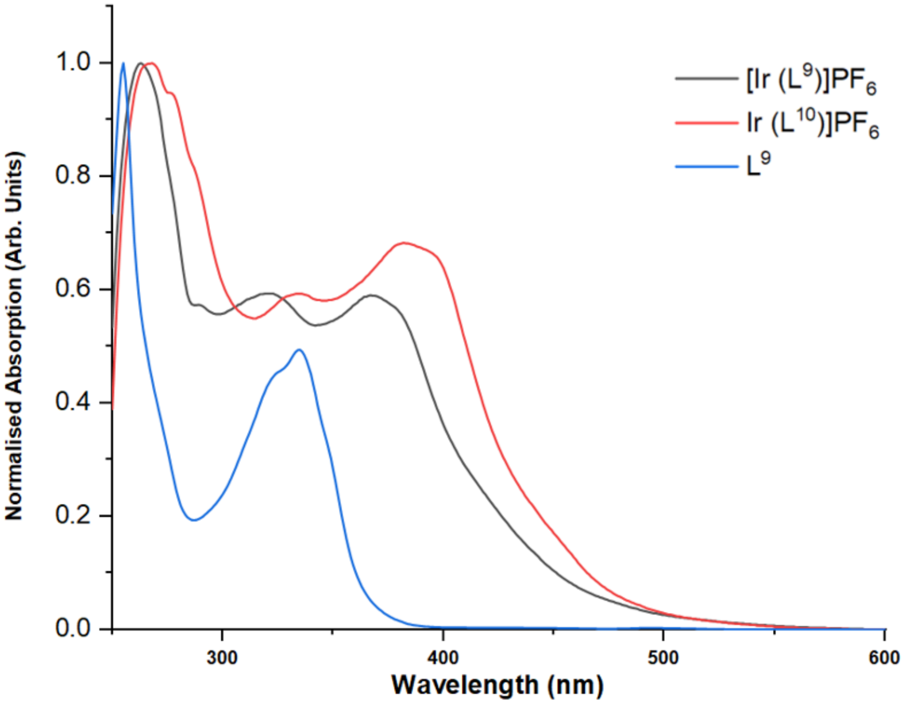

Figure 3.18 UV-vis. Absorption spectra of $[Ir(L^9)_2]PF_6$ (black line), $[Ir(L^{10})_2]PF_6$ (red line) and L^9 (blue line) in chloroform ($1x10^{-5}$M)

The two complexes display almost identical spectral profiles with three distinct maxima which is remarkably different from those of the bidentate Ir complexes discussed above (figure 3.7). The spectra show two strong bands λ < 350 nm which were initially assigned as ligand centered transitions ($\pi\pi^*$) due to their similarity with the free ligand spectrum. Another strong feature is seen 350 < λ < 400 nm with a shoulder extending to 550 nm. This band does not exist in the free ligand spectrum and can therefore be identified as the MLCT transition from the *d*-orbital of the Ir-metal centre to the unoccupied π^* orbital of the ligand, mixed with an appreciable degree of intraligand charge transfer (ILCT) transitions. This is confirmed by DFT calculations which indicate that the visible transitions occur from orbitals localized on the Ir and C-quinoxaline moieties to orbitals localized on the N-quinoxaline moieties and pyridine rings of both tridentate ligands (discussed in more detail later in this chapter). There is a very weak absorption shoulder around λ = 450 nm which is assigned to a spin-forbidden ^{3}MLCT/^{3}ILCT transition. The methyl-substituted complex exhibits a bathochromic shift in comparison to the unsubstituted one, in agreement with the trend seen in iridium complexes discussed earlier.

3.3.3 Emission Spectra

The emission spectra of both complexes were recorded at room temperature after the excitation at 355 nm and are shown in figure 3.19.

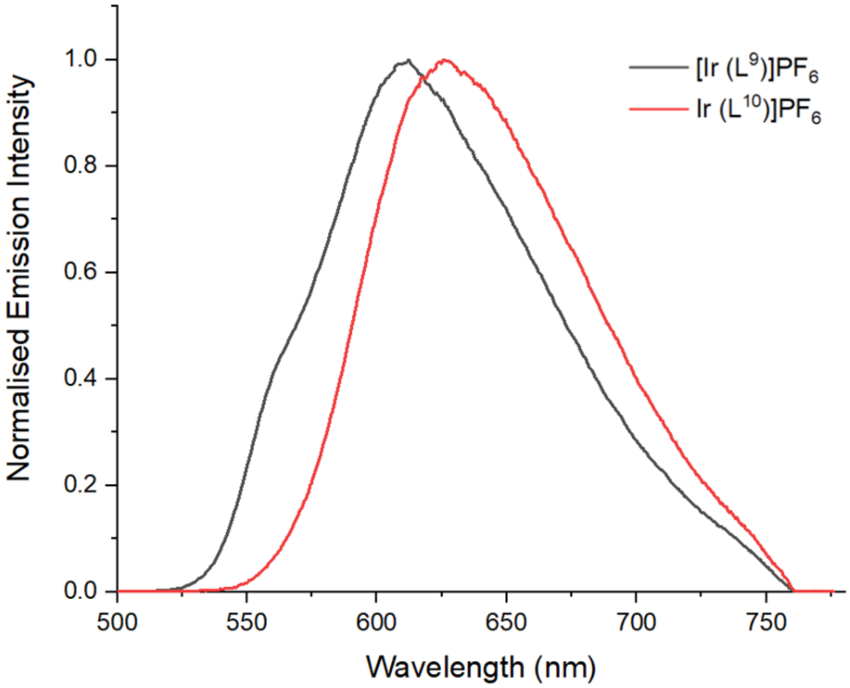

Figure 3.19 Normalised emission spectra of [Ir (L^9)$_2$)]PF$_6$ and [Ir (L^{10})$_2$)]PF$_6$ complexes in chloroform (1x10^{-5} M) at room temperature.

Both complexes emit similar broad emission profiles in the red region of the spectrum. The emission band center of the [Ir(L^9)$_2$)]PF$_6$ complex is located at approximately λ = 612 nm whilst the [Ir(L^{10})$_2$)]PF$_6$ complex shows a red-shifted emission maximum located around 627 nm. Interestingly, the emission spectra of both complexes show a concentration-dependent profile at room temperature, as displayed in figure 3.20.

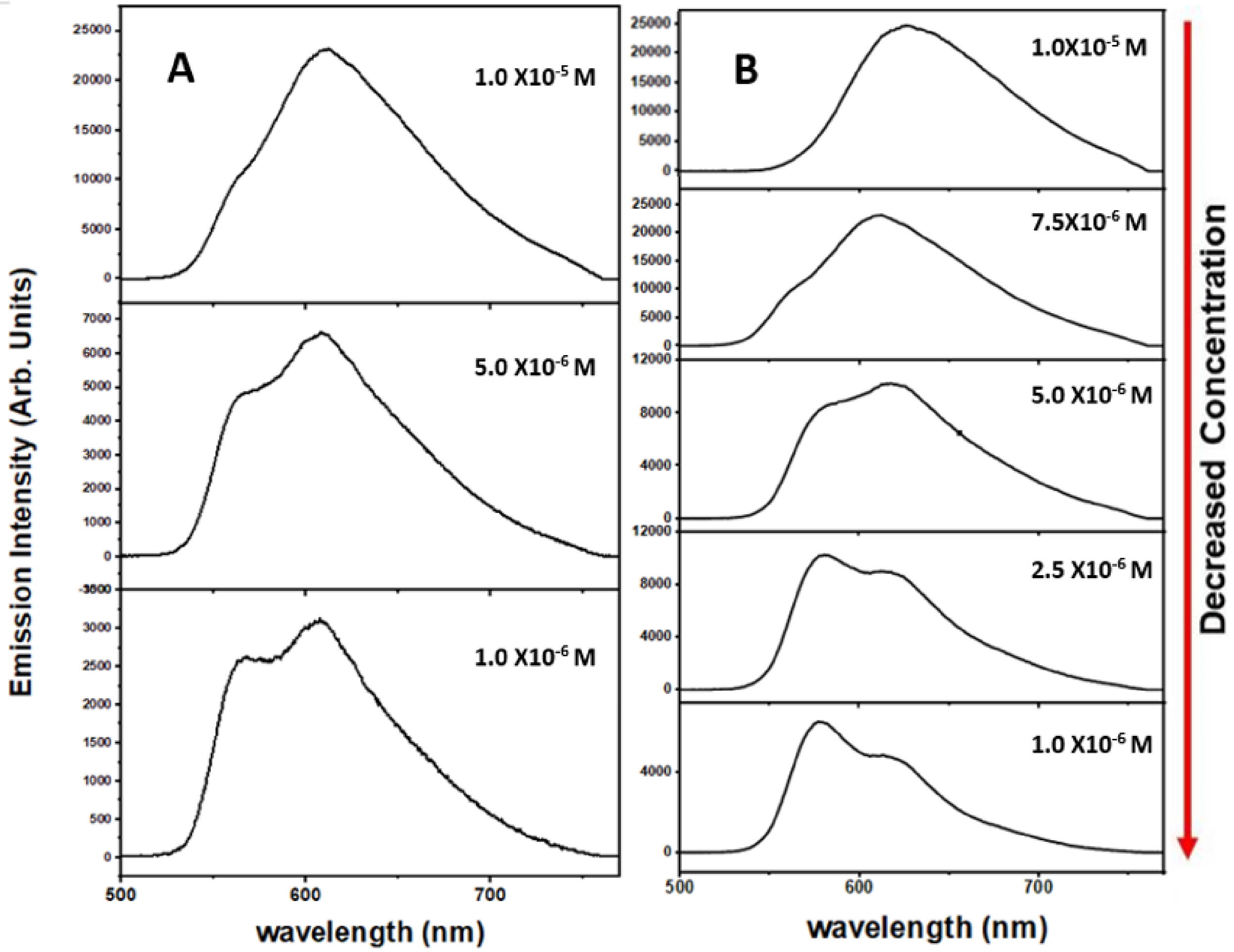

Figure 3.20 Emission intensities of A) [Ir(L^9)$_2$]PF_6 and B) [Ir(L^{10})$_2$]PF_6 complexes in chloroform at various dilutions, showing a clear spectral response to complex concentration.

As can be seen in the above figure it is evident that a singular emission band dominates the emission spectra in concentrated solutions. However, as the concentration decreases, the intensity of this band wanes, accompanied by the emergence of an additional emission peak at a lower wavelength, eventually becoming predominant in the emission spectra at very diluted concentrations, more pronounced in the case of [Ir(L^{10})$_2$)]PF_6. The different behaviour between the two features suggests different states of origin. The shorter-wavelength peak did not appear in the pure solvent which excludes contamination. Supported by kinetic studies (figure 3.23), the longer wavelength emission feature shows a decrease in intensity during dilution and is ascribed to a spin-forbidden phosphorescence transition whilst the shorter wavelength emission that increases in intensity is attributed to spin-allowed fluorescent emission. To confirm that the second emission feature does not arise from a non-bonded ligand, the emission spectrum of the free ligand was also recorded in chloroform and is displayed below in figure 3.21.

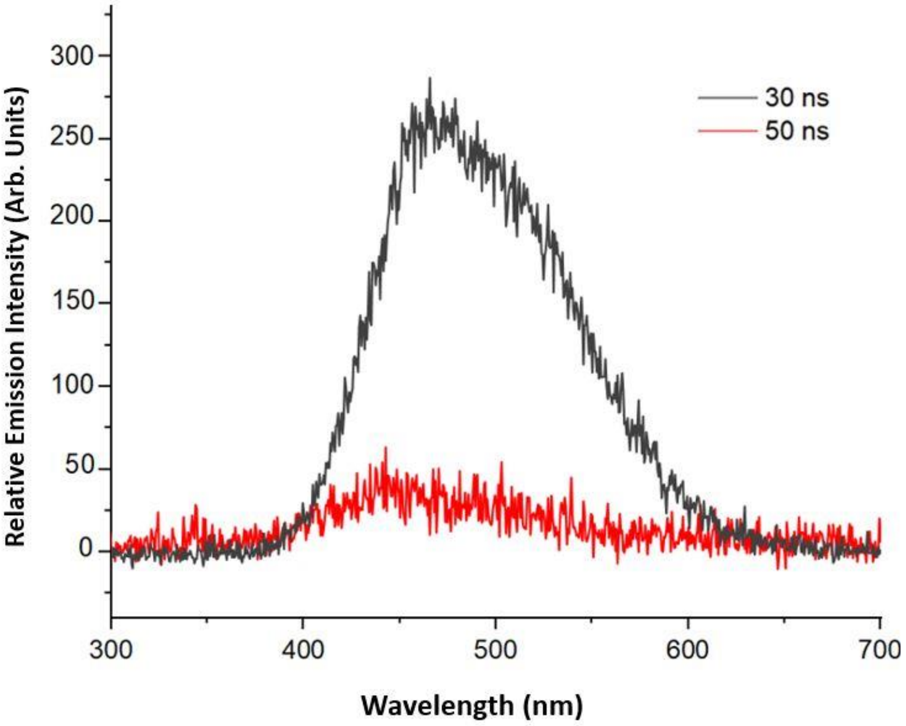

Figure 3.21 Emission spectra of the free L^9 ligand in chloroform (1x10-5 M) at two different gate delays

The free ligand shows a broad emission spectrum with an emission center at around λ = 475 nm. The emission band shows a significant drop off with even short time delays between the excitation laser and camera gate (50 ns), consistent with spin-allowed fluorescence. This rules out the contribution of the free ligand to the complex emission in figure 3.18 as the emission spectrum was recorded at a 50 ns gate delay.

As with the spin-forbidden absorption band, the phosphorescence is attributed to a mixed ^{3}MLCT/^{3}ILCT excited state. The emission of both compounds is comparable in emission profile, maxima, and lifetimes to those of bidentate Ir^{III} complexes discussed above. However, it is different from the emission profile of their analogues terpyridine $[Ir(terpy)2]^{3+}$ which displays a very structured spectrum in the blue-green region attributed to ligand-centred triplet state ^{3}LC. This supports that the binding mode in studied complexes is N^N^C. (Collin et al. 1999; Titos-Padilla et al. 2013)

3.3.4 TA Spectra

Time-resolved transient absorption (TA) spectra of all Ir^{III} complexes were again recorded in aerated chloroform after excitation at 355 nm and are presented in Figure 3.22.

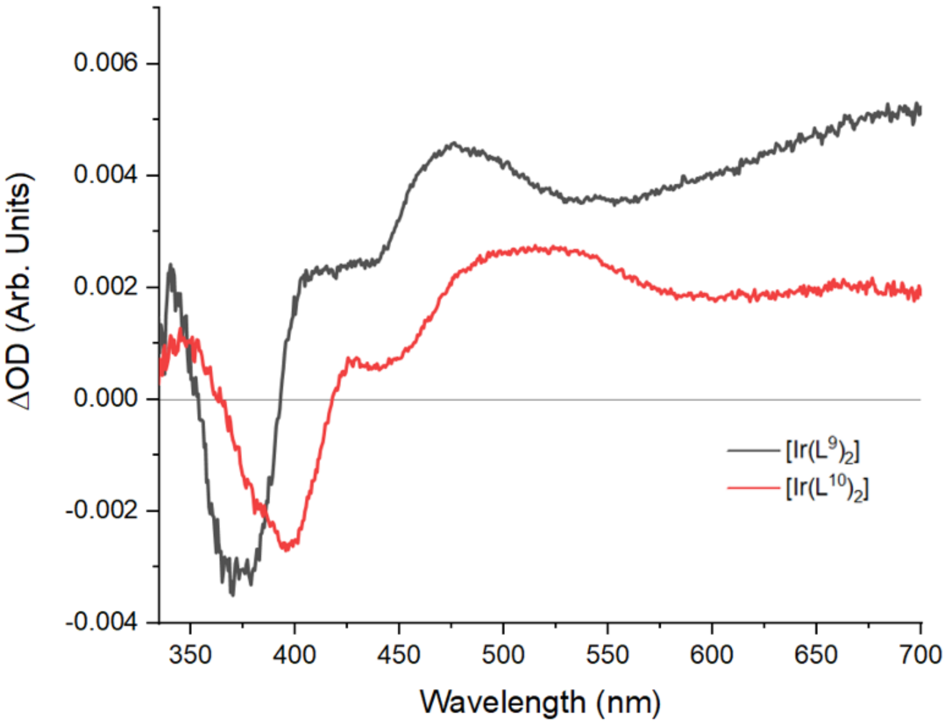

Figure 3.22 Transient absorption spectrum of the $[Ir(L^9)_2]^+$ and $[Ir(L^{10})_2]^+$ complexes in chloroform ($1x10^{-5}$M), λ_{ex} = 355 nm, delay time = 50 ns . The grey line represents ΔOD = 0

The transient absorption spectra of the two complexes are almost identical, displaying similar features to those found in bidentate complexes discussed earlier. Both show a prominent bleaching feature at 350 < λ < 430 nm due to the depletion of spin-allowed absorption bands. The excited state absorption bands are observed as an increase in optical density located between 450 < λ < 525 nm in the $[Ir(L^9)_2]^+$ complex and 475 < λ < 600 nm in the $[Ir(L^{10})_2]^+$ complex. The complexes all exhibit another structure-less broad absorption band observed in the longer wavelength region of the spectra, more prominent in the $[Ir(L^9)_2]^+$ complex. These absorption features are attributed to the transitions from the lowest energy triplet state to higher triplet states. Each feature, including the ground state bleaching and the two positive bands in TA spectra, exhibits similar lifetimes (Figure 3.22), suggesting that each peak relates to the same photoexcitation, ISC process and deactivation.

3.3.5 Kinetics Studies

The photomultiplier tube (PMT) detector was used to investigate the transient kinetics of the major features observed using the ICCD. The measurements were carried out in aerated chloroform at ambient temperature, and the results of both $[Ir(L^9)_2]^+$ and $[Ir(L^{10})_2)]^+$ complexes are shown in figure 3.23.

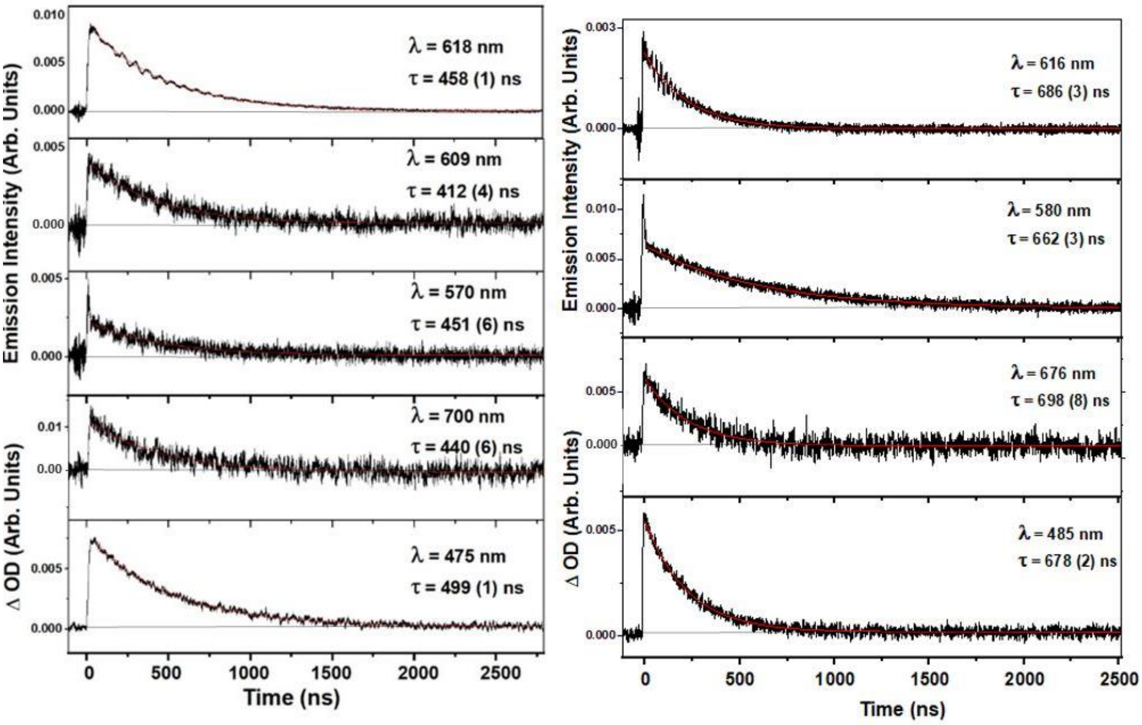

Figure 3.23 Transient absorption kinetic traces of the major spectral features of $[Ir(L^9)_2]^+$ (left) and $[Ir(L^{10})_2]^+$ (right) complexes in aerated chloroform ($1X10^{-5}$M). Wavelengths and lifetimes of each trace are inset

As seen in above figure, transient kinetic spectra of all feature show a complete return to baseline showing no evidence for transient species associated with any chemical changes caused by photoexcitation. The features all exhibit signs of a single state of origin, save for shorter wavelength emission bands at 570 nm and 580 nm for the $[Ir(L^9)_2]^+$ and $[Ir(L^{10})_2]^+$ complexes respectively. The kinetic traces of short wavelength emission demonstrate a sharp, short-lived peak immediately after the laser pulse (t = 0), indicating the presence of another short-lived emissive state. This sharp feature is assigned to the spin-allowed fluorescent process. All features are tail-fit (ie. excluding the sharp feature) to a mono-exponential decay function, giving similar decay lifetimes for all features exhibited by each complex, as shown in figure 3.22. The average lifetime in aerated CH_3Cl was 452 ns and 681 ns for $[Ir(L^9)_2]^+$ and $[Ir(L^{10})_2]^+$ complexes, respectively. Noteably, the complexes with tridentate ligands emission maxima did not change comparative to those with the bidentate ligands (although a batchromic shift of emission band by around 10 nm is expected when use more polar solvent), but these tridentate systems have increased luminescence lifetimes. For example, the emission of the iridium complex with methylated tridentate ligand $[Ir(L^{10})_2]^+$ is located at 627 nm with a lifetime of 686 nm while its analogous methylated bidentate complex $[Ir(L^2)(bipy)]^+$ emits at 629 nm and the emission lifetime is 215 nm.

3.3.6 DFT analysis

DFT calculations were performed to compare the two coordination modes that were considered possible for the ligand–metal combination. Therefore, different functionals (B3LYP/SDD, B3LYP/LANL2DZ, M062X/LANL2DZ) were used to optimize two hypothetical structures (derived from L^9) with the aim of comparing the relative energies of the [Ir(N^N^N)2]3+ and $[Ir(N^N^C)_2]^+$ coordination isomers, displayed in scheme 3.4.

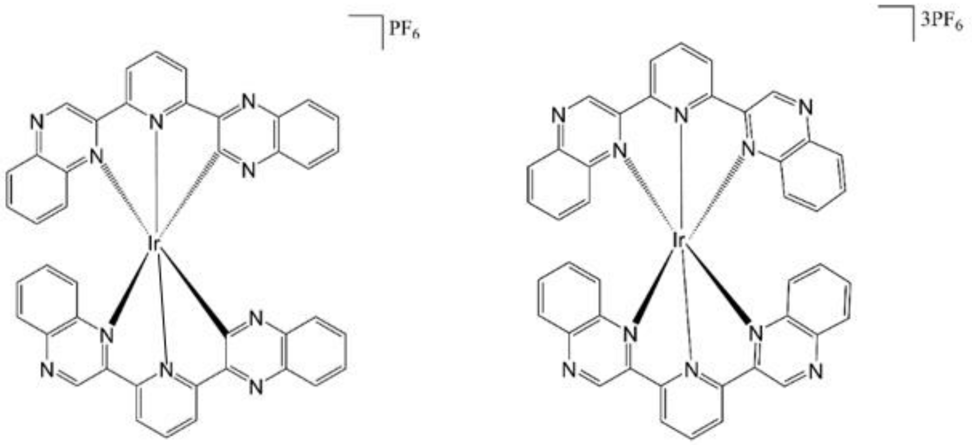

Scheme 3.4 Hypothetical structures comparing the N^N^C and N^N^N homoleptic coordination modes of the tridentate ligands.

For each applied functional, it was found that the computed energies for both isomers are generally similar, although the $[Ir(N^N^N)_2]^{3+}$ structure was predicted to be more energetically favorable, as shown below in table 3.8.

Table 3.8 Calculated energies of the two different coordination modes using different functionals and basis sets

	N^N^C mode	***N^N^N mode***
B3LYP/SDD	-2266.8188 Hartree -61683.31 eV	-2267.5832Hartree -61704.11eV
B3LYP/LANL2DZ	-2266.1273 Hartree -61691.71 eV	-2267.8926 Hartree -61712.53 eV
M062X/LANL2DZ	-2266.15195 Hartree -61665.16 eV	-2266.9041 Hartree -61685.63 eV

The optimized geometries of the ground states of both complexes obtained using the DFT (B3LYP/SDD,6-31G* level of theory) are displayed in figure 3.24. All optimizations were confirmed as minima through harmonic vibrational frequency calculations. The computed bond lengths for the investigated compounds are in good agreement with the corresponding X-ray crystallographic values, with an average deviation of less than 0.05 Angstroms. Generally, the computed bond lengths were slightly longer compared with the experimental data, which could be because the DFT calculations were performed in the implicit solvent while the experimental data was recorded in the solid state.

To investigate the effect of tridentate binding on the complex's electronic structure, molecular orbital decomposition analyses were performed on both complexes using the GaussSum software package. Each ligand was split into three separate groups, N-quinoxaline (R1), C-quinoxaline (R3) and pyridinyl groups (R2), with the iridium metal centre forming its own group. This allows a better understanding of the complex contributions than treating each whole ligand as an individual group, as shown in figure 3.24

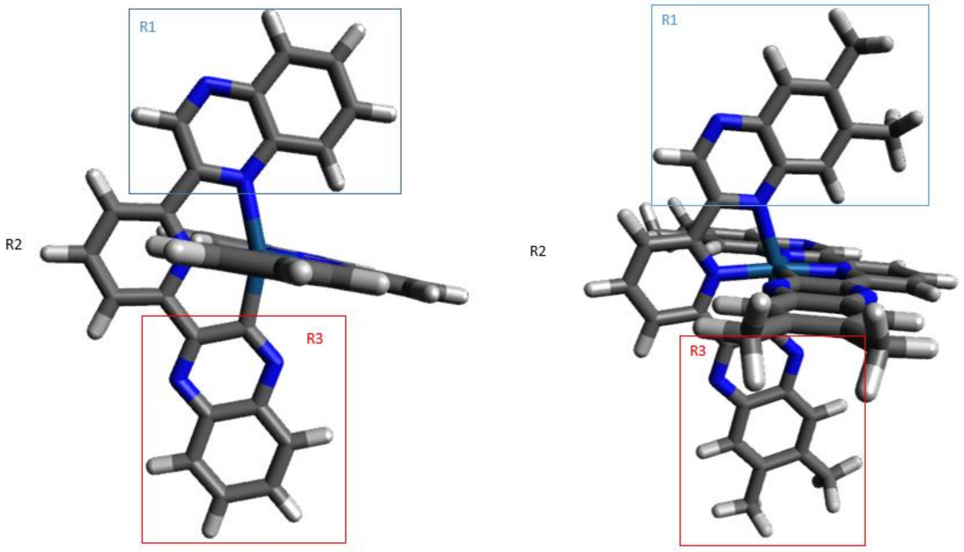

Figure 3.24 Optimized geometries of $[Ir(L^9)_2]^+$ (left) and $[Ir(L^{10})_2]^+$ (right). The two complexes have three moieties highlighted, each of which is used to provide a more effective molecular orbital decomposition of the system (R1 = N-quinoxaline; R2 = pyridine; R3 = C-quinoxaline).

Table 3.9 The decomposition analysis of the ground state frontier orbitals of $[Ir(L^9)_2]^+$

$[Ir(L^9)_2]^+$	Ir (*5d*) (%)	L1			L2		
		R1 (%)	R2 (%)	R3 (%)	R1 (%)	R2 (%)	R3 (%)
LUMO +4	1	33	15	0	34	15	0
LUMO +3	1	0	21	28	0	21	28
LUMO +2	1	1	19	29	1	20	29
LUMO +1	4	38	11	0	35	10	0
LUMO	4	34	12	1	37	13	1
HOMO	29	2	3	30	2	3	30
HOMO -1	8	3	3	38	3	4	40
HOMO -2	10	2	5	40	2	4	37
HOMO -3	6	1	3	42	1	4	43
HOMO -4	7	3	4	39	3	4	39

Consistent with bidentate phenyl-quinoxaline Ir^{III} complexes discussed above, the HOMO in both complexes is primarily made up from the contributions from the Ir *d*-orbital and *π*-orbitals of both ligands, located mainly on the C-quinoxaline moieties. The metal contribution to the HOMO is slightly less than that predicted for their bidentate analogues. The LUMO, however, is predominantly localized on the N-quinoxaline moieties, with some contributions from pyridyl rings. The two tridentate ligands in the $[Ir(L^9)_2]^+$ complex are almost degenerate, with contribution values for any given orbital differing by a just a few percentage points where they differ at all, as shown in table 3.10. This is due to the distortion in the C_2 symmetry of the complex. The $[Ir(L^{10})_2]^+$ complex shows similar contributions as $[Ir(L^9)_2]^+$, with a further reduction in the metal contribution to the HOMO (26%). The $[Ir(L^{10})_2]^+$ complex exhibits a more distorted geometry which leads to a clearer splitting of the degeneracy in its LUMO orbitals. In both complexes, the contribution from the frontier orbitals suggests that the lowest excited state is a mixed ^{1}MLCT/^{1}ILCT with less ^{1}MLCT character than in $[Ir(L^{1-8})_2(bipy)]^+$ complexes. Typically, increasing ^{1}ILCT contribution to the excited state results in longer lifetimes. This explains the longer lifetime observed in tridentate complexes in comparison to their bidentate counterparts that emit at similar wavelengths. It also clarifies the extended lifetime of the $[Ir(L^{10})_2]^+$ complex, despite emitting at longer wavelength, compared with its counterpart $[Ir(L^9)_2]^+$. Renderings of the frontier molecular orbitals of the $[Ir(L^9)_2]^+$ complex are shown in figure 3.25 below.

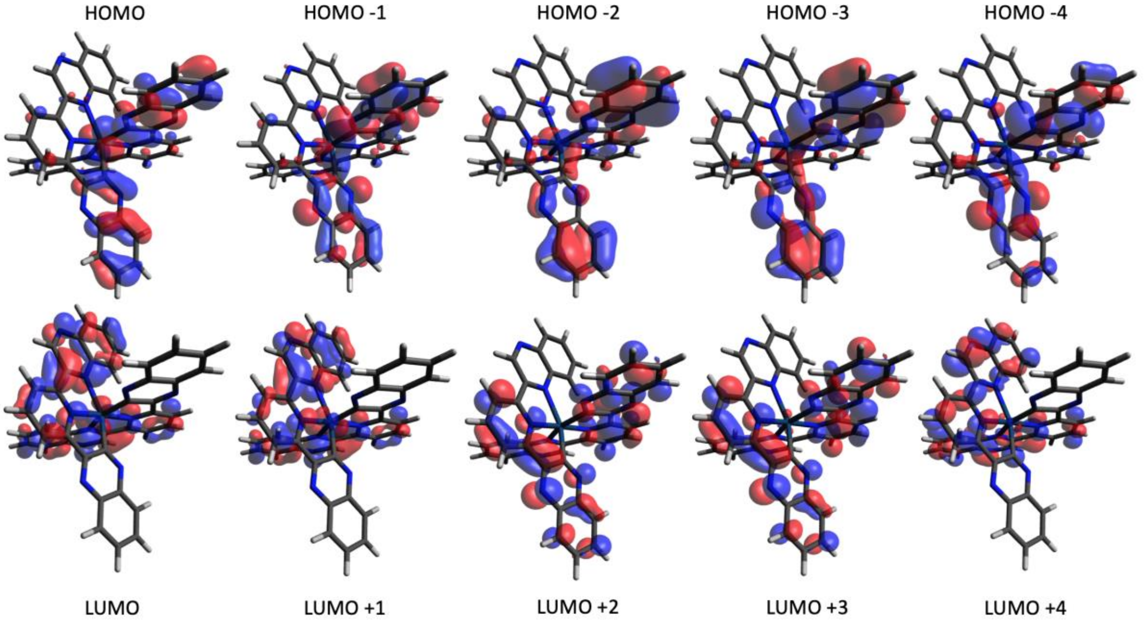

Figure 3.25 Calculated Kohn-Sham frontier molecular orbitals for $[Ir(L^9)_2)]^+$.

TD-DFT using the CAM-B3LYP functional was performed on the two complexes to calculate the spin-allowed transitions. The vertical and adiabatic spin-forbidden transitions of the complexes were also estimated using stationary point calculations based on the optimized singlet ground state and triplet excited state geometries. The first five singlet-to-singlet transitions of the complexes derived from the singlet geometry are reported below in table 3.10 while table 3.11 shows predicted spin-forbidden transitions.

Table 3.10 Excited state descriptions and their associated transitions for the $[Ir(L^9)_2]^+$ (top) and $[Ir(L^{10})_2]^+$ (below) complex. Molecular orbital contributions less than 10% have been omitted for clarity

$[Ir(L^9)_2]^+$	
Transition	Contributing MOs
1 383.91 nm, f = 0.0099	HOMO → LUMO (76.8%)
2 383.64 nm, f = 0.0179	HOMO → LUMO +1 (74.68%)
3 354 nm, f = 0.0011	HOMO -5 → LUMO +3 (29.22%) HOMO -4 → LUMO +2 (47.06%)
4 352.64 nm, f = 0.0007	HOMO -5 → LUMO +2 (35.74%) HOMO -4 → LUMO +3 (40%)
5 350.12 nm, f = 0.0067	HOMO -7 → LUMO +1 (11.99%) HOMO -6 → LUMO (40.22%)
$[Ir(L^{10})_2]^+$	
Transition	Contributing MOs
1 389.73nm, f= 0.0218	HOMO → LUMO +1 (77.21%)
2 388.5 nm, f = 0.0162	HOMO → LUMO (79.17%)
3 352.33 nm, f = 0.0024	HOMO -6 → LUMO +3 (23.81%) HOMO -4 → LUMO +2 (45.35%)
4 350.92 nm, f = 0.0003	HOMO -6 → LUMO +2 (10.57%) HOMO -5 → LUMO +2 (29.27%) HOMO -4 → LUMO +3 (38.64%)
5 349.04 nm, f = 0.0311	HOMO -6 → LUMO (27.34%) HOMO -5 → LUMO (21.7%) HOMO -3 → LUMO (11.74%)

Table 3.11 Computed values for the vertical and adiabatic spin forbidden transitions for the $[Ir(L^{9\text{-}10})_2]^+$ complexes

Complex	**$S_0 \rightarrow T_n$ Abs. (nm)**	**Vertical $T_1 \rightarrow S_0$ Em. nm)**	**Adiabatic $T_1 \rightarrow S_0$ Em. (nm)**
$[Ir(L^9)_2]^+$	513	698	581
$[Ir(L^{10})_2]^+$	527	689	587

As seen in table 3.10, the two lowest transition bands predicted from the spin-allowed absorption components only extend as far towards the visible as 384 – 390 nm, for $[Ir(L^9)_2]^+$ and $[Ir(L^{10})_2]^+$ respectively, attributed to the electron transition from HOMO to LUMO and from HOMO to LUMO+1, possessing mixed ^{1}MLCT/^{1}ILCT character. The oscillator strengths of these transitions are relatively small which is likely due to the spatial separation between the R3 moiety (representing HOMO) and

R1 and R2 moieties (forming the LUMO orbital) such that a low wavefunction overlap is expected between these orbitals. The spin-forbidden absorptions are predicted to occur in the same region as the phenyl-quinoxaline Ir^{III} complexes, $[Ir(L^{1-8})_2(bipy)]^+$ discussed early, indicating that there should be a shoulder peak at longer wavelengths (> 425 nm) in the experimental UV-Vis absorption spectra. Indeed, this is evident and can therefore be attributed to direct photoexcitation to low lying triplet states. Similarly, adiabatic emission estimations are in good quantitative and qualitative agreement with experimentally determined emission band maxima, supporting the assignment of the long-lived emission feature being spin-forbidden in nature. The spin density distributions of the $[Ir(L^9)_2]^+$ complex in the $\mathbf{T_1}$ state (shown in figure 3.26) show contributions from both tridentate ligands and the Ir metal centre, suggesting that the emission in these iridium complexes is ascribed to the metal to ligand charge transfer transition (^{3}MLCT) mixed with the intraligand charge transfer transition (^{3}ILCT).

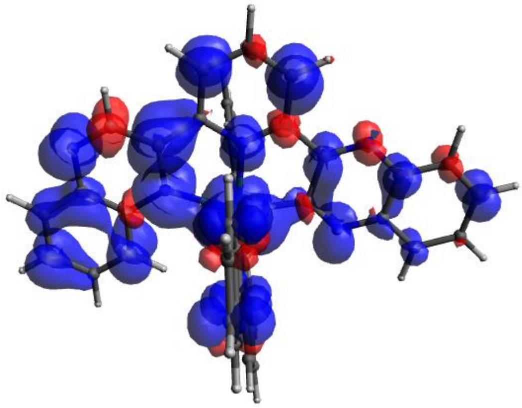

Figure 3.26 Calculated spin densities of the $[Ir(L^9)_2]^+$ complex.

3.4 Conclusion

A combination of spectroscopic and computational analyses was used to investigate the optical properties of two sets of Ir^{III} complexes. It was found that the spectroscopic features of the bidentate phenyl-quinoxaline iridium complexes are broadly similar with subtle variations depending on the nature and the position of the substituents of their quinoxaline ligands. The variations induce a shifting of absorption and emission band positions, as well as the changing in their emission lifetimes. The substitution on the phenyl ring in a cyclometalated ligand leads to a broader shift in the emission bands, whereas the substitution on the quinoxaline moiety allows more fine-tuning of the emission. Extended π-conjugation in the tridentate ligand did not alter the emission maxima but it significantly elongated the excited state lifetime due to increased ^{1}ILCT character in the excited state. The DFT computational technique nicely predicted the trend and extent of the band shifting caused by different substituents on cyclometallated ligands. The combination of the two substitution patterns of the ligands enables excellent tuning of the phosphorescent emission wavelengths of the Ir^{III} complexes ranging from yellow to deep red wavelengths. The emission lifetime could be tuned as well by introducing fluorine substituents or extended π-conjugation in the ligand backbone. This ability to easily tune emission properties of such Ir^{III} complexes is a key to diverse and ever-expanding optoelectronic and photoredox applications.

4. Transient Spectroscopic and Computational Analysis of poly-substituted Iridium (III) Quinoline Complexes

Following the characterisation of Ir^{III} complexes with bidentate and tridentate quinoxaline ligands in the previous chapter, this chapter aims to investigate how the adjustment of the cyclometallating ligand backbone or ancillary ligand changes the nature of the triplet excited state and thus tunes the photophysical properties of complexes, which consequently determine their possible applications. For example, increasing ^{3}MLCT character in the triplet state is predicted to shorten the phosphorescence lifetime which reduces the non-radiative decay and enhances the quantum yield, making such complexes more suitable for efficient OLED applications. Increasing ^{3}LLCT character prolongs the lifetime of excited states which could cause efficiency roll-off in OLEDs and thus complexes with long lifetimes are better in other applications, such as triplet-triplet annihilation (TTA), biological imaging and phosphorescence-based sensing applications. (Nazeeruddin et al. 2003; Han et al. 2015; Ma et al. 2017; Zhang and Qiao 2021) Understanding the nature of the excited state and how it can be tuned by modifying different ligands coordinated to the Ir^{III} centre is therefore helpful in predicting the photophysical properties for this class of complexes particularly when tailoring the system for a particular application. Towards this aim, the same spectroscopic and analytical techniques used in the previous chapter are applied here to examine a new variety of structurally related cyclometalated Ir^{III} complexes in which quinoxaline ligands are replaced by substituted naphthyl-quinoline-type ligands. Different modification approaches will be investigated in the new series of iridium complexes including changing the chelating position in the main ligand framework, changing the ancillary ligand as well as changing the substituents on both main and ancillary ligands.

4.1 Cyclometallating Ligand Variation

4.1.1 Complex Structures

Firstly, the six iridium complexes could be divided into two groups: the first one incorporates two substituted 2-(naphthalen-1-yl)quinoline-4-carboxylate ligands, while the second group is made of two 2-(naphthalen-2-yl)quinoline-4-carboxylate ligands, wherein the naphthyl quinoline ligands differ from each other in the position of chelation at the naphthyl unit. The ancillary ligand used in both groups is bipyridine. The naphthyl-quinoline ligand variations feature H, F and -OMe groups as substituents, which enables the examination of the subtle variations between the complexes in a similar way to the quinoxaline complexes discussed previously. These six complexes are all monocationic in nature and paired to PF_6^- counterions. This set of complexes was synthesised by the Pope group at Cardiff university, and their chemical structures are displayed in scheme 4.1.

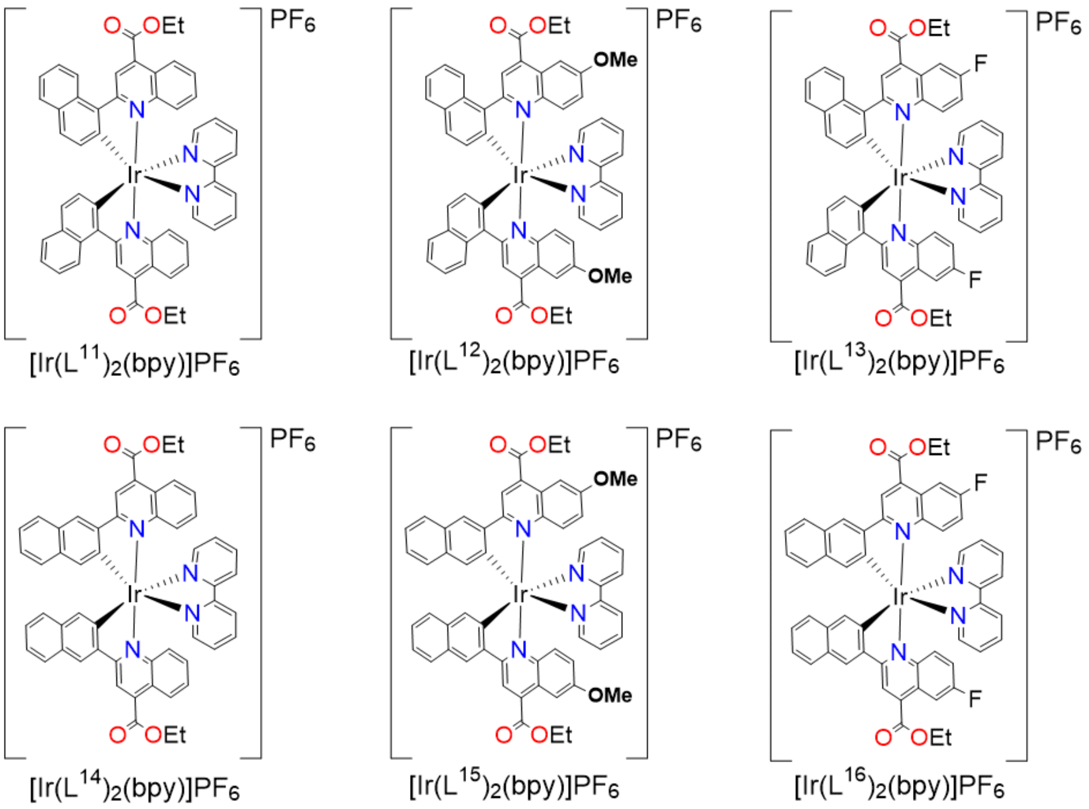

Scheme 4.1 The chemical structures of the six naphthyl-quinoline-based complexes [Ir(L$^{11\text{-}16}$)$_2$(bipy)]PF$_6$ analysed in this chapter.

4.1.2 DFT analysis

All six complexes were experimentally characterised by the Pope group at Cardiff University using the same spectroscopic techniques described in the previous chapter. Also, the complexes were examined for their potential application as upconversion sensitisers. All the complexes were found to be red emitters with subtle differences in emission profiles as the ligands were varied. Their experimental spectroscopic data indicates that direct ligand substitution has little influence on their emission properties, but instead the primary tuning parameter for these complexes is the position of chelation at the naphthyl unit. In addition, TTA upconversion measurements showed that the complexes of the ligands incorporating the 1-naphthyl moiety are viable photosensitisers with upconversion quantum efficiencies of 1.6–6.7%. DFT computational studies are performed here in an effort to interpret the experimental results with respect to emission profiles.

DFT//B3LYP/6-31G* was once again used to optimise all Ir^{III} complexes in their lowest electronic singlet and triplet states. Calculations were performed within an implicit acetonitrile solvent (IEFPCM), consistent with the spectroscopic measurements. The calculated geometric parameters were generated using crystal structure data as a starting point and confirmed through harmonic vibrational frequency calculations. The modelled structures display near C_2 symmetry, with a distorted octahedral geometry around the iridium metal centre. The computational method applied gave structural values in excellent agreement with the crystallographic data, as shown in figure 4.1. The difference between optimised geometric parameters and those derived from the experiment was typically less than 0.05Å (bond distances), and 1° (bond angles) (Table 4.1), with the DFT bond lengths typically being longer than those reported in the X-ray crystal structures.

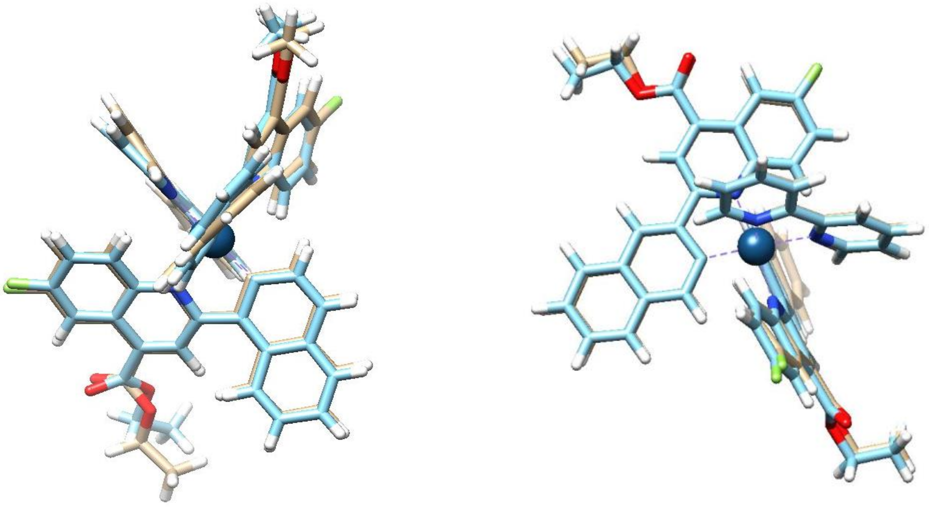

Figure 4.1 Overlay of the crystal structure (blue) and DF-DFT//B3LYP/6-31G(SDD) optimized structures (brown): left for $[Ir(L^{13})_2(bipy)]^+$, and right for $[Ir(L^{16})_2(bipy)]^+$*

Table 4.1 Selected bond lengths (Å) and angles (°) of the $[Ir(L^{11})^2(bipy)]$+ complex.

Bond lengths (Å)				Bond angles (°)			
bond	**Calc.**	**Exp.**	**∆**	**Bond**	**Calc.**	**Exp.**	**∆**
Ir(1)-N(2)	2.128	2.079	0.049	N2-Ir1-C5	79.01	79.48	0.47
				N2-Ir1-C46	96.27	96.52	0.25
Ir(1)-C(5)	2.018	2.001	0.017	N2-Ir1-N84	100.91	100.87	0.04
Ir(1)-N(43)	2.129	2.08	0.049	C5-Ir1-N43	96.24	96.43	0.19
				C5-Ir1-C46	88.57	88.37	0.2
Ir(1)-C(46)	2.018	1.994	0.024	C5-Ir1-N99	98.79	98.41	0.38
				N43-Ir1-C46	79.02	79.70	0.68
Ir(1)-N(84)	2.237	2.168	0.069	N43-Ir1-N84	83.96	83.60	0.36
Ir(1)-N(99)	2.236	2.143	0.093	N46-Ir1-N84	98.84	98.02	0.82

Molecular orbital decomposition analysis was carried out for singlet states of the six complexes using the GaussSum software package. This was performed with the aim of analysing the processes and transitions involved in the experimental spectra, and investigating the effects the ligand variations have on the electronic structure of the molecules. Figures 4.2 and 4.3 display the visualisation of the frontier molecular orbitals for the key isomeric variants within the series, $Ir(L^{11})_2(bipy)]^+$ and $[Ir(L^{14})_2(bipy)]^+$. The decomposition analysis for the six complexes is displayed in table 4.2.

Table 4.2 A summary of the major calculated contributions to each MO from each part of the complex. Q1 and Q2 are the different quinoline ligands; bipy = bipyridine.

Complex	**Ir 5d**		**Q1**		**Q2**		**bipy**
	HOMO-1	HOMO	LUMO	LUMO+1	LUMO	LUMO+1	LUMO+2
$[Ir(L^{11})_2(bipy)]^+$	2	21	46	49	49	46	97
$[Ir(L^{12})_2(bipy)]^+$	1	19	48	46	46	49	96
$[Ir(L^{13})_2(bipy)]^+$	1	20	44	50	51	45	97
$[Ir(L^{14})_2(bipy)]^+$	3	30	50	47	47	50	97
$[Ir(L^{15})_2(bipy)]^+$	3	30	49	48	48	49	97
$[Ir(L^{16})_2(bipy)]^+$	3	29	49	48	48	49	97

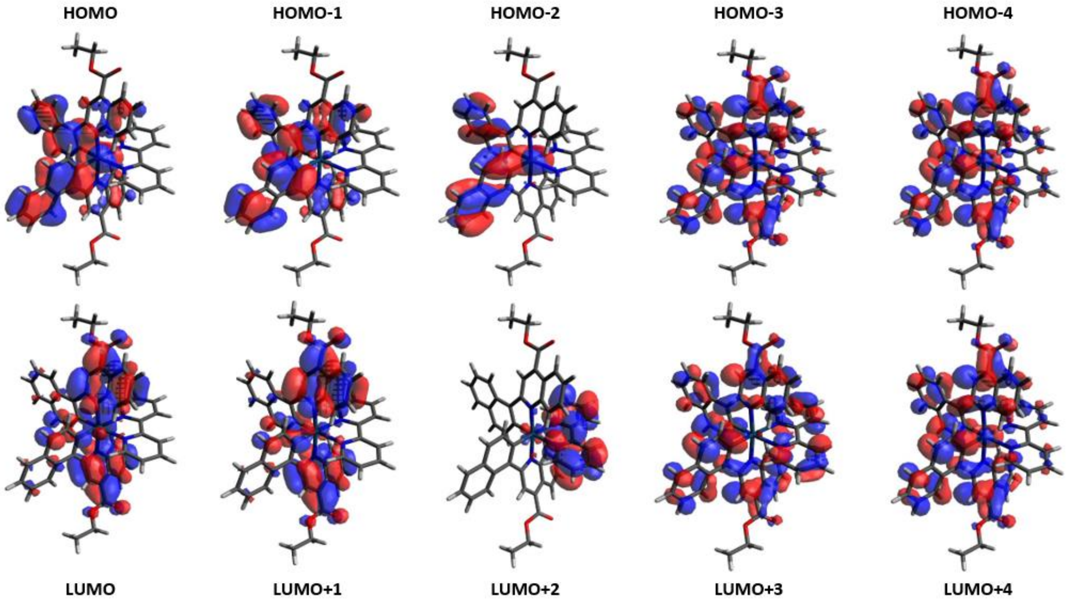

Figure 4. 2 The calculated Kohn-Sham frontier molecular orbitals for $[Ir(L^{11})_2(bipy)]^+$.

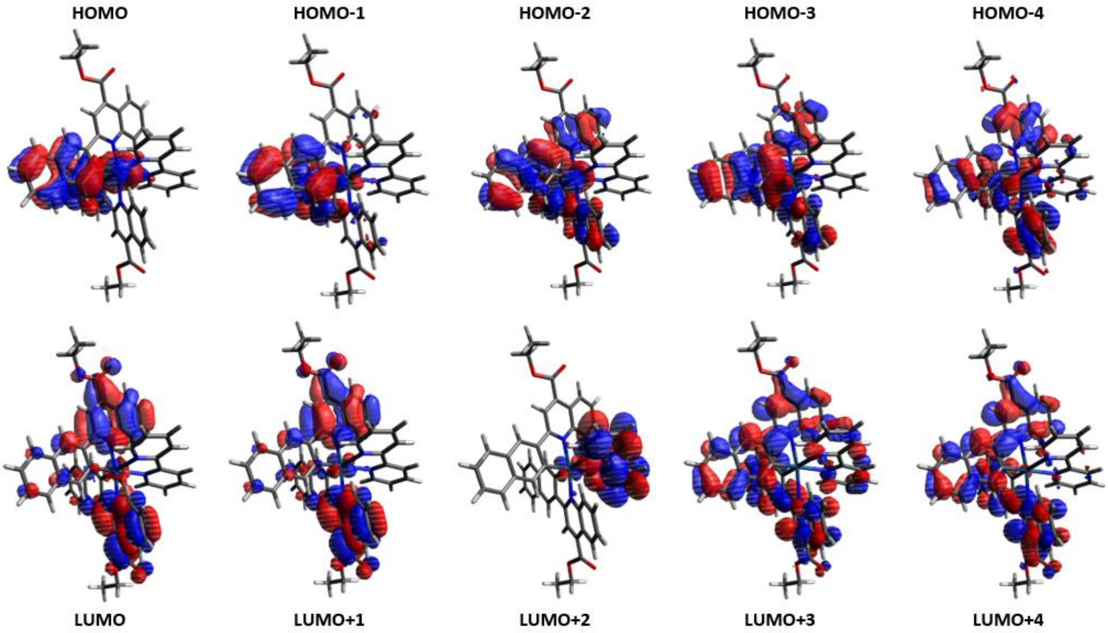

Figure 4.3 Calculated Kohn-Sham frontier molecular orbitals for $[Ir(L^{14})_2(bipy)]^+$.

Molecular orbital decomposition analysis predicts that the HOMO for the six Ir^{III} complexes is composed predominantly of contributions from the naphthyl moieties of both C^N ligands, and a significant but smaller contribution from the iridium centre; whilst the LUMO is found to be located primarily on the quinoline part of the C^N ligands. This reduction of the iridium contribution to the unoccupied molecular orbitals, LUMOs, suggests that the transitions involved in the spectroscopy of these complexes have a reasonable degree of metal to ligand charge transfer (MLCT) character.

As observed in table 4.3 below, the HOMO of 1-naphthyl derivative $[Ir(L^{11})_2(bipy)]^+$ is comprised of contributions of the Ir centre (21%) and equal contributions from naphthyl moieties on both C^N ligands (39 %), with just a 1% contribution from the bipyridine. Similarly, the HOMO of 2-naphthyl derivative $[Ir(L^{14})_2(bipy)]^+$ is made of contributions from 5*d* orbitals of Ir^{III} (28 %) and from *π* orbitals of the naphthyl moieties of both C^N ligands (36, 34 %), table 4.4. The HOMO-1 of the six complexes is found to be equally divided between the naphthyl moieties of both ligands (49 %) and a negligible contribution from the metal centre (≤3 %). The contribution of metal *d*-orbital to the HOMO orbitals is less than the ligand contributions, suggesting that the singlet excited states have a greater degree of intra-ligand charge transfer (ILCT) mixed with some metal to ligand charge transfer (MLCT) character.

Table 4.3 The decomposition analysis of the singlet ground state frontier orbitals of $[Ir(L^{11})_2(bipy)]^+$ complex (Q1 and Q2 are the different quinoline ligands; bipy = bipyridine).

	Moiety Contribution to Orbital (%)			
Orbital	**Ir (5d)**	**bipy**	**Q1**	**Q2**
LUMO +4	2	5	46	46
LUMO +3	2	21	38	39
LUMO +2	2	97	1	1
LUMO +1	3	1	49	46
LUMO	5	1	46	49
HOMO	21	1	39	39
HOMO -1	2	0	49	49
HOMO -2	16	1	41	42
HOMO -3	38	5	30	27
HOMO -4	35	1	30	34

Table 4.4 The decomposition analysis of the singlet ground state frontier orbitals of $[Ir(L^{14})_2(bipy)]^+$ complex (Q1 and Q2 are the different quinoline ligands; bipy = bipyridine).

	Moiety Contribution to Orbital (%)			
Orbital	**Ir (5d)**	**bipy**	**Q1**	**Q2**
LUMO +4	1	3	48	48
LUMO +3	1	13	43	43
LUMO +2	2	97	0	0
LUMO +1	3	0	47	50
LUMO	2	1	50	47
HOMO	30	2	34	34
HOMO -1	3	1	48	48
HOMO -2	10	0	45	45
HOMO -3	12	2	43	43
HOMO -4	38	5	28	29

Table 4.2 shows that the two quinoline ligands in the $Ir(L^{15})_2(bipy)]^+$ and $[Ir(L^{16})_2(bipy)]^+$ complexes are almost degenerate, with contribution values showing a just a few percentage points difference from each other, given the symmetric nature of the system. However, the complexes $Ir(L^{11-14})_2(bipy)]^+$ display a loss of degeneracy similar to that observed in the quinoxaline complexes, $Ir(L^{1-8})_2(bipy)]^+$, with the two ligands forming pairs of pseudo-degenerate orbital contributions. This indicates that the geometries of $Ir(L^{11-14})_2(bipy)]^+$ complexes are not as close to the C_2 point group as those of the $Ir(L^{15-16})_2(bipy)]^+$ complexes.

TD-DFT calculations with the CAM-B3LYP functional were carried out from the optimised singlet ground states of the complexes to investigate singlet and triplet electronic transitions of these complexes, as in the case of the quinoxaline complexes. Due to the non-relativistic nature of the calculations, it examines mainly the spin-allowed transitions; however, the spin-forbidden excitation energies are also helpful in defining absorption bands‘ characters. The results of the singlet TD-DFT calculations for the lowest five singlet excited states are shown below in table 4.5 for $Ir(L^{11})_2(bipy)]^+$ and $Ir(L^{14})_2(bipy)]^+$ complexes.

Table 4.5 The wavelength, oscillator strengths and contributing molecular orbital transitions of the first five singlet-to-singlet excited states for $[Ir(L^{11})_2(bipy)]^+$ and $[Ir(L^{14})_2(bipy)]^+$ complexes. Molecular orbital contributions less than 10% have been omitted for clarity

$[Ir(L^{11})_2(bipy)]^+$	
Excited State	**Orbital Contribution to Excited State Contributing Transitions (> 10 %)**
1 (432 nm f=0.1150)	HOMO-1 → LUMO +1 (13.57%) HOMO → LUMO (67.65%)
2 (432 nm f=0.1978)	HOMO-1 → LUMO (15.04%) HOMO → LUMO +1 (65.20%)
3 (351 nm f=0.1827)	HOMO -2 → LUMO+1 (15.38%) HOMO -1 → LUMO (51.81%)
4 (347 nm f=0.1456)	HOMO -2 → LUMO (18.14%) HOMO -1 → LUMO+1 (59.94%)
5 (343 nm f=0.0480)	HOMO → LUMO+2 (73.77%)

$[Ir(L^{14})_2(bipy)]^+$	
Excited State	**Orbital Contribution to Excited State Contributing Transitions (> 10 %)**
1 (407 nm f=0.0004)	HOMO → LUMO (84.43%)
2 (404 nm f=0.0400)	HOMO → LUMO +1 (82.86%)
3 (356 nm f=0.4125)	HOMO -2 → LUMO+1 (28.29%) HOMO -1 → LUMO (52.16%)
4 (353 nm f=0.3334)	HOMO -2 → LUMO (18.14%) HOMO -1 → LUMO+1 (59.94%)
5 (343 nm f=0.0017)	HOMO -2 → LUMO (38.27 %) HOMO -1 → LUMO+1(39.23%)

Vertical transitions were also calculated using the lowest optimized geometries for each singlet and triplet state and the single point energy calculations for the opposing spin state from each of these geometries. This allows estimation of the wavelength of any spin-forbidden absorption and emission of each complex. The lowest computed spin allowed and spin-forbidden transitions of each complex are displayed in table 4.6.

Table 4.6 Computed values for the vertical spin allowed and spin-forbidden absorption wavelengths of the $[Ir(L^{11-16})_2(bipy)]^+$ complexes

Complex	$S_o \rightarrow S_1$ Abs. (nm)	$S_o \rightarrow T_n$ Abs. (nm)
$[Ir(L^{11})_2(bipy)]^+$	432	622
$[Ir(L^{12})_2(bipy)]^+$	442	636
$[Ir(L^{13})_2(bipy)]^+$	441	635
$[Ir(L^{14})_2(bipy)]^+$	407	571
$[Ir(L^{15})_2(bipy)]^+$	405	560
$[Ir(L^{16})_2(bipy)]^+$	414	581

DFT calculations predict that the six complexes possess very similar spectroscopic features, all derived from the same underlying process, with the 1-naphthyl derivatives exhibiting bathochromically shifted absorption bands compared to those of the 2-naphthyl derivatives, which is in an agreement with the experimental UV-Vis spectra. In addition, a subtle shift in absorption features is predicted due to different substituents on naphthyl-quinoline ligands, as shown in table 4.6.

Once again, the isomeric $Ir(L^{11})_2(bipy)]^+$ and $[Ir(L^{14})_2(bipy)]^+$ will be used as representatives for all variants within the series. For $[Ir(L^{11})_2(bipy)]^+$, the lowest spin-forbidden transition to $\mathbf{T_1}$ is expected to occur at 622 nm, matching well to the low-intensity absorption tail at 550-620 nm observed in the experimental absorption spectra. The longest wavelength singlet excitation is predicted to occur at 433 nm, comprised of mixed HOMO → LUMO (68%) and HOMO-1 → LUMO+1 (14%) transitions. This is accompanied by another intense HOMO → LUMO+1 (31%) and HOMO-1 → LUMO+1 (35%) transition at 432 nm ($f = 0.1987$). These two transitions reflect the effect of pseudo-degenerate splitting of the orbitals on the absorption spectra, similar to prior observations in the quinoxaline complexes. The contribution from the HOMO-1, which is centred almost entirely on the 1-naphthyl quinoline ligands, suggests a significant degree of ^{1}ILCT character mixed with ^{1}MLCT. More intense absorption bands are predicted to be between $300 < \lambda < 350$ nm all with mixed ^{1}ILCT/^{1}LLCT/^{1}MLCT character. The TD-DFT calculations also suggest an increase in ligand-centred transitions when moving to shorter wavelengths (higher energy), at $\lambda < 300$ nm. The computed values nicely correlate with the experimental absorption bands. The calculated spin allowed and spin forbidden UV-Vis transitions for $[Ir(L^{14})_2(bipy)]^+$ complex were almost identical to those predicted for $[Ir(L^{11})_2(bipy)]^+$, save for a slight hypsochromic shift. Notably, the predominant contributions for the lowest two singlet excitations arise only from the HOMO, which features a greater contribution from the metal centre. This suggests that the ^{1}MLCT character in the mixed excited state (^{1}MLCT/ ^{1}ILCT) is higher than those found in $[Ir(L^{11})_2(bipy)]^+$.

The spin-forbidden emission wavelengths from the lowest triplet state $\mathbf{T_1 \rightarrow S_0}$ were also calculated by DFT, and are shown in table 4.7.

Table 4.7 Computed values for the vertical and adiabatic spin-forbidden emission wavelengths for the $[Ir(L^{11\text{-}16})_2(bipy)]^+$ complexes along with experimental values.

Complex	**$T_1 \rightarrow S_o$ Em. (nm) Vertical**	**$T_1 \rightarrow S_o$ Em. (nm) Adiabatic**	**$T_1 \rightarrow S_o$ Em. (nm) Exp.**
$[Ir(L^{11})_2(bipy)]^+$	811	705	679
$[Ir(L^{12})_2(bipy)]^+$	891	755	693
$[Ir(L^{13})_2(bipy)]^+$	836	725	687
$[Ir(L^{14})_2(bipy)]^+$	746	649	673
$[Ir(L^{15})_2(bipy)]^+$	756	645	668
$[Ir(L^{16})_2(bipy)]^+$	761	661	675

As shown in the above table, the computed phosphorescence bands are in good agreement with experimentally determined values, with predicted wavelengths falling within the same region as the experimental emission bands. Similar to the trends found between the absorption spectra, the emission maxima of 1-naphthyl derivatives are bathochromic shifted compared with those of the 2-naphthyl derivatives. The substitution on the naphthyl quinoline ligand leads to a minor shift of emission bands of the complexes. Although the positions of emission centres are overestimated, the adiabatic band positions provide a reasonable quantitative match, and qualitative agreement with the experimental data. The estimation of vertical emission bands shows less satisfying results, as the emission energies are systematically underestimated, and the positions of predicted emission centres of $[Ir(L^{14})_2(bipy)]^+$ and $[Ir(L^{15})_2(bipy)]^+$ complexes are opposite to that observed experimentally. Therefore, the adiabatic approach is considered more accurate and preferable for estimating band positions because it takes into account the relaxation of nuclear positions in response to changing electronic configuration, while the vertical approach assumes that nuclear positions do not change upon electronic excitation. (Ferrer and Santoro 2012; Alia and Flack 2020)

As with the triplet absorption band, the emission bands are expected to be dominated by ^{3}ILCT and ^{3}MLCT contributions. This assignment is verified by Mulliken spin-density analysis for the lowest triplet **T_1** states of these Ir^{III} complexes, displayed in figure 4.4.

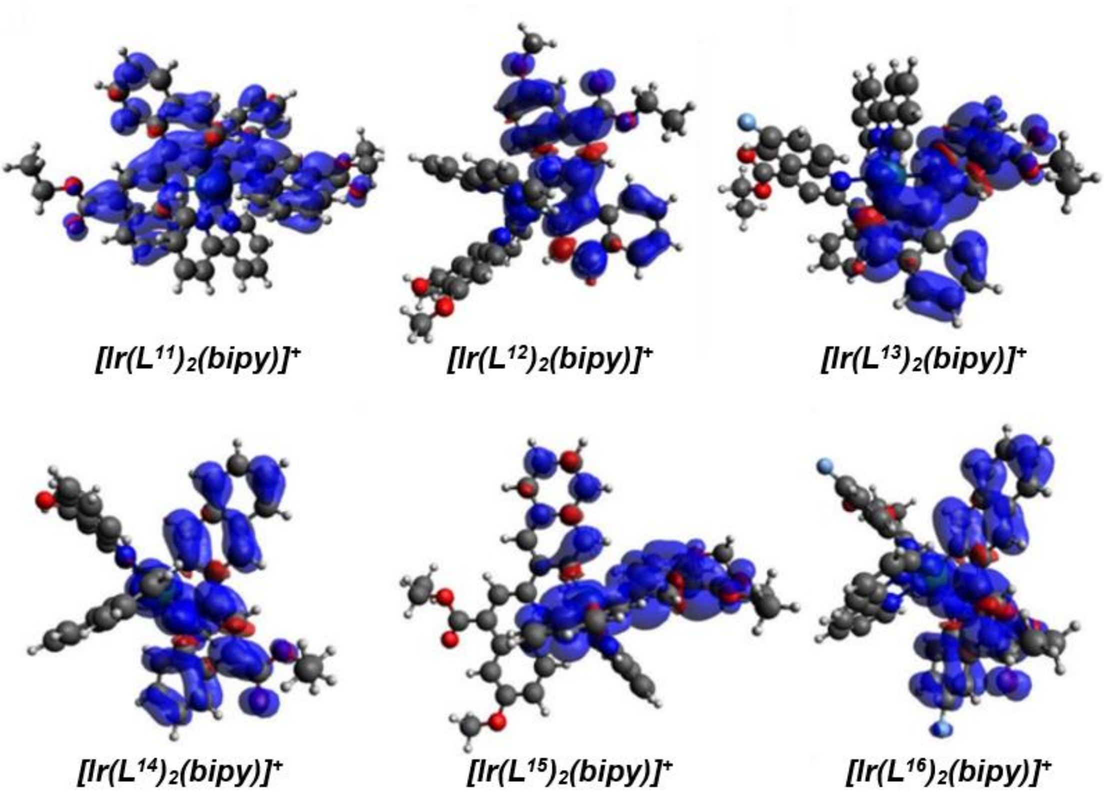

$[Ir(L^{11})_2(bipy)]^+$ $[Ir(L^{12})_2(bipy)]^+$ $[Ir(L^{13})_2(bipy)]^+$

$[Ir(L^{14})_2(bipy)]^+$ $[Ir(L^{15})_2(bipy)]^+$ $[Ir(L^{16})_2(bipy)]^+$

Figure 4.4 Calculated spin densities of $[Ir(L^{11\text{-}16})_2(bipy)]^+$

The spin density distributions of Ir^{III} complexes at the $\mathbf{T_1}$ minimum energy geometry predominantly lie on both the cyclometalating ligands and Ir^{III} metal centre, confirming that the phosphorescence of these iridium complexes is ascribed as a mixed character of metal to ligand charge transfer transition (^{3}MLCT) and intraligand charge-transfer transition (^{3}ILCT) within the CN ligand moieties. This correlates nicely with experimentally emission measurements collected in a range of solvents of varying polarity. The emission spectra were relatively independent of the change in the polarity of the medium, which contrasts with classical MLCT complexes such as $[Ru(bipy)_3]^{2+}$. (Juris et al. 1988) This is because ILCT is typically less polar than MLCT due to charge transfer occurring within the ligand itself, with localized redistribution of electron density within the ligand, resulting in smaller changes in dipole moment, whereas MLCT transitions involve electron transfer from a metal *d*-orbital to a ligand, resulting in a significant change in electron density and a large change in dipole moment. (Housecroft and Sharpe 2008; Sutton et al. 2021) These observations strongly indicate that the emissive triplet state has a ^{3}ILCT character with less ^{3}MLCT contributions. Additionally, the emission lifetimes obtained in aerated acetonitrile, displayed in table 4.8, are found to be significantly longer for 1-naphthyl derivatives compared with their 2-naphthyl analogues, which is consistent with the changing degree of ILCT versus MLCT character in their emissive excited electronic states. (Liu et al. 2014; Kuo et al. 2017; Wang et al. 2017)

Table 4. 8 Emission lifetimes for $[Ir(L^{11-16})_2(bipy)]^+$ complexes

Complex	Emission Wavelength (nm)	Emission lifetimes (ns)
$[Ir(L^{11})_2(bipy)]PF_6$	679	240
$[Ir(L^{12})_2(bipy)]PF_6$	693	223
$[Ir(L^{13})_2(bipy)]PF_6$	687	217
$[Ir(L^{14})_2(bipy)]PF_6$	673	36
$[Ir(L^{15})_2(bipy)]PF_6$	668	89
$[Ir(L^{16})_2(bipy)]PF_6$	675	17

4.2 Ancillary Ligand Variation

Continuing our investigation into the relationship between chemical structure and spectroscopic properties, the following section explores how adjustments to the ancillary ligand impact the photophysical and electronic properties of this class of iridium complexes. For this, a series of new complexes were developed by the Pope group at Cardiff university by using novel substituted diimine ligands (2-(2′-pyridinyl/pyrazinyl)-quinoline-4-carboxylic acids) as a replacement for bipy ancillary ligand on naphthyl-quinoline complexes studied above, shown in scheme 4.2. Each of the new diimine ligands feature H, OMe and F groups as substituents. This enables the examination of fine variations between the complexes.

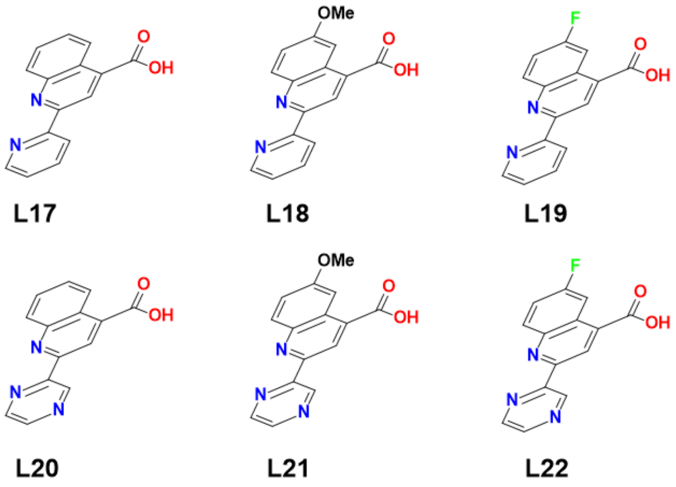

Scheme 4.2 Structures of pyridinyl/pyrazinyl diimine ligands

The above diimine ancillary ligands have been used to develop two sets of iridium complexes, and each contains six variants. The first group utilizes the 2-naphthalen-1-yl quinoline group L^{11} as the main C^N bidentate ligand, while the second group incorporates a 2-naphthalen-2-yl quinoline ligand L^{14}. All of these complexes are monocationic and studied either as BF_4^- or PF_6^- salts, seen in schemes 4.3 and 4.4.

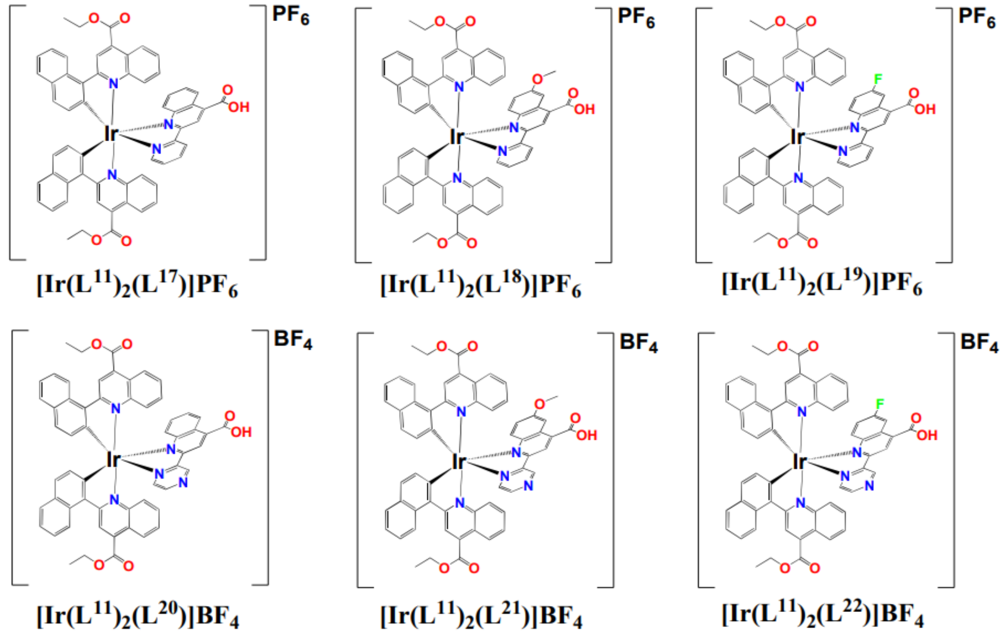

$[Ir(L^{11})_2(L^{17})]PF_6$ $[Ir(L^{11})_2(L^{18})]PF_6$ $[Ir(L^{11})_2(L^{19})]PF_6$

$[Ir(L^{11})_2(L^{20})]BF_4$ $[Ir(L^{11})_2(L^{21})]BF_4$ $[Ir(L^{11})_2(L^{22})]BF_4$

Scheme 4.3 Structure of the diimine-based complexes $[Ir(L^{11})_2(L^{17-22})]^+$ investigated in this study.

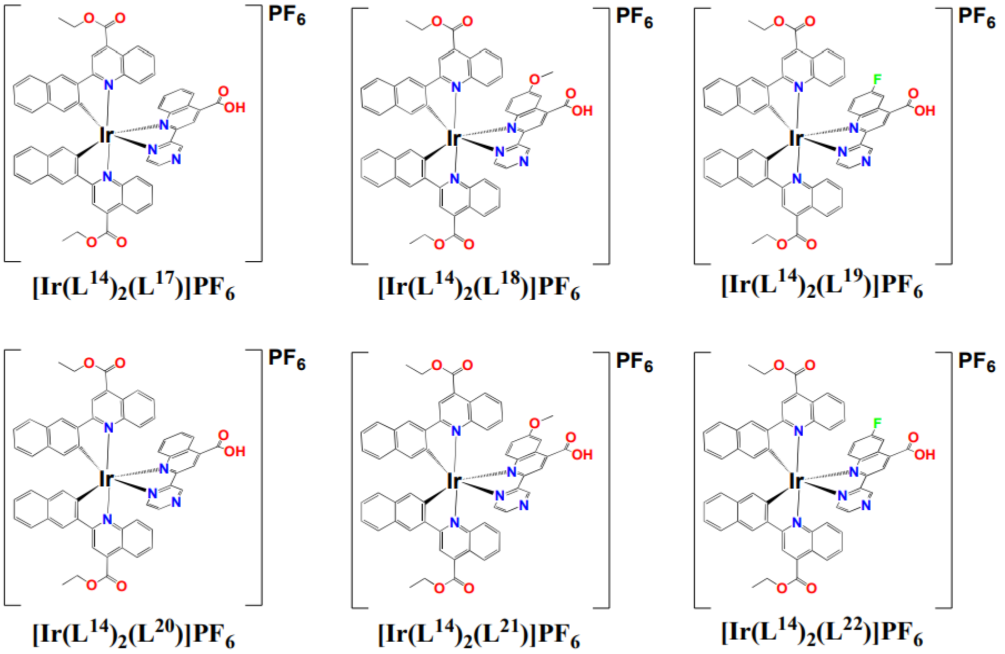

$[Ir(L^{14})_2(L^{17})]PF_6$ $[Ir(L^{14})_2(L^{18})]PF_6$ $[Ir(L^{14})_2(L^{19})]PF_6$

$[Ir(L^{14})_2(L^{20})]PF_6$ $[Ir(L^{14})_2(L^{21})]PF_6$ $[Ir(L^{14})_2(L^{22})]PF_6$

Scheme 4.4 Structure of the diimine-based complexes $[Ir(L^{14})_2(L^{17-22})]^+$ investigated in this study

4.2.1 Steady State Absorption Spectra

4.2.1.a 1-naphthyl quinoline complexes with pyridinyl / pyrazinyl diimine ancillary ligands

UV-Vis spectra for the complexes of $[Ir(L^{11})_2(L^{17-22})]^+$ were recorded in aerated acetonitrile solutions at 10^{-5} M and can be seen in figure 4.5 along with the absorption spectrum of $[Ir(L^{11})_2(bipy)]PF_6$ for ease of comparison. The absorption spectra of the six Ir^{III} complexes are similar to their bipyridine counterparts studied previously, with each comprising of three main features, although the intensities and the appearance of the higher energy bands, $\lambda < 450$ nm, are different in comparison with their bipyridine counterparts. These variations result from the change in the ancillary ligand structure, while the subtle shift observed in these features is associated with different substituents on the ancillary ligand. Similar to the previously studied Ir^{III} complexes and supported by DFT calculations, the strong absorption bands between 200 – 320 nm are attributed to the various $\pi\pi^*$ transitions from the different aromatic fragments of both C^N and ancillary ligands. The intense lower wavelength bands between 330-450 nm arise from the different types of spin-allowed CT transitions, including ^{1}MLCT, ^{1}ILCT and ^{1}LLCT, as indicated by DFT. The weaker broad band extending to 600 nm is assigned to spin forbidden CT transitions. Noticeably, this CT band does not appear to be affected by the modification of ancillary ligand structures or by the nature of different substituents, indicating that the transitions and underlying processes involved in this band are the same in all cases. Therefore, it is expected that the ancillary ligand orbitals do not contribute to this feature, and it arises from ^{3}MLCT/ ^{3}ILCT transitions. This will be discussed in more detail in the DFT section below.

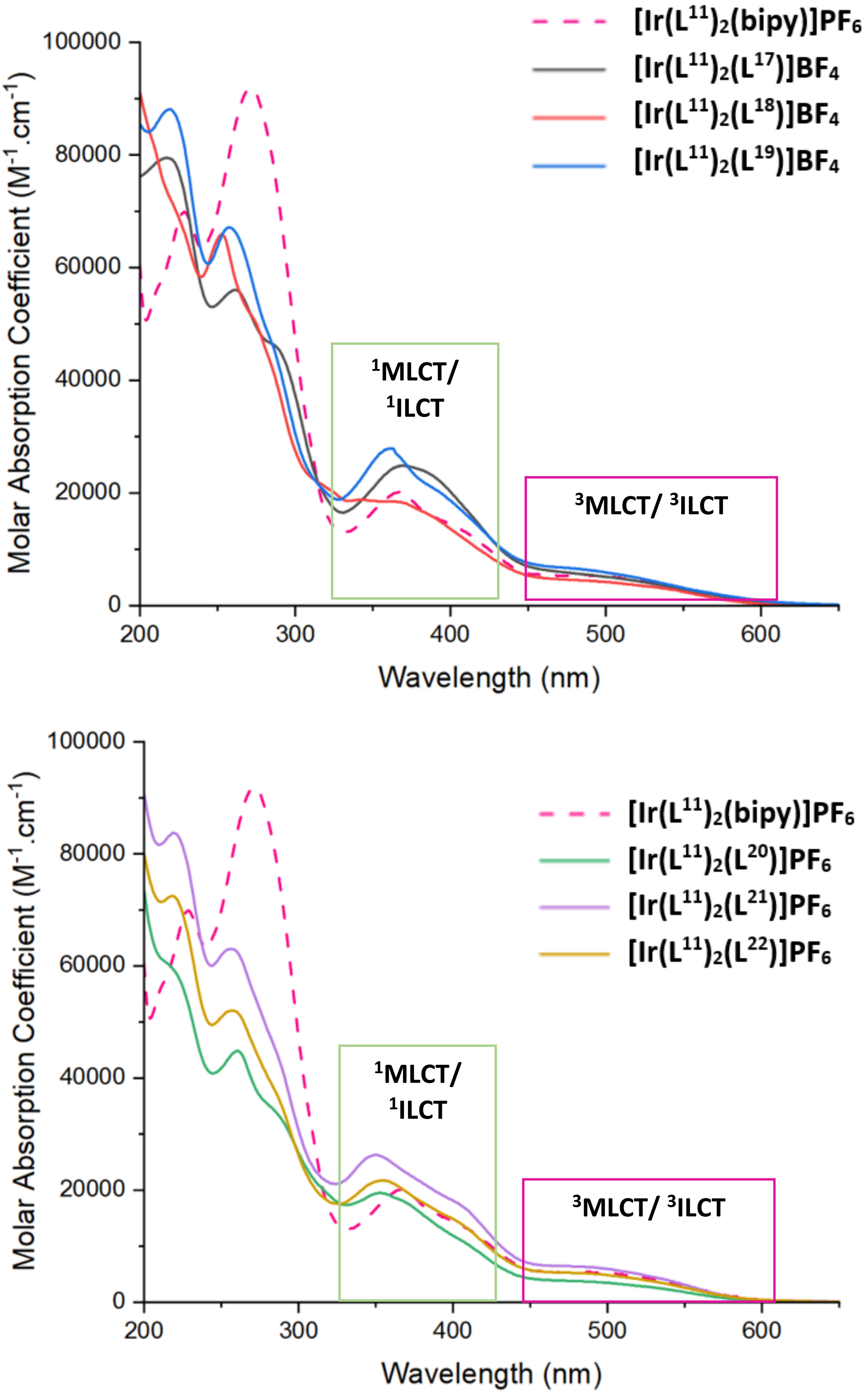

Figure 4.5 Normalised UV-Vis absorption spectra of $[Ir(L^{11})_2(L^{17-19})]^+$ complexes (top) and $[Ir(L^{11})_2(L^{20-22})]^+$ (below) in acetonitrile ($1X10^{-5}$ M).

4.2.1.b 2-naphthyl quinoline complexes with pyridinyl / pyrazinyl diimine ancillary ligands

The absorption spectra for $[Ir(L^{14})_2(L^{17-22})]PF_6$ complexes are shown below in figure 4.6.

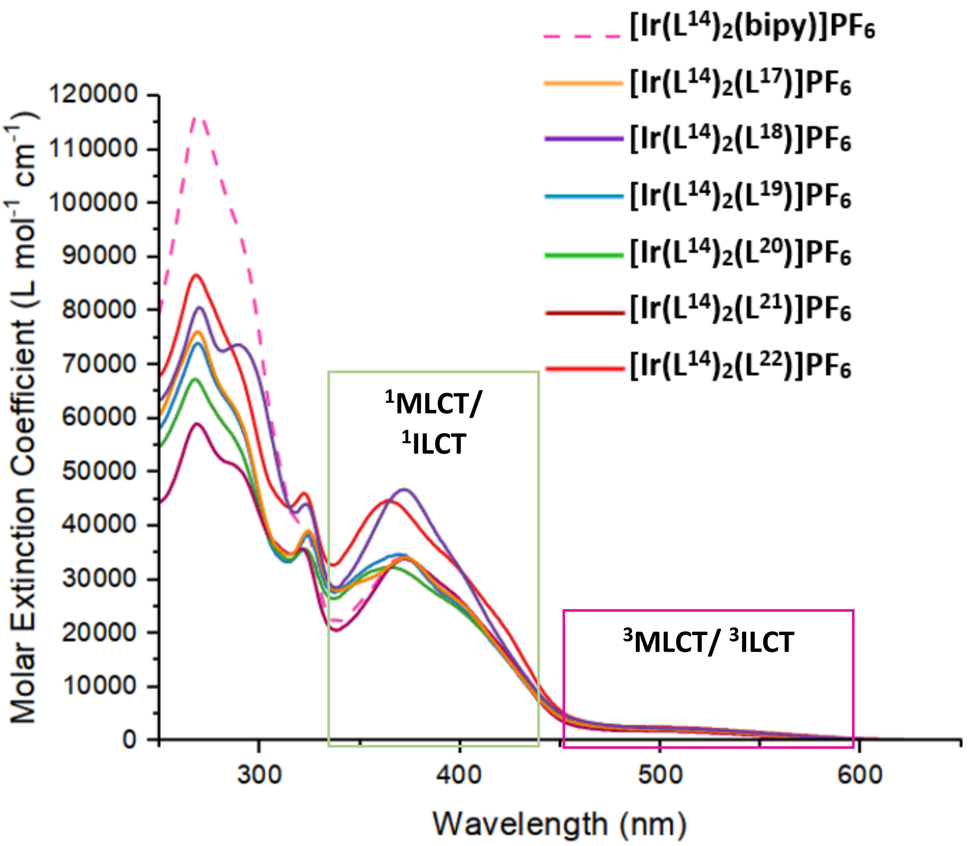

Figure 4.6 Normalised UV-Vis absorption spectra of $[Ir(L^{11})_2(L^{17-22})]^+$ complexes in acetonitrile ($1X10^{-5}M$).

The complexes all display an absorption profile comparable to the previous iridium complexes discussed in this chapter. Consequently, the band features are assigned to the same transitions and underlying processes as those found in other naphthyl quinoline complexes studied above. Once again, the weak spin forbidden bands at $450 < \lambda < 600$ nm remain relatively unperturbed when alternating the ancillary ligands. However, the triplet feature for each complex in this set is weaker and less resolved in comparison with their 1-naphthyl quinoline variants. This is likely because 2-naphthyl quinoline complexes have a larger spatial separation between the naphthyl moieties and quinoline moieties, representing HOMO and LUMO, respectively, which leads to lower wavefunction overlap between their orbitals and thus lower oscillator strengths of this transition.

4.2.2 Emission Spectra

4.2.2.a 1-naphthyl quinoline complexes with pyridinyl/ pyrazinyl diimine ancillary ligands

The luminescence properties of $[Ir(L^{11})_2(L^{17-22})]^+$ complexes were recorded in aerated acetonitrile solutions (10^{-5} M) after excitation at 355 nm, and are shown in figure 4.7. The complexes all display broad structureless profiles with emission maxima ranging between 674 - 679 nm. The pyrazinyl-based complexes, $Ir(L^{11})_2(L^{20-22})]^+$, exhibit a subtle blue shift in emission wavelength (by less than 5 nm) when compared to their pyridinyl analogues Ir(L^{11})$_2$(L^{17-19})]$^+$ or their bipy base complex, Ir(L^{11})$_2$(bipy)]$^+$ that emits at λ_{max} = 679 nm. This is the opposite outcome to that observed in quinoxaline-based complexes studied previously by our group, in which the replacement of bipy ancillary ligand with picolinate or pyrazinate resulted in a remarkable shift of emission wavelength. (Phillips et al. 2018; Stonelake et al. 2020) Similar to the absorption spectra, the incorporation of substituents into the ancillary ligand has very little impact on the emission profile.

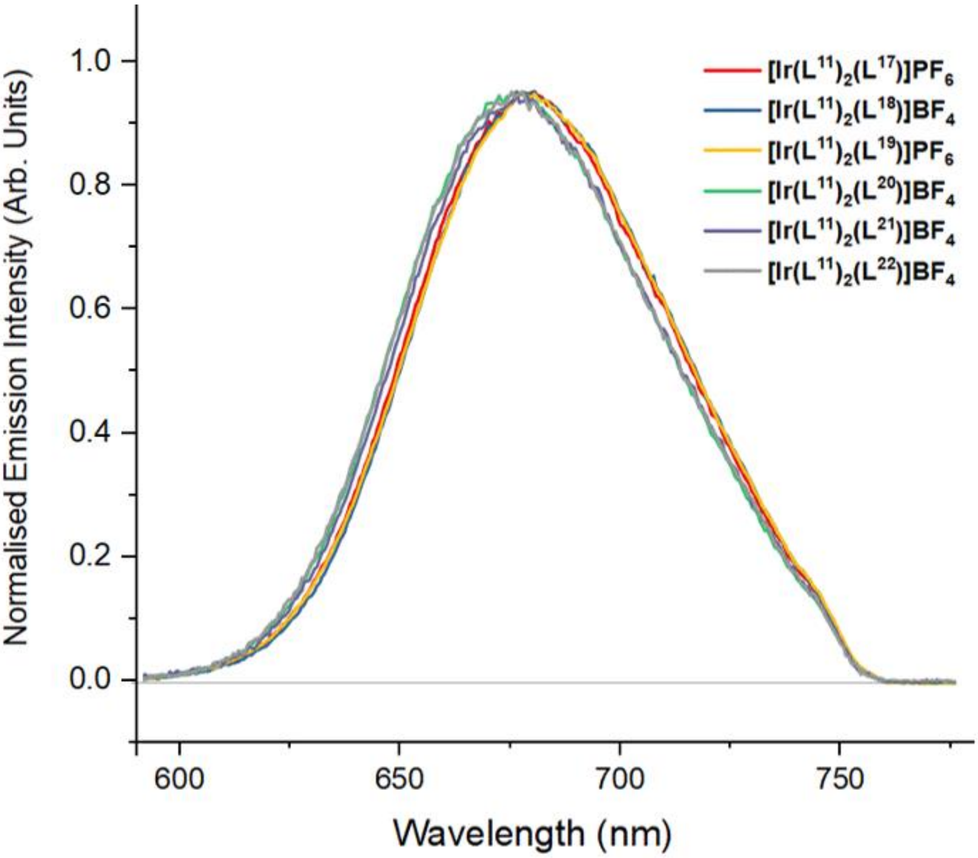

Figure 4.7 Normalised emission spectra of [Ir(L^{11})$_2$(L^{17-22})]$^+$ complexes obtained in aerated acetonitrile solution (1X10^{-5}M) at room temperature.

The emission spectra were also obtained for all complexes under degassed conditions to investigate the effect of dissolved oxygen on the intensity and the positions of emission bands. It was found that the intensity of the emission peaks was significantly increased under deoxygenated conditions, but the emission centre and shape were unperturbed. This indicates that the presence of oxygen reduces the quantum yield by quenching the excited state of the complexes, but does not interact with the system or change its molecular geometry in either ground or excited states.

Room temperature lifetime values were in the range 268 ns < τ < 411 ns which is longer than for the base complex [Ir(L^{11})$_2$(bipy)]$^+$ at τ = 240 ns. The lifetime values extend substantially under deoxygenated conditions to 866 ns < τ < 1212 ns, as displayed in table 4.9. This supports the assignment of the emitting state being triplet in character.

Table 4.9 Emission lifetimes of$[Ir(L^{14})_2(L^{17-22})]^+$ complexes under atmospheric and deoxygenated conditions along with the emission lifetime of base complex $[Ir(L^{14})_2(bipy)]^+$ for ease of comparison.

Complex	λ_{em} / nm	t / ns aerated	t / ns deoxygenated
$[Ir(L^{11})_2(bipy)]^+$	679	240	
$[Ir(L^{11})_2(L^{17})]^+$	678	411 ± 0.8	985 ± 1.4
$[Ir(L^{11})_2(L^{18})]^+$	679	268 ± 0.8	866 ± 2.1
$[Ir(L^{11})_2(L^{19})]^+$	679	275 ± 0.2	811 ± 1.8
$[Ir(L^{11})_2(L^{20})]^+$	674	323 ± 0.9	1212 ± 2.5
$[Ir(L^{11})_2(L^{21}]^+$	677	385 ± 0.7	1151 ± 2.7
$[Ir(L^{11})_2(L^{22})]^+$	673	313 ± 1.8	1207 ± 3.4

The $Ir(L^{11})_2(L^{19})]^+$ and $Ir(L^{11})_2(L^{21})]^+$ complexes exhibit an additional emission band centred at 450 nm, which can be seen in figure 4.8. In degassed solutions, the short-wavelength feature undergoes a subtle reduction in band intensity, accompanied by a slight bathochromic shift of the band center. This is in contrast to the long-wavelength emission band, which shows a significant increase in emission intensity. The different behaviour of the two emission features under both atmospheric and degassed conditions suggests a different underlying photophysical process as origin of each of these bands. The longer wavelength emission band that is quenched in an aerated solution indicates the involvement of triplet excited states in the emission pathway, making it more likely to be quenched by oxygen. Therefore, this emission band is ascribed to a spin-forbidden phosphorescent process as in the cases studied in the previous chapter. In contrast, the lower wavelength emission is assigned as spin-allowed fluorescent transitions.

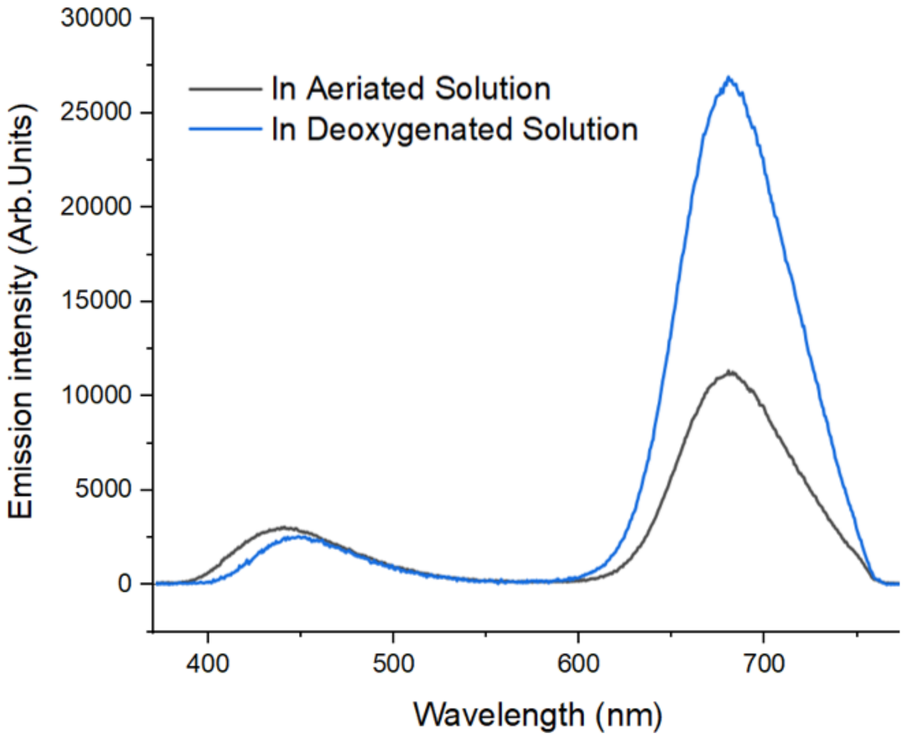

Figure 4.8 Emission spectra of $[Ir(L^{11})_2(L^{21})]^+$ complexes recorded in aerated and deoxygenated acetonitrile.

4.2.2.b 2-naphthyl quinoline complexes with pyridinyl/ pyrazinyl diimine ancillary ligands

The $[Ir(L^{14})_2(L^{17-22})]^+$ complexes once again showed a broad featureless band profile with emission centres occurring at $630 < \lambda < 680$ nm, as displayed in figure 4.9.

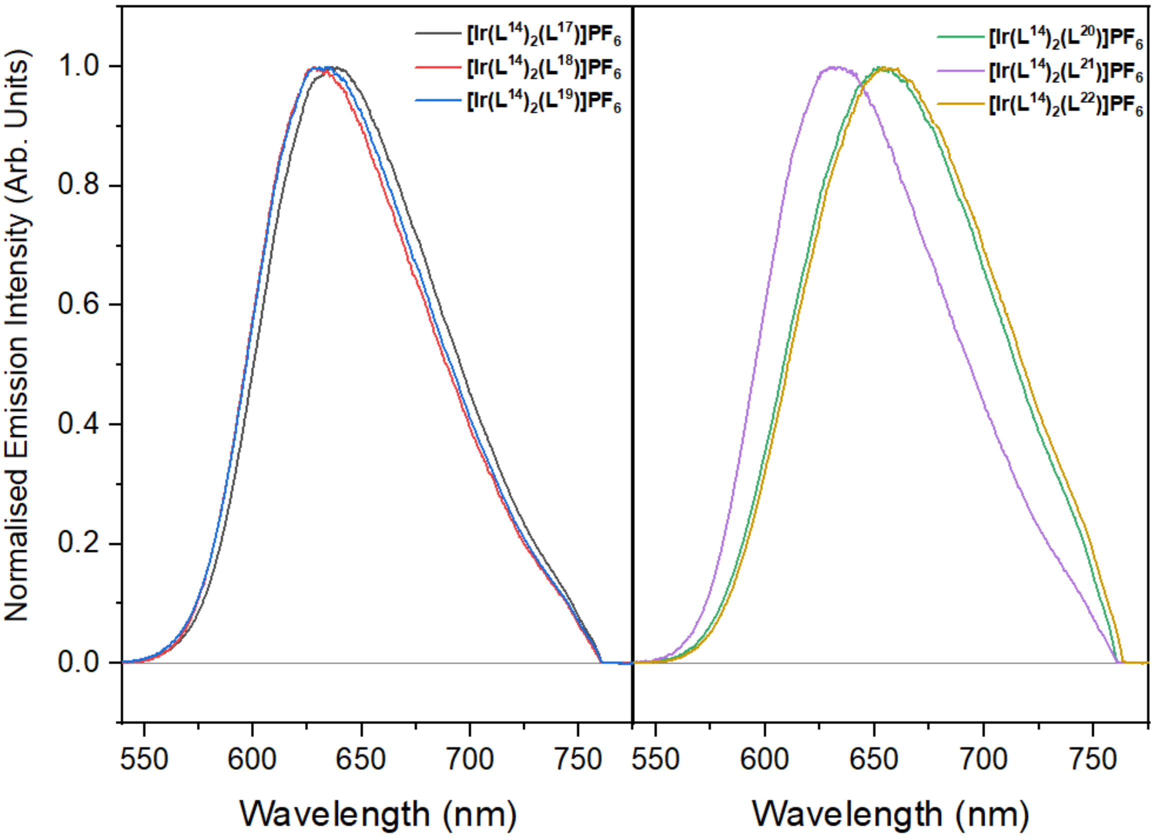

Figure 4.9 Normalised emission spectra of $[Ir(L^{14})_2(L^{17-22})]^+$ complexes obtained in aerated acetonitrile solution ($1X10^{-5}M$) at room temperature.

As shown above, the position of emission bands is now more dependent on the ancillary ligand structure and substituent groups attached to it. This is in contrast to the observations made for the 1-naphthyl analogues, $[Ir(L^{11})_2(L^{17-22})]^+$, which is indicative of a different electronic structure of each set of complexes. This is similar to what was observed for the tridentate quinoxaline Ir^{III} complexes discussed in the previous chapter. The set as a whole is hypsochromically shifted in comparison to the 1-naphthyl counterparts and the base complex $[Ir(L^{14})_2(bipy)]^+$, with pyridinyl-based variants $[Ir(L^{11})_2(L^{17-19})]^+$ exhibiting a further hypsochromic shift. These observations highlight the tunability of this class of complexes, as fine tuning can be achieved through the incorporation of different substituents on the ancillary ligand, while the modification of the backbone of the ancillary ligand enables broad wavelength tuning of the emissive bands.

Similarly, emission lifetimes measured in atmospheric conditions for the complexes were slightly longer than their base complex and ranged between 51 ns < τ < 133 ns (table 4.10), discussed in more detail in the kinetic study section.

Table 4.10 Emission lifetimes for $[Ir(L^{14})_2(L^{17-22})]^+$ complexes under atmospheric conditions along with the base complex $[Ir(L^{14})_2(bipy)]^+$ for ease of comparison.

Complex	λ_{em} / nm	τ / ns aerated
$[Ir(L^{14})_2(bipy)]^+$	673	32
$[Ir(L^{14})_2(L^{17})]^+$	639	52 ± 0.1
$[Ir(L^{14})_2(L^{18})]^+$	630	133 ± 0.7
$[Ir(L^{14})_2(L^{19})]^+$	632	50 ± 0.1
$[Ir(L^{14})_2(L^{20})]^+$	650	119 ± 0.9
$[Ir(L^{14})_2(L^{21}]^+$	633	61 ± 0.5
$[Ir(L^{14})_2(L^{22})]^+$	653	118 ± 1.2

4.2.3 TA Spectra

4.2.3.a 1-naphthyl quinoline complexes with pyridinyl/ pyrazinyl diimine ancillary ligands

Time-resolved transient absorption (TA) spectra of all Ir^{III} complexes were again recorded in aerated acetonitrile using a pump wavelength of 355 nm and are presented in Figure 4.10. The general appearance of TA spectra for this set of complexes is comparable to that observed for base complex $[Ir(L^{11})_2(bipy)]^+$.

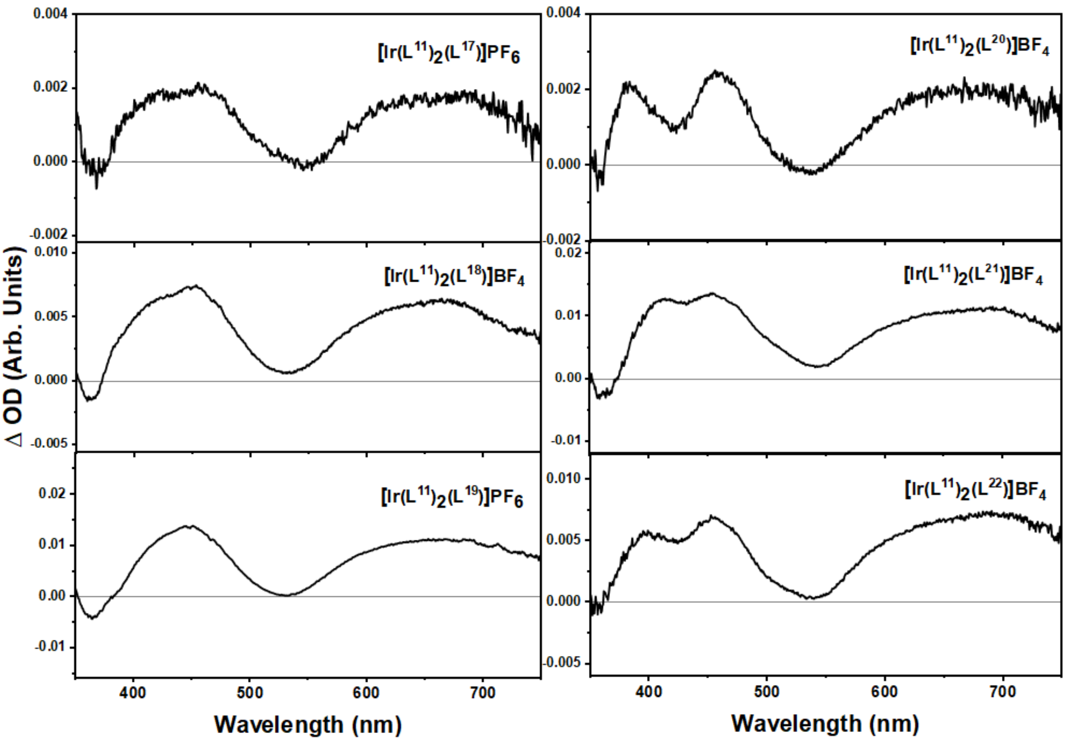

Figure 4.10 Background and fluorescence subtracted transient absorption spectra of $[Ir(L^{11})_2(L^{17-22})]^+$ complexes in aerated acetonitrile, λ_{ex} = 355 nm, delay time = 50 ns. The grey line represents ΔOD = 0 in all cases.

The general profile of the spectra of all six complexes is largely similar, albeit with a few noticeable differences. All spectra display a weak ground state bleach appearing in the shorter wavelength region, 350 < λ < 380 nm, resulting from a depletion of the ground state absorption band. Strong positive features were also observed at 380 < λ < 550 nm and 550 < λ < 760 nm regions, assigned to triplet-triplet transitions as indicated by the magnitude of the associated lifetime values. The absorption feature between 380 < λ < 550 nm seems to be a single broad band in pyridinyl-based complexes, although it is split into a doublet for pyrazinyl-based complexes. This is probably because the modification of the ancillary ligand leads to varying degrees of alteration in molecular orbitals involved in the transitions contributing to this feature.

4.2.3.b 2-naphthyl quinoline complexes with pyridiny/ pyrazinyl diimine ancillary ligands

The transient absorption spectra of complexes all present a similar overall profile, despite a few distinct variations that can be observed in $[Ir(L^{14})_2(L^{20})]^+$ and $[Ir(L^{11})_2(L^{22})]^+$ complexes. The TA spectra for the six complexes are shown in figure 4.11.

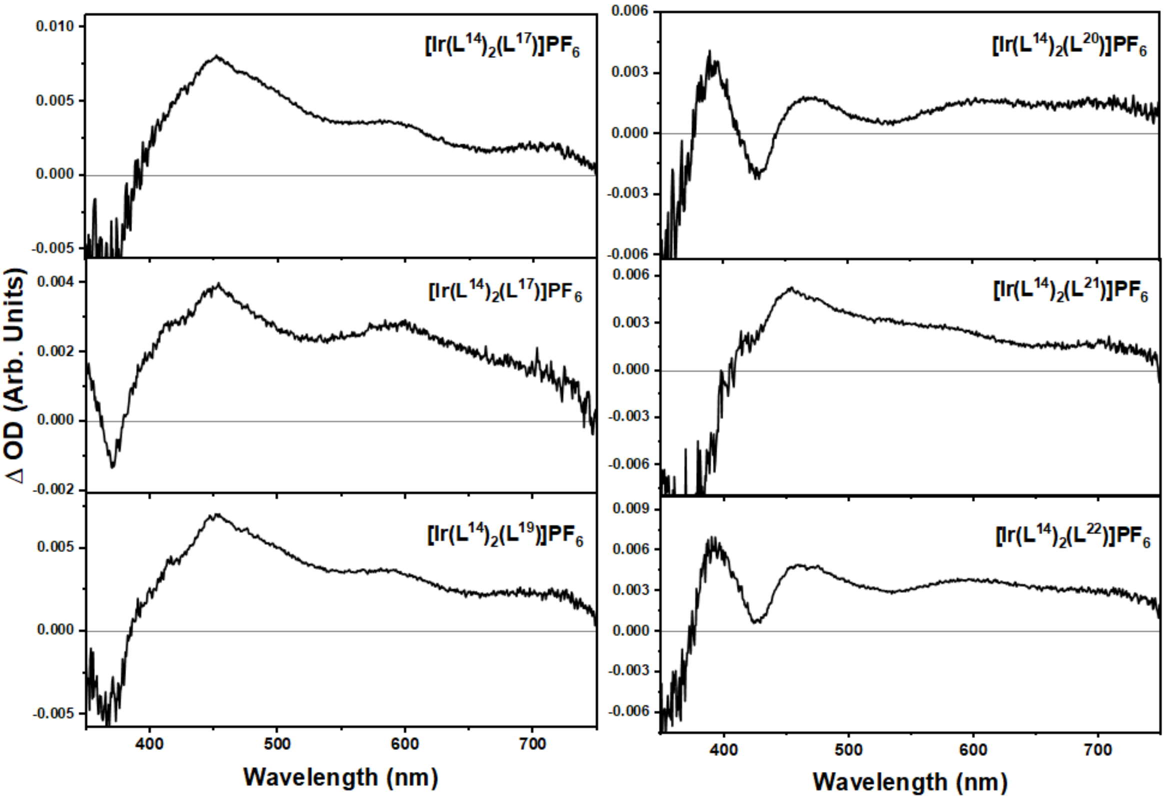

Figure 4.11 Background and fluorescence subtracted transient absorption spectra of $[Ir(L^{14})_2(L^{17-22})]^+$ complexes in aerated acetonitrile, λ_{ex} = 355 nm, delay time = 50 ns. The grey line represents ΔOD = 0 in all cases.

As seen above, the spectra consist of a prominent bleach feature visible at around 370 nm and two broad and less resolved positive bands, which are the excited state absorption transitions of the $\mathbf{T_1}$ state ($\mathbf{T_1} \rightarrow \mathbf{T_n}$ transitions). Both $[Ir(L^{14})_2(L^{20})]^+$ and $[Ir(L^{11})_2(L^{22})]^+$ complexes exhibit a further intense positive feature visible at 375 < λ < 425 nm, also assigned to triplet-triplet transitions, as it bears a similar lifetime to other triplet features. This band is comparable to those observed in 1- naphthyl complexes. The positions of different TA features undergo varying degrees of shift depending on the alternation of the ancillary ligand. Once again, the TA spectra of the complex set as a whole are slightly blue-shifted compared with the 1-naphthyl variants.

4.2.4 Transient Kinetics

4.2.4.a 1-naphthyl quinoline complexes with pyridinyl/ pyrazinyl diimine ancillary ligands

The kinetic analysis of the major spectroscopic features observed for these complexes was carried out using the PMT and monochromator detector system in the same way as in the quinoxaline complexes studied in chapter 3. The transient kinetics of the $[Ir(L^{11})_2(L^{17})]BF_6$ and $[Ir(L^{11})_2(L^{22})]BF_4$ complexes in aerated acetonitrile at room temperature are visible in figure 4.12.

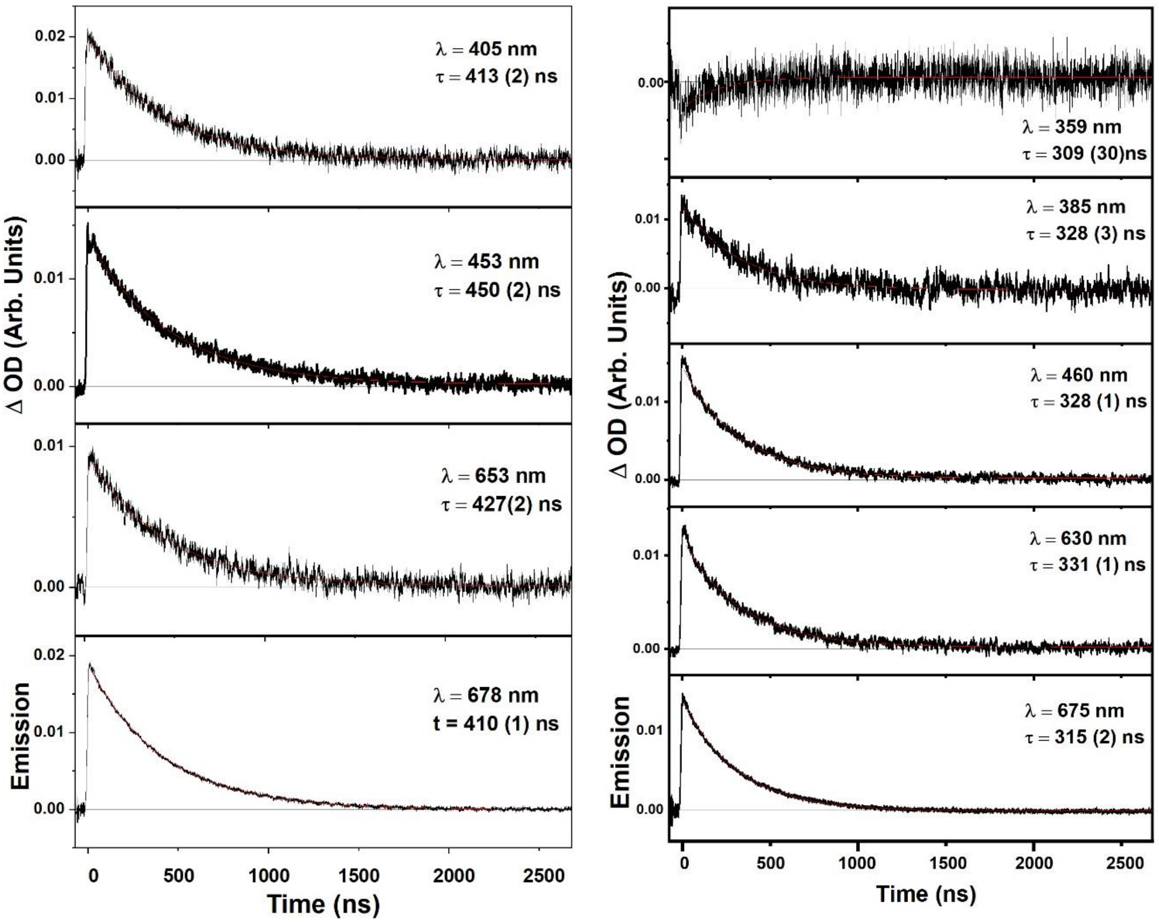

Figure 4. 12 Fitted (red line) kinetic traces of the major features of the transient spectrum of $[Ir(L^{11})_2(L^{17})]BF4$ (left) and $[Ir(L^{11})_2(L^{22})]BF4$ (right) in acetonitrile at room temperature, aerated. The wavelengths and lifetimes of each trace are inset

All transient kinetic spectra return to baseline showing no evidence for transient species associated with any chemical changes caused by photoexcitation. The kinetic traces were fit to a mono-exponential decay function, and show similar decay lifetimes for all features displayed by each complex, indicating that these features have the same photophysical origin. The lifetime values for each feature of the six complexes are presented in table 4.11.

Table 4.11 Kinetic data obtained from the fitted time-resolved transient absorption spectra of the complexes in aerated acetonitrile $[Ir(L^{11})_2(L^{17-22})]^+$*, λexc = 355 nm*

	Lifetime (ns)		**Lifetime (ns)**
$[Ir(L^{11})_2(L^{17})]^+$	405 nm (412.6 ± 2.0) 453 nm (449.6 ± 1.5) 653 nm (426.7 ± 2.4) 678 nm (410.3 ± 0.8)	**$[Ir(L^{11})_2(L^{20})]^+$**	357 nm (295.3 ± 27) 382 nm (355.7 ± 2.0) 460 nm (345.6 ± 1.6) 630 nm (343.8 ± 2.1) 674 nm (323.5 ± 0.9)
$[Ir(L^{11})_2(L^{18})]^+$	366 nm (275.9 ± 9.3) 403 nm (253.3 ± 1.5) 453 nm (263.1 ± 1.6) 651 nm (260.0 ± 0.6) 679 nm (267.9 ± 0.8)	**$[Ir(L^{11})_2(L^{21})]^+$**	367 nm (382.8 ± 9.2) 415 nm (356.9 ± 7.5) 475 nm (387.3 ± 3.7) 635 nm (397.3 ± 1.0) 677 nm (364.3 ± 0.7)
$[Ir(L^{11})_2(L^{19})]^+$	366 nm (253.8 ± 2.9) 410 nm (271.2 ± 0.9) 650 nm (271.3 ± 0.7) 679 nm (275.6 ± 0.2)	**$[Ir(L^{11})_2(L^{22})]^+$**	359 nm (309.3 ± 3.9) 385 nm (327.6 ± 3.2) 460 nm (327.7 ± 1.0) 630 nm (330.6 ± 1.2) 673 nm (314.7 ± 1.8)

The lifetimes obtained for all complexes are noticeably longer than for their bipyridine analogue (t_1 = 240 ns), with $[Ir(L^{11})_2(L^{17})]^+$ complex showing the most extended lifetimes. The lifetime values range between 449 – 260 ns depending on the change in the structure of the ancillary ligand and the nature of the substituents. When measurements are carried out in free oxygen conditions, the emission lifetimes are significantly elongated into the microsecond domain (866 ns < τ < 1212 ns), as seen in figure 4.13, further supporting the assignment of these features as originated from the triplet emissive state, **T_1**.

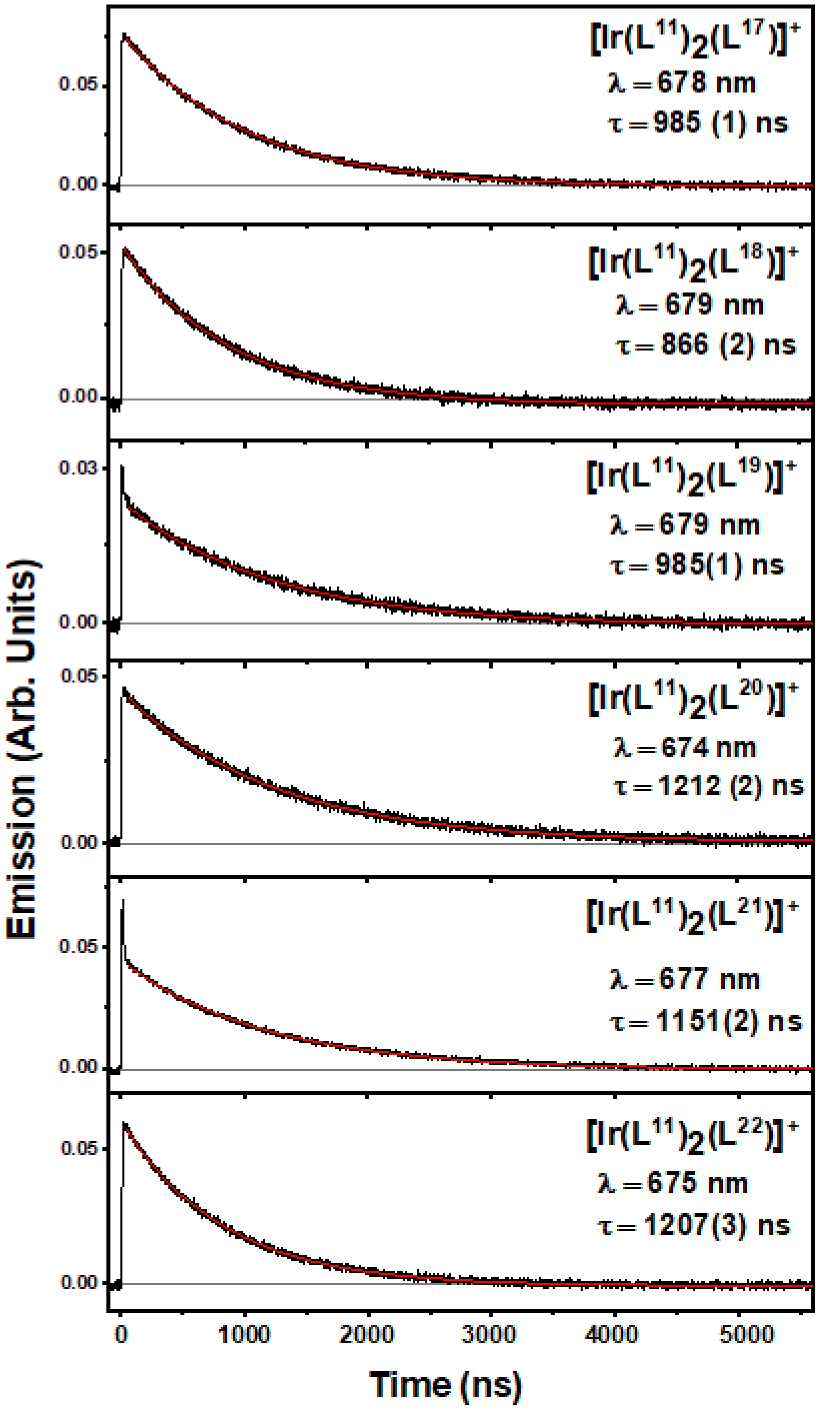

Figure 4.13 Fitted (red line) kinetic traces of emission features of $[Ir(L^{11})_2(L^{17\text{-}22})]^+$ in deoxygenated acetonitrile at room temperature, Wavelengths and lifetimes of each trace are inset.

4.2.4.b 2-naphthyl quinoline complexes with pyridinyl / pyrazinyl diimine ancillary ligands

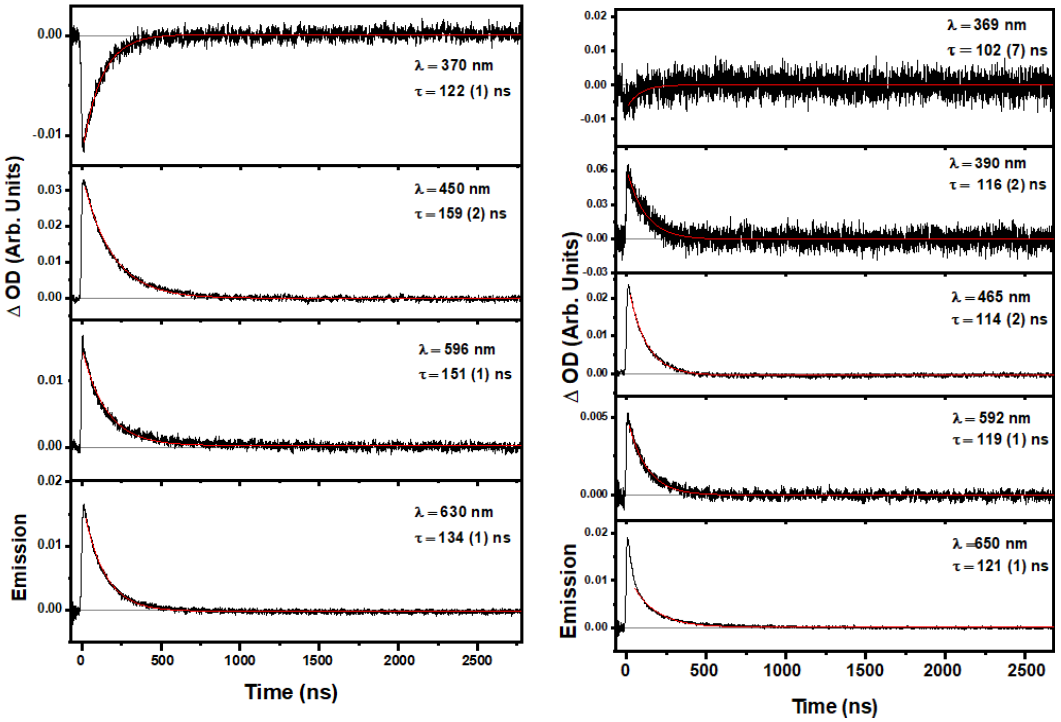

Figure 4.14 Fitted (red line) kinetic traces of the major features of the transient spectrum of [Ir(L^{14})$_2$(L^{18})]BF4 (left) and [Ir(L^{14})$_2$(L^{20})]BF4 (right) in acetonitrile at room temperature, aerated. The wavelengths and lifetimes of each trace are inset

All complexes, [Ir(L^{14})$_2$(L^{17-22})]$^+$, exhibit transient kinetic spectra with similar profiles that decay completely to the baseline (figure 4.14). All kinetic profiles were fit to mono-exponential decay functions, giving very similar lifetimes for all features belonging to a given complex, again indicative of a single state origin. The spectra show no sign of a spin-allowed fluorescence. The features‘ lifetimes are remarkably shorter than their 1-naphthyl analogues, [Ir(L^{11})$_2$(L^{17-22})]$^+$, albeit they are longer than those for their bipyridine base complex [Ir(L^{14})$_2$(bipy)]$^+$, suggesting that emission lifetimes can be tuned by modifiying the ancillary ligand. The values of lifetimes are presented in table 4.12.

Table 4. 12 Kinetic data obtained from the fitted time-resolved transient absorption spectra of the complexes [Ir(L^{14})$_2$(L^{17-22})]$^+$, in aerated acetonitrile, λexc = 355 nm

	Lifetime (ns)		Lifetime (ns)
[Ir(L^{14})$_2$(L^{17})]$^+$	365 nm (74.3 ± 3.9) 450 nm (76.1 ± 0.4) 590 nm (54.3 ± 0.2) 639 nm (52.1 ± 0.1)	**[Ir(L^{14})$_2$(L^{20})]$^+$**	355 nm (101.5 ± 6.7) 390 nm (116.1 ± 1.9) 456 nm (114.2 ± 1.6) 592 nm (119.1 ± 0.8) 650 nm (120.7± 0.9)
[Ir(L^{14})$_2$(L^{18})]$^+$	370nm (121.9 ± 0.8) 450 nm (158.8 ± 2.5) 596 nm (150.5± 0.6) 630 nm (133.9 ± 0.7)	**[Ir(L^{14})$_2$(L^{21})]$^+$**	370 nm (70.4 ± 2.6) 450 nm (88.1 ± 3.1) 635 nm (61.4 ± 0.5)
[Ir(L^{14})$_2$(L^{19})]$^+$	372 nm (57.5 ± 2.9) 450 nm (61.1 ± 0.3) 588 nm (50.9 ± 0.2) 632 nm (50.6 ± 0.1)	**[Ir(L^{14})$_2$(L^{22})]$^+$**	365 nm (118.2 ± 10.6) 385 nm (124.8 ± 1.7) 455 nm (144.9 ± 2.1) 587 nm (135.4 ± 1.7) 654 nm (118.2 ± 1.2)

4.2.5 DFT analysis

4.2.5.1 Geometry Optimisation

Geometries of all complexes were optimised using the B3LYP functional with an SDD ECP for the central iridium atom and a 6-31G* basis set for all other atoms. The calculations were conducted within an implicit acetonitrile solvent, consistent with the spectroscopic measurements. The optimised minimum energy structures have been compared against X-ray crystallographic data to assess the efficiency of the method. The DFT-derived structures of Ir^{III} complexes correlate well with the crystallographic data. Figure 4.15 and shows the singlet ground state geometry calculated for the $[Ir(L^{11})_2(L^{17})]^+$ and $[Ir(L^{14})_2(L^{21})]^+$ complexes overlayed on the experimentally X-ray structures.

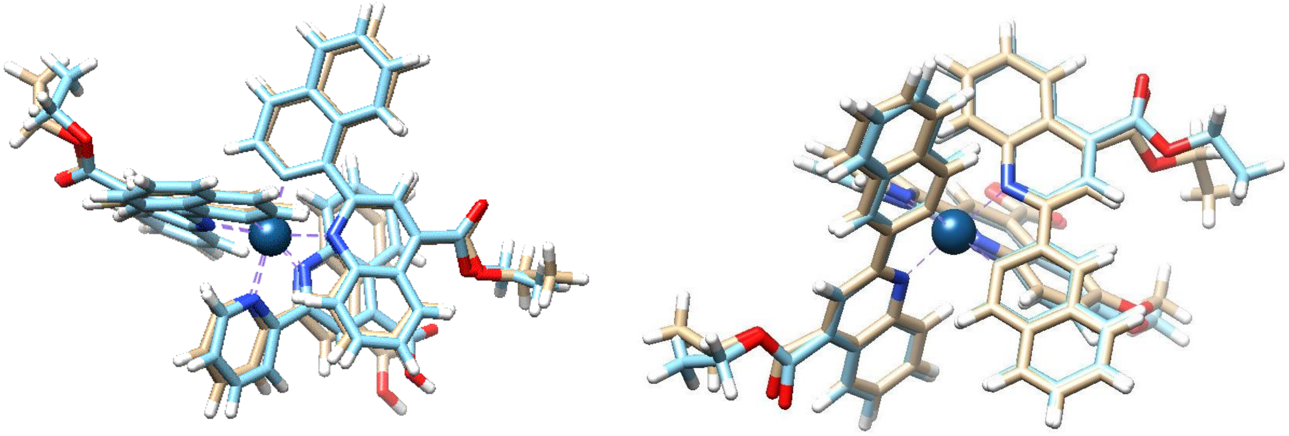

Figure 4.15 Overlay of the crystal structure (blue) and DF-DFT//B3LYP/6-31G(SDD) optimised structures (brown) for $[Ir(L^{11})_2(L^{17})]^+$(left) and $[Ir(L^{14})_2(L^{21})]^+$(right).*

4.2.5.2 Molecular Orbital Decomposition

4.2.5.2.a 1-naphthyl quinoline complexes with pyridinyl / pyrazinyl diimine ancillary ligands

Molecular orbital decomposition analysis was carried out to calculate the percentage contributions of each of the ligands and metal centre to the molecular orbitals. Molecular orbital decomposition was performed on the optimised singlet ground state geometry of each complex using the GaussSum software package in the same procedure as described previously. The results of the decomposition analysis for the frontier orbitals for the six complexes are shown in table 4.13, with graphical plots of the frontier orbitals for $Ir(L^{11})_2(L^{17})]^+$ $Ir(L^{11})_2(L^{20})]^+$ complexes shown in figures 4.16 and 4.17.

Table 4.13 A summary of the major calculated contributions to each MO from each part of the complex. Q1 and Q2 are the inequivalent quinoline ligands.

	Ir	**1nq**			**1nq’**			**L^n**
Complex	HOMO	HOMO	LUMO	LUMO+1	HOMO	LUMO	LUMO+1	LUMO
$[Ir(L^{11})_2(L^{17})]^+$	19	48	4	70	33	1	23	93
$[Ir(L^{11})_2(L^{18})]^+$	19	48	5	39	32	1	55	91
$[Ir(L^{11})_2(L^{19})]^+$	18	49	3	46	31	1	46	93
$[Ir(L^{11})_2(L^{20})]^+$	18	48	2	60	33	1	34	94
$[Ir(L^{11})_2(L^{21})]^+$	17	49	3	78	33	1	14	96
$[Ir(L^{11})_2(L^{22})]^+$	18	48	2	61	33	1	32	94

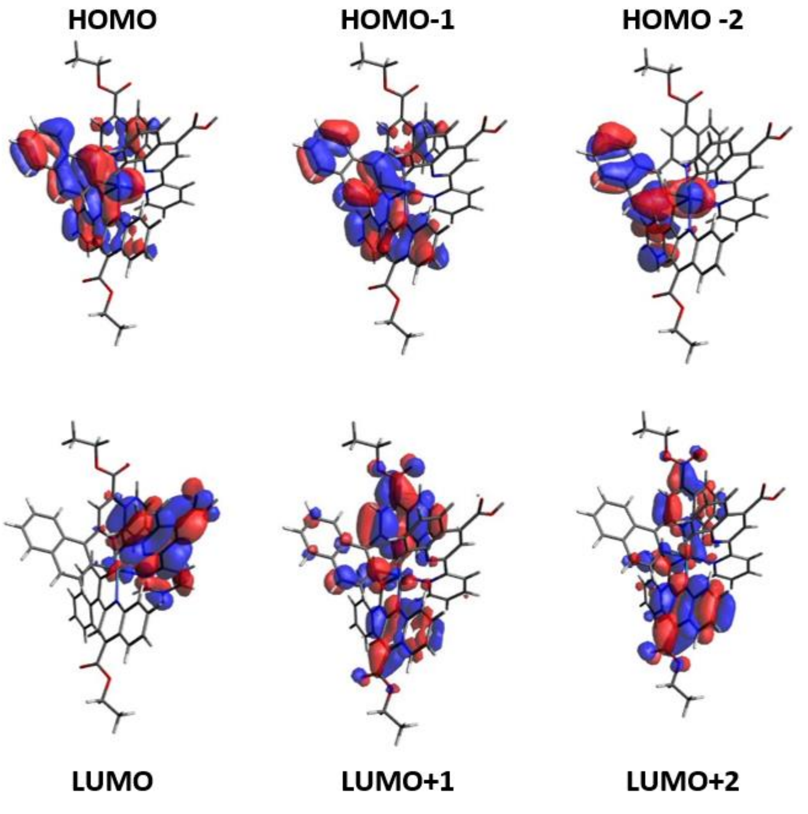

Figure 4.16 Calculated Kohn-Sham frontier molecular orbitals for $[Ir(L^{11})_2(L^{17})]^+$.

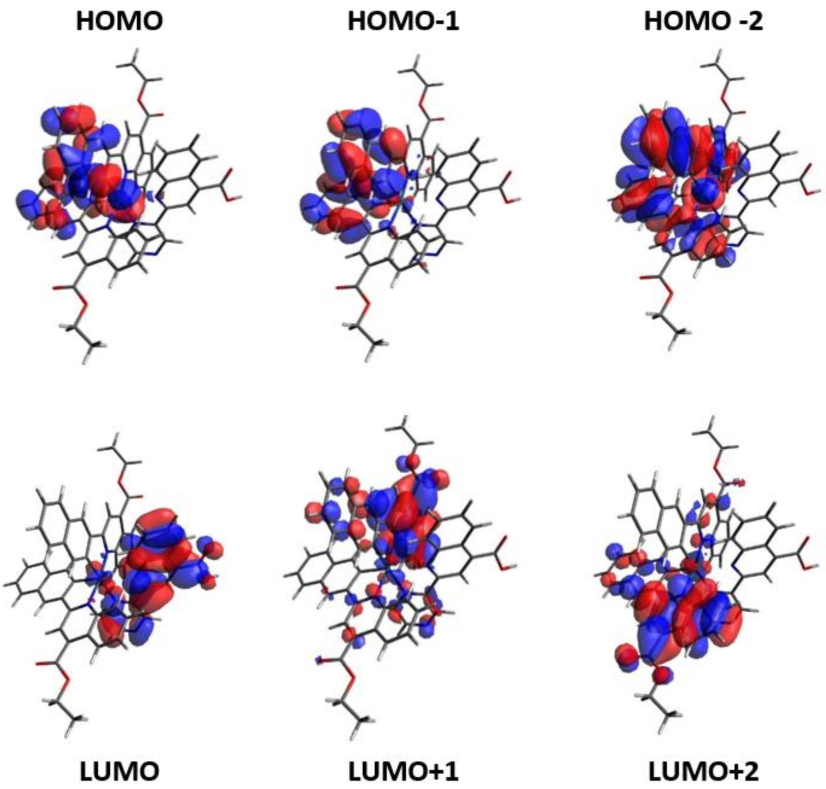

Figure 4.17 Calculated Kohn-Sham frontier molecular orbitals for $[Ir(L^{11})_2(L^{20})]^+$.

The results of MO analysis for each of the $[Ir(L^{11})_2(L^{17\text{-}22})]^+$ complexes (table 4.13) reveal that the HOMO orbital is localised on iridium *d*-orbitals together with the naphthyl moieties orbitals of the cyclometalated ligands, while the HOMO-1 is mainly made of contributions from each of cyclometalated ligand (ca. 97% in total), and a negligible contribution from the Ir center, 2%. This is almost identical to that for their bipy base complex, which suggests that the alternation of ancillary ligand does not change HOMO orbitals characters. However, the LUMO of these complexes is predicted to be predominantly centred on the diimine ancillary ligands, (91-96%); whereas the LUMO+1 and LUMO+2 form a pair of alternating contributions from each of the cyclometalated ligands, as in table 4.14. This is entirely opposite to the prediction for $[Ir(L^{11})_2(bipy)]^+$, where the LUMO and LUMO+1 are dominated by the cyclometalated ligands; and the ancillary ligand contributes to the higher energy LUMO+2 and LUMO+3. Therefore, it is expected that the replacement of bipyridine with diimine ligands leads to a change in the ordering of the LUMOs across the different ligands. Keeping that in mind, the singlet excited states are expected to have an appreciable degree of ligand$_{(C\text{\^{}}N)}$ to ligand$_{(N\text{\^{}}N)}$ charge transfer, LLCT, and intraligand$_{(C\text{\^{}}N)}$ charge transfer ILCT mixed with metal to ligand charge transfer MLCT character.

Table 4.14 The decomposition analysis of the singlet ground state frontier orbitals of $[Ir(L^{11})_2(L^{17})]^+$ complex (Q1 and Q2 are the different quinoline ligands; L^n = diimine ligand).

	Moiety Contribution to Orbital (%)			
Orbital	**Ir (5d)**	**L^n**	**Q1**	**Q2**
LUMO +4	2	48	9	42
LUMO +3	1	98	1	0
LUMO +2	4	3	21	72
LUMO +1	3	4	70	23
LUMO	3	93	4	1
HOMO	19	1	48	33
HOMO -1	2	1	47	54
HOMO -2	17	2	41	40
HOMO -3	26	9	36	29
HOMO -4	27	1	45	26

4.2.5.2.b 2-naphthyl quinoline complexes with pyridinyl / pyrazinyl diimine ancillary ligands

The molecular orbital decomposition analysis for the 2-naphthyl quinoline variants, $[Ir(L^{14})_2(L^{17-22})]^+$, is displayed in table 4.15, and renderings of the frontier molecular orbitals of the $[Ir(L^{14})_2(L^{17})]^+$ and $[Ir(L^{14})_2(L^{20})]^+$ complexes are shown in figures 4.18 and 4.19.

Table 4.15 A summary of the major calculated contributions to each MO from each part of the $[Ir(L^{14})_2(L^n)]^+$ complex. Q1 and Q2 are the inequivalent quinoline ligands.

	Ir	**1nq**			**1nq'**			**L^n**
Complex	HOMO	HOMO	LUMO	LUMO+1	HOMO	LUMO	LUMO+1	LUMO
$[Ir(L^{14})_2(L^{17})]^+$	27	39	3	94	33	1	0	94
$[Ir(L^{14})_2(L^{18})]^+$	27	36	5	91	34	1	2	92
$[Ir(L^{14})_2(L^{19})]^+$	27	38	3	94	34	1	0	94
$[Ir(L^{14})_2(L^{20})]^+$	25	40	1	86	33	1	6	95
$[Ir(L^{14})_2(L^{21})]^+$	26	37	2	90	35	1	3	95
$[Ir(L^{14})_2(L^{22})]^+$	25	39	1	88	35	1	3	95

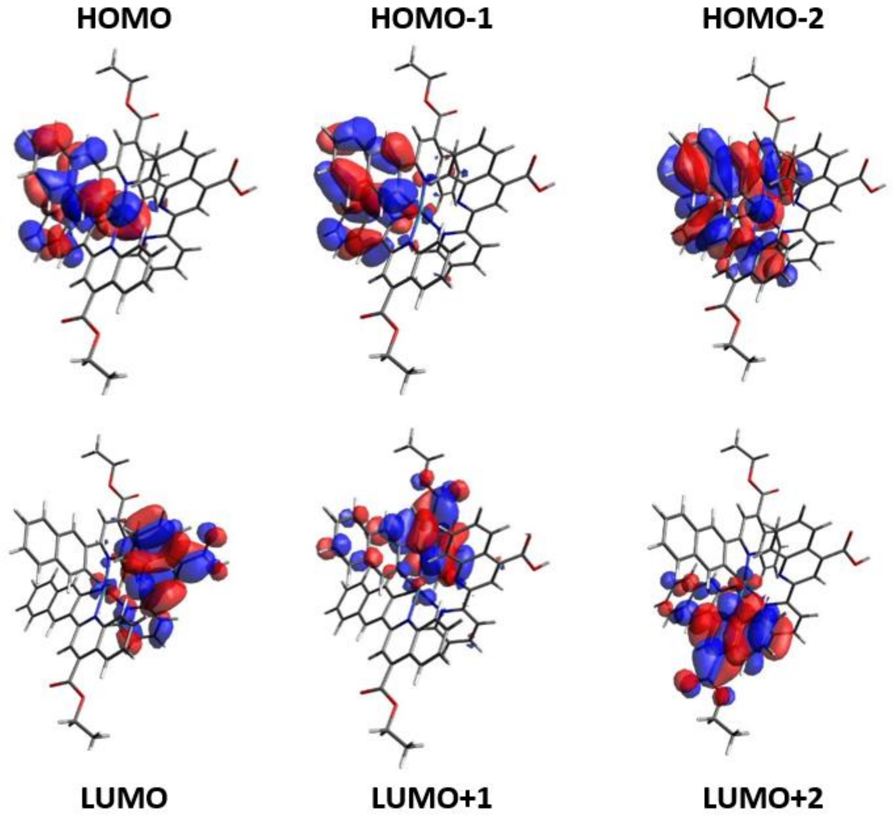

Figure 4.18 Calculated Kohn-Sham frontier molecular orbitals for $[Ir(L^{14})_2(L^{17})]^+$.

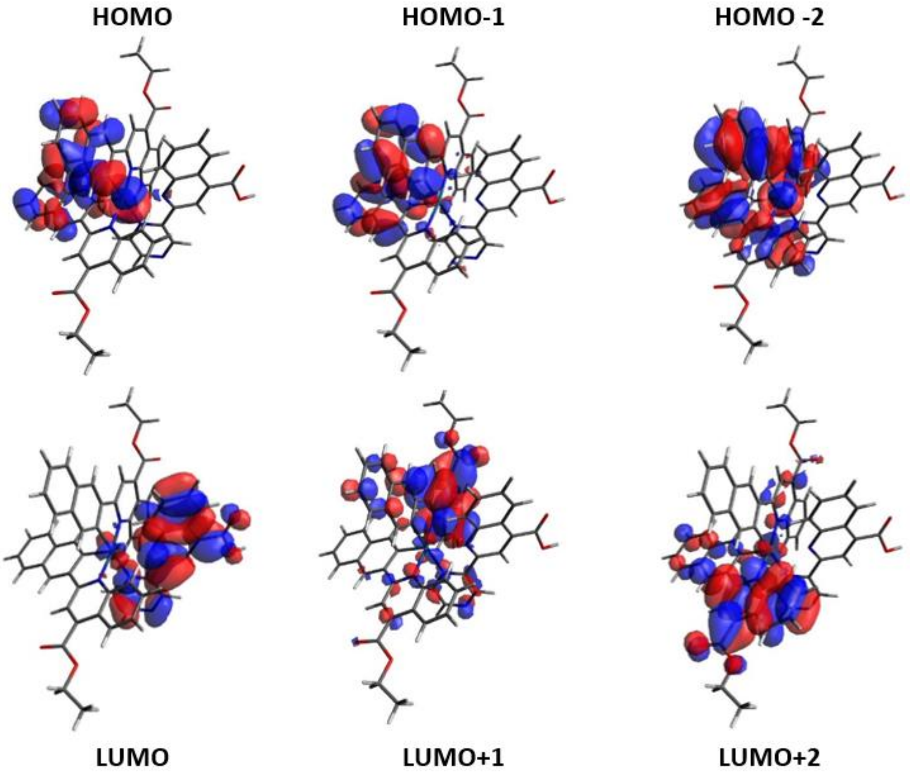

Figure 4.19 Calculated Kohn-Sham frontier molecular orbitals for $[Ir(L^{14})_2(L^{20})]^+$.

As seen above, the distribution of electron density over the orbitals in each of the $[Ir(L^{14})_2(L^n)]^+$ complexes is largely similar to their 1-naphthyl quinoline analogues, with the HOMO being delocalised over the metal centre (25 – 27%), and naphthyl part of both C^N ligands (ca. 70% in total), but the LUMO is predominantly located on the diimine ancillary ligand. It is notable that the iridium 5*d* orbitals demonstrated a higher contribution to the HOMO compared to that predicted for 1-naphthyl quinoline analogues, suggesting a higher degree of MLCT character in their excited states. This trend is reminiscent of that seen in the naphthyl quinoline iridium complexes with bipy ancillary ligand, $[Ir(L^{11-16})_2(bipy)]^+$, discussed earlier in this chapter. The LUMO+1 is almost entirely located in one of the cyclometallating ligands, while the LUMO+2 lies predominantly on the other C^N ligand which is due to asymmetric structure geometry of these complexes, displayed in table 4.16.

Table 4.16 The decomposition analysis of the singlet ground state frontier orbitals of $[Ir(L^{14})_2(L^{17})]^+$ complex (Q1 and Q2 are the different quinoline ligands; L^n = diimine ligand).

	Moiety Contribution to Orbital (%)			
Orbital	**Ir (5d)**	**L^n**	**Q1**	**Q2**
LUMO +4	1	23	26	50
LUMO +3	1	98	10	1
LUMO +2	2	1	0	96
LUMO +1	2	4	94	0
LUMO	2	94	3	1
HOMO	27	2	39	33
HOMO -1	2	1	48	50
HOMO -2	11	1	51	38
HOMO -3	8	2	38	52
HOMO -4	36	17	30	16

4.2.5.3 TD-DFT and vertical transitions calculations

4.2.5.3.a 1-naphthyl quinoline complexes with pyridinyl / pyrazinyl diimine ancillary ligands

For a more in-depth analysis of the transitions and underlying processes that contribute to each feature observed in the experimentally measured spectra described in the previous section, TD-DFT calculations were conducted using CAM-B3LYP functional from the singlet ground states of the complexes. In each case, the lowest 30 singlet-to-singlet spin-allowed were calculated, and the 4.20 The simulated singlet excited states of $[Ir(L^{11})_2(L^{17})]^+$ and $[Ir(L^{11})_2(L^{20})]^+$ complexes are displayed in figure 4.20 and table 4.17.

Table 4.17 The wavelength, force oscillator strengths and contributing molecular orbital transitions of the first five singlet-to-singlet excited states for $[Ir(L^{11})_2(L^{17})]^+$ and $[Ir(L^{11})_2(L^{20})]^+$ complexes. Molecular orbital contributions less than 10% have been omitted for clarity.

$[Ir(L^{11})_2(L^{17})]^+$	
Excited State	**Orbital Contribution to Excited State Contributing Transitions (> 10 %)**
1 (440 nm f=0.1524)	HOMO → LUMO (31.02%) HOMO → LUMO +1 (34.71%) HOMO → LUMO+2 (12.58%)
2 (421 nm f=0.1435)	HOMO-1 → LUMO+1 (23.51%) HOMO → LUMO +1 (29.3%) HOMO → LUMO+2 (28.68%)
3 (397 nm f=0.0370)	HOMO → LUMO (48.13%) HOMO → LUMO+2 (26.96%)
4 (357 nm f=0.1715)	HOMO-1 → LUMO (36.35%) HOMO-1 → LUMO+2 (9.13%)
5 (347 nm f=0.0814)	HOMO-1 → LUMO+1 (46.91%) HOMO → LUMO+2 (11.29%)

$[Ir(L^{11})_2(L^{20})]^+$	
Excited State	**Orbital Contribution to Excited State Contributing Transitions (> 10 %)**
1 (441 nm f=0.1255)	HOMO → LUMO (43.91%) HOMO → LUMO+1 (30.77%)
2 (420 nm f=0.1758)	HOMO-1 → LUMO+1 (13.19%) HOMO-1 → LUMO+2 (10.93%) HOMO → LUMO (14.31%) HOMO → LUMO+1 (32.54%)
3 (413 nm f=0.0420)	HOMO-1 → LUMO+1 (11.02%) HOMO → LUMO (27.45%) HOMO → LUMO+2 (40.21%)
4 (366 nm f=0.0189)	HOMO-1 → LUMO (83.01%)
5 (347 nm f=0.2214)	HOMO-1 → LUMO+1(39.70%) HOMO → LUMO+2 (13.03%)

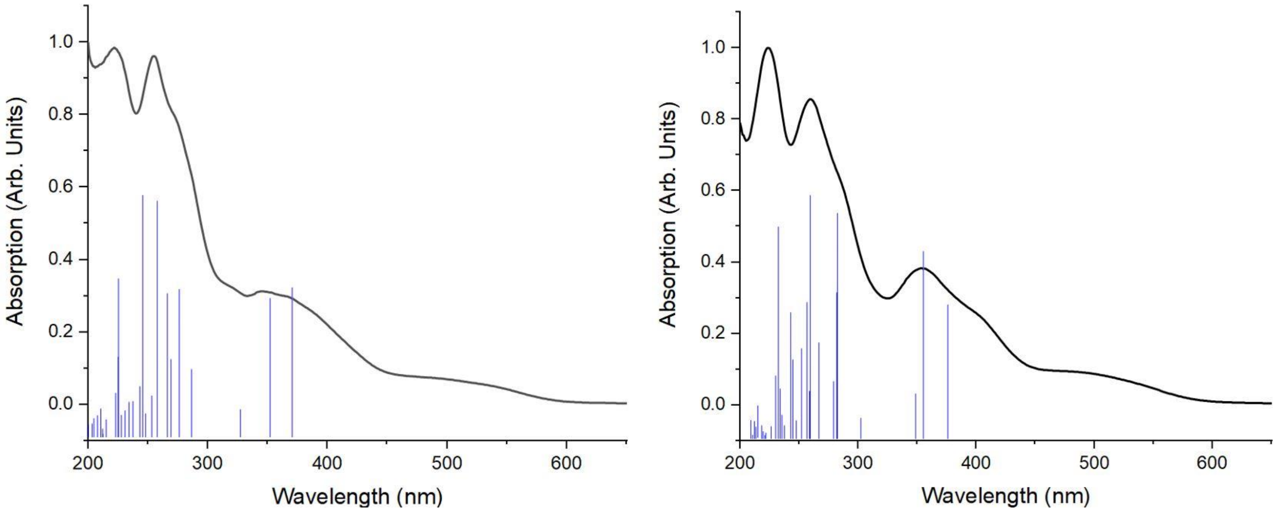

Figure 4.20 The simulated singlet excited states of $[Ir(L^{11})_2(L^{17})]^+$ (left) and $[Ir(L^{11})_2(L^{20})]^+$ (right) complexes are overlaid as vertical blue lines on the experimental spectra. In both cases a shift by -70 nm was applied on calculated spectra for ease of comparison.

From the above analysis, the predicted transitions for pyridinyl-based and pyrazinyl-based complexes are similar and are in good agreement with the experimental spectra. For the $[Ir(L^{11})_2(L^{17})]^+$ complex, excitation to the **S_1** state arises from an admixture of HOMO → LUMO, HOMO → LUMO+1 and HOMO → LUMO+2, taking place at 440 nm, with high oscillator strength. This is followed by excitation to S_2 at 421 nm, comprised of transitions from HOMO and HOMO-1 orbitals to LUMO+1 and LUMO+2 orbitals, with high oscillator strength as well. These excitations correlated well with the broad feature observed in the experimental absorption spectrum at $325 < \lambda < 450$ nm. The first two excited state transitions mainly originated from metal to ligand$_{\text{CN}}$ and intra-ligand$_{\text{CN}}$ transitions, with less degree of ligand$_{\text{C\^{}N}}$ to ligand$_{\text{N\^{}N}}$ and metal to ligand$_{\text{N\^{}N}}$ transitions, and therefore should be described as mixed ^{1}ILCT/^{1}LLCT/^{1}MLCT character. A less intense absorption band is predicted to occur at 397 nm, and is dominated by transitions from the metal and cyclometallating ligand to the diimine ancillary ligand. As can be seen, there is no singlet excitation predicted at a wavelength long than 430 nm, supporting the assignment of the low-intensity broad band, observed at 450 < λ < 600 nm as a spin forbidden absorption into the triplet manifold. To support this assignment, the time-dependent DFT (TD-DFT) approach was used again to calculate the 30 singlet-to-triplet spin-forbidden transitions for each complex. Table 4.18 lists the values of the lowest singlet to singlet transitions and singlet to triplet transitions. Table 4.19 displays the vertical excitation wavelengths and the electronic transitions that contribute to the three first triplet excited states for the $[Ir(L^{11})_2(L^{17})]^+$ complex.

Table 4.18 Computed values for the vertical spin allowed and spin-forbidden absorption for the $[Ir(L^{11})_2(L^{17-22})]^+$ complexes.

Complex	**$S_0 \rightarrow S_1$ (nm)**	**$S_0 \rightarrow T_1$ Em. (nm)**
$[Ir(L^{11})_2(L^{17})]^+$	440	639
$[Ir(L^{11})_2(L^{18})]^+$	439	640
$[Ir(L^{11})_2(L^{19})]^+$	441	641
$[Ir(L^{11})_2(L^{20})]^+$	441	640
$[Ir(L^{11})_2(L^{21})]^+$	439	641
$[Ir(L^{11})_2(L^{22})]^+$	443	640

Table 4. 19 The wavelength, energy and contributing molecular orbital transitions of the first three singlet-to-triplet excited states for $[Ir(L^{11})_2(L^{17})]^+$ complex. Molecular orbital contributions less than 10% have been omitted for clarity

$[Ir(L^{11})_2(L^{17})]^+$		
Triplet Excited State	**Energy (eV)**	**Orbital Contribution to Excited State Contributing Transitions (> 10 %)**
1(693 nm)	1.91	HOMO-1 → LUMO+2 (15.68%) HOMO → LUMO +1 (14.58%) HOMO → LUMO+2 (18.23%)
2 (627 nm)	1.97	HOMO-1 → LUMO+1 (26.68%) HOMO → LUMO +1 (16.81%) HOMO → LUMO+2 (10.23%)
3 (556 nm)	2.21	HOMO → LUMO (48.13%) HOMO → LUMO+2 (26.96%)

Unexpectedly, the first two triplet states are formed mainly through transitions from the HOMO and HOMO-1 to the LUMO+1 and LUMO+2, and have to be described as a mixed metal to ligand$_{CN}$ (^{3}MLCT) and intra-ligand$_{CN}$ charge transfer given that all these orbitals involve the cyclometallating ligands, with some contribution from Ir^{III} core in the HOMO. In contrast, the T_3 excited state mainly originates from the HOMO → LUMO excitation with a contribution from HOMO → LUMO+2 transitions. The lowest two states are very close in energy, with only a 0.06 eV difference (Table 4.19), and thus a high mixing between them should be expected. The lowest triplet states (**T_1**) for all complexes were further examined by optimising their geometries using the B3LYP functional as described above, and then the unpaired-electron spin-density distribution was calculated for the **T_1**

optimised geometries. Figure 4.21 shows the computed spin densities of the [Ir(L^{11})$_2$(L^{17})]$^+$ and the [Ir(L^{11})$_2$(L^{20})]$^+$. In both Ir^{III} complexes, the spin density distributions of the **T_1** state are predominantly centred on the cyclometalating ligands and Ir metal centre, confirming that the lowest triplet state of these iridium complexes is metal to ligand$_{CN}$ charge transfer (^{3}MLCT) in character, mixed with some ligand centre component (^{3}LC) on the CN ligands. This corresponds with the broad structureless emission band observed experimentally. This would also justify why the structural variety of L^n (through changes in substituents and heterocycle) does not lead to a noticeable shift of the emission centres, nor produce a substantial modulation of the electronic properties.

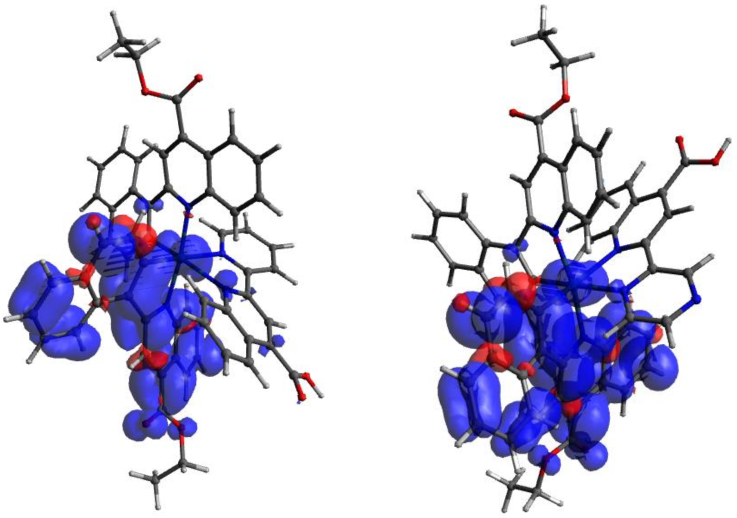

Figure 4.21 Calculated spin densities of [Ir(L^{11})$_2$(L^{17})]$^+$ (left) and the [Ir(L^{11})$_2$(L^{20})]$^+$ (right).

Phosphorescent emission energies were estimated using two different approaches: the adiabatic energies were obtained by calculating the difference (ΔE) between **T_1** and **S_0**, while vertical transitions were calculated using the minimum energy geometries of the triplet states for all complexes and single-point calculations. The results of these calculations for all complexes are listed in table 4.20.

Table 4.20 Computed values for the vertical and adiabatic emission wavelengths for the [Ir(L^{11})$_2$(L^{11-22})]$^+$ complexes along with experimental values.

Complex	**$T_1 \rightarrow S_o$ Em. (nm) Vertical**	**$T_1 \rightarrow S_o$ Em. (nm) Adiabatic**	**$T_1 \rightarrow S_o$ Em. (nm) Exp.**
[Ir(L^{11})$_2$(L^{17})]$^+$	818	713	678
[Ir(L^{11})$_2$(L^{18})]$^+$	819	712	679
[Ir(L^{11})$_2$(L^{19})]$^+$	816	713	679
[Ir(L^{11})$_2$(L^{20})]$^+$	805	712	675
[Ir(L^{11})$_2$(L^{21})]$^+$	816	711	677
[Ir(L^{11})$_2$(L^{22})]$^+$	813	712	674

The predicted luminescent bands are in good agreement with measured values, occurring within the same region as the experimental emission bands. The adiabatic band positions again display more reasonable quantitative agreement with experimental values. Although the calculation overestimates the emission wavelengths, and did not perfectly reflect all the trends observed experimentally, it clearly demonstrates that the structural modification of the ancillary ligand almost has no effect on the position of the emission centres.

4.2.5.3.b 2-naphthyl quinoline complexes with pyridinyl/ pyrazinyl diimine ancillary ligands

TD-DFT with the CAM-B3LYP functional was also performed on the optimised singlet ground states of the $Ir(L^{14})_2(L^{17-22})]^+$ complexes to investigate singlet and triplet electronic transitions of these complexes, and the results of the lowest spin-allowed and spin-forbidden transitions are displayed in table 4.21. The singlet TD-DFT calculations for the lowest five singlet excited states are shown below in table 4.22 for $Ir(L^{14})_2(L^{17})]^+$ and $Ir(L^{14})_2(L^{20})]^+$ complexes.

Table 4.21 Computed values for the vertical spin allowed and spin-forbidden absorption for the $[Ir(L^{14})_2(L^{17-22})]^+$ complexes.

Complex	**$S_o \rightarrow S_1$ Abs. (nm)**	**$S_o \rightarrow T_n$ Abs. (nm)**
$[Ir(L^{14})_2(L^{17})]^+$	426	614
$[Ir(L^{14})_2(L^{18})]^+$	424	607
$[Ir(L^{14})_2(L^{19})]^+$	432	625
$[Ir(L^{14})_2(L^{20})]^+$	441	641
$[Ir(L^{14})_2(L^{21})]^+$	437	531
$[Ir(L^{14})_2(L^{22})]^+$	447	651

Table 4.22 The wavelength, force oscillator strengths and contributing molecular orbital transitions of the first five singlet-to-singlet excited states for $[Ir(L^{14})_2(L^{17})]^+$ and $[Ir(L^{14})_2(L^{20})]^+$ complexes. Molecular orbital contributions less than 10% have been omitted for clarity.

$[Ir(L^{14})_2(L^{17})]^+$	
Excited State	**Orbital Contribution to Excited State Contributing Transitions (> 10 %)**
1 (426 nm f=0.087)	HOMO → LUMO (70.37%) HOMO → LUMO+2 (11.79%)
2 (401 nm f=0.0153)	HOMO → LUMO +1 (75.00%)
3 (393 nm f=0.0145)	HOMO → LUMO (11.53%) HOMO → LUMO+2 (64.00%)
4 (365 nm f=0.3207)	HOMO-2 → LUMO (10.19%) HOMO-2 → LUMO+2 (24.54%) HOMO-1 → LUMO (16.01%) HOMO → LUMO+2 (18.02%)
5 (356 nm f=0.4542)	HOMO-3 → LUMO+1 (10.02%) HOMO-2 → LUMO+1 (29.92%) HOMO-1 → LUMO+1 (32.76%)

$[Ir(L^{14})_2(L^{20})]^+$	
Excited State	**Orbital Contribution to Excited State Contributing Transitions (> 10 %)**
1 (441 nm f=0.0033)	HOMO → LUMO (78.54%)
2 (399 nm f=0.0030)	HOMO → LUMO+1 (79.12%)
3 (397 nm f=0.0316)	HOMO → LUMO+2 (76.76%)
4 (367 nm f=0.2384)	HOMO-2 → LUMO (12.12%) HOMO-2 → LUMO+1 (13.59%) HOMO-1 → LUMO (26.10%) HOMO-1 → LUMO+1 (18.68%)
5 (356 nm f=0.4273)	HOMO-2 → LUMO+2 (23.98%) HOMO-1 → LUMO+2 (33.68%)

The above tables show that the predicted transitions for all $[Ir(L^{14})_2(L^{17-22})]$+ complexes are generally similar, and correlate reasonably well with measured UV-Vis spectra. The position of each band is dependent on the modification of the ancillary ligand. It can be seen that the pyrazinyl-based derivatives exhibit bathochromic shifted absorption bands compared to those for the pyridinyl-based derivatives, with the set as a whole being hypsochromically shifted compared to their 1-naphthyl analogues.

For $[Ir(L^{14})_2(L^{17})]^+$, the lowest singlet-singlet transition is predicted to occur at 426 nm, with low oscillator strength. This band mainly originates from the HOMO→LUMO transition, which involves excitation from the metal and cyclometalating ligands orbitals to diimine ancillary ligand orbitals, and thus ascribed as a mixed $ML_{N{\wedge}N}CT/L_{C{\wedge}N}L_{N{\wedge}N}CT$ character. This is followed by two excitations at 401 nm and 393 nm, that arise from HOMO and proceed to either the LUMO+1 or LUMO+2, respectively. These transitions are ascribed as $ML_{C{\wedge}N}CT$ and $IL_{CN}CT$ transitions. This behaviour reflects the pseudo-degeneracy splitting due to the asymmetrical diimine ancillary ligand. The lowest three excitation transitions are associated with small oscillator strengths, which is opposite to the predictions made for their 1-naphthyl analogues discussed above. The first three calculated transitions are well correlated with the absorption band observed in the absorption spectrum at 450 nm > λ > 350 nm. The lowest spin-forbidden singlet-triplet transition is predicted at 614 nm, assigned to a mixed $^3ML_{N^\wedge N}CT$/ $^3L_{C^\wedge N}L_{N^\wedge N}CT$, and correlates with the long tail of the lowest energy absorption feature in the experimental data. The assignment of $\mathbf{S_0{\rightarrow}T_1}$ transitions is strongly supported by the spin-density distribution for the lowest triplet $\mathbf{T_1}$ state determined by Mulliken spin-density analysis, as shown in figure 4.22

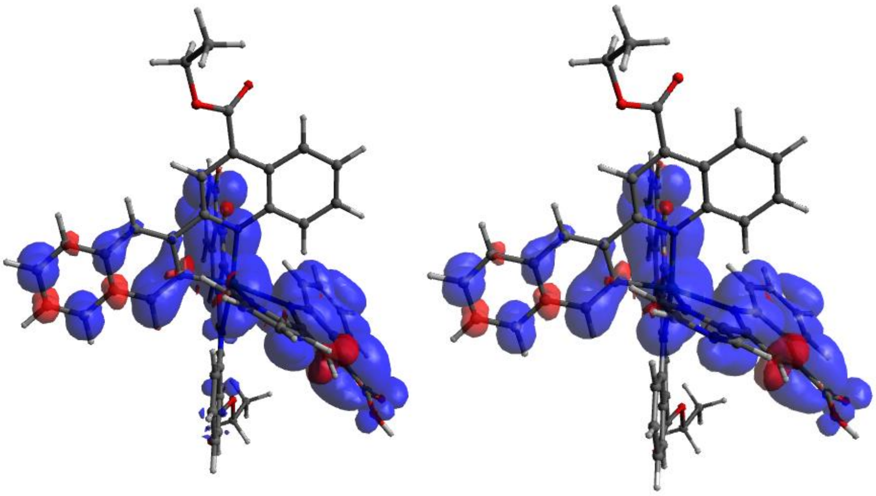

Figure 4.22 Calculated spin densities of the [Ir(L^{14})$_2$(L^{17})]$^+$ (left) and the [Ir(L^{14})$_2$(L^{20})]$^+$ (right).

The spin density distributions of $[Ir(L^{14})_2(L^{17\text{-}22})]^+$ complexes at the T_1 minimum energy geometry are mainly localised on the N^N ligand, Ir metal centre, and naphthyl moieties of C^N ligands, proving that the lowest triplet states are ascribed to the metal to $\text{ligand}_{N^\wedge N}$ charge transfer transition (^3MLCT) and the $\text{ligand}_{C^\wedge N}$ to $\text{ligand}_{N^\wedge N}$ charge-transfer transition (^3LLCT). The high degree of $ML_{N^\wedge N}CT$ character in the lowest excited state explains the shift in spectroscopic features introduced by the adjustment of the substituents on these ligands, as seen in the absorption and emission spectra.

DFT calculations were also used to estimate vertical and adiabatic spin-forbidden $\mathbf{T_1{\rightarrow}S_0}$ emission energies from the optimised minimum-energy geometry of the singlet and triplet states. The results are shown in table 4.23.

Table 4.23 Computed values for the vertical and adiabatic spin-forbidden emission for the $[Ir(L^{14})_2(L^{17-22})]^+$ complex along with experimental values.

Complex	**$T_1 \rightarrow S_0$ Em. (nm) Vertical**	**$T_1 \rightarrow S_0$ Em. (nm) Adiabatic**	**$T_1 \rightarrow S_0$ Em. (nm) Exp.**
$[Ir(L^{14})_2(L^{17})]^+$	804	692	639
$[Ir(L^{14})_2(L^{18})]^+$	784	675	630
$[Ir(L^{14})_2(L^{19})]^+$	820	705	632
$[Ir(L^{14})_2(L^{20})]^+$	853	734	650
$[Ir(L^{14})_2(L^{21})]^+$	802	696	633
$[Ir(L^{14})_2(L^{22})]^+$	865	741	653

The above table shows that the computational method underestimates the energy of emission bands. However, the adiabatic emission wavelengths fall within a similar spectral region as the experimentally observed emission. An important result to note is that this approach affords a good insight into the effect of the modification of the ligand structure on the position of the emission band. For example, the calculation predicts that the emission centres of the two complexes $[Ir(L^{14})_2(L^{20})]^+$ and $[Ir(L^{14})_2(L^{22})]^+$ are significantly bathochromically shifted compared with the rest of the set, whilst the emission wavelengths of the other four complexes exhibit only slight shift from each other. Additionally, the emission centre of the $[Ir(L^{14})_2(L^{22})]^+$ complex is expected to be located at the longest wavelength followed at higher energy by the $[Ir(L^{14})_2(L^{20})]^+$ complex, whereas the $[Ir(L^{14})_2(L^{17})]^+$ complex is predicted to have the highest energy emission band. These predictions are perfectly reflected in the experimental spectra.

However, I have also attempted to better match the absolute experimental values by changing the functional used in these calculations to M06-2X. (Song et al. 2013; Song et al. 2015; Morello 2017; Zhang et al. 2018) Again, the geometric parameters of the ground and lowest triplet excited states were optimised and a comparison of relative singlet and triplet excited-state energies used for the prediction of the adiabatic spin-forbidden emission wavelengths. The vertical emission energies were also estimated by performing stationary point energy calculations for each optimised geometry targeting the opposing spin state (ie. a single point energy for the singlet ground state was computed at the triplet minimum energy geometry to get an estimation of the vertical electronic energy difference between states). The results are shown in table 4.24.

Table 4.24 Computed values for the vertical and adiabatic spin-forbidden emission for the $[Ir(L^{14})_2(L^{17-22})]^+$ complexes using M062X functional.

Complex	**$T_1 \rightarrow S_o$ Em. (nm) Vertical**	**$T_1 \rightarrow S_o$ Em. (nm) Adiabatic**	**$T_1 \rightarrow S_o$ Em. (nm) Exp.**
$[Ir(L^{14})_2(L^{17})]^+$	627	534	639
$[Ir(L^{14})_2(L^{18})]^+$	611	525	630
$[Ir(L^{14})_2(L^{19})]^+$	625	532	632
$[Ir(L^{14})_2(L^{20})]^+$	615	526	650
$[Ir(L^{14})_2(L^{21})]^+$	611	525	633
$[Ir(L^{14})_2(L^{22})]^+$	614	525	653

The change in functional leads to both vertical and adiabatic energies being overestimated, with adiabatic bands being systematically blue-shifted compared with experimental emission spectra. Although the vertical transition energies are quantitively comparable to experimentally measured values, especially for pyridinyl-based complexes (a deviation from experimental data of less than 12 nm), this method unfortunately fails to predict the correct energy ordering of the emission for the set of complexes. Moreover, this functional misestimates the degree by which emission bands are shifted from each other; missing the significant shift of $[Ir(L^{14})_2(L^{20})]^+$ and $[Ir(L^{14})_2(L^{22})]^+$ complexes that were observed experimentally and estimated nicely using the previous functional. This emphasises that the DFT\\B3LYP level of theory is much more appropriate for the prediction of photophysical properties of this class of Ir^{III} complexes.

4.3 Discussion of Ligand Effects

4.3.1 Comparison of Quinoxaline, 1-Naphthyl Quinoline and 2-Naphthyl Quinoline Effects in Bipyridine Complexes

The effect of the modification of the backbone of the main cyclometallating ligands can be determined by a direct comparison of the optical properties of the key complex of each set, shown in table 4.25.

Table 4.25 Emission wavelengths and emission lifetimes for $[Ir(L^1)_2(bipy)]^+$,$[Ir(L^{11})_2(bipy)]^+$ and $[Ir(L^{14})_2(bipy)]^+$ complexes under atmospheric.

Complex	**λ_{em} / nm**	**τ / ns**
$[Ir(L^1)_2(bipy)]PF_6$	629	243
$[Ir(L^{11})_2(bipy)]PF_6$	679	240
$[Ir(L^{14})_2(bipy)]PF_6$	673	36

As can be seen in the above table, the 1-naphthyl quinoline complex and 2-naphthyl quinoline complex emissions are more similarly positioned to one another, as is to be expected due to their close structural similarity that only differs in the position of chelation at the naphthyl unit. However, the emission centre of the quinoxaline complex is significantly hypsochromically shifted compared to both naphthyl quinoline complexes. This is attributed to a higher degree of conjugation in the naphthyl quinoline cyclometallating ligand that lowers the energy of the LUMO orbital, whereas the energy level of the HOMO remains around the same energy. Consequently, the energy gap is reduced, resulting in a lower energy emission, displayed in table 4.26.

Table 4.26 Energies of the singlet state frontier orbitals of the key complex of each set.

Complex	HOMO energy (eV)	LUMO energy (eV)	ΔE
$[Ir(L^{1})_2(bipy)]^+$	-5.62	-2.54	3.08
$[Ir(L^{11})_2(bipy)]^+$	-5.60	-2.76	2.84
$[Ir(L^{14})_2(bipy)]^+$	-5.55	-2.76	2.79

The energies of the LUMO orbitals are essentially identical for both naphthyl quinoline complexes, whilst the energy of the HOMO, which is located in the naphthyl moieties of C^N ligand, is more stabilised in the 1-naphthyl quinoline complex, leading to an increase in the energy gap. Therefore, the emission to $[Ir(L^{11})_2(bipy)]^+$ shifts to a shorter wavelength compared to $[Ir(L^{14})_2(bipy)]^+$.

In addition, it was found that using different substituents on the quinoxaline or quinoline moieties in C^N ligands allows a subtle tuning of emission centres, compared with a much broader shift in the emission bands caused by the substitution on the phenyl ring in the quinoxaline ligand, $[Ir(L^{1-10})_2(bipy)]^+$, or by the position of chelation at the naphthyl in quinoline C^N ligand, $[Ir(L^{11-16})_2(bipy)]^+$.

Based on the results of the DFT analysis, the emissive triplet excited state for all bipyridine-based complexes, $[Ir(L^{1-16})_2(bipy)]^+$, are ascribed as mixed ^{3}MLCT/^{3}ILCT, with 1-naphthyl quinoline complexes demonstrating a much higher degree of ^{3}ILCT character in their excited state. The variation in the nature of the excited state, due to the alternation of the structure of the main C^N ligands, affects the emission lifetimes, as seen in table 4.25. The 1-naphthyl quinoline-based complex displays a deep red emission with a comparatively longer lifetime, reflecting the significant ^{3}ILCT character of the emissive state; whereas the emission lifetime for the 2-naphthyl quinoline-base complex, which possesses a greater ^{3}MLCT character in its emissive state, is considerably shorter. In contrast, the quinoxaline-based complex shows a blue-shifted emission band from a predominantly ^{3}MLCT excited state with the most extended lifetime, consistent with the energy gap law.(Caspar et al. 1982; Kober et al. 1986; Chou et al. 2011; DiLuzio et al. 2021)

4.3.1 Comparison of Bipyridine, Pyridinyl and Pyrazinyl Ancillary Effects in Naphthyl Quinoline Complexes

The effect of the modification of the ancillary ligands on the emission centres can be seen in table 4.27 below.

Table 4.27 Emission wavelengths for a key complex of each set of complexes studied in this chapter.

Complex	**λ_{em} / nm**	**Complex**	**λ_{em} / nm**
$[Ir(L^{11})_2(bipy)]^+$	679	**$[Ir(L^{14})_2(bipy)]^+$**	673
$[Ir(L^{11})_2(L^{17})]^+$	678	**$[Ir(L^{14})_2(L^{17})]^+$**	639
$[Ir(L^{11})_2(L^{20})]^+$	674	**$[Ir(L^{14})_2(L^{20})]^+$**	650

It is clear that the alternation of ancillary ligands has a limited impact upon the emission centres in 1-naphthyl complexes (L^{11} complexes), but displays a more remarkable effect on 2-naphthyl complexes (L^{14} complexes). For example, when replacing the bipyridine with L^{17}, the emission wavelength shifted by only 1 nm in 1-naphthyl complexes, comparing with 35 nm in its 2-naphthyl analogues. This is attributed to the different nature of emissive states in these complexes. The DFT analysis suggests that the emissive states for $[Ir(L^{11})_2(L^n)]^+$ are dominated by the intra-ligand$_{C^N}$ charge transfer mixed with contribution from the metal to ligand$_{C^N}$ charge transfer, $^3IL_{C^N}CT$/ $^3ML_{C^N}CT$. In contrast, the triplet emissive states for $[Ir(L^{14})_2(L^n)]^+$ complexes are centred on the ancillary ligand, suggesting the emissions are likely mixed $^3ML_{N^N}CT$ and $^3L_{C^N}L_{N^N}CT$ in character and, thus, more affected by the change in ancillary ligand structure. Varying the substituents on the ancillary ligands once again leads to fine tuning of the emission energy for $[Ir(L^{14})_2(L^n)]^+$ complexes, while the emission maxima for $[Ir(L^{11})_2(L^n)]^+$ appear relatively unperturbed.

4.4 Designing red emitter iridium complexes

The development of organometallic phosphors that emit at both deep red or near-infrared (NIR) wavelengths is indeed a highly active area of research due to their crucial role in a number of optoelectronic applications. For example, they are used in organic light-emitting diodes (OLEDs), night-vision readable displays, optical communications and also in biological applications such as photodynamic therapy or as fluorescence imaging and biological labelling for probing biochemical and biological systems since cellular and tissue imaging in these wavelengths has better tissue penetration. In addition, pure red phosphors are important to balance the spectral composition of white LEDs, making the white light produced by these devices warmer and more natural-looking. For some practical applications, a long lifetime of the triplet state of organometallic phosphors (several tens of nanoseconds or more) is crucial. In biological imaging, for example, if the emission lifetime of the phosphor ranges between hundreds of picoseconds to tens of nanoseconds, it is difficult to be distinguished from the short-lived NIR autofluorescence contributed by heme and melanin in tissues.

Similarly, in photosensitizers, a long excited state lifetime is desirable to allow electron-transfer quenching to occur. (Goldsmith et al. 2005; Majumdar et al. 2014; Kim et al. 2018; Buckle et al. 2020; Jiang et al. 2021)

The detailed analysis of different iridium complexes studied so far in this work provides a clear insight into the different factors that affect the excited states and optical properties, such as emission wavelength and lifetime, of iridium complexes. These results create a promising template for the rational design of new deep-red or NIR emitting Ir^{III} complexes with relatively long excited state lifetimes (hundreds of nanoseconds). For this aim, I designed ten cyclometalated iridium complexes with a diimine ancillary ligand and used DFT calculations to predict their excited state character and calculate their absorption and emission lifetimes.

4.4.1 Predicting red emitters

This thesis has already discussed the fact that the deep red region of the EM spectrum is an important target for novel Ir^{III} phosphors. Based on all the prior experimental and computational work, here I present a predictive set of DFT calculations of new complexes that may emit within this region. This work is designed as a guide for the synthetic chemists with whom we have collaborated towards a new set of emitters with useful properties. Three different factors were considered when I designed these deep red-emitting iridium complexes: choosing cyclometallating and ancillary ligands that support a long *π*-conjugated system; introducing an electron withdrawing group (F) into the N-moiety of these ligands; introducing electron donating groups (Me) to the C-moiety of cyclometalating ligands, and introducing high electronegativity atoms (N) to the diimine ancillary ligand. Increasing *π*-conjugation within the diimine ancillary ligand is also expected to extend the triplet state lifetime of the Ir^{III} complexes as it is known to alter the nature of the $\mathbf{T_1}$ from being dominated by ^{3}MLCT to containing some ^{3}LLCT/$^3\pi\pi^*$ character. The complexes are all monocationic and consist of two substituted 2-(naphthalen-2-yl) quinoline ligands chelatiing to an Ir^{III} core. Four types of diimine ancillary ligands were used, namely: phenanthroline, 2,2-biquinoline, 2-(2-Quinolinyl)quinoxaline and 2,2-biquinoxaline, to afford tuning of the emission throughout the red and NIR regions of the spectrum, as seen in scheme 4.5.

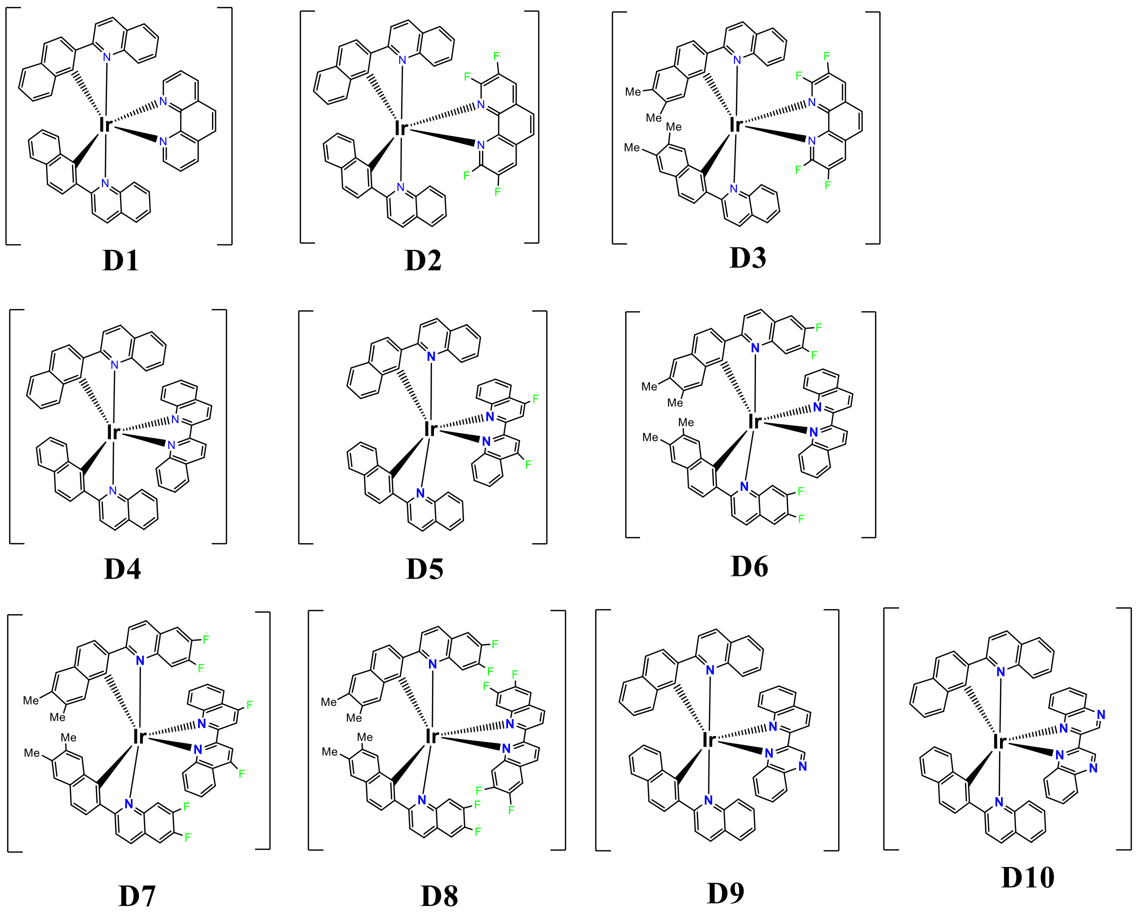

Scheme 4.5 The chemical structures of the ten designed complexes.

The above scheme shows different variants of the novel iridium complexes which I have explored. Based on the results of the iridium complexes analyzed throughout this thesis, it is expected that the D1 will display the shortest emission wavelength while D10 will have the longest emission wavelength.

4.4.2 DFT analysis

All Ir complexes in their lowest electronic singlet and triplet states were optimized using the same DFT//B3LYP/6-31G* level of theory. Calculations were performed within an implicit acetonitrile solvent (IEFPCM), consistent with that used in the previous studies. The calculated geometric parameters were confirmed as minima through harmonic vibrational frequency calculations. Molecular orbital decomposition analysis was performed on the calculated singlet state geometries of the ten complexes using the GaussSum software package. This was undertaken with the aim of determining the nature of the excited state and investigating the effects the ligand variations have on the electronic structure of the molecules. Figures 4.23 and 4.24 display the visualisation of the frontier molecular orbitals for the two variants representing the series, D1 and D4. The decomposition analysis for all complexes is displayed in table 4.28.

Table 4.28 A summary of the major calculated contributions to each MO from each part of the complex. Q1 and Q2 are the inequivalent quinoline ligands; N^N = diimine ligand.

	Ir	**1nq**			**1nq'**			**N^N**
Complex	HOMO	HOMO	LUMO	LUMO+1	HOMO	LUMO	LUMO+1	LUMO
D1	20	40	33	5	40	33	5	31
D2	18	41	2	29	40	2	36	94
D3	17	41	2	23	41	2	29	95
D4	19	40	1	44	40	1	43	95
D5	19	40	1	42	40	1	44	95
D6	17	41	2	43	41	1	46	95
D7	17	41	2	42	41	1	46	95
D8	17	41	1	41	41	1	45	95
D9	19	41	1	44	40	1	43	96
D10	18	40	1	22	40	1	22	96

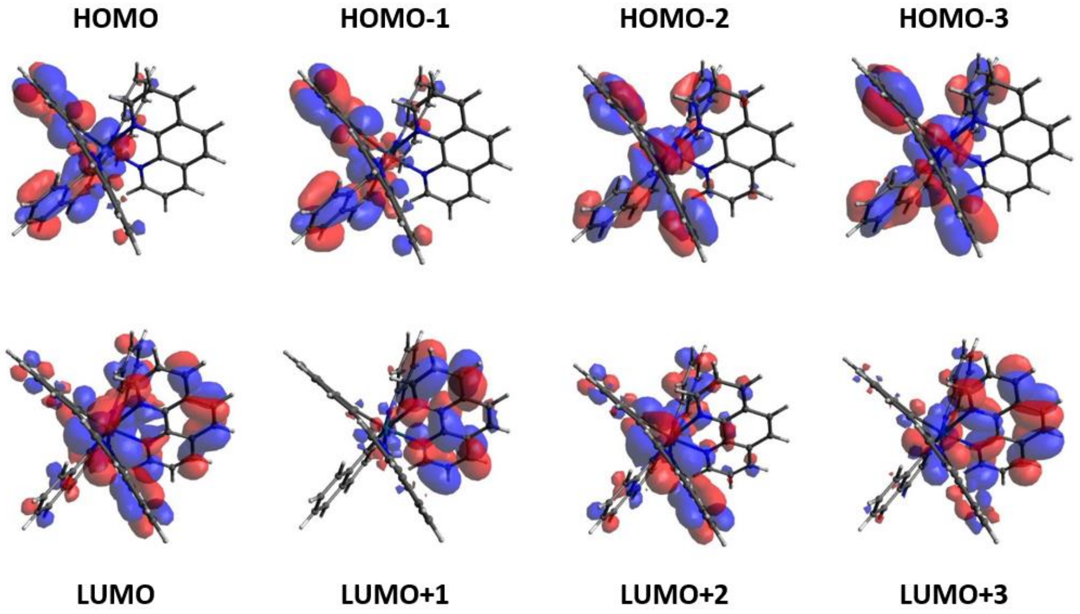

Figure 4.23 Calculated Kohn-Sham frontier molecular orbitals for D1.

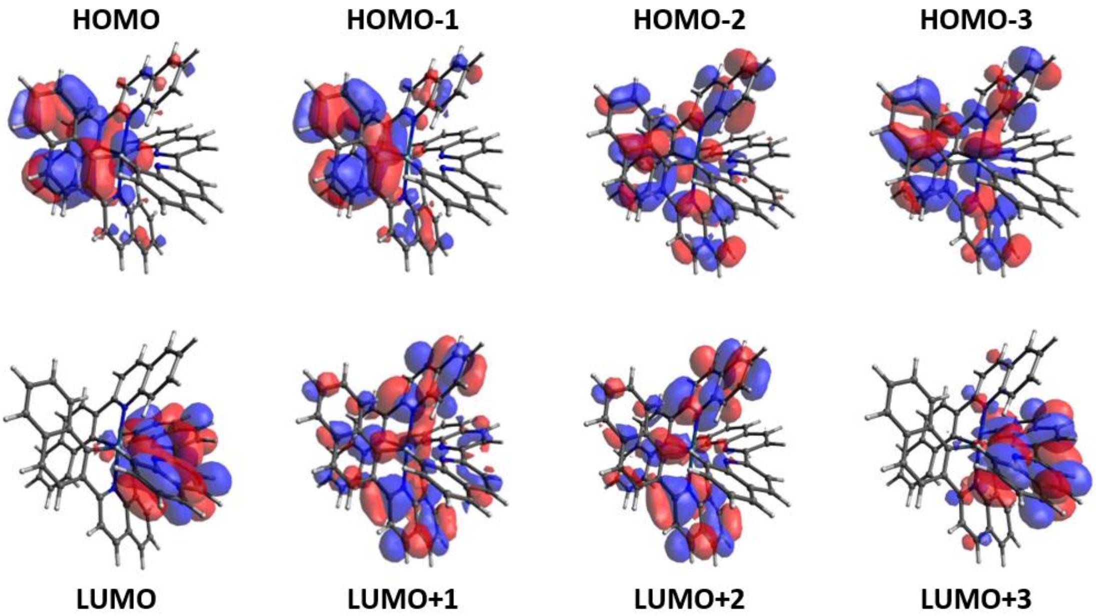

Figure 4.24 Calculated Kohn-Sham frontier molecular orbitals for D4.

According to molecular orbital decomposition analysis (table 4.28), the HOMO of the ten Ir^{III} complexes are mainly composed of equal contributions from the naphthyl moieties of both C^N ligands, with a smaller contribution from the iridium center. The HOMO-1 orbitals are mainly comprised of contributions from each of the cyclometalated ligands (ca. 97-98% in total), and a negligible contribution from the Ir core, 2%, in a manner similar to $[Ir(L^{11})_2(L^{17-22})]^+$ complexes. On the other hand, the LUMO of all complexes are primarily located on the diimine N^N ligand, save for in the D1 complex in which the LUMO is made up of equal contributions from diimine ligand and the quinoline part of the C^N ligands. This indicates that modifying the diimine ligand by introducing electron-withdrawing groups, as in D2 and D3 complexes, or by extending its *π*-conjugation, as in D4-D10 complexes, lowers its orbital energy, making it the predominant contributor to the LUMO. This behaviour is reminiscent of that seen in other complexes in this chapter when changing the bipy ligand $[Ir(L^{11})_2\ (bipy)]^+$ and $[Ir(L^{14})_2\ (bipy)]^+$ with pyridinyl/pyrazinyl)-quinoline ligands (L^{17-22}). Similarly, for complexes D2-D10, the LUMO+1 is made of equal contributions from both the C^N and N^N ligands, with a smaller contribution from the N^N ligand. However, in the D1 complex, the LUMO+1 is mainly located on the N^N ligand. The contribution of metal *d*-orbitals to the HOMO orbitals is less than the ligand contributions, suggesting that the excited states have a reasonable degree of ligand$_{(C\text{^}N)}$ to ligand$_{(N\text{^}N)}$ charge transfer (LLCT) character mixed with intra- ligand$_{(C\text{^}N)}$ charge transfer ILCT character and less metal to ligand charge transfer (MLCT) character. The reduction of MLCT character in the excited state suggests a longer excited state lifetime.

4.4.3 TD-DFT and vertical transitions calculations

TD-DFT calculations were conducted using the CAM-B3LYP functional from the singlet ground states of the complexes in order to estimate the absorption transitions and determine the orbitals that contribute to those transitions and the extent to which they contribute. For each complex, the lowest 30 singlet-to-singlet spin-allowed and 30 singlet-to-triplet spin-forbidden transitions were calculated, and the results for the first 5 singlet excited states for D1 and D4 complexes are displayed in tables 4.29 and 4.30. The lowest predicted singlet and triplet transitions for each of the complexes are presented in table 4.31.

Table 4.29 The wavelength, force oscillator strengths and contributing molecular orbital transitions of the first five singlet-to-singlet excited states for D1 complex. Molecular orbital contributions less than 10% have been omitted for clarity. Q1 and Q2 are the inequivalent quinoline ligands; N^N = diimine ligand

D1	**Moiety Contribution to Orbital (%)**				**Orbital Contribution to Excited State**	
Orbital	**Ir (5d)**	**N^N**	**Q1**	**Q2**	**Excited State**	**Contributing Transitions (> 10 %)**
LUMO +4	3	1	46	51	1 (414 nm f=0.0392)	HOMO → LUMO (82%)
LUMO +3	1	69	15	15		
LUMO +2	6	9	43	42	2 (399 nm f=0.2171)	HOMO → LUMO+1 (21%)
LUMO +1	1	89	5	5		HOMO → LUMO+2 (60%)
LUMO	3	31	33	33	3 (361 nm f=0017)	HOMO → LUMO+1 (70%)
HOMO	20	1	40	40		HOMO → LUMO+2 (21%)
HOMO -1	1	1	49	49	4 (326 nm f=0.0206)	HOMO -1 → LUMO+1 (11%)
HOMO -2	26	3	36	35		HOMO → LUMO (10%)
HOMO -3	14	1	42	43		HOMO → LUMO+3 (65%)
HOMO -4	8	5	44	43	5 (324nm f=0.1590)	HOMO-1→ LUMO (75%)

Table 4.30 The wavelength, force oscillator strengths and contributing molecular orbital transitions of the first five singlet-to-singlet excited states for D4 complex. Molecular orbital contributions less than 10% have been omitted for clarity. Q1 and Q2 are the inequivalent quinoline ligands; N^N = diimine ligand.

D4	Moiety Contribution to Orbital (%)				Orbital Contribution to Excited State	
Orbital	**Ir (5d)**	**N^N**	**Q1**	**Q2**	**Excited State**	**Contributing Transitions (> 10 %)**
LUMO +4	0	84	8	8	1 (421 nm f=0.0580)	HOMO → LUMO (68%)
LUMO +3	1	90	5	5		HOMO → LUMO+2 (17%)
LUMO +2	4	3	46	47	2 (408 nm f=0.0484)	HOMO → LUMO+1 (84%)
LUMO +1	3	10	44	43		
LUMO	2	95	1	1	3 (383 nm f=1533)	HOMO → LUMO (22%)
HOMO	19	1	40	40		HOMO → LUMO+2 (59%)
HOMO -1	2	2	48	48	4 (337 nm f=0.0561)	HOMO -2 → LUMO (74%)
HOMO -2	25	4	35	35		
HOMO -3	18	2	40	40	5 (327 nm f=0.1361)	HOMO-2→ LUMO+1 (75%)
HOMO -4	8	17	38	37		HOMO -1 → LUMO+2 (11%)

Table 4.31 Computed values for the vertical spin allowed and spin-forbidden absorption for D1-D10 complexes

Complex	**$S_o \rightarrow S_1$ Abs. (nm)**	**$S_o \rightarrow T_1$ Abs. (nm)**
D1	414	581
D2	416	587
D3	421	586
D4	420	589
D5	423	587
D6	425	589
D7	431	590
D8	438	590
D9	460	589
D10	500	591

Table 4.31 shows that the calculated wavelengths of triplet absorption bands are significantly red-shifted in comparison with the singlet absorption bands. As expected, the D1 complex displays the shortest wavelength absorption bands while the D10 complex demonstrates the most red-shifted absorption band. For the D1 complex, the excitation to the **S_1** state is mainly HOMO → LUMO in nature, taking place at 414 nm, followed at higher energy by an intense HOMO to LUMO+1 transition occurring at 399 nm (f = 0.2171). Both transitions are combinations of metal to ligand, intra-ligand$_{CN}$, and ligand$_{C^N}$ to ligand$_{N^N}$ transitions. The lowest spin-forbidden absorption band is predicted to be at 581 nm. As with the lowest singlet excited state, the triplet absorption band is predicted to be of mixed

^{3}MLCT/^{3}ILCT/^{3}LLCT character. Similar absorption transitions were predicted for the D4 complex, but bathochromically shifted. The longest wavelength singlet excitation of D4 is predicted to arise from HOMO to LUMO and LUMO+2 transitions at 421 nm whereas the excitation to the S_2 state is predominantly HOMO → LUMO+1 occurring at 408 nm. Both transitions are defined as ^{1}MLCT/^{1}ILCT. The calculated triplet absorption transition is found to be at 589 nm. The rest of the complexes display similar electronic transitions to those of D4, suggesting that the modification of the diimine ancillary ligand does not substantially change the electronic structure of these complexes but leads only to smalls shift in the absorption bands.

In order to estimate emission wavelengths, DFT was used to compute adiabatic emission energies, as the analysis of prior iridium complexes suggests that the adiabatic emission energies are better matched to experimental data than vertical energies. This was again performed by comparing the energies of optimized singlet ground state and triplet excited state geometries, and the results are displayed in table 4.32.

Table 4.32 Computed values of adiabatic emission wavelengths for D1-D10 complexes.

Complex	**$T_1 \rightarrow S_o$ Em. (nm) Adiabatic**
D1	627
D2	642
D3	651
D4	665
D5	675
D6	681
D7	700
D8	722
D9	785
D10	907

The table above indicates that the complexes are expected to emit in the red and near-infrared regions, with wavelengths ranging from 627 nm to 907 nm. However, the actual emission wavelengths are expected to be slightly higher in energy than the values listed in table 4.32. This is because the B3LYP functional seems to underestimate the emission energies of the complexes as discussed earlier in this chapter. Among the complexes, those containing the phenanthroline ancillary ligand (D1-D3) exhibit notable blue-shifted emissions compared to those containing longer π-conjugated N^N ligands (D4-D10). The introduction of substituents on the C^N and N^N ligands causes a slight shift in the predicted emission wavelengths, with the magnitude of the shift being consistent with the type, position and number of the substituents, consistent with all the prior complexes investigated in this thesis. For instance, the presence of an electron-withdrawing group, F, on the N^N ligand (D5 complex) results in a shift of the emission centre by 10 nm while shifting by 15 nm when attached to C^N ligand (D6 complex). Furthermore, the emission centre experiences an additional red shift when substituents are attached to both C^N and N^N ligands simultaneously (D7 complex) or when increasing the number of substituents (D8 complex). A significant bathochromic shift of emission energy is predicted when an electronegative atom, nitrogen, is introduced into one of the pyridinyl rings of the N^N ligand (D9 complex). A further red shift is predicted when another N atom is inserted into the second pyridinyl ring of N^N ligand (D10 complex). These results indicate that a significant shift of emission bands can be achieved by extending longer *π*-conjugation or by inserting a nitrogen atom into pyridinyl rings of N^N ligand while a subtle tune can be accomplished by attaching substituents to C^N or N^N ligands. The high tunability of the complexes makes them versatile and expands their areas of potential application.

The spin density distributions of the D8 complex within the $\mathbf{T_1}$ state (shown in figure 4.25) mainly lie on the N^N ligand, the C-moiety of C^N ligand and the Ir metal centre, supporting the early assignment of the triplet emissive state of these complexes as a mixed ^{3}LLCT/^{3}ILCT/^{3}MLCT. Therefore, the lifetime of the triplet excited state is expected to be relatively long (a few hundred nanoseconds), indicating a possibility of using the complexes in photosensitizers and TTA applications. The spectroscopic properties of the complexes align with the desirable characteristics that were considered during their design, meaning that the developed methodology is significantly valuable for analysing such complexes.

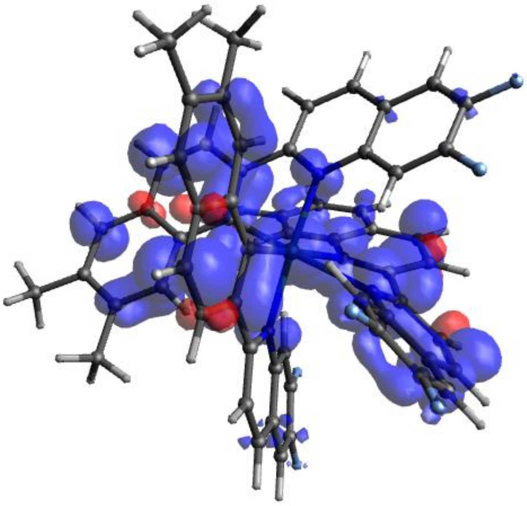

Figure 4.25 Calculated spin densities of the D8 complex.

4.5 Conclusion

The methodology employed in this work to analyse the spectroscopic properties of a range of related iridium complexes provides a deep insight into the role of each of the ligand types and how the modification of each ligand affects the luminescent properties of these complexes. The degree of conjugation of the C^N or ancillary N^N ligand of the complexes is shown to induce a significant tune of the emission centre and increase the lifetime of emission by reducing the MLCT character in the emissive excited state. Additionally, the substitution on cyclometalated ligands leads to varying magnitudes of shifts in the emission spectra depending on the nature, position, and number of the substituents. The computational methodology employed in this analysis consistently predicts the spectroscopic features of the entire range of complexes examined in this work, and proves the efficacy of the combined methodology of experimental and computational techniques in investigating the photophysical properties of this class of complexes. The findings of this study were used to guide the design of novel iridium complexes that emit in the deep red and near-infrared regions, with relatively long excited-state lifetimes. This methodology is promising in the rational design of efficient luminescent iridium complexes with tailored properties for specific applications, such as organic light-emitting diodes (OLEDs), biological imaging, and photocatalysis. The ability to predict and fine-tune the luminescent properties of these complexes using this methodology can lead to the development of more efficient and cost-effective materials for commercially relevant applications.

5. Spectroscopic and Computational Analysis of the Excited-state Dynamics of Organic N-substituted Naphthalimide Dyads

5.1 Introduction

Chromophores with populated triplet excited states after excitation (either photoexcitation or electrical excitation) have important practical applications in many areas of science and biology. These include electroluminescence, `display` applications (such as TVs and phone screens), use as triplet photosensitizers (PSs) in applications such as phosphorescent bioimaging or molecular sensing, solar cells, photodynamic therapy, photocatalytic organic reactions, and triplet–triplet annihilation (TTA) upconversion. (Kolosov et al. 2002; Bui et al. 2018; Poddar et al. 2018; Adachi and Sandanayaka 2020) As mentioned earlier in this thesis (figures 1.16 and 1.17), phosphorescent materials can yield both direct and indirect triplet states upon electrical excitation, resulting in high quantum efficiencies (theoretically reaching up to 100%) for phosphorescent light-emitting devices, such as OLEDs. However, in photoexcitation, which is used in triplet photosensitizer (PSs) applications, the triplet state of a chromophore can not readily be populated directly, as it is formally spin forbidden. Assuming a singlet ground state for the photosensitizer, the population of triplet states is normally generated via $\mathbf{S_1} \rightarrow \mathbf{T_n}$ intersystem crossing which is a forbidden non-radiative transition but becomes weakly allowed by spin−orbit coupling (SOC) mixing the singlet and triplet wavefunctions. In inorganic compounds, SOC is enhanced by using heavy transition metals, as discussed in previous chapters. Nevertheless, the high cost and toxicity of transition metal ions limit their biological applications. As a result, organic dyads, which are composed of two different chromophores that are covalently linked together, have drawn much attention due to their ability to generate very long-lived triplet excited states. (Pearce et al. 2018; Hou et al. 2019; Tang et al. 2022; Ye et al. 2022) Organic dyads are commonly referred to as donor-acceptor dyads (D-A dyads) because one chromophore usually has a higher electron density and acts as an electron donor while the other serves as an electron acceptor. These molecules are characterized by a spatial separation of the two chromophores, and electron transfer occurs between the donor and acceptor, producing charge transfer excited states (CT). Although these dyads promote charge transfer excited states there are still many cases in which electronic transitions occur within one chromophore, leading to the formalisation of locally excited (LE) states. By combining the properties of two different organic chromophores, organic D-A dyads can provide a way to tune the physical, chemical, and electronic properties of materials, leading to improved performance and efficiency. Among organic dyads, naphthalimide dyads are extensively used as photosensitizers in various biological and medical applications, such as in live-cell imaging and anticancer agents. Additionally, they are used in industrial applications like liquid-crystal displays and optical brighteners. (Sebők-Nagy and Biczók

2004; Wei et al. 2012; Jin and Tang 2013; Kitai 2018; Poddar et al. 2018; Zeng et al. 2019; Adachi and Sandanayaka 2020; Ward et al. 2020; Nakanotani et al. 2021; Li et al. 2022)

In triplet photosensitizer applications, an ideal chromophore should exhibit strong absorption of excitation light (typically red light in biological applications to promote skin penetration), a high intersystem crossing (ISC) rate for efficient population of the triplet state, and a relatively long triplet lifetime to allow chemical reactions to occur whilst the triplet state is populated. In transition metal complexes, intersystem crossing can occur due to strong spin-orbit coupling induced by heavy metal atoms, which facilitates population of the triplet state. In organic compounds with only light atoms the magnitude of spin orbit coupling is reduced and the triplet state is less accessible and is typically considered an optically dark triplet state. (Turro et al. 2010; Reineke and Baldo 2014). Therefore, different strategies have been used to facilitate ISC between singlet and triplet states, such as double excitation and exciton coupling. (Bröring et al. 2008; Cakmak et al. 2011; Duman et al. 2012) Changing the orbital symmetry of excited singlet and triplet states (eg. $n\pi^* \leftrightarrow \pi\pi^*$) is another approach that can enhance ISC following El-Sayed rules (figure 5.1). This can be synthetically accomplished by adding main group elements with at least one lone pair of electrons (such as N, P, O or S) to the organic systems. (An et al. 2015; Gao et al. 2019; Franca et al. 2021)

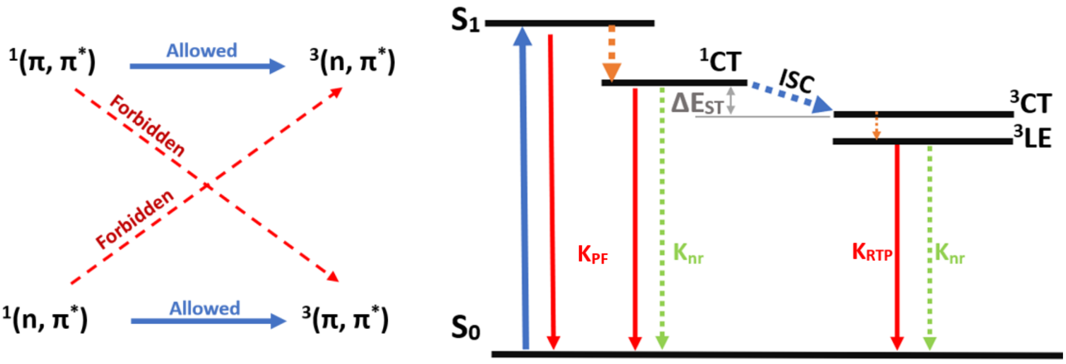

Figure 5.1 Schematic representation of El-Sayed's rules (left) and schematic depiction of the Jablonski diagram in orthogonal organic dyads (right) showing non-radiative decay K_{nr} and radiative decay of prompt fluorescence K_{PF} and room temperature phosphorescence K_{RTP}. ΔE_{ST} is the difference in energy between singlet and triplet excited states.

Another useful approach to enhance the ISC is by decreasing the energy difference between the singlet and triplet excited states, denotted ΔE_{ST}, (figure 5.1) which can be achieved in organic dyads by ensuring an orthogonal geometry is adopted between the electron donor and acceptor moities. (Chen et al. 2017; Dias et al. 2017; Hou et al. 2019; Filatov 2020; Tang et al. 2022) In such geometries, the orbitals of the donor and acceptor barely overlap which reduces wavefunction overlap between them. This leads to a decrease in the electron exchange energy, resulting in a small energy gap between ^{1}CT and ^{3}CT (small ΔE_{ST}). The very small ^{1}CT/ ^{3}CT energy gap affords an increase in hyperfine coupling between them leading to more efficient ISC. In orthogonal dyads with a large separation between electron donor and acceptor units, the change of molecular orbital angular momentum can compensate for the electron spin angular momentum change of the ISC. Therefore, the ISC can be enhanced due to the conservation of angular momentum. This type of intersystem crossing is called charge-transfer mediated ISC, (Bassan et al. 2021; Serdiuk et al. 2021; Ye et al. 2022) and can occur through two different mechanisms: radical-pair intersystem crossing (RP-ISC) in which ^{3}CT is populated at first and then ^{3}LE. However, in optimal orthogonal geometries, the energy gap between ^{1}CT and ^{3}CT is too small (due to the weak overlap between donor and acceptor units leading to small exchange interaction) which reduces the possibility of efficient spin-flip transition, making ^{1}CT → ^{3}CT an unlikely channel to populate the triplet state significantly. Therefore, the presence of another triplet state with ^{3}LE character that is close in energy to ^{1}CT is important to mediated ISC, so that intersystem crossing occurs between the ^{1}CT→^{3}LE states instead of the forbbiden ^{1}CT→^{3}CT process (El Sayed rule), as displayed in figure 5.2. This mechanism is called spin–orbit charge-transfer ISC (SOCT-ISC) and it is the typical mechanism followed in rigid orthogonal dyads with a dihedral angle close to 90°.

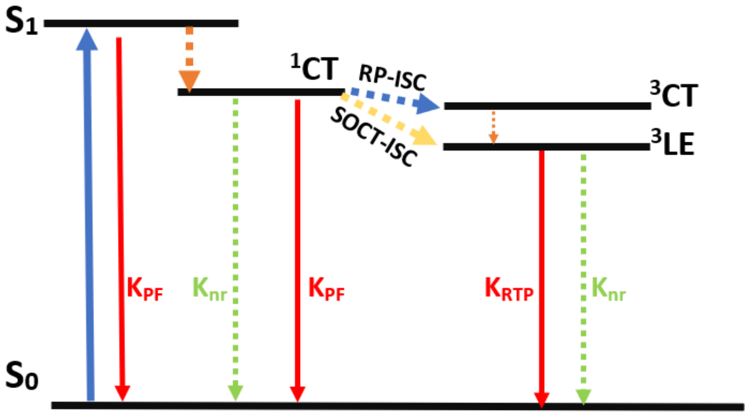

Figure 5.2 Population of triplet excited state by radical-pair intersystem crossing (RP-ISC) or by spin–orbit charge transfer intersystem crossing (SOCT-ISC).

By exploitation of these concepts, several organic D-A dyads with long-lived triplet states have been developed and used as triplet photosensitizers in photocatalysis, triplet-triplet annihilation (TTA) upconversion and photodynamic therapy.(Shi and Xia 2012; Hari and Koenig 2013; Kamkaew et al. 2013; Majumdar et al. 2014; Ye et al. 2016; Guo et al. 2018)

Organic compact dyads have also shown delayed emission (normally considered thermal activated delayed fluorescence (TADF) and phosphorescence) with very long lifetimes and higher luminescence quantum yield compared with traditional fluorescent molecules, making them more appealing in organic light-emitting diode (OLED) applications. Although both thermally activated delayed fluorescence (TADF) and room temperature phosphorescence (RTP) utilize excited triplet states and ISC, they are theoretically opposite processes, as displayed below in figure 5.3. RTP radiates directly after the excited electron undergoes ISC to the triplet state at room temperature whereas TADF radiates after the excited molecule undergoes a forward ISC from singlet to triplet state and then reverses through ISC back to the singlet manifold. (Dias et al. 2017).

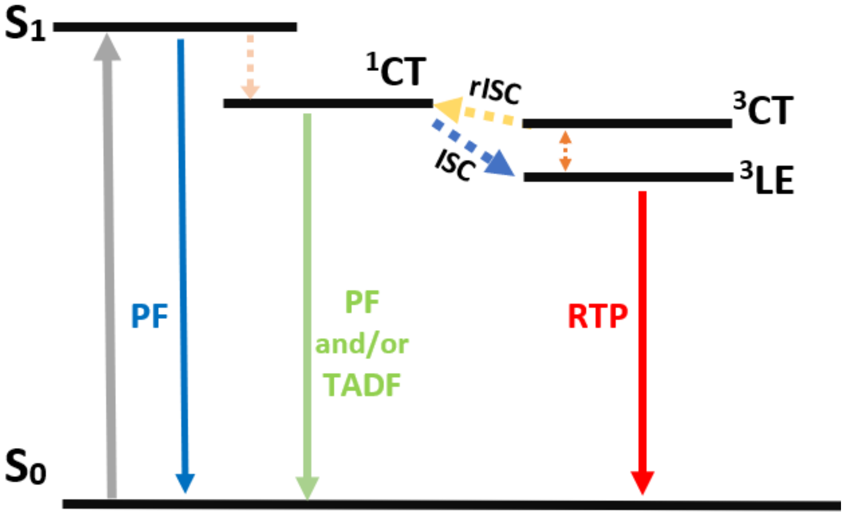

Figure 5.3 Simplified Jablonski diagram of prompt fluorescence PF, TADF and RTP mechanisms.

In order to observe TADF, an efficient reverse intersystem crossing (rISC) to the singlet state must occur. Although hyperfine coupling enhances ISC, the rISC rate between CT states is typically small as the transitions between ^{1}CT and ^{3}CT are forbidden. Recently, it was found that an effective mechanism for efficient rISC, involves a vibronic coupling between the local triplet state ^{3}LE and ^{3}CT. (Etherington et al. 2016; Gibson et al. 2016) The smaller the energy difference between ^{3}LE and ^{3}CT, the more vibronic coupling between them and the greater the rISC rate. Therefore, the rISC is largely dependent on the energy ordering of the three excited states ^{1}CT, ^{3}CT and ^{3}LE, and when they all have similar energies, an intense TADF emission is expected. TADF notably increases at high temperatures due to the increase in molecular motion and vibration that prompts rISC. In contrast, restricting the molecular motions and vibrations enhances phosphorescence from the triplet state. (Etherington et al. 2016; Gibson et al. 2016; Chen et al. 2022; Ye et al. 2022)

Among various kinds of organic dyads, 1,8-naphthalimide derivatives have attracted much attention due to their high photoluminescence quantum yields and good optical, thermal and chemical stabilities. (Ding et al. 2008; Liu et al. 2008) The excited states of napthalimide dyads and thus their photophysical properties can be easily tuned based on modification of the π-conjugated system or by introducing electron-withdrawing or electron-donating substituents to the aromatic ring. For example, attaching nitro groups at the 4-position induces a strongly fluorescent polar charge-transfer (CT) excited state, instead of a non-polar $\pi\pi^*$ excited state found in unsubstituted naphthalimide. (Alexiou et al. 1990; Wintgens et al. 1996; Kucheryavy et al. 2009) In addition, the modification of the molecular geometry and the magnitude of electronic coupling between the donor and acceptor play important roles in the photophysical properties of the dyads. As mentioned above, an orthogonal geometry is favourable for producing small ΔE_{ST} and enhances both TADF and RTP emissions. However, It was proven that a degree of freedom in the molecular structure is required for TADF as molecular rotation and vibration accelerate reverse intersystem crossing (rISC) from the triplet state to the singlet excited state. (Ward et al. 2016; Data and Takeda 2019) In many dyads this motion is achieved through intramolecular torsion between the perpendicular aromatic groups. This rISC process must compete with phosphorescence rates, and therefore for effective phosphorescence emitters, the coupling between donor and acceptor units should be reduced by restricting the intramolecular rotation. Using this concept, many different studies have successfully developed organic dyads that have an increased yielding of room temperature phosphorescence by introducing side groups as a steric hindrance to restrict intramolecular rotation, and therfore reduce rISC rates. (Ward et al. 2016; Data and Takeda 2019; Tang et al. 2022; Ye et al. 2022)

Another approach that has been used to alter the photophysical properties of the organic dyads is replacing one or both oxygen atoms in naphthalimides with sulfur atoms. It has been demonstrated that thionation of carbonyl groups lowers the LUMO energy, leading to significant shifts of absorption bands to longer wavelengths along with a significant increase in absorption coefficients. In addition, the newly created $^1n\pi^*$ excited-state character introduced by the thiocarbonyl (C=S) leads to a remarkable enhancement of ISC due to an energy gap reduction (ΔE_{ST}). Consequently, the fluorescence of these compounds is significantly quenched due to the increased rate of triplet state population. Such characterizations make thionated naphthalimied excellent options as photosensitizers that could be used in multible applications. (Shokri et al. 2017; Pearce et al. 2018; Luo et al. 2020; Symons et al. 2022)

The aim of this chapter is to analyse an N-substituted naphthalimide dyad and three of its chemical variants to investigate the formation of the triplet state and the effect of the thionation of C=O group upon their photophysical properties. For this goal, a joint spectroscopic and computational approach will be used in a similar way to that previously applied to study iridium complexes.

5.2 Molecular Structures

The base compound in this chapter is a novel, compact dyad comprised of 1,8-naphthalimide as an electron acceptor unit and phenyl-piperidine chromophore as an electron donor. A phenyl-piperidinyl (PhPip) is attached to the N-position of naphthalimide (NMI), as displayed in Scheme 5.1. Three more derivatives were prepared by the thionation of one or both carbonyl units as well as substituting phenyl-piperidinyl with piperidinyl in one variant. The compounds were synthesized and purified by Anna Wright at Cardiff University, within the Yi-Lin group. The crystal X-ray structures of all compounds adopt a near orthogonal geometry with a dihedral angle close to 90^o. Therefore, these dyads are more likely to show a small energy difference between singlet and triplet excited states ΔE_{ST} and thus an efficient SOCT-ISC and high population of the triplet state.

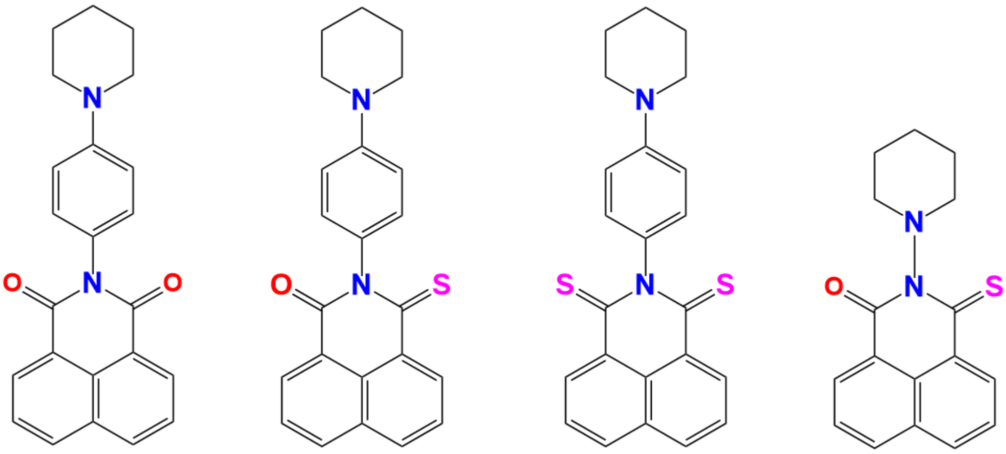

Scheme 5.1 Structure of the donor-acceptor dyads investigated in this chapter. Insert their shorthand names.

5.3 Steady State UV-Vis Absorption Spectra

5.3.1 N-PhPipNMI

The UV–vis absorption spectra of N-PhPipNMI were recorded in toluene and DCM at room temperature and are displayed in figure 5.4.

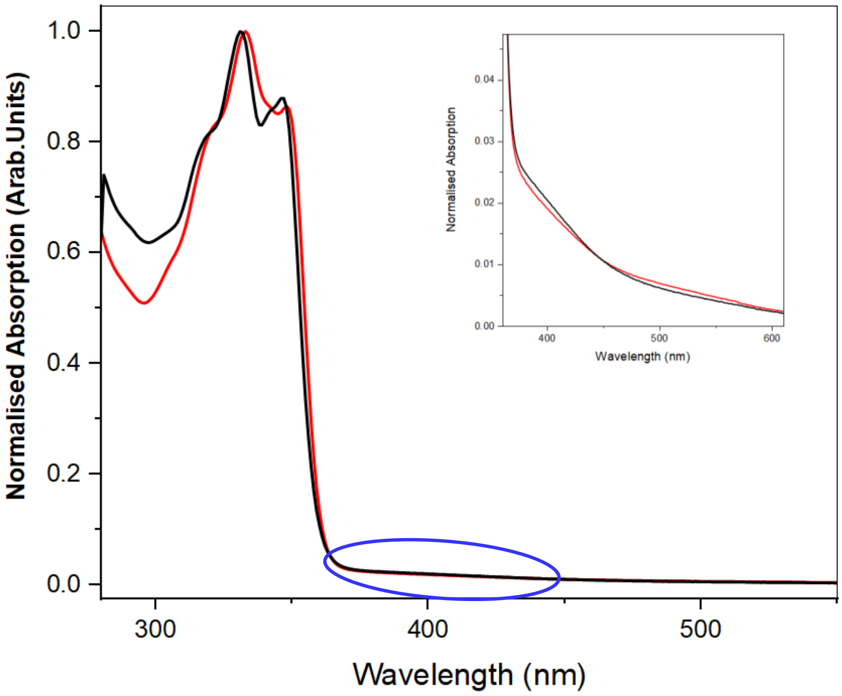

Figure 5.4 Normalised UV-Vis absorption spectra of N-PhPipNMI in toluene (1X10^{-5}M) (black trace) and DCM (1X10^{-5}M) (red trace). The inset shows the weak tail attributed to intramolecular charge transfer.

N-PhPipNMI displays a clear vibronic absorption profile (Fig 5.4) with distinguishable maxima at 318, 330 and 346 nm in toluene and bathochromically shifted by 2 nm in DCM, which is typical for ^{1}LE ($\pi\pi^*$) transitions. The spectrum is similar to the absorption spectrum of the un-substituted naphthalimide compounds reported previously. (Wintgens et al. 1994) The spectra show no sign of intramolecular charge transfer (CT), save for a very weak tail seen between 370-450 nm (circled in blue in figure 5.4), suggesting that the absorption spectrum is mainly derived from molecular orbitals localized on the naphthalimide moiety. Such behaviour is expected in these compounds, given the orthogonal geometry of the molecular dyad that restricts optical electronic interaction between PhPip and NMI units.

5.3.2 Thionated derivatives

As mentioned above, the thionation of the carbonyl group changes the orders of singlet excited states, making $^1n\pi^*$ the lowest excited state. Such modification should be evident in steady state absorption spectra. Therefore, the steady state absorption spectra for the thionated molecules were recorded in toluene at ambient conditions, and they are presented in figure 5.5 along with the N-PhPipNMI spectrum for comparison.

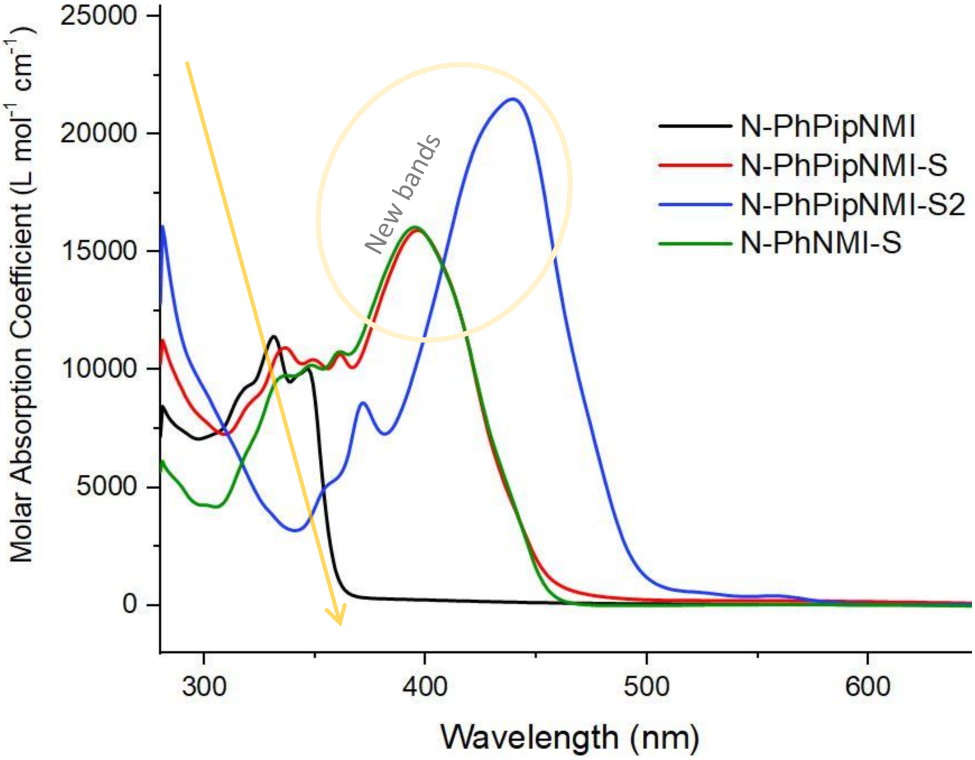

Figure 5.5 UV-Vis absorption spectra of the four dyads in toluene (1X10^{-5} M) at room temperature. The yellow line shows the shift in the absorption features of N-PhPipNMI induced by thionation.

As seen in figure 5.5, the absorption spectra of the thionated naphthalimide variants demonstrate a significant red shift to longer wavelengths, with the dithionated compound showing the most bathochromicly shifted spectrum. Moreover, the vibronic structure of the naphthalene core appears to gradually wane upon the thionation of the compounds; this was in conjunction with the emergence of a new broad feature at longer wavelengths with very high absorption coefficients. The new band is attributed to the excitation to a $^1n\pi^*$ excited state induced by the thiocarbonyl (C=S). The monothionated dyads, N-PhPipNMI-S and N-PipNMI-S, present near-identical absorption maxima, each located at the same wavelength, although they bear different donor units, further supporting the concept that all absorption features can be attributed to ^{1}LE transitions in the naphthalimide moiety. The significant red shift is due to the reduction in LUMO energy when replacing the carbonyl unit with C=S, in agreement with other thionated naphthalimides and a rylene diimides reported previously. (Patsenker and Artyukhova 2003; Hussain et al. 2017; Shokri et al. 2017; Luo et al. 2020; Palmer et al. 2020)

5.4 Emission Spectra

5.4.1 N-PhPipNMI

The emission spectrum of NPhPipNMI was recorded in two solvents with different dielectric constants (toluene: 2.38, DCM:8.93), at ambient conditions, and the spectra are shown in figure 5.6.

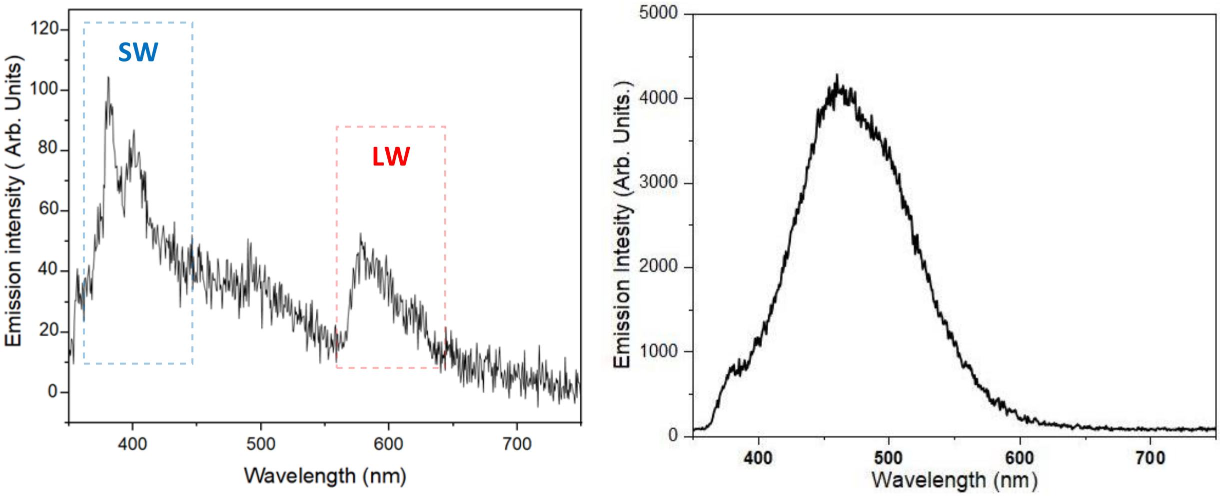

Figure 5.6 Emission spectra of NPhPipNMI obtained in aerated toluene (left) and DCM (right) solutions ($1X10^{-5}$M) at room temperature, λ_{ex} = 355 nm.

Upon excitation at 355 nm in aerated toluene at room temperature, NPhPipNMI displays a very weak dual emission profile, with a structured feature at a shorter wavelength (referred to by SW) and another less intense band in the red region of the spectrum, at λ~ 578 nm, (referred to by LW). The SW feature shows vibrational structures with maxima around 382, 403 and 426 nm, which is in agreement with the emission profile of the parent 1,8-naphthalimide fluorophore and its derivatives reported previously. (Aveline et al. 1997; Chatterjee et al. 2007; Manna and Chakravorti 2010) The spectral shape of SW emission feature is a mirror image of the absorption spectrum and can be defined as a prompt fluorescence (PF) originating from the singlet locally excited state ^{1}LE, $^1\pi\pi^*$, of the naphthalimide moiety. In DCM, which has a higher dielectric constant, the structured SW band loses its resolution and displays a noticeable bathochromic shift, which are typical characteristics of charge transfer emission (CT). Thus, the broad emission feature at 455 nm with a small shoulder in DCM should have a significant contribution from an intramolecular charge transfer transition, CT, from the PhPip moiety to the naphthalimide moiety. The red shift of the emission band could be interpreted by considering the solvent stabilization of the intermolecular charge transfer state more than the ground state. These observations are similar to those found for some previously reported N-substituted 1,8-naphthalimide derivatives and other D–A systems such as coumarines, arylaminonaphthalene sulfonates and bianthryl derivatives. These studies have proven that the LE state is the lowest excited state in nonpolar solvents whereas the CT states become lower than the LE state in more polar solvents.(Kosower 1982; Cichos et al. 1997; Piet et al. 2001; Chatterjee et al. 2007; Song et al. 2019; Jena et al. 2020) The lifetime of the prompt fluorescence in DCM solvent was found to be slightly longer than for that recorded in toluene, 14 ns for the former and 10 ns for the latter.

As mentioned above, NPhPipNMI in toluene displays an additional broad structureless band at the spectrum's low energy region, which completely disappeared in DCM. It is noteworthy that the LW emission band is located in the same region of the spectrum as the phosphorescence bands observed in iridium complexes discussed in previous chapters, thus the LW band might be attributed to phosphorescence. However, to precisely determine the origin of this low-energy band, the photoluminescence spectrum has been recorded in degassed toluene at room temperature, and the result is shown in figure 5.7. Oxygen dependent experiments are generally used to investigate emission processes that involve the triplet excited state. The long-lived emissions, such as direct phosphorescence and delayed fluorescence, have triplet excited states involved in their pathways, and thus they are likely to be quenched by oxygen. In contrast, the fast radiative decay of prompt fluorescence originated from singlet states makes the oxygen quenching of the emissions unlikely to occur.

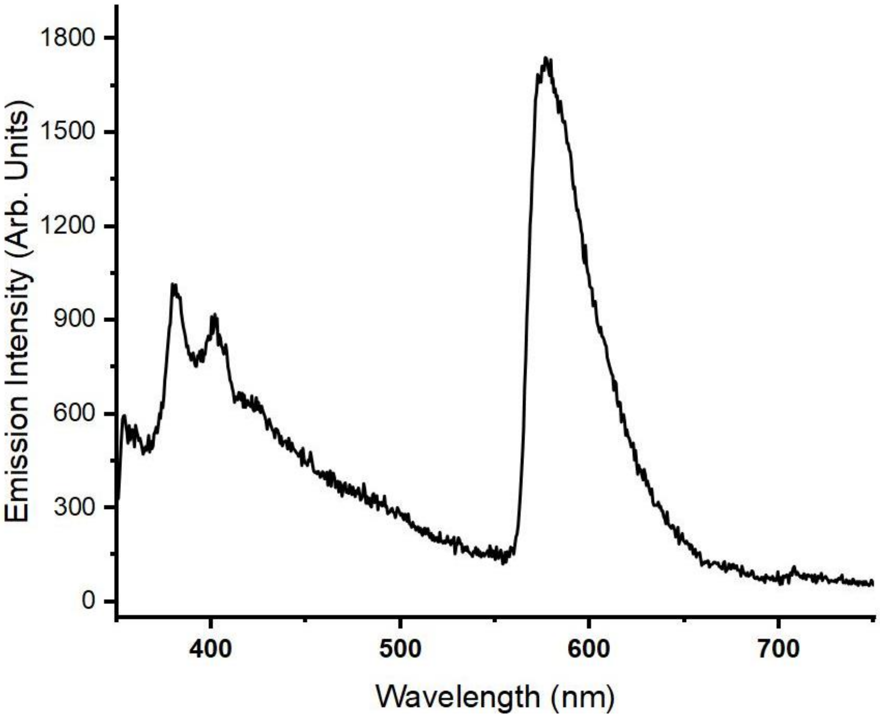

Figure 5.7 Emission spectrum of NPhPipNMI obtained in degassed toluene (1X10^{-5}M) at room temperature.

As in the above spectrum, NPhPipNMI shows a more intense and well resolved emission profile under deoxygenated conditions, suggesting a contribution from the triplet state. However, it is important to note that the intensity of the LW band in the above spectrum appears artificially higher than that for the prompt fluorescence band at a shorter wavelength. This is an artifact of the experimental conditions: the intensity of the excitation laser pulse is too high for the ICCD to safely examine close to the onset of the pulse. The laser pulse could be filtered out using a bandpass filter, however it is often more convenient to simply gate the ICCD camera to open shortly after the end of the excitation laser pulse. Thus, although the lifetime of prompt fluorescence is typically on the order of ten nanoseconds, the ICCD was gated to 25 ns to avoid interference from the excitation laser. To overcome the limitation of ICCD, the PMT detector was used to record the emission spectra by performing a wavelength map method. This approach allows us to obtain a 3D spectrum showing the change in the emission intensity after the onset of the laser pulse and over a selected time scale at a chosen wavelength range, 350-700 nm in this case. Utilizing this method allows us to avoid wavelengths that include laser scatter through judicious use of the monochromator. The spectrum is displayed in figure 5.8, and it clearly shows the significantly higher intensity of the short wavelength band compared to that of the low energy feature, confirming the assignment of the SW band to be fluorescence originating from an allowed singlet to singlet transition.

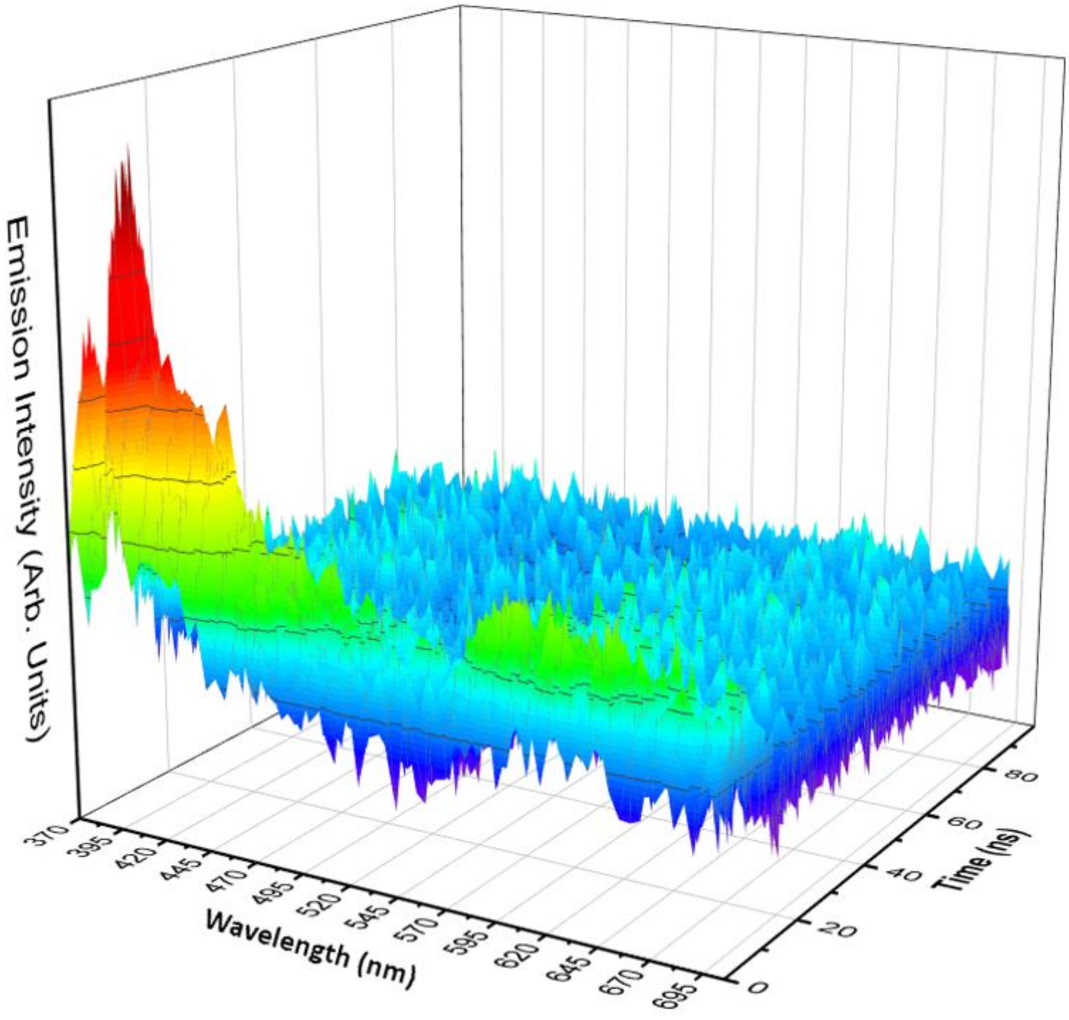

Figure 5.8 3D map of the emission spectrum of NPhPipNMI obtained in degassed toluene (1X10^{-5}M) at room temperature.

In order to get an in-depth assessment of the effect of oxygen on the intensity of each emission feature, the emission spectrum was first recorded in degassed toluene. Then, the sample was opened to the air and its emission was recorded in five-minute intervals for 30 minutes, and then recorded again after 24 hours of exposure to air. The intensity of emission after 24 hours was very weak, and it was important to increase the detector gain to record a clear emission signal. The recorded spectra are displayed in figure 5.9 below.

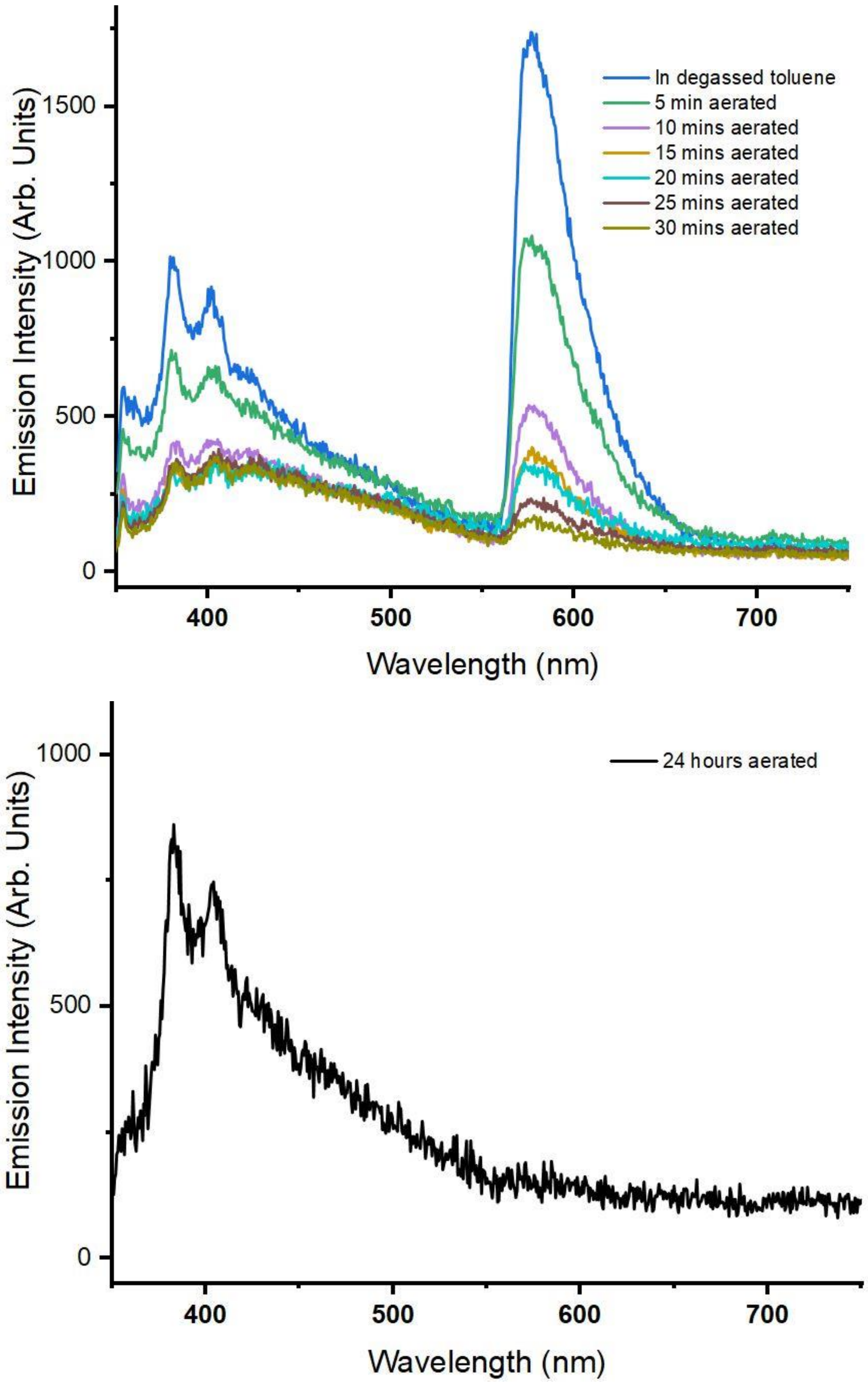

Figure 5.9 Emission spectrum of NPhPipNMI obtained in toluene (1X10^{-5}M) at different aeration times (top) and after 24 hours of aeration (below): the measurements were performed at room temperature.

The above data shows that the intensities of both emission bands are significantly increased in the absence of oxygen, but notably they appear to be quenched to different degrees as oxygen is introduced. Interestingly, the SW emission feature, which was initially assigned as prompt fluorescence, displayed a decrease in the intensity straight away after aerating the solution, but no further reduction was seen after 15 minutes of aeration, and it was still evident even after one day of aeration. This suggests that the emission band at short wavelength can be assigned as prompt fluorescence, but with additional underlying features which rely on the triplet manifold. On the other hand, the reduction in the intensity and lifetime of LW emission feature is directly proportional to the aeration time (increasing the concentration of dissolved O_2 in the solution). This band totally disappeared when exposed to the air for 24 hours. These observations clearly indicate that the triplet excited state plays an integral role in the emission processes. There are several different transitions and processes should be taken in consideration when interrupting oxygen-dependent emissions; such as phosphoresce and different types of delayed fluorescence (thermally activated delayed fluorescence and triplet-triplet annihilation); as well as emissions induced by π-stacking in solutions (in aggregated solution) due to the formation of excimers and exciplexes. All these emission types are primarily observed in oxygen-free solutions and have been reported in naphthalimide derivatives emitters. Nevertheless, it is more likely that LW emission band can be assigned as room temperature phosphorescence given the emission spectrum was recorded in a very dilute solution, $1\text{x}10^{-5}$ M.

As mentioned earlier in this chapter, RTP occurs when excited molecular systems return to the ground state from the lowest triplet excited state $\mathbf{T_1}$ whose energy is less than the singlet excited state $\mathbf{S_1}$, thus it typically displays a noticeable red shift and lower intensity compared with prompt fluorescence. In contrast, TADF takes place when excited molecules process from the triplet manifold to the singlet manifold via rISC and then return to the ground state ($\mathbf{S_0}$) through a radiative transition, thus, it typically overlaps with prompt fluorescence or is only slightly shifted to a longer wavelength. Based on this, I can revise the previous assignment such that the LW band is assigned as phosphorescence whilst the SW band is more likely to be TADF overlapped with prompt fluorescence. In order to assess this hypothesis, temperature dependent measurements have been performed for NPhPipNMI in toluene using an optical cryostat and both ICCD and PMT detectors. Temperature dependent measurements have been widely used to determine whether the observed emission band has TADF contribution or simply arises from room temperature phosphorescence/ fluorescence. Phosphorescence is more efficient at cryogenic temperatures because lowering the temperature slows down or even suppresses the molecular motion leading to reducing the collisions and interactions between molecules, and thus decreasing the rate of non-radiative decay (K_{nr}). For thermally activated delay fluorescence, cooling the solution causes a reduction in the intensity and quantum yield of TADF. This is because thermal energy is needed to increase molecular vibration which induces vibronic coupling and facilitates reverse intersystem crossing (rISC) from the triplet state to the singlet excited state, as in figure 5.10.

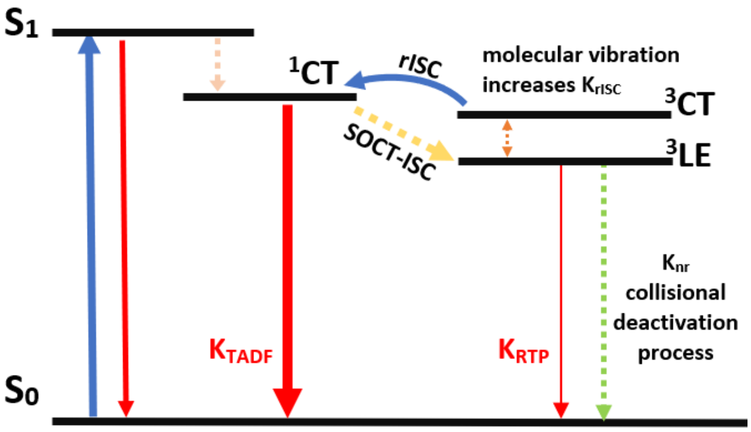

Figure 5.10 Simplified Jablonski diagram explains the effect of increasing the temperature on the decay rate of TADF and RTP.

The emission spectrum in toluene at a low temperature, 77K, is displayed in figure 5.11 along with the spectrum recorded in degassed toluene at room temperature for ease of comparison.

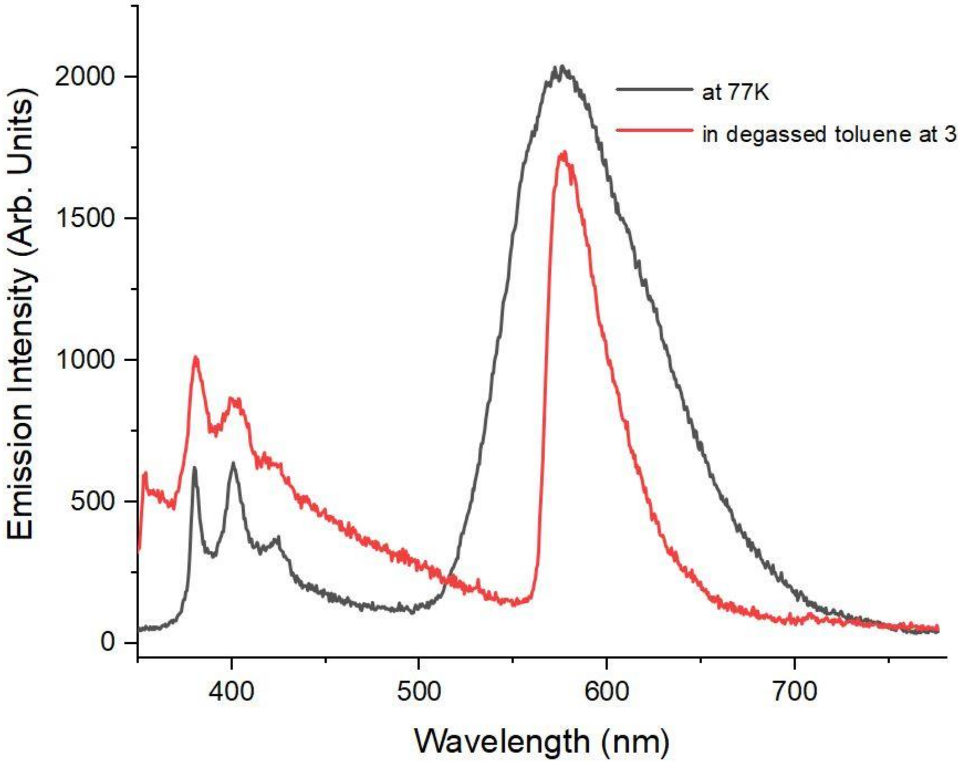

Figure 5.11 Emission spectra of NPhPipNMI obtained in toluene ($1X10^{-5}$M) at 300K and 77K

As seen in figure 5.11 above, the emission spectrum measured at 77K exhibits two emission features that are clearly similar in spectral appearance, vibronic structure and wavelengths of peak maxima to those observed in degassed solution at 300K, although the emission profile of the SW band is better resolved at 77K, due to the reduction of molecular rotation and vibrations in the frozen solution. It is apparent that the intensities of both features display an opposite behaviour under cryoconditions. For

SW band, the emission exhibits a considerable reduction in relative intensity when cooling the solution, which is not surprising if this band has a contribution from TADF. As mentioned earlier, TADF is effectively quenched at low temperatures, due to freezing the molecular vibration, and consequently it is responsible for the drop in emission intensity observed in the spectrum. However, this band did not fully quench by freezing the solvent, but it instead shows a more structured emission profile, owing to the contribution from the prompt fluorescence. These observations provide a definitive assignment of this band to prompt fluorescence overlapped with thermally activated delay fluorescence. Lifetime measurements also validate this conclusion as will be discussed in more detail later in this chapter.

In the case of LW feature, the emission profile at 77K appears to show a significant broadening with a notable increase in its intensity compared with that measured in degassed solvent under ambient conditions. This clearly rules out TADF contributions in favour of direct phosphorescence. Surprisingly, kinetic measurements did not support this assignment at this point of the study, because although the lifetime of this band increased in degassed and frozen solutions, they were very short for the phosphorescence process, 29 ns and 32 ns for degassed and frozen solutions, respectively. The typical phosphorescence lifetimes, found in D-A organic compounds, are in microseconds to millisecond timescale. (Ventura et al. 2014; Chen et al. 2016; Ward et al. 2019; Jena et al. 2020; Franca et al. 2021) Therefore, more experimental evidence is required for reasonably defining this feature.

Aggregation induced emission due to the formation of excimers is also expected in naphthalimides derivatives. Two types of excimers have been found in this class of organic compounds: intermolecular excimers and/or intramolecular excimers. The formation of intramolecular excimers is unexpected here, owing to the rigidity of the compounds investigated in this study. In contrast, intermolecular excimers from the interactions between naphthalimide moieties in the ground and excited states NI/NI* are entirely possible. Several studies have reported intermolecular excimer emission with lifetimes < 20 ns at the long wavelength region in 1,8-naphthalimides dyads. In addition, the intensity and the quantum efficiency of intermolecular excimer emissions are found to be significantly enhanced at low temperatures. This is because increasing temperature accelerates molecular vibration leading to disrupting the π-stacking interactions. (Barros et al. 1995; Cho et al. 2006; Ferreira et al. 2011; d'Agostino et al. 2013; Cho 2014; Felip-León et al. 2018; Jena et al. 2020) (Förster 1969; Horrocks 1971; Musser et al. 2017; Das et al. 2021) Therefore, it was important to investigate if this LW band is due to π-stacking interactions, even though very diluted solutions have been used so far in this study. To this end, emission measurements have been performed using a solution with a higher concentration,$1x10^{-4}$ M. Emission spectra were recorded in degassed and aeriated solutions at room temperature, and the results are displayed in figure 5.12.

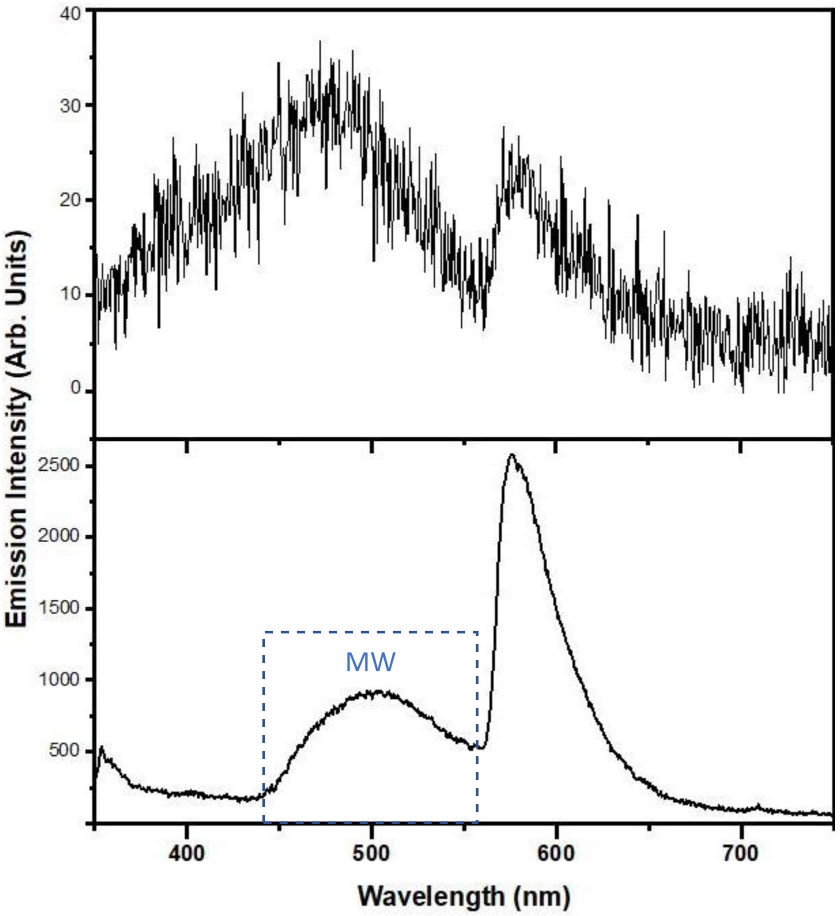

Figure 5.12 Emission spectra of NPhPipNMI obtained in aerated (top) and degassed (below) toluene (1X10^{-4} M) at room temperature, λ_{ex} = 355 nm.

The above figure interestingly shows a new broad structureless emission band that appears at around 500 nm in the concentrated solution, with a lifetime of ~15 ns. The growth of the new band is accompanied by a large decrease in the emission feature at short wavelengths. Therefore, the band at 500 nm is assigned as intermolecular excimer emission resulting from the associative interaction between excited NI* and ground state NI molecules. This result is consistent with the emission band seen between 470-500 nm in the previously reported naphthalimide molecules. (Barros et al. 1995; Cho et al. 2006; Cho 2014) The presence of excimer emission in these dyads, which is enhanced in aggregate solutions, could extend their potential applications. Organic dyads display emissions in aggregation states have been used as luminescent sensors and biological probes, for instance, in biomolecular sensing and biological imaging. (Xu et al. 2010; Chen et al. 2012; Leung et al. 2013) However, the LW feature behaves the same way as in the diluted solution, its intensity increases in the oxygen free solution and drops in the aerated solution. It is clear that this band is concentration independent since there is no shift in its λ_{max}, and its intensity is not enhanced or quenched in the concentrated solution, confirming that this band originates from the naphthalimide monomer. A finding that the aggregation has no contribution to the LW emission feature supports the assignment of phosphorescence from naphthalimide monomer, despite its relatively short lifetime. Indeed, due to significantly low intensity of LW band compared with the prompt fluorescence, it is expected that the measured lifetime using PMT detector would be less accurate. This is because the sensitivity of PMT had to be reduced to avoid the damage caused by the significantly high intensity of prompt fluorescence. Accordingly, the intensity of the phosphorescence is also decreased, making the signal-to-noise ratio too high, as seen in the 3D spectrum in figure 5.8. Therefore, to examine whether this band still persists beyond the timeframe recorded by PMT, the ICCD detector was used and gated to few hundred nanoseconds after the laser pulse, the resulting spectra are shown in figure 5.13. This approach enables the exploration of whether the lifetime of the LW band extends to a timeframe typical for phosphorescence, facilitating a definite assignment of this band.

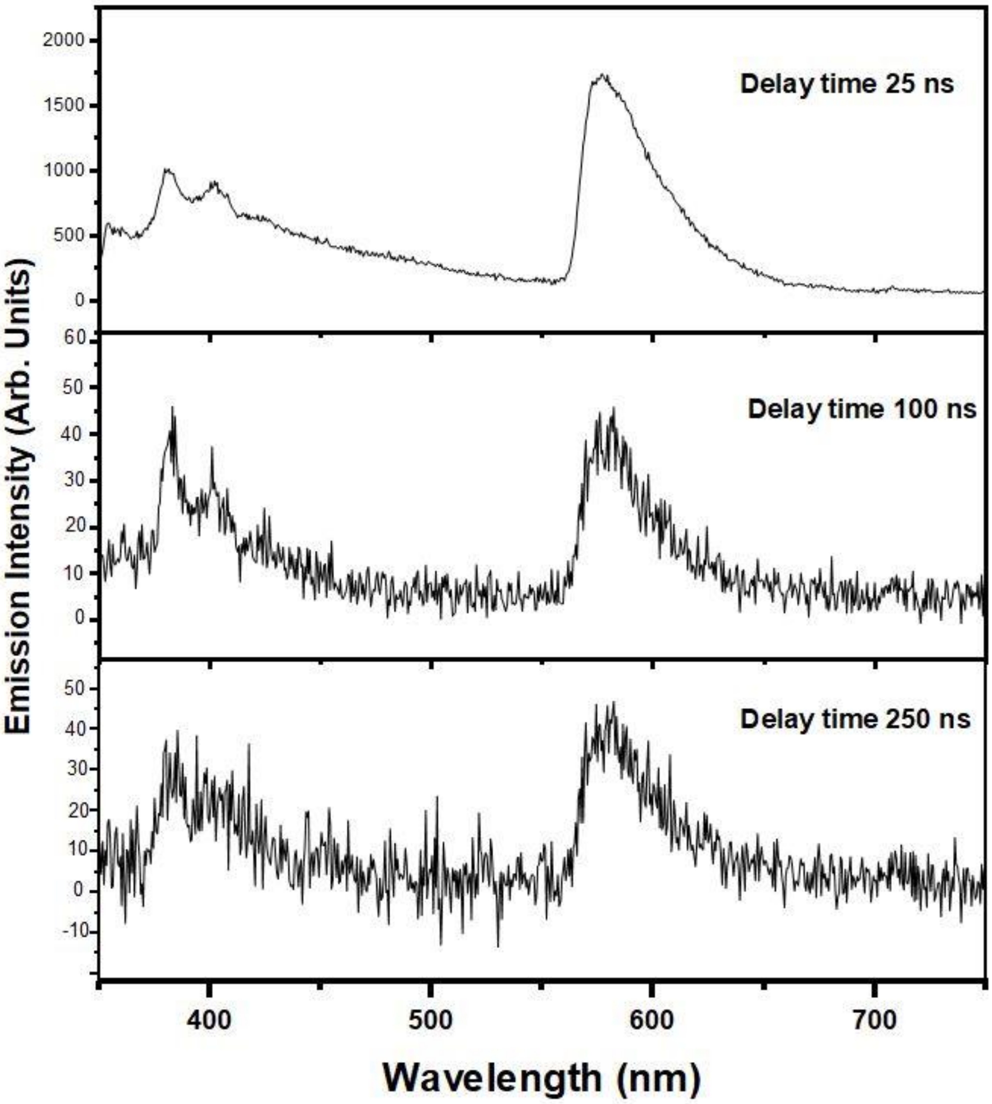

Figure 5.13 Emission spectra of NPhPipNMI obtained in degassed toluene (1X10^{-5}M) at room temperature and at different camera gate delays after the pump pulse.

Figure 5.13 displays that the emission band at 400 nm is not fully quenched at a long gate delay, owing to the contribution of TADF to this band as described earlier in this chapter. The LW band also still exists after 250 ns post the laser pulse which indicates that the lifetime of this band is much longer than that recorded by PMT (32 ns). More accurate kinetics measurements are required to calculate the decay time of this emission band, nonetheless, it can be defined as phosphorescence. Prior literature shows several naphthalimide derivatives (including the parent 1,8-naphthalimide compound) exhibit phosphorescence between 550-650 nm in nonpolar solvents which completely disappeared in polar ones. The phosphorescence of the reported compound was weak, if found, in ambient conditions but notably increased in degassed solutions or at low temperatures, consistent with the results observed in our study.(Wintgens et al. 1994; Manna and Chakravorti 2010; Ventura et al. 2014; Chen et al. 2016; Jena et al. 2020)

The presence of the phosphorescence band in toluene (dielectric constant: 2.38) is attributed to the restriction of the intramolecular rotation in non-polar solvents which causes phosphorescence from ^{3}LE, given the orthogonal geometry which reduces electronic interaction between PhPip and NMI moieties. However, a contribution from triplet intramolecular charge transfer ^{3}CT is expected here given the shape of this band. By contrast, the phosphorescence vanished in DCM (dielectric constant: 8.93), even in degassed solution. This is likely because the more polar solvent stabilizes the ^{3}CT state, which reduces the energy between ^{3}CT/^{3}LE and increases the vibronic coupling between them. Consequentially, ISC and rISC rates will increase between ^{1}CT/^{3}CT which increases the TADF and quenches RTP. (Duan et al. 2018; Data and Takeda 2019; Tang et al. 2019; Ward et al. 2019; Jena et al. 2020; Serdiuk et al. 2021) Figure 5.14 displays a proposed mechanism accounting for TADF and RTP of NPhPipNMI in toluene and DCM solvents.

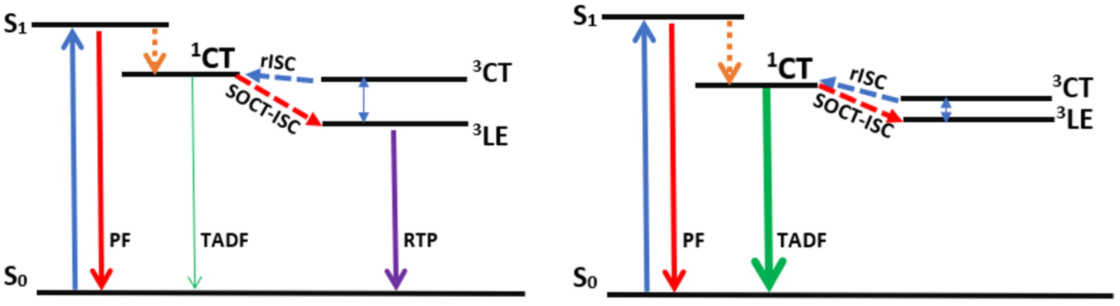

Figure 5.14 Proposed mechanism accounting for the spectral properties of NPhPipNMI in toluene (dielectric constant: 2.38)(left) and in DCM (dielectric constant: 8.93) (right)

5.4.2 Thionated derivatives

To gain a better understanding of how the thionation of the naphthalimide dyads alters the spectroscopic characteristics, the luminescence spectra of all molecules have been recorded in deoxygenated/aerated toluene.

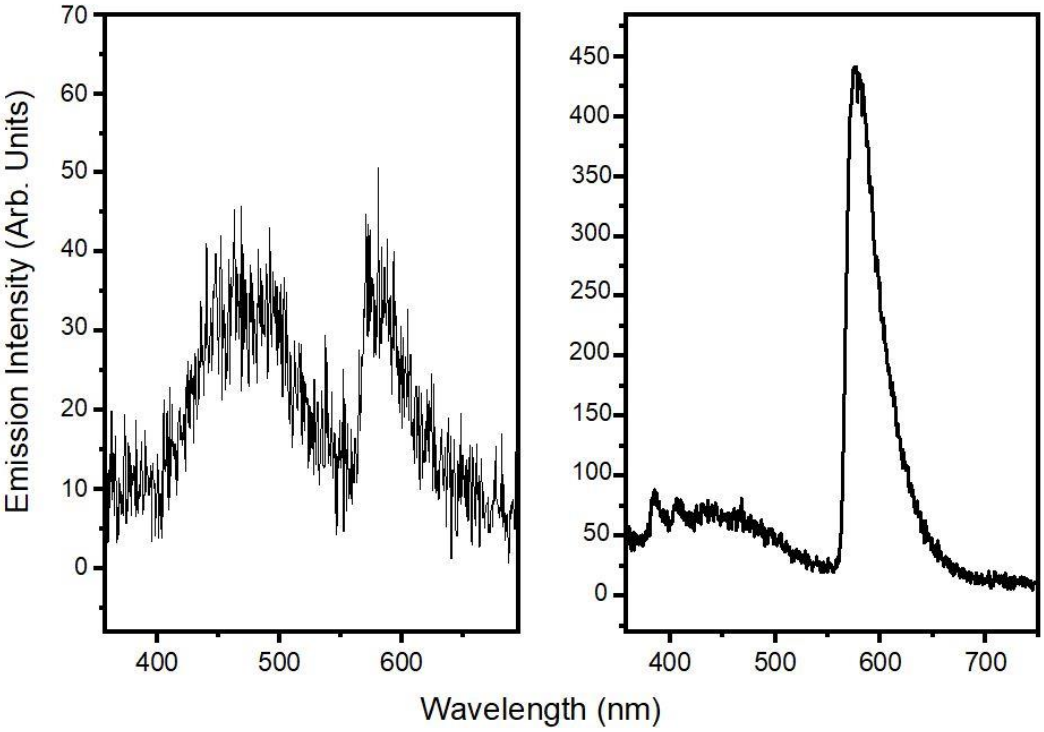

Figure 5.15 Emission spectra of NPhPipNMI-S obtained in aerated (left) and degassed (right) toluene ($1x10^{-5}$ M) at room temperature.

The N-PhPipNMI-S variant displays a relatively weak emission spectrum in aerated toluene but a stronger, better resolved profile in deoxygenated solutions, as shown in figure 5.15. There are two features that can be distinguished: firstly, a high energy feature with vibronic structure at $400 < \lambda < 550$ nm. This band is comparable with the prompt fluorescence feature observed in the base molecule N-PhPipNMI. Notably, this band appears to be less intense and less resolved in the thionated compound, likely due to fluorescence quenching resulting from efficient ISC and formation of the triplet excited state. Such a phenomenon has been widely reported in thionated naphthalimides and naphthalenediimide dyads. (Tilley et al. 2014; Hussain et al. 2017; Palmer et al. 2020; Deiana et al. 2022) The second emission band is located in the red region of the spectrum (approximately at 590 nm) and is substantially enhanced in degassed toluene. This band is identical to the triplet emission band in non-thionated N-PhPipNMI, and thus, it can reasonably be assigned to phosphorescence.

The emission spectra for N-PhPipNMI-S2 are shown in figures 5.16 and 5.17.

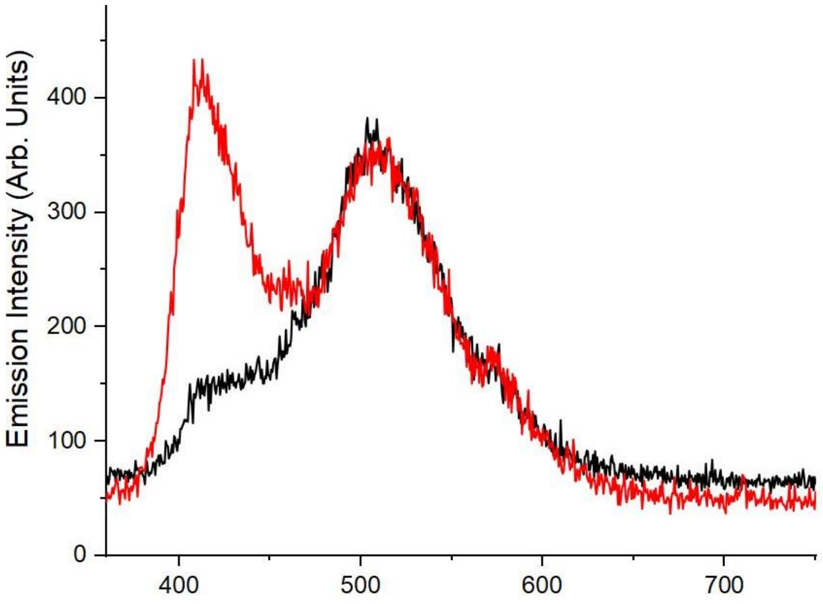

Figure 5.16 Emission spectra of NPhPipNMI-S2 obtained in aerated toluene (1x10^{-5} M) at delay gate 25 ns (red trace) and 35 ns (black trace) at room temperature.

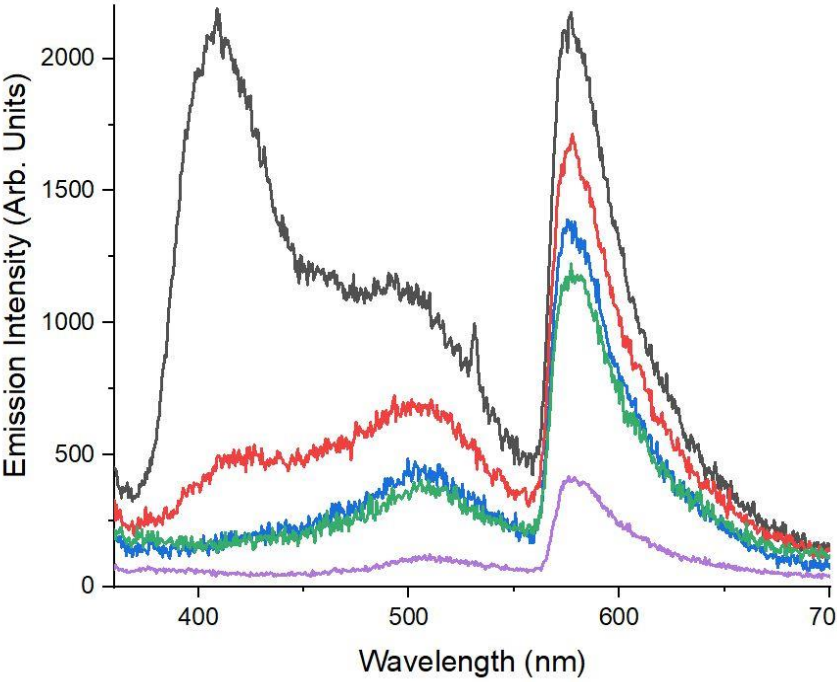

figure 5.17 Emission spectra of NPhPipNMI-S2 obtained in degassed toluene (1x10^{-5} M) at delay gate 20 ns (black trace), 25 ns (red trace), 30 ns (blue trace), 40 (green trace) and 50 ns (purple trace) at room temperature.

N-PhPipNMI-S2 displays an emission spectrum with a spectral appearance similar to that of the base compound. The prompt fluorescence shows a bathochromic shift due to the reduction in the LUMO energy upon the thionation, in agreement with the UV-Vis absorption spectra. The phosphorescence band, again, is identical to the non-thionated compound, indicating that the lowest triplet state was not perturbed by replacing the carbonyl group with C=S. Interestingly, an additional emission band is shown at around 500 nm. Transient emission measurements in degassed and aerated solvent demonstrate that the spectrum recorded at 20 ns after the laser pulse is dominated by the prompt fluorescence, while as the delay time increases the intensity of the prompt fluorescence decreases at a faster rate than the feature at 500 nm, suggesting different origins of the two emission bands. This additional band nicely matches (in emission maximum and lifetime, ~ 15 ns) the emission feature observed in concentrated N-PhPipNMI solution and is tentatively assigned to the intermolecular excimer resulting from π-stacking. Previous studies have demonstrated that the thionation of organic dyads increases intermolecular interactions, which supports our assignments. (Cho et al. 2006; Symons et al. 2022)

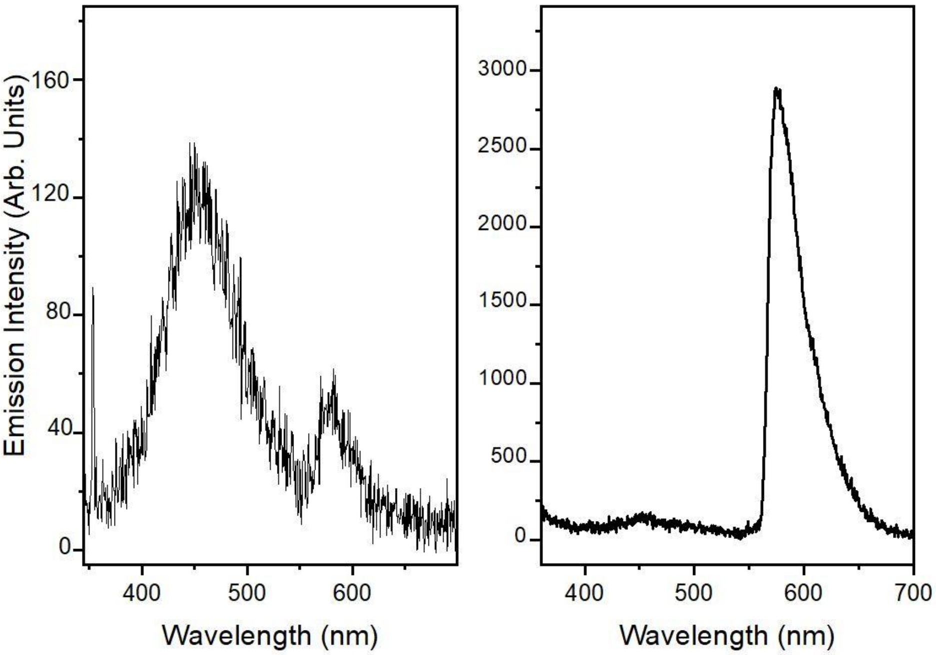

Figure 5.18 Emission spectra of N-PipNMI-S obtained in aerated (left) and degassed (right) toluene (1x10^{-5} M) at room temperature

The above figure shows the emission spectra of N-PipNMI-S in degassed and aerated toluene. A direct comparison of the ratios between the SW and LW emission bands in N-PipNMI-S and the base compound NPhPipNMI, reveals a significant quenching of the prompt fluorescence in N-PipNMI-S. This fluorescence quenching phenomenon has been reported widely in thiocarbonyl organic dyads due to fast ISC leading to a high population of the triplet excited state. This high ISC efficiency suggest a possibility of using such compound as photosensitizers with wide applications. Once again, there is no significant change observed in the position and the shape of the phosphorescence band, suggesting that the thionation of carbonyl group does not perturb the lowest excited state.

5.5 TA Spectra

5.5.1 N-PhPipNMI

To confirm the formation of triplet excited states, nanosecond transient absorption spectra of the N-PhPipNMI compound were recorded in degassed toluene and DCM solvents. The measurements were performed using the ICCD detector that is gated at different delay times after the laser pulse, and the results are displayed in figure 5.19.

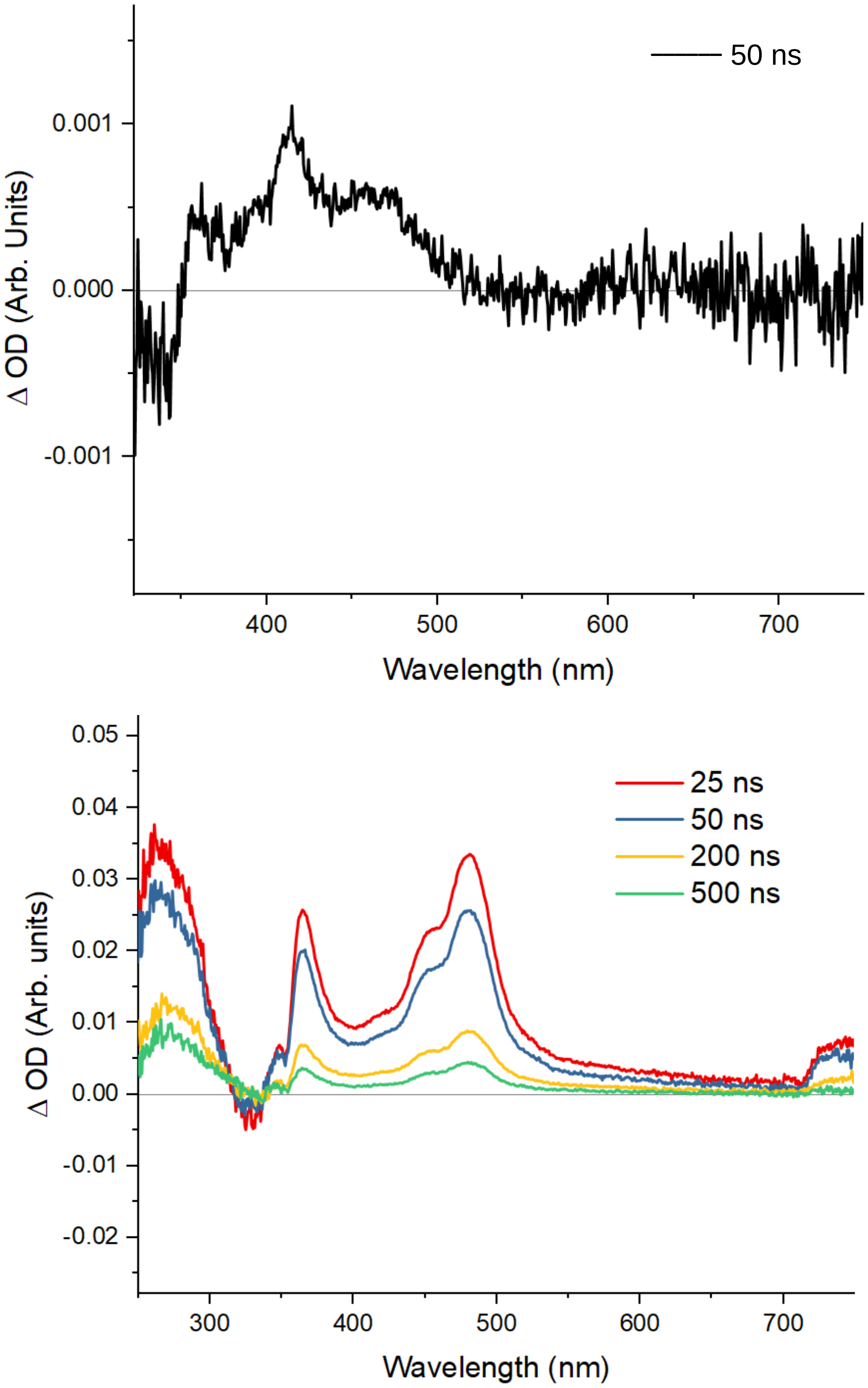

Figure 5.19 Background and fluorescence subtracted transient absorption spectra of N-PhPipNMI recorded at different delay times after the laser pulse in degassed toluene (1x10^{-5} M) (top) and in degassed DCM (1x10^{-5} M) (below), λ_{exc} = 355 nm. The grey line represents ΔOD = 0.

As seen in the above figures, N-PhPipNMI displays similar transient absorption spectra in both solvents, each with three strong positive excited state absorption bands (triplet to triplet transitions) and weak ground state bleach located at around 335 nm which is due to the depletion of the ground state of the naphthalimides. The excited state absorption bands are red shifted and better resolved in DCM. In toluene, the triplet absorption bands centered at around 359, 414 and 466 nm, perfectly match the features observed in the transient absorption spectrum of the naphthalimide moiety recorded in non-polar solvent and reported previously. (Tang et al. 2019; Zhang et al. 2022) This suggests that the lowest triplet state is predominantly located on the naphthalimide moiety (^{3}LE in character). This is expected given the orthogonal geometry of the molecule which reduces electronic coupling between the donor and acceptor. In DCM the nanosecond TA spectrum exhibits a large absorption band at 482 nm with a shoulder around 455 nm and another intense band at 366 nm which, once again, nicely match the spectrum of the naphthalimide moiety previously studied in polar solvents.(Demeter et al. 1993; Wintgens et al. 1994; Aveline et al. 1997)

The ΔOD values were more significant in DCM in comparison with those in the non-polar toluene, suggesting more efficient ISC in the more polar solvent DCM.

5.5.2 Thionated derivatives

Transient absorption spectra of thionated naphthalimide derivatives were also recorded in degassed toluene solutions (1×10^{-5} M). The spectra are displayed in figure 5.20.

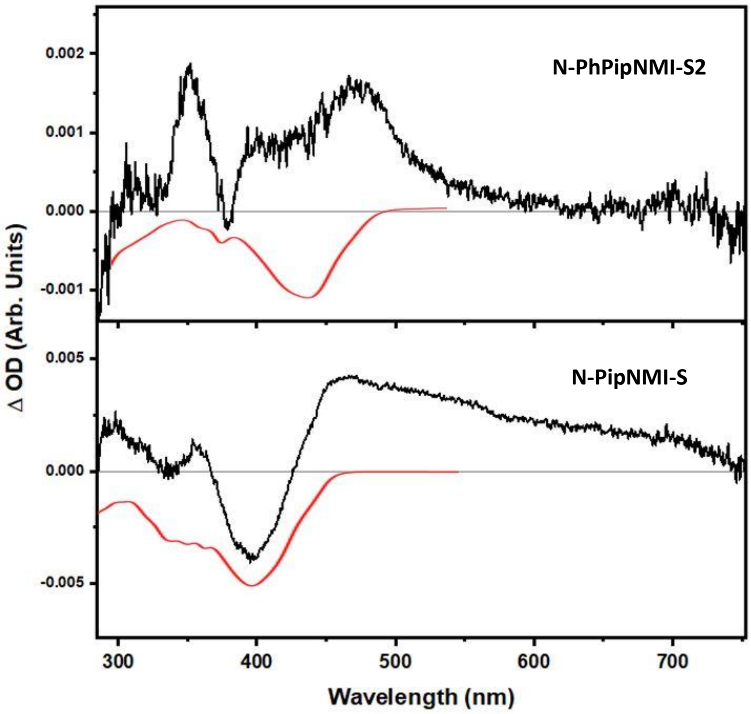

Figure 5.20 Background and fluorescence subtracted transient absorption spectra (black lines) and inverted steady state UV-Vis spectra (red lines) of N-PhPipNMI-S2 (top) and N-PipNMI-S (below) in degassed toluene(1×10^{-5} M), λ_{exc} = 355 nm, delay time = 50ns. The grey line represents ΔOD = 0.

The TA spectra displayed in the above figures show a similar profile as the non-thionated compound, albeit some differences are observed. The ground state bleaching is noticeably red shifted (by ~ 50 nm), corresponding with the bathochromic shift seen in the steady state UV-vis features. The relatively small signal of the ground state bleach in N-PhPipNMI-S2 is consistent with the reduction in the relative intensity of the naphthalene core absorption band seen in the steady state absorption spectrum (figure 5.5). The other absorption band observed at 440 nm in the ground state absorption spectrum is not distinguished as a negative bleach in the TA spectra because of the overlap with the strong excited state absorption bands in this range, as seen in base compound N-PhPipNMI. Both compounds show positive absorption features at around 359 nm and 470 nm, which are the typical bands of the triplet states in naphthalimide. These observations emphasize that, unlike the singlet state, the lowest triplet state is not perturbed by the thionation of carbonyl units or by the adjustment in the donor moiety.

5.6 Kinetic study

The kinetics of the NPhPipNMI compound have been investigated at selected wavelengths based on the ICCD transient absorption and emission spectra, with the aim of monitoring the progression of emission and transient absorption features and determining their decay lifetimes. The PMT and monochromator detection system was used in the same way as in the case of the iridium complexes in previous chapters.

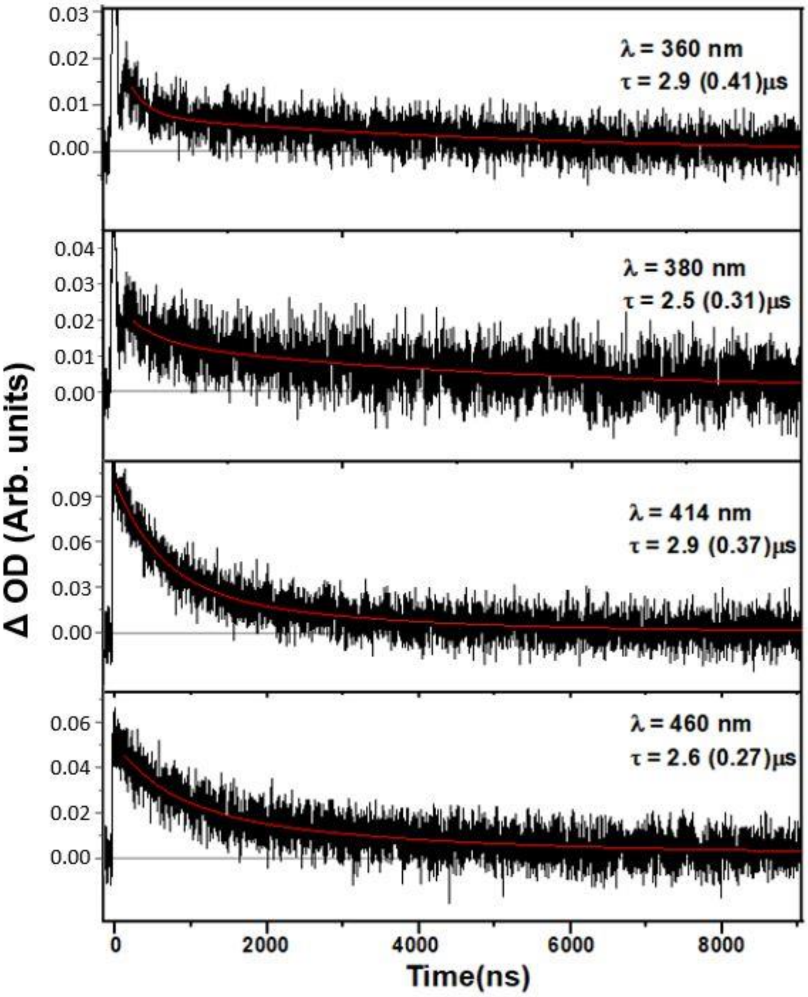

Figure 5.21 Transient kinetic traces of the major features of the transient absorption spectrum of PhPipNMI in degassed toluene ($1x10^{-5}$ M). All are fitted to mono-exponential decay function. Wavelengths and lifetimes of each trace are inset.

Figure 5.21 displays the transient kinetics of the major features of the molecule recorded in degassed toluene. The features all exhibit similar monoexponential decay traces that completely return to the baseline, suggesting no prominent change induced by photo-excitation. This indicates that this dyad may have good stability and potential for use in practical applications, such as in solar cells. The transient absorption traces at 360 and 380 nm show a sharp peak immediately after the laser pulse. This is because the output of the excitation Xe flash lamp is low and less efficient at these wavelengths which increases the noise, leading to poor background subtraction. All triplet transient features have similar lifetimes that are sensitive to the presence of oxygen molecule. The average lifetime in degassed toluene was 2.7 µs and reduced to 0.6 µs in the aerated solution, consistent with those reported previously. (Tang et al. 2019)

In DCM, the transient kinetics are more intense and better resolved, even in the aerated solvent compared to those in toluene, suggesting that the intersystem crossing occurs at a much high rate. The transient kinetic spectra of the major features of the NPhPipNMI molecule in the aerated DCM are shown in figure 5.22 below.

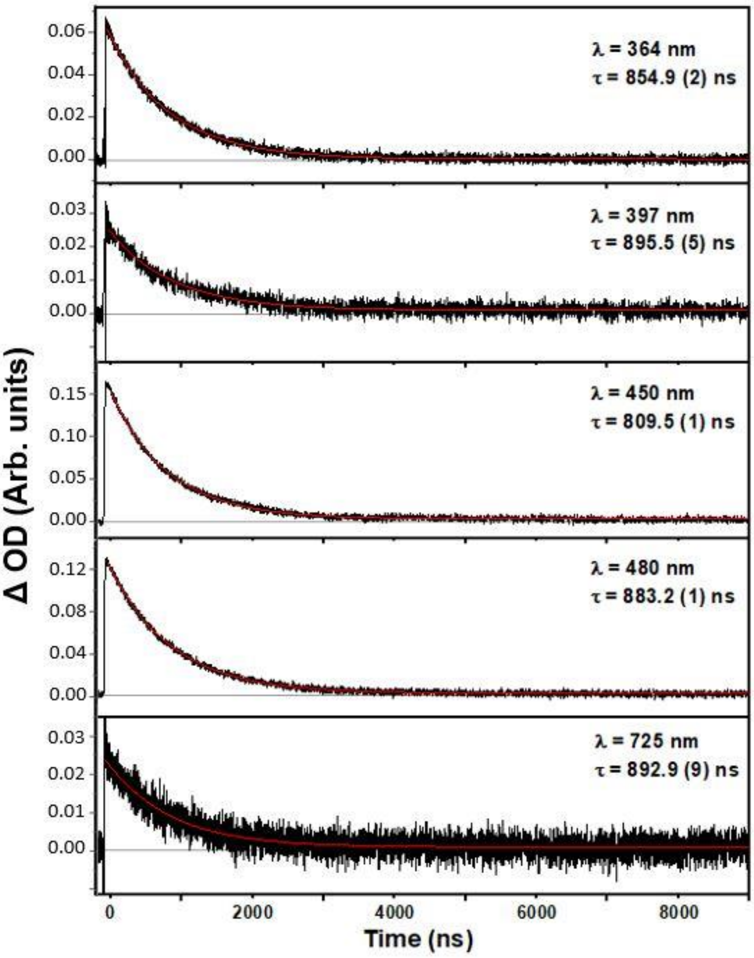

Figure 5.22 Transient kinetic traces of the major transient absorption features of the NPhPipNMI compound in aerated DCM (1x10^{-5} M). All are fitted to mono-exponential decay function. Wavelengths and lifetimes of each trace are inset.

As seen above, all transient traces bear similar lifetimes to each other and each feature can be fit to a mono-exponential decay function, suggesting a single state of origin. The kinetics do not appear to show any evidence of an additional singlet-to-singlet process or any other process. The average lifetime is found to be 0.85 µs under ambient conditions and remarkably increases to 8 µs in the degassed solution.

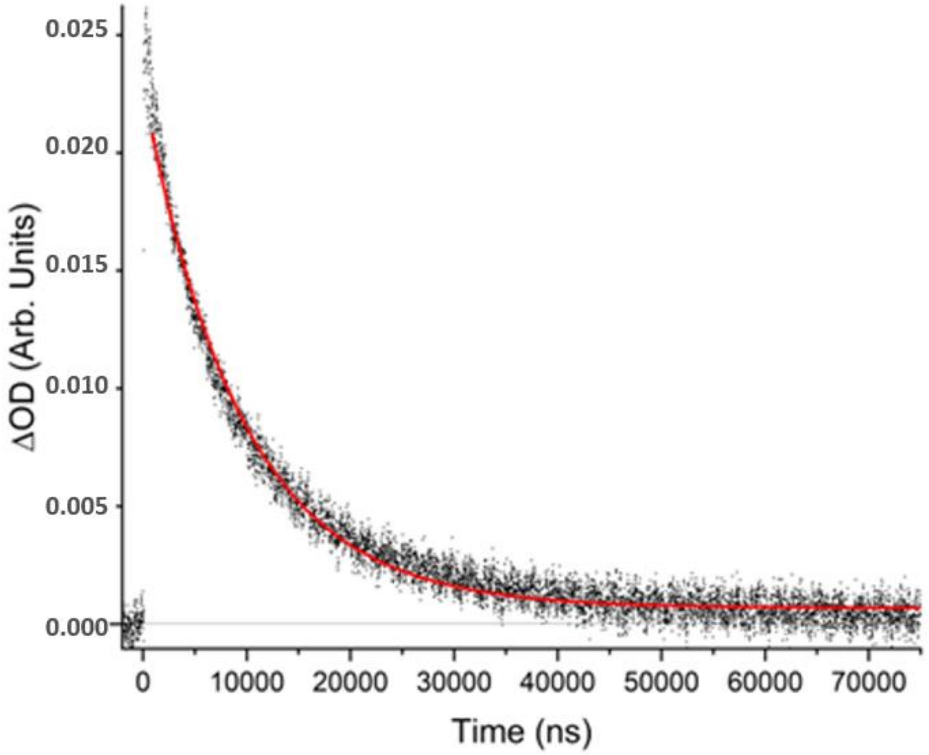

Figure 5.23 The transient absorption kinetics at 480 nm for NPhPipNMI in degassed DCM (1x10^{-5} M).

For the thionated molecules, the average lifetimes of transient absorption features in degassed toluene are 2.45 µs and 0.6 µs for N-PhPipNMI-S2 and N-PipNMI-S, respectively.

Kinetic emission measurements of the prompt fluorescence were performed in both solvents under different conditions, and the results are displayed in figures 5.24 and 5.25 below.

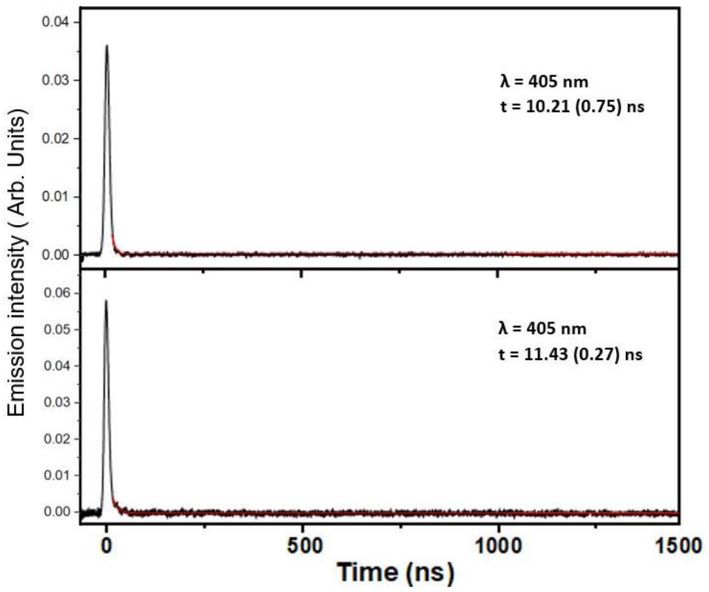

Figure 5.24 Kinetic traces of the emission of N-PhPipNMI in aerated (top) and degassed (below) toluene. The wavelengths and lifetimes of each trace are inset.

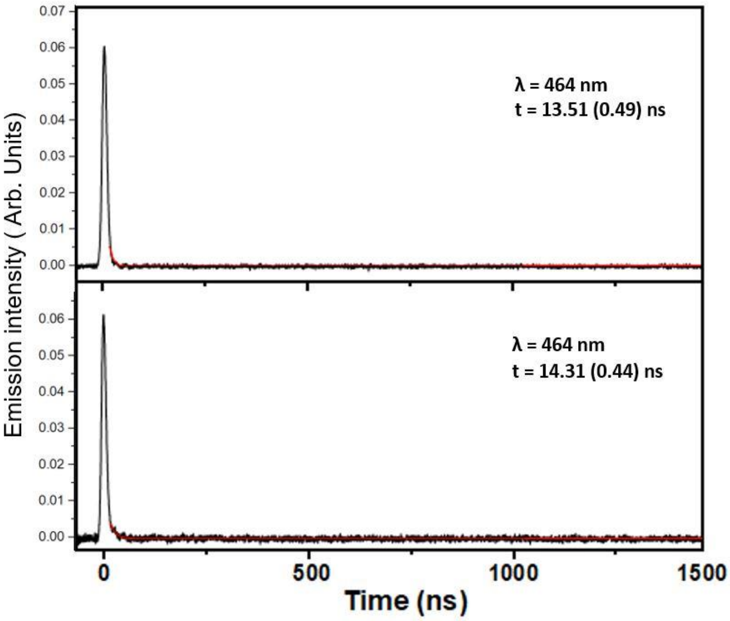

Figure 5.25 kinetic traces of the emission feature of N-PhPipNMI in aerated (top) and degassed (below) DCM (1x10^{-5} M). The wavelengths and lifetimes of each trace are inset.

As can be seen, the spectra all display identical sharp profiles with fast decay to the baseline. Each kinetic feature was fitted to a mono-exponential decay function, giving average lifetimes of 10.2 ns and 13.5 ns in deaerated toluene and DCM, respectively. These values are comparable with fluorescence lifetimes reported in naphthalimide dyads, which means that these measurements are reasonable, although they are only a few nanoseconds longer than the pulse width of the excitation laser. The emission lifetime did not exhibit a noticeable change when recorded in degassed or frozen solvents, emphasising the assignment of this feature to prompt fluorescence. These measurements did not display any signs of long-lived emissions although the presence of the TADF and phosphorescence have been proven by using the ICCD. As explained early in this chapter, the PMT's sensitivity had to be reduced to prevent damaging the detector by the very high intensity of the prompt fluorescence, making it difficult for the PMT to respond to the small signal from the delayed emissions. Therefore, an attempt was made to estimate the lifetime utilizing the gating function in the ICCD detector. In this way, the ICCD was gated to avoid the prompt fluorescence and then multiple measurements were taken at different time steps. This affords a rough estimate of the lifetime of the delayed emission even in the presence of the incredibly intense prompt fluorescence. This approach has been applied for NPhPipNMI in degassed and aerated DCM solvent, and the results are shown in figure 5.26. The spectra clearly show an increase in the delayed fluorescence in deoxygenated solutions with the lifetime being approximately 10 µs.

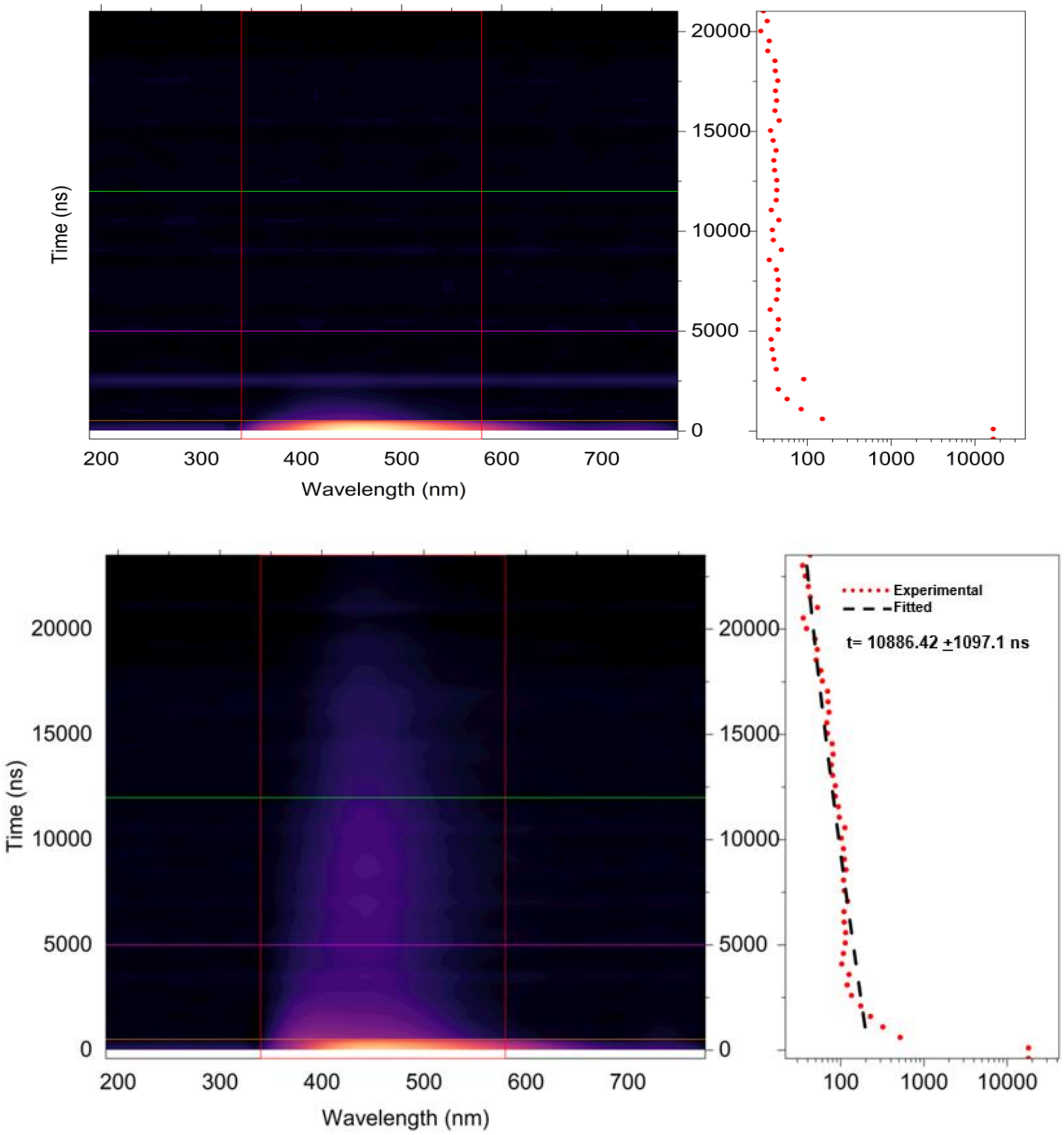

Figure 5.26 Time resolved emission spectra heat maps of N-PhPipNMI in aerated (top) and degassed (below) DCM (1x10^{-5} M) with approximate lifetime on the right as a mean of the region enclosed in the red box.

5.7 DFT

DFT calculations using the B3LYP/6-31G* level of theory were used to optimize each of the above compounds in the lowest electronic singlet state. Calculations were performed within implicit toluene or DCM solvents (IEFPCM), consistent with the spectroscopic measurements. The compounds all exhibit a near orthogonal geometry with a dihedral angle close to 90^{o} in both solvents, albeit DCM displays a slight decrease in the dihedral angle compared with toluene. Therefore, these complexes are more likely to show a small energy difference between singlet and triplet excited states Δ_{ST} and thus more efficient ISC. The computed structures are presented in figure 5.27.

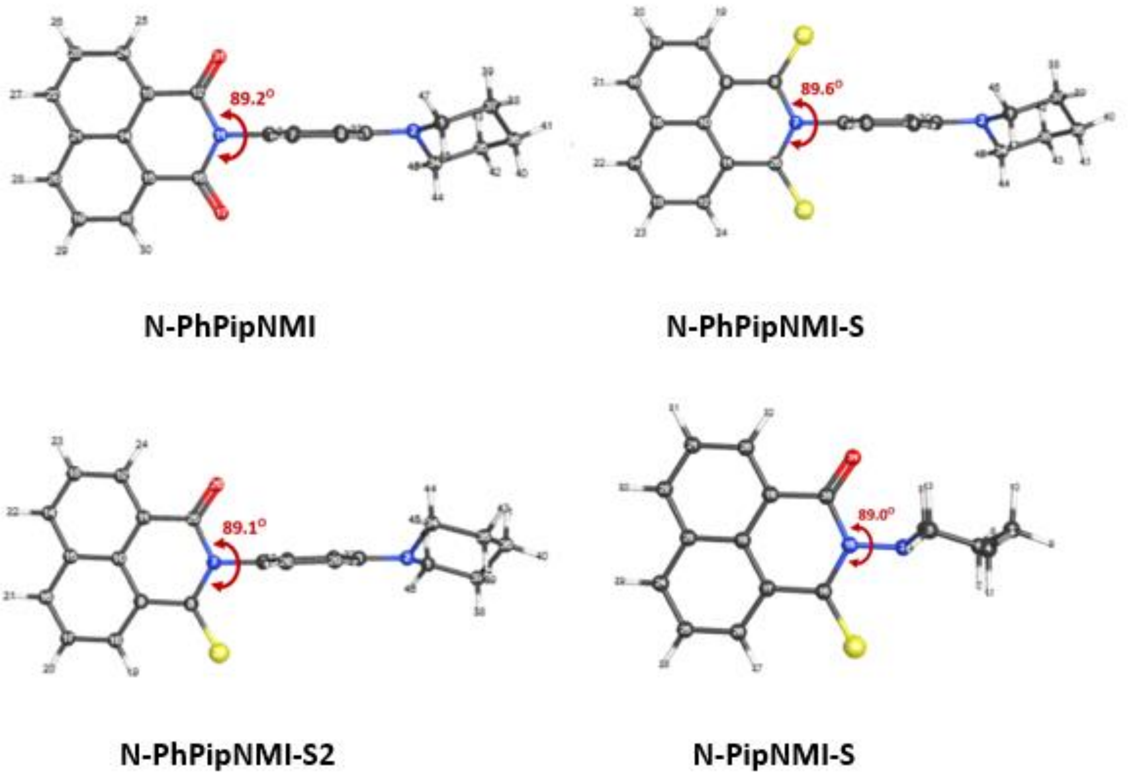

N-PhPipNMI **N-PhPipNMI-S**

N-PhPipNMI-S2 **N-PipNMI-S**

Figure 5.27 Computed structures of the four compounds studied in this chapter. The dihedral angle ϑ between the donor-acceptor moieties is inset.

5.8 Molecular orbital decomposition and TDDFT

Molecular orbital decomposition analysis was performed on the computed singlet state geometries within an implicit toluene solvent (IEFPCM), consistent with the spectroscopic measurements, with the aim of analysing the processes and transitions involved in the experimental spectra, and examining the effects that the thionation has on the electronic structure of the molecules. TD-DFT with the CAM-B3LYP functional were also carried out from the optimized singlet ground states of the complexes to identify singlet and triplet electronic transitions seen in experimental data and to simulate the absorption spectra.

5.8.1 N-PhPipNMI

The renderings of frontier molecular orbitals of the singlet ground state of N-PhPipNMI in toluene can be seen in figure 5.28 below.

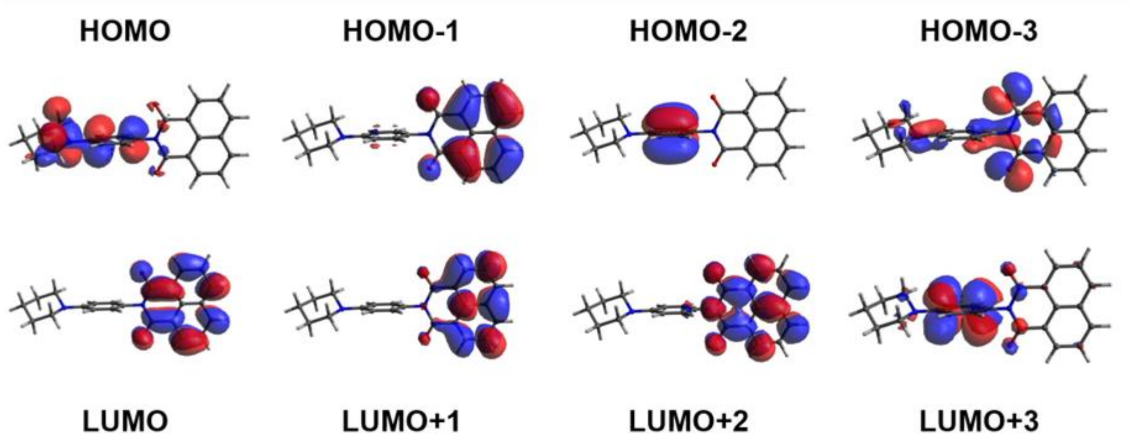

Figure 5.28 Calculated Kohn-Sham frontier molecular orbitals for N-PhPipNMI in toluene.

Molecular orbital decomposition analysis predicts that the HOMO for the N-PhPipNMI compound in toluene is located predominantly in the donor unit (PhPip) of the dyad; whilst the HOMO-1 is found to be located mainly on the naphthalimid moiety. The HOMO -2 is entirely located on the phenyl ring in the donor unit. In contrast, the lowest three unoccupied molecular orbitals are predominantly localised on the naphthalimide unit and the LUMO+3 is centred on the phenyl ring of the donor unit, suggesting both LE and CT transitions can occur in this compound. In order to study the effect of the solvent polarity has on the electronic structure, the same analysis on the singlet ground state was carried out in DCM. The results show identical electron distribution in the frontier orbitals to those found in toluene, although the energies of both the HOMOs and LUMOs are more stabilised in DCM.

The results of the singlet TD-DFT calculations for the lowest six singlet excited states are shown below in table 5.1, and the simulated spectrum using GaussView is presented in figure 5.29. The broadening is artificial in the simulated spectra, and is intended as a guide to the eye, to allow for the comparison of datasets.

Table 5.1 The wavelength, force oscillator strengths and contributing molecular orbital transitions of the first six singlet-to-singlet excited states for N-PhPipNMI. Molecular orbital contributions less than 10% have been omitted for clarity.

N-PhPipNMI	
Excited State	**Orbital Contribution to Excited State Contributing Transitions (> 10 %)**
1 (316 nm f=0.0003)	HOMO → LUMO (89.75%)
2 (306 nm f=0.4100)	HOMO-1 → LUMO (97.00%)
3 (287 nm f=0.0545)	HOMO -3 → LUMO (76.54%) HOMO -1 → LUMO +1 (18.50%)
4 (285 nm f=0.0012)	HOMO -6 → LUMO (10.53%) HOMO -4 → LUMO (56.23%)
5 (264 nm f=0.0001)	HOMO -7 → LUMO (70.33%) HOMO -4 → LUMO +2 (13.86%)
6 (251 nm f=0.0369)	HOMO -2 → LUMO +4 (10.01%) HOMO → LUMO +3 (80.21%)

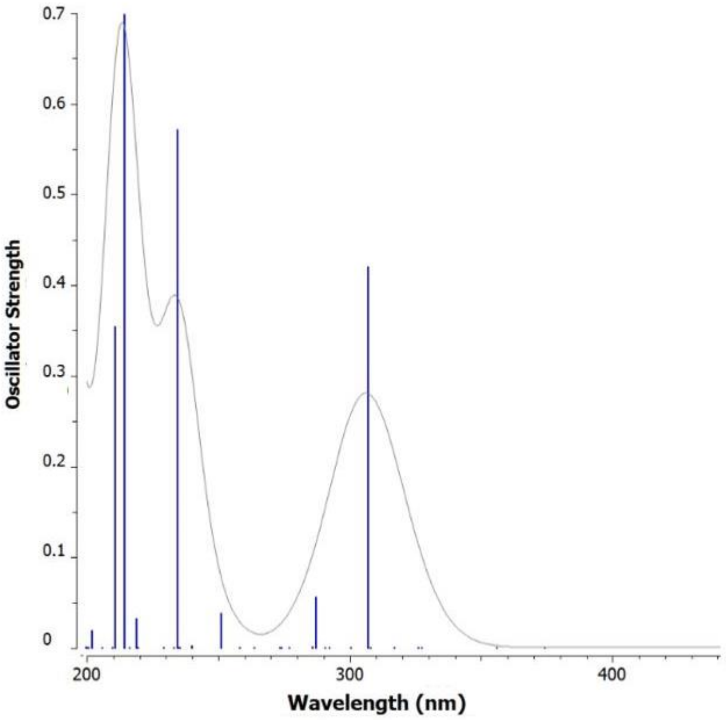

Figure 5.29 Simulated steady state absorption spectrum of N-PhPipNMI

As can be observed above, the simulated spectrum does not quantitatively match the experiment, as the calculation overestimates the energy of the features, leading to a significant hypsochromic shift. However, it is in a good qualitative agreement. The first predicted transition is at 316 nm with extremely low oscillator strength (f=0.0003) attributed to CT between HOMO and LUMO. The low oscillator strength is likely due to the low wavefunction overlap expected between PhPip (HOMO) and naphthalimide (LUMO), given their spatial separation due to an orthogonal geometry. This transition is barely observed in the computed spectrum and seen as a very weak tail at around 400 nm in the experimental spectrum. This followed by very intense transitions (f= 0.4100) at 303, 236 and 215 nm arising from orbitals localized at the naphthalimide moiety. The strong transitions can be assigned to absorption bands observed between 300 - 350 nm in the UV-Vis spectrum.

5.8.2 Thionated derivatives

Figure 5.30 below displays the renderings of the orbitals for N-PhPipNMI-S.

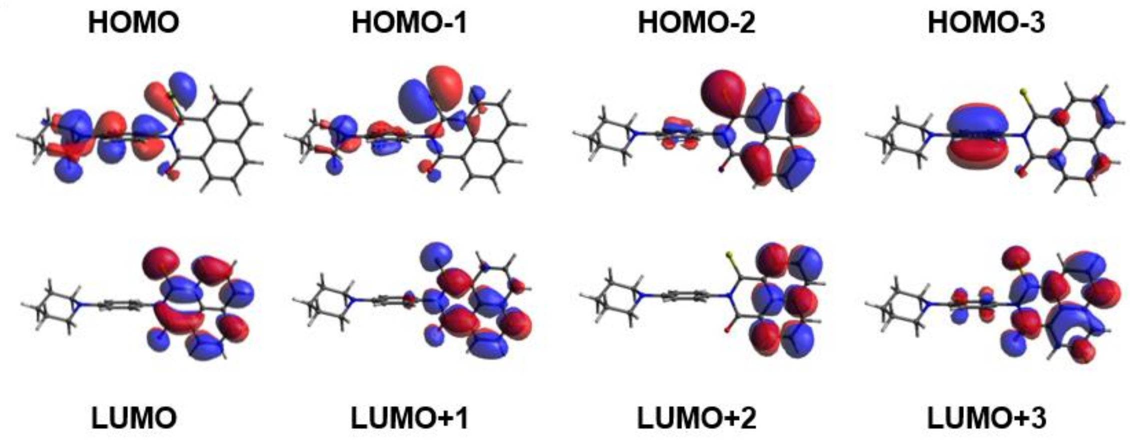

Figure 5.30 Calculated Kohn-Sham frontier molecular orbitals for N-PhPipNMI-S in toluene.

It is clear from the above figure that replacing the carbonyl group with C=S, leads to a change in the electronic structure of the molecule. For example, unlike the C=O group, the thiocarbonyl orbitals contribute effectively to the HOMO along with the contributions from the donor units. The HOMO-1 displays the greatest change from the thionation; although it was located entirely on the naphthalimide moiety in N-PhPipNMI, it is now localised mainly in the C=S unit with a smaller contribution from the PhPip moiety. The LUMO orbitals are almost identical to those observed in the non-thionated compound, save for the LUMO+2 that is located in the naphthalene core but not in C=S nor C=O. The contribution from the thiocarbonyl unit reduces the energy gap between HOMO and LUMO, leading to the red shift notice in the experimental spectra, as in table 5.2 below.

Table 5. 2 Energies of the singlet state frontier orbitals of the naphthalimide dyads

compound	**HOMO energy (eV)**	**LUMO energy (eV)**	**ΔE**
N-PhPipNMI	-5.305	-2.35	2.955
N-PhPipNMI-S	-5.229	-2.74	2.489
N-PhPipNMI-S2	-5.127	-3.07	2.057
N-PipNMI-S	-5.503	-2.778	2.725

These observations seem to be repeated in the dithionated compound N-PhPipNMI-S2 with the contribution from both thiocarbonyl groups, as shown in figure 5.31 below.

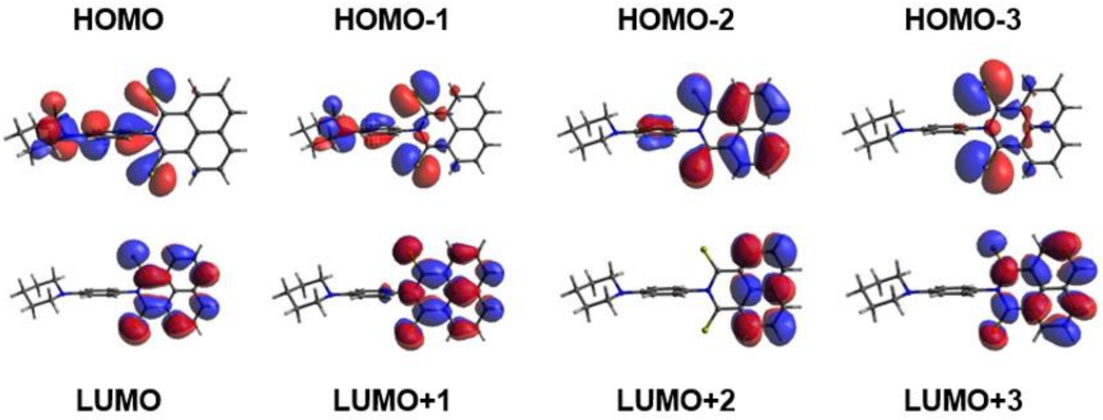

Figure 5.31 Calculated Kohn-Sham frontier molecular orbitals for N-PhPipNMI-S2 in toluene

Once again, the rendered molecular orbitals of the singlet ground state of N-PhPip-S, displayed in figure 5.32, show the same motif as the other variants, as the unoccupied orbitals predominantly arise from the naphthalimide moiety. For the occupied orbitals, HOMO and HOMO-2 are located in the piperidine ring and C=S group, whilst HOMO-1 and HOMO-3 are centred predominantly on the naphthalimide molecule. These results suggest that the electronic structure of the N-PhPipNMI molecule is not significantly perturbed by the thionation.

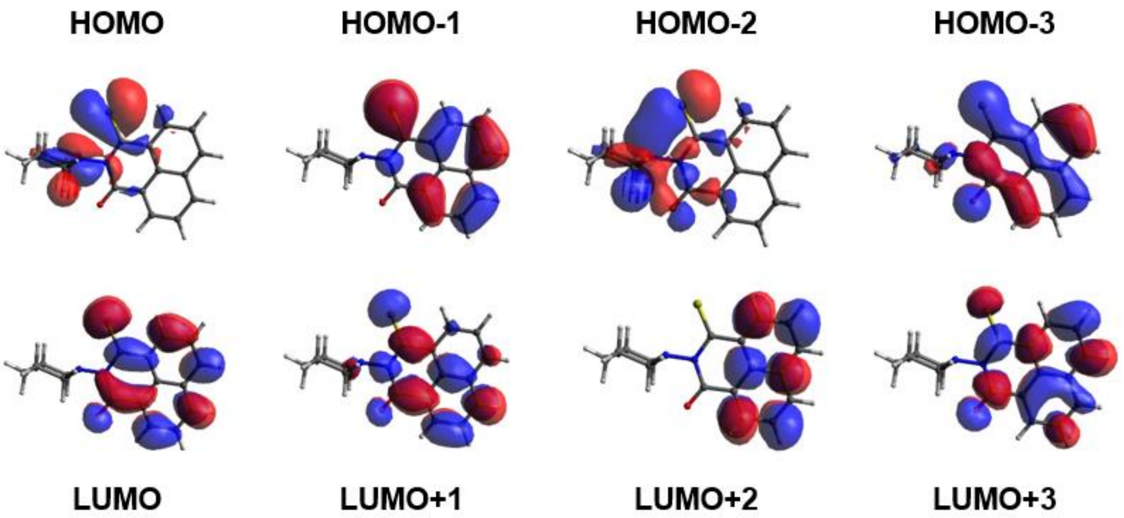

Figure 5.32 Calculated Kohn-Sham frontier molecular orbitals for N-PipNMI-S in toluene.

TD-DFT calculations for the lowest six singlet excited states of N-PhPipNMI-S are shown below in table 5.3, and the simulated spectrum is displayed in figure 5.33.

Table 5.3 The wavelength, force oscillator strengths and contributing molecular orbital transitions of the first six singlet-to-singlet excited states for N-PhPipNMI-S. Molecular orbital contributions less than 10% have been omitted for clarity

N-PhPipNMI-S	
Excited State	**Orbital Contribution to Excited State Contributing Transitions (> 10 %)**
1 (506 nm f=0.0001)	HOMO -3→ LUMO (54.86%) HOMO → LUMO (31.15%)
2 (361 nm f=0.4325)	HOMO-1 → LUMO (91.17%)
3 (357 nm f=0.0334)	HOMO -2 → LUMO (26.11%) HOMO → LUMO (58.58%)
4 (303 nm f=0.0362)	HOMO -5 → LUMO (37.17%) HOMO -4 → LUMO (43.30%)
5 (287 nm f=0.0019)	HOMO -7 → LUMO (59.90%) HOMO -6 → LUMO (11.38%)
6 (286 nm f=0.2120)	HOMO -5 → LUMO (40.03%) HOMO -4 → LUMO (31.32%) HOMO -3→ LUMO (15.75%)

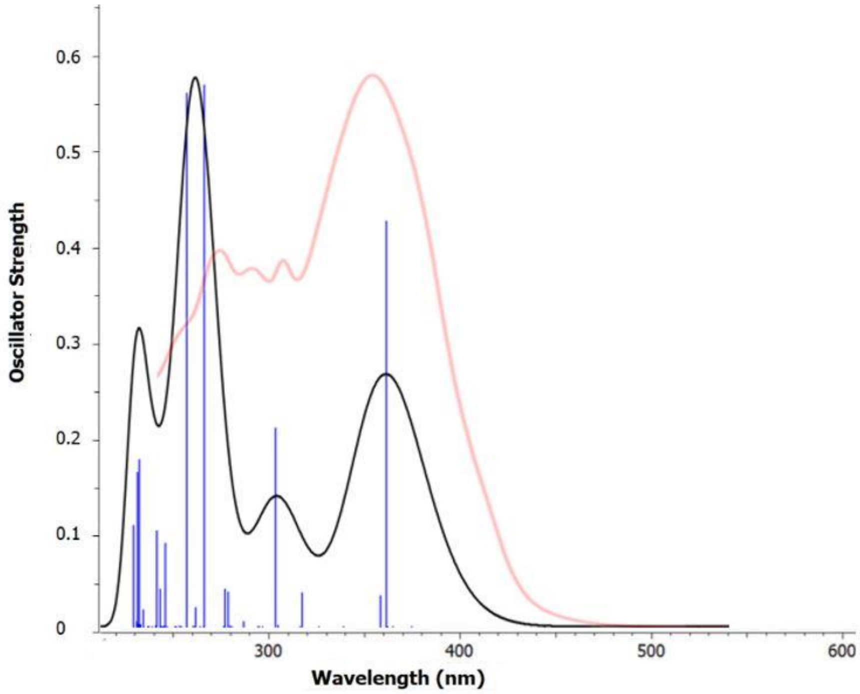

Figure 5.33 Comparison of TD-DFT simulated (black) and experimental (red) absorption spectra of N-PhPipNMI-S . A shift by +50 nm was applied to the calculated spectrum for ease of comparison.

As seen in the above figure, an additional absorption feature with large oscillator strength is predicted to occur at lower energy than that for the base compound, which nicely matches the experimental results. The new band is expected at 361 nm from electron transitions from HOMO-1 and LUMO which are dominated by the thiocarbonyl group and naphthalimide moiety, respectively; indicating that this transition has *nπ*** character. An intramolecular charge transition character is expected in this band since the donor unit has a small contribution to the HOMO-1. This new band is predicted to exhibit a further red shift in the dithionated molecule N-PhPipNMI-S2, which is again in agreement with experiments. The singlet TD-DFT calculations for the N-PhPipNMI-S2 compound are shown in table 5.4 and figure 5.34.

Table 5.4 The wavelength, force oscillator strengths and contributing molecular orbital transitions of the first six singlet-to-singlet excited states for N-PhPipNMI-S2. Molecular orbital contributions less than 10% have been omitted for clarity

N-PhPipNMI-S2	
Excited State	**Orbital Contribution to Excited State Contributing Transitions (> 10 %)**
1 (622 nm f=0.0002)	HOMO -3 → LUMO (31.87%) HOMO → LUMO (58.27%)
2 (486 nm f=0.000)	HOMO -4→ LUMO (76.74%) HOMO -2→ LUMO +1(10.10%)
3 (400 nm f=0.4930)	HOMO -1 → LUMO (96.67%)
4 (392 nm f=0.0134)	HOMO -2 → LUMO (50.13%) HOMO → LUMO (36.68%)
5 (355 nm f=0.2048)	HOMO -6 → LUMO (84.17%)
6 (316 nm f=0.1524)	HOMO -3→ LUMO (97.65%)

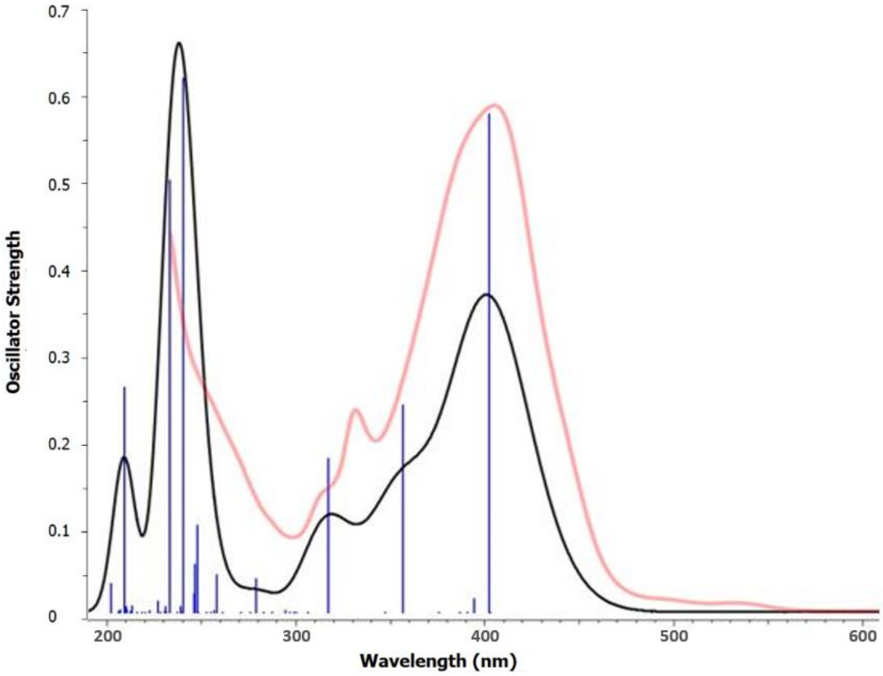

Figure 5.34 Comparison of TD-DFT simulated (black) and experimental (red) absorption spectra of N-PhPipNMI-S2 . A shift by +50 nm was applied to the calculated spectrum for ease of comparison.

The simulated spectrum of N-PipNMI-S, shown in figure 5.35, is identical to that for N-PhPipNMI-S2, with the lowest singlet transitions predicted at 361 nm, in accordance with experimental results. This transition originates from the HOMO-1 orbital and proceeds to LUMO, suggesting *nπ** character mixed with a small amount of CT.

The simulated spectra in all four compounds were generated from TD-DFT of singlet transitions, suggesting that the features in steady-state absorption spectra arise from the singlet ground state.

Table 5.5 The wavelength, force oscillator strengths and contributing molecular orbital transitions of the first six singlet-to-singlet excited states for N-PipNMI-S. Molecular orbital contributions less than 10% have been omitted for clarity.

N-PipNMI-S	
Excited State	**Orbital Contribution to Excited State Contributing Transitions (> 10 %)**
1 (542 nm f=0.0000)	HOMO → LUMO (80.30%)
2 (361 nm f=0.4326)	HOMO-1 → LUMO (97.87%)
3 (348 nm f=0.0001)	HOMO -2 → LUMO (82.38%)
4 (303 nm f=0.0328)	HOMO -4 → LUMO (38.08%) HOMO -3 → LUMO (47.46%)
5 (284 nm f=0.1828)	HOMO -4 → LUMO (41.15%) HOMO -3 → LUMO (47.04%)
6 (274 nm f=0.0003)	HOMO -5 → LUMO (67.45%) HOMO -6 → LUMO +1 (14.02%)

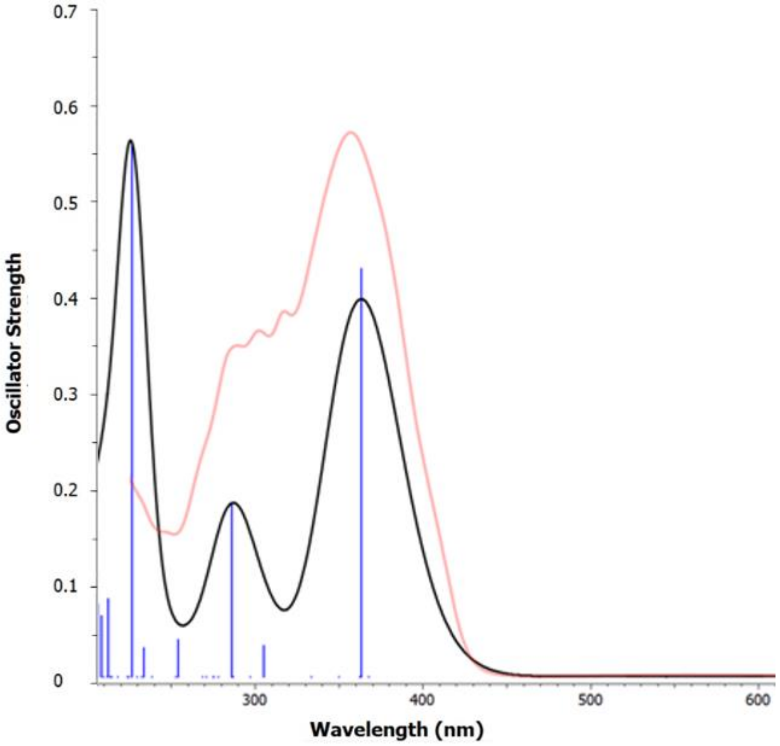

Figure 5.35 Comparison of TD-DFT simulated (black) and experimental (red) absorption spectra of N-PipNMI-S . A shift by +50 nm was applied to the calculated spectrum for ease of comparison.

The strong absorption by the thionated compounds along with the efficient production of the triplet state, make the thionated compounds good candidates for photosensitizer applications.

5.9 Conclusion

Analysis of the naphthalimide dyad and its variants has been performed using different spectroscopic techniques to confirm the formation of a triplet state with a long lifetime, that influences all spectral emission signatures. The molecular geometry and the degree of the electronic interaction between the two moieties of naphthalimide dyads play a critical role in determining the photophysical properties of these systems. The N-PhPipNMI dyad shows thermally activated delay fluorescence overlapped with prompt fluorescence, in both toluene and DCM solvents, which significantly increased in degassed solutions. The presence of room temperature phosphorescence in toluene was evidenced by performing emission measurement at low temperatures, 77K. It appears that restricting the molecular motion and vibration in frozen solutions remarkably enhances phosphorescence. It was found that increasing the solvent polarity quenches RTP and enhances TADF due to the stabilization of the CT state. The thionation of the carbonyl group has a significant effect on singlet excited states as it was found to reduce the LUMO energy leading to a red shift in the absorption bands, and quenching the prompt fluorescence. Conversely, no significant change was observed in the triplet state upon the thionation. Spectroscopic analysis was in good agreement with findings from the literature. DFT calculations nicely reproduce the absorption bands, predicting the change in relative intensities and the bathochromic shift observed experimentally upon the thionation, providing a good insight into the electronic transitions responsible for spectral features. More kinetic studies are required to accurately measure emissions lifetimes. Temperature-dependent measurements are also important to determine if TADF exists in thionated compounds.

The analysis of N-PhPipNMI can be utilized for the rational design of organic emitters with desirable photochemical properties for future applications. As previously discussed, freezing the rotation between the donor and acceptor units enhances direct phosphorescence emission while reducing the likelihood of the opposite TADF process. Therefore, one possible approach to achieve high RTP is to introduce large substitution groups to the molecular structure to restrict intramolecular rotation. Scheme 5.2 presents proposed structures for new N-PhPipNMI variants that are expected to exhibit strong RTP.

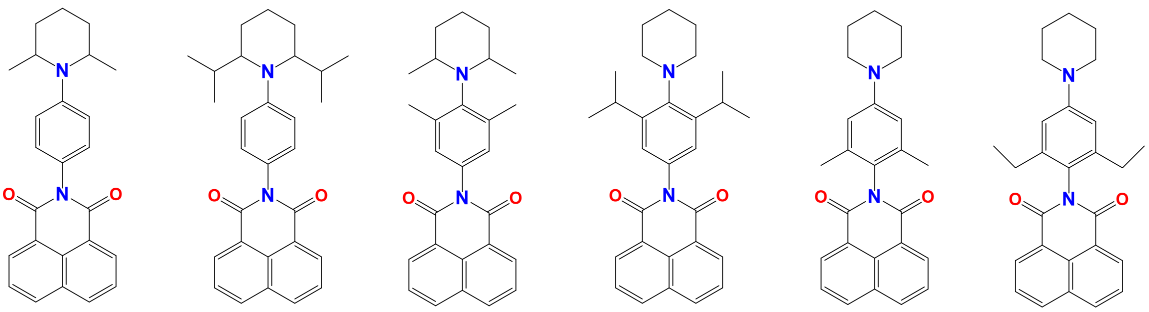

P1 **P2** **P3** **P4** **P5** **P6**

Scheme 5.2 Proposed structures for new N-PhPipNMI variants that are expected to exhibit strong RTP.

It is expected that the side groups will work as a steric hindrance, restricting intramolecular rotations and reducing rISC while enhancing RTP. Indeed, at the end of this project, the proposed structure **P4** was synthesized by Anna Wright and analyzed by Liam McGrath from the Beames group. The emission spectrum of **P4** was recorded in DCM at room temperature, and displayed a single emission band with clear vibrational structures, consistent with the emission profile of the parent compound N-PhPipNMI recorded in toluene. However, when performing the measurements at low temperature, the emission spectra display an additional emission feature at long wavelengths, ca. 610 nm, as shown in figure 5.36. This new peak did not appear in the emission spectra of the parent compound N-PhPipNMI recorded under the same conditions (DCM solvent and low temperature). The new emission band looks characteristic of phosphorescence, with a lifetime of a few microseconds (figure 5.37), suggesting that side groups play a role in restricting molecular rotation and thus reducing rISC and enhancing phosphorescence.

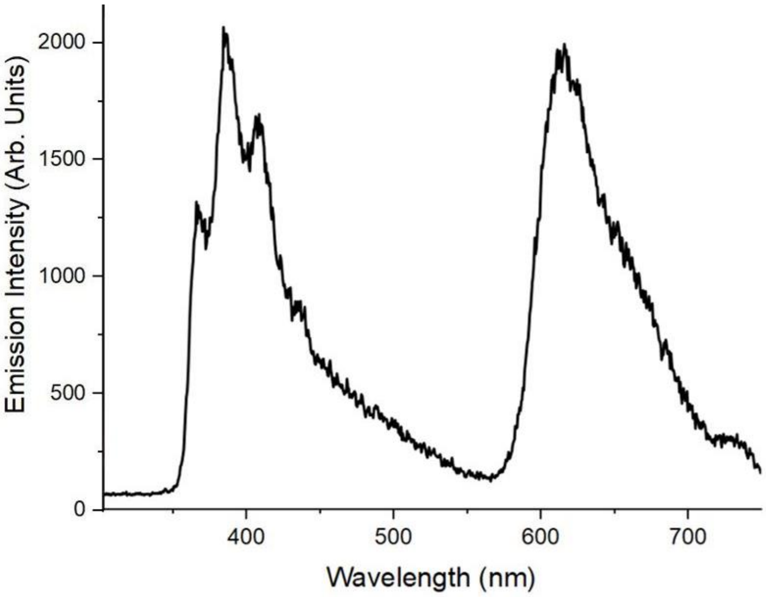

*Figure 5.36 Emission spectra of **P4** in DCM at low temperature*

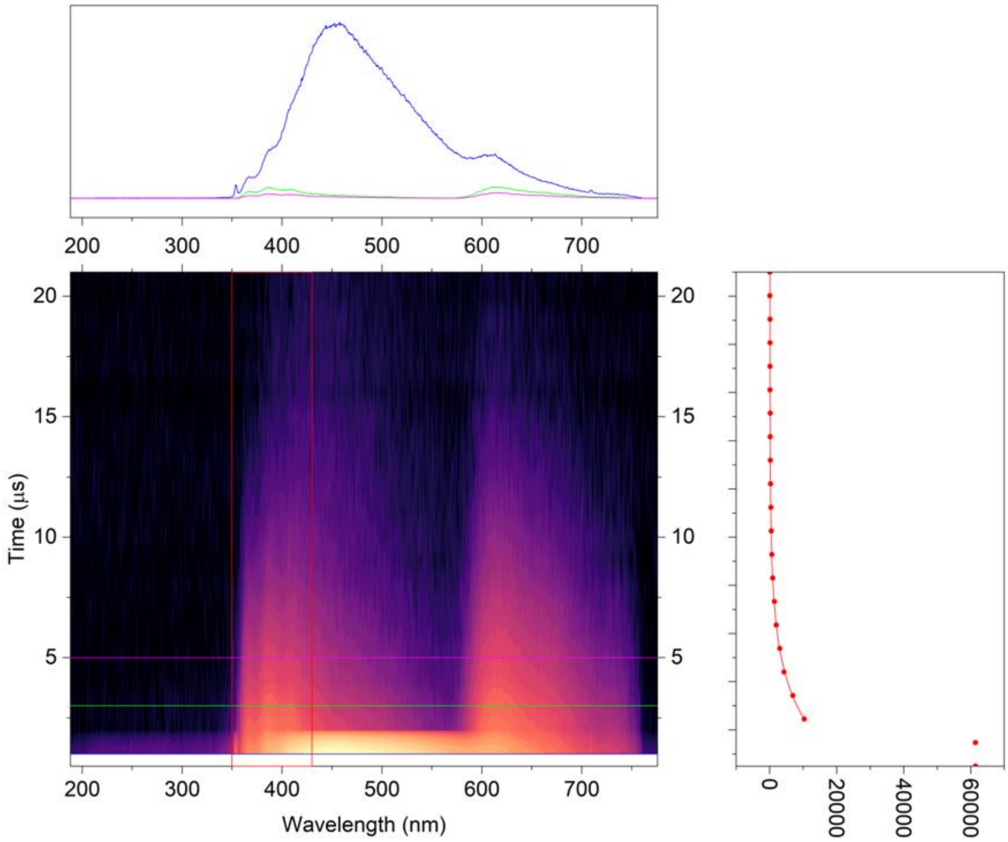

*Figure 5.37 Time resolved emission spectra heat maps of **P4** in degassed DCM (1x10^{-5} M) with both time slices above showing spectra at multiple time steps 0 µs, 3 µs and 5 µs with approximate kinetics on the right as a mean of the region enclosed in the red box with a lifetime of 2.3 µs.*

As in the case of N-PhPipNMI, the emissive triplet state in the **P4** compound is dominated by locally excited triplet state, ^{3}LE, character with a small contribution from charge-transfer triplet state, ^{3}CT, given the orthogonal geometry of the dyad and the restriction of molecular rotation. This was confirmed using electron paramagnetic resonance measurements (EPR), similar to those of Drummond et al. (Drummond et al. 2021) as displayed in figure 5.38.

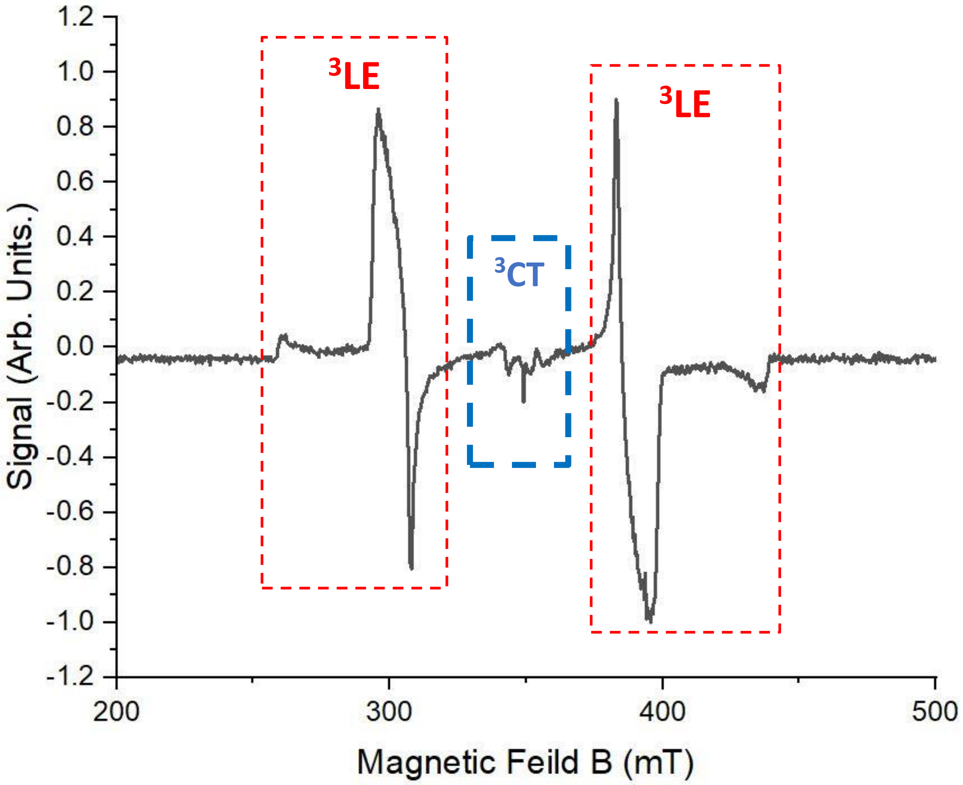

Figure 5.38 Transient EPR spectrum of the triplet states of the ***P4*** *dyad in degassed DCM (1x10^{-5} M).*

Figure 5.38 shows a transient EPR spectrum of dyad P4, recorded on a Bruker E580 pulsed EPR spectrometer. The signal was recorded in pulsed mode, at a laser-EPR delay time of 100 ns, and in a frozen solvent (acetonitrile) matrix at 10 K. The spectrum shows two distinct spin systems (shown in the overlaid boxes), both centred around free spin. The two spin systems can be assigned based on their zero field splitting parameters, following a similar procedure to those reported by Drummond et al. The spin system that gives rise to the wider spectral features and which shows the greatest EPR intensity has been assigned on the basis of SOC-DFT calculations and in comparison with the Drummond work to arising from a ^{3}LE state which is indicative of ISC in these dyad systems (the spin-state populations alongside the D-frame tensor can also be used to infer these processes). The ^{3}CT spin system that is also observed has substantially different zero field splitting parameters and is much less EPR-active. Again Drummond et al. observed evidence of a weak ^{3}CT state. These two systems have been modelled using EPR simulations to generate spin state populations along with zero field splitting parameters, but this is beyond the scope of this thesis. The combination of these two signals is characteristic of these dyads.

6. The Development of a Fluorescence Polarization Spectrophotometer

6.1 Introduction and Background

Fluorescence polarization (FP) or fluorescence anisotropy (FA) is a powerful analytical technique that allows the studying of molecular interactions and binding processes in solution by monitoring how a fluorophore changes its orientation in solution as a function of the time. This time component is measured between absorption and emission events. (Jameson and Ross 2010) This technique relies on the fact that molecules or particles in solution can rotate at different rates dependent on molecular size and solution conditions, such as pH and viscosity and this is monitored by examining the polarization of the fluorescence. FP/FA measurements can provide valuable information about the binding affinity, and kinetics of a wide range of different molecular interactions, including protein-ligand, DNA-protein, and antibody-antigen interactions, where a binding event for example typically involves an increase in molecular size and therefore a reduction in the rotational period.

Fluorescence polarization was first observed by Weigert in 1920, and then developed by Perrin in 1926 who described relationships between polarization and the rotation and excited state lifetimes of fluorophores. (Perrin 1926) Later, the fluorescence polarization method rapidly gained popularity as a screening tool for studying molecular interactions in many areas of application, especially in biological research and medical testing. This is in part because FP/FA assays are nonradioactive and homogeneous and therefore can be directly carried out in solution without washing or separation steps, making the measurements faster and repetitive without destroying the samples through radiation bombardment. Moreover, it is highly sensitive, meaning it can accurately detect even the slightest changes in molecular motion, due to changing the molecular size or varying solution conditions. This is especially important for biological and medical applications, where small changes can have a big impact. Fluorescence polarization/ anisotropy has also been utilized in applications including detecting chemical contaminants in food safety and environmental screening. Likewise, the sensitivity of FP/FA measurements to the change in molecular weight allows interrogation of biological mechanisms of protein binding events and enzymatic activities, monitoring therapeutic drug levels in body fluids, and diagnosing certain diseases. The FP/FA has recently been widely adopted in high-throughput screening (HTS) and drug discovery due to its homogeneous phase, accuracy, simplicity, low cost per run, and insensitivity to environmental interferences. (Jolley 1981; Ruta et al. 2009; Lea and Simeonov 2011; Hall et al. 2016)

6.1.1 The principles of fluorescence polarization/ anisotropy measurement

The basis of FP/FA depends on the fact that the degree of polarization of fluorescent molecules in solution is inversely related to their molecular rotation during the lifetime of their excited state. (Kumke et al. 1997) In general, molecular rotation decreases with increasing molecular weight and solvent viscosity, and with decreasing temperature. In solution, a free and small fluorescent molecule, excited by linearly polarized light, rotates faster than a typical fluorescence lifetime, which results in a small polarization value (depolarized emission) (Perrin 1926; Jolley 1981; Kumke et al. 1997; Ruta et al. 2009; Lea and Simeonov 2011; Hall et al. 2016). This is described by Perrin's equation:

$$r = (r_0) / [1 + (tRT / \eta V)] \qquad \textbf{(Equation 6.1)}$$

Where r_o = the value of anisotropy at t = 0 after short pulse excitation, t =the fluorescence lifetime of the fluorophore, η = solvent viscosity, T = temperature, R = gas constant and V = molecular weight of the fluorescent molecule.

When the temperature and viscosity of the solvent are constant, the fluorescence polarization largely depends on molecular weight. The principles of emission polarization upon which this is based is described more extensively in the introduction.

6.1.2 The measurement of fluorescence polarization/ anisotropy

In steady-state polarization measurements, a fluorescent sample is placed in a cuvette and irradiated with vertically polarized light which specifically excites fluorophores that have their absorption transition moments aligned properly with the polarized incident light, as in figure 6.1. Then, the light emitted by the sample is passed through an emission polarizer, placed in the light path between the sample and detector, to separate parallel ($I_{\parallel}$) and perpendicular ($I_{\perp}$) components of the emission.

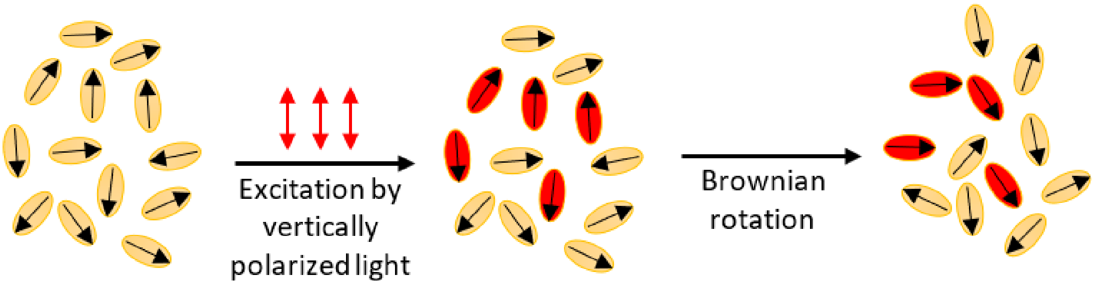

Figure 6.1 Illustration of the photo-selection of randomly oriented fluorophores using vertically polarized light, and the subsequent Brownian rotation of excited fluorophores.

Two experimental setups are typically used: the L-format method, where a single emission channel (emission polarizer and detector) is used, and the intensities of both polarized components are detected separately in two sequential measurements. The vertical (parallel) polarized intensity I_{VV} ($I_{\parallel}$)

is detected in the first measurement. Then the emission polarizer is rotated by 90° to detect the horizontally polarized emission I_{VH} ($I_\perp$). The other method is the T-format measurements, in which two separate emission channels are used to record parallel and perpendicular components,(Lakowicz 1999,2006) as shown in figure 6.2.

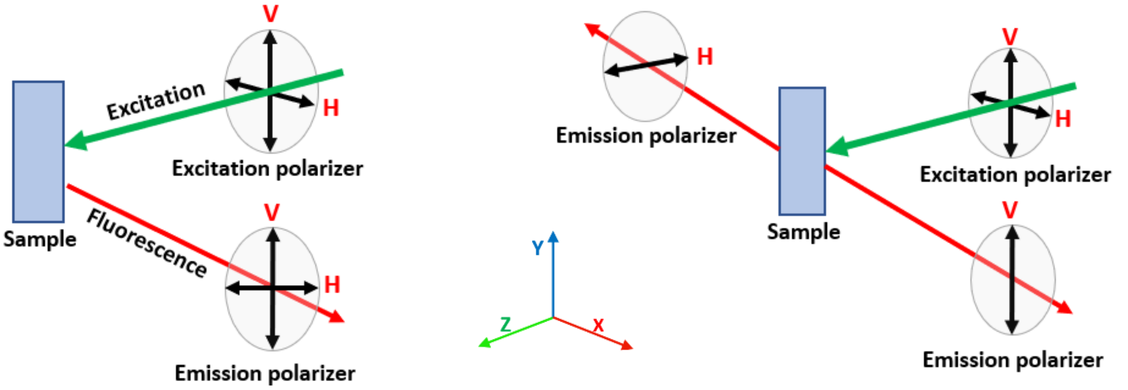

Figure 6.2 Diagram of L-format (left) and T-format (right) fluorescence polarization measurements. Vertical (V) and horizontal (H) orientations of each polarizer are shown.

Here, the X-axis is horizontal and oriented in the direction of the emission plane. The Y-axis represents the vertical direction perpendicular to the plane of emission while the Z-axis is horizontal and defined perpendicular to the X-axis. The emission polarization (***p***) and anisotropy (***r***) are calculated by normalizing the difference, $I_\parallel - I_\perp$, to the total fluorescence intensity observed by a photodetector placed along either the Y- or Z-axis, $I_\parallel + I_\perp$ (polarization), or to the total emission intensity from the sample, $I_\parallel + 2I_\perp$ (anisotropy). (Arkin et al. 2012)

$$p = (I_{\parallel} - I_\perp) / (I_{\parallel} + I_\perp) \qquad \textbf{(Equation 6.2)}$$

$$r = (I_{\parallel} - I_\perp) / (I_{\parallel} + 2I_\perp) \qquad \textbf{(Equation 6.3)}$$

Polarization and anisotropy terms are interrelated and describe the same phenomena. Clearly, anisotropy does not provide any additional information, and the relationship between ***p*** and ***r*** is given by:

$$p = 3r / (2 + r) \qquad \textbf{(Equation 6.4)}$$

$$r = 2p / (3 - p) \qquad \textbf{(Equation 6.5)}$$

Typically, fluorescence polarization is most often used in clinical chemistry and drug discovery, whereas anisotropy is more common in biophysics and biological mechanistic studies. (Correia and Detrich III 2009)

In a ‘real world’ experiment, the detection system may exhibit differential sensitivity to the vertical and horizontal components of the polarized fluorescence emission. The transmission efficiency of the grating monochromator is particularly dependent on the polarization direction of the light. Therefore, the G-factor (grating factor) is used to correct for any bias in the detection system. The G-factor is defined as the ratio of the sensitivities of the detection system for vertically and horizontally polarized light. (Lakowicz 1999,2006)

$$G = S_V / S_H \quad \textbf{(Equation 6.6)}$$

The G factor is easily determined using horizontally polarized light to excite the sample, and then subsequently collecting emission intensities when the emission polarizer is mounted horizontally I_{HH} and vertically I_{HV}. Using horizontally polarized light, both the excitation and emission components of the excited-state distribution are equal and proportional to $I_{\perp}$. Thus, measured changes between I_{HV} and I_{HH} must be due to the detection system. (Lakowicz 1999)

$$G = I_{HV}/I_{HH} \quad \textbf{(Equation 6.7)}$$

The revised equations for polarization and anisotropy incorporating the G factor term are:

$$p = (I_{//} - GI_{\perp}) / (I_{//} + GI_{\perp}) \quad \textbf{(Equation 6.8)}$$

$$r = (I_{//} - GI_{\perp}) / (I_{//} + 2GI_{\perp}) \quad \textbf{(Equation 6.9)}$$

As mentioned before, at constant temperature and solution conditions, the fluorescence polarization largely depends on molecular weight which allows one to monitor molecular interactions and bindings, such as measuring the association of proteins with DNA or other macromolecules. In this approach, a small probe molecule is labelled with a fluorescent dye, often referred to as the tracer or ligand. The molecular weight of dye-labelled molecules is small and typically less than 1,500 Da. Following the binding of this fluorescently labelled molecule to a macromolecule with molecular weight > 10,000 Da (such as a protein), its rotational rate will significantly decrease, resulting in a high degree of polarization of emitted fluorescence. Therefore, the binding of a fluorescently labelled small molecule to a protein can be monitored by the change in polarization from low to high. (Arkin et al. 2012)

The aim of this chapter is to develop a spectrofluorometer in order to construct a low-cost and highly sensitive fluorescence polarization/ anisotropy system. The spectrofluorometer will be used to monitor the change in the emission polarization of a newly synthesized dye-doped polymer due to changing the type of fluorescent as well as studying the binding interaction between colistin and the bacterial membrane of Escherichia coli.

6.2 Design of the Measurement System

Figure 6.3. below shows the L-format alignment used to build the spectrofluorometer. The pump excitation source was a Nd:YAG laser which emits a linearly polarized light beam. Two pump wavelengths (λ=355 or 532 nm) were used depending on the sample under investigation, however,

most samples used in this work were excited using 532 nm light. The nascent polarization plane of the excitation light source was found to be either horizontal (at 355nm) or vertical (at 532 nm). The instrument was equipped with a (λ/2) half-wave plate placed directly after the laser source to allow the alteration of the orientation of the linearly polarized light beam as the experiments required. A rotating Glan-Taylor polarizer was placed between the sample and the detector (PMT) and used as an emission polarizer. The polarizer is mounted in a frame that allows the user to rotate the polarizer through 360 degrees, and thus pass only the parallel or perpendicular components towards the detection system. As aforementioned, the monochromator has different transmission efficiencies for vertically and horizontally polarized light, which could result in an artificial increase or decrease in emission intensities when switching between vertical and horizontal polarization planes, and which was observed in early testing of this setup. Therefore, a depolarizing optic (liquid crystal optical diffuser) was placed between the emission polarizer and the detector to scramble the polarization of light passing from the emission polarizer. In polarization studies, the alignment of the different optical and mechanical components is a critical step that must be done before conducting quantitative analysis. Polarizers and half-wave plate should be correctly positioned in the light pathway, and precisely mounted in the vertical and horizontal orientations (set the correct angle). A series of alignment steps have been performed as described in the following section.

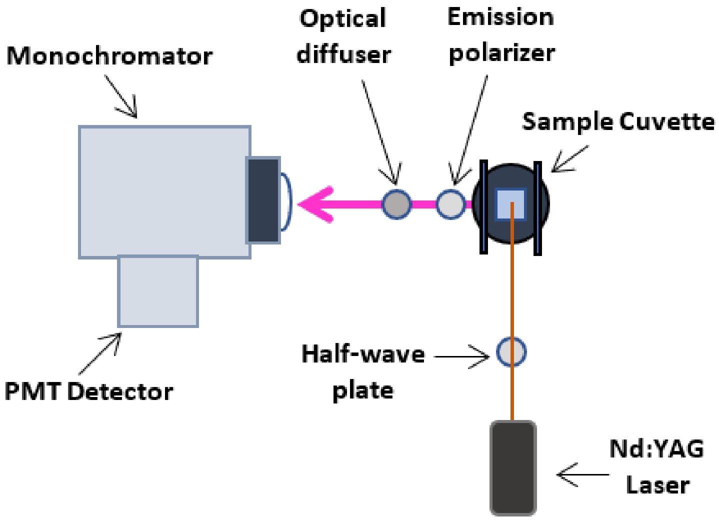

Figure 6.3 Diagram of the developed spectrofluorometer used in this work to perform FP/FA measurements.

6.2.1 Alignment of the emission polarizers and half-wave plate

The alignment of the polarizer is carried out using a dilute suspension of LUDOX (10%) to scatter the incident light, as scattered light is perfectly polarized. LUDOX is a colloidal solution that is composed of discrete, amorphous, spherical silica particles dispersed in water. It fits the criteria of an ideal

Rayleigh scatterer that is expected to show a high degree of polarization (close to 1.0) with minimal absorption of the input wavelengths (Goring 1953; Deželić and Kratohvil 1960; Zimnyakov et al. 2015). The vertically polarized laser beam at 532 nm was allowed to pass through the LUDOX solution placed in the cuvette and the intensity of the scattered light was recorded while the emission polarizer was rotated through different degree angles, as displayed in figure 6.4. Notably, the emission intensities were recorded as a function of time since the scattered light has Gaussian peak shape. The peak intensity is used in the data analysis.

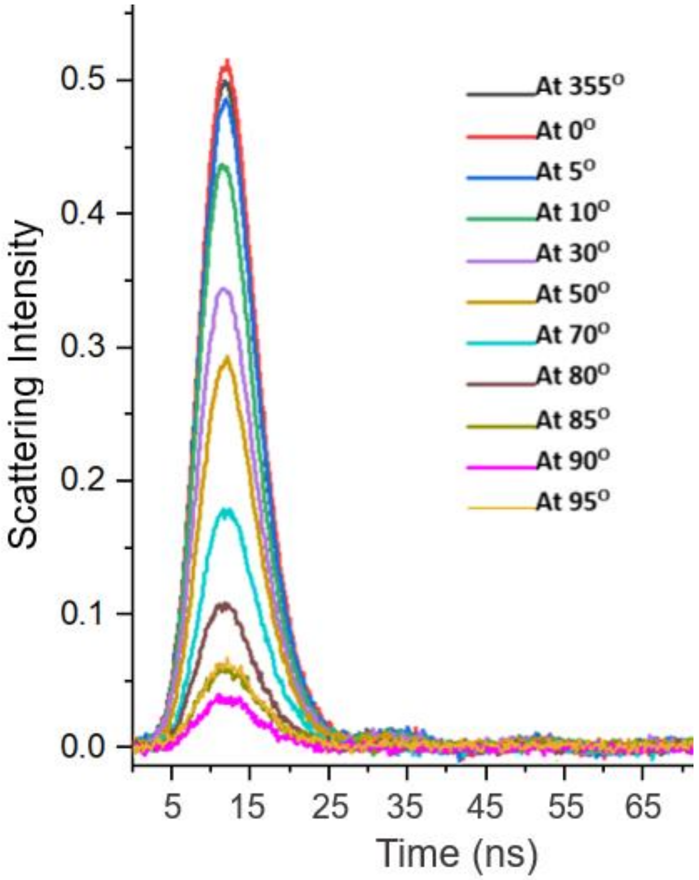

Figure 6.4 Kinetic traces of LUDOX 10% using vertically polarized light. The intensities of the scattered light were recorded while the emission polarizer was mounted at different polarization angles.

As seen in the above figure, the lowest emission intensity is observed when the emission polarizer is mounted at 90-degree angle. Therefore, this angle is considered as a horizontal (or perpendicular) orientation of emission, I_{VH} or $I_{\perp}$ since the incident light is vertically polarized. Rotating the polarizer by 90 degrees should result in the vertical orientation of emission, I_{VV} or $I_{\parallel}$, which should show the highest emission intensity. This nicely matches the spectra above which shows the highest emission intensity at 0^{o}.

Following the assignment of vertical and horizontal angles of the emission polarizer, the alignment of the half-wave plate has been checked. This was performed by rotating the half-wave plate to switch the polarization of the incident light to a horizontal orientation, and then recording the scattering intensities while the emission polarizer is mounted in parallel and perpendicular orientations. With the depolarizer in the scattering beam-path, here the detector exhibits equal scattering intensities at different orientations of the emission polarizer, $I_{\perp} = I_{\parallel}$, as in figure 6.5, indicating that different optical devices are well aligned and that with the depolarizer in the system there is minimal bias towards a particular polarization detection.

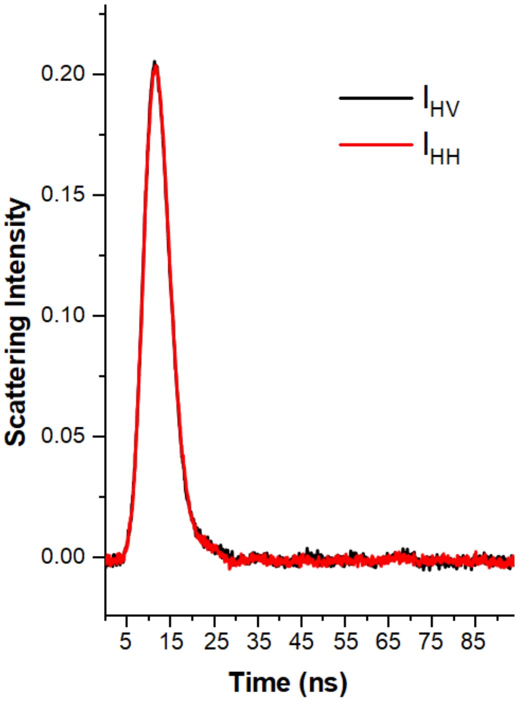

Figure 6.5 Kinetic traces of LUDOX 10% using horizontally polarized light and the intensities of the scattered light were recorded while the emission polarizer was mounted parallel and perpendicular to the incident light.

Experimentally, the alignment is considered to be satisfactory for accurate measurements when the measured polarization value is 0.97 or larger. (Lakowicz 2006) To verify the accuracy of the developed instrument described above, the vertically polarized light was passed through this dilute LUDOX solution, and the intensity of the scattered light was recorded in parallel and perpendicular orientations. The measurements were repeated after switching the incident light to the horizontal plane using the half-wave plate. Each measurement was repeated three times and then averaged. The resulting spectra are shown in figure 6.6.

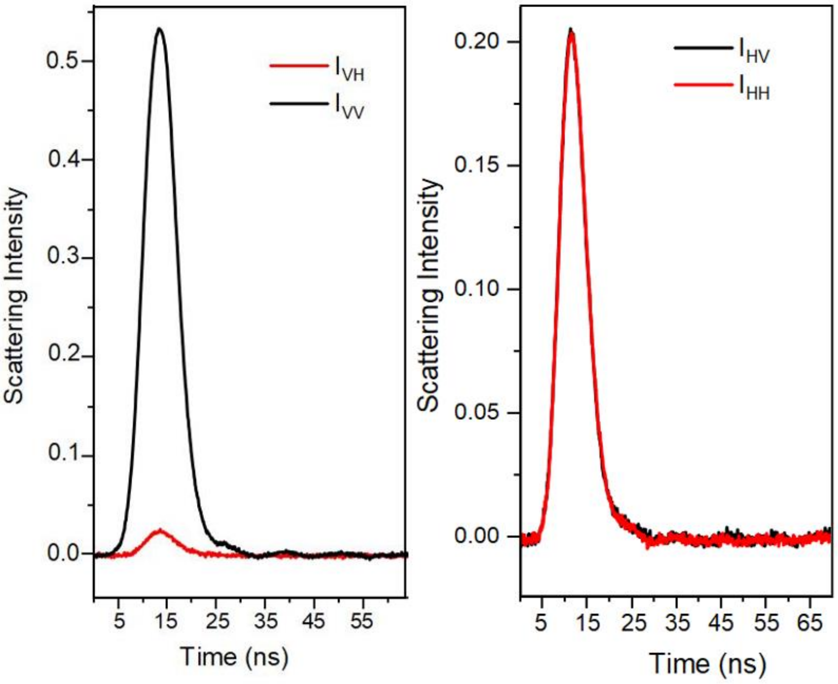

Figure 6.6 Kinetic traces of LUDOX 10% using vertically polarized light (left) and horizontally polarized light (right). In both cases, the emission intensities were recorded while the emission polarizer was mounted parallel and perpendicular to the incident light.

The fluorescence polarization and anisotropy values were calculated using equations 6.7, 6.8 and 6.9, and are found to be 0.94 and 0.92 respectively, indicative of the high sensitivity of the system to the polarization of emission. However, these values are slightly less than those typically required for conducting highly sensitive measurements, suggesting that the output of the laser used as the excitation source is not particularly clean with respect to it’s polarisation. This can be observed in figure 6.4, as the intensity of the scattered light is not completely extinct when the emission polarizer is mounted at horizontal orientation, I_{VH}. Therefore, to improve the sensitivity of the system an additional double Glan-Taylor polarizer was placed between the half-wave plate and the sample to ensure complete filtering of the unwanted light components before reaching the sample, as in figure 6.7.

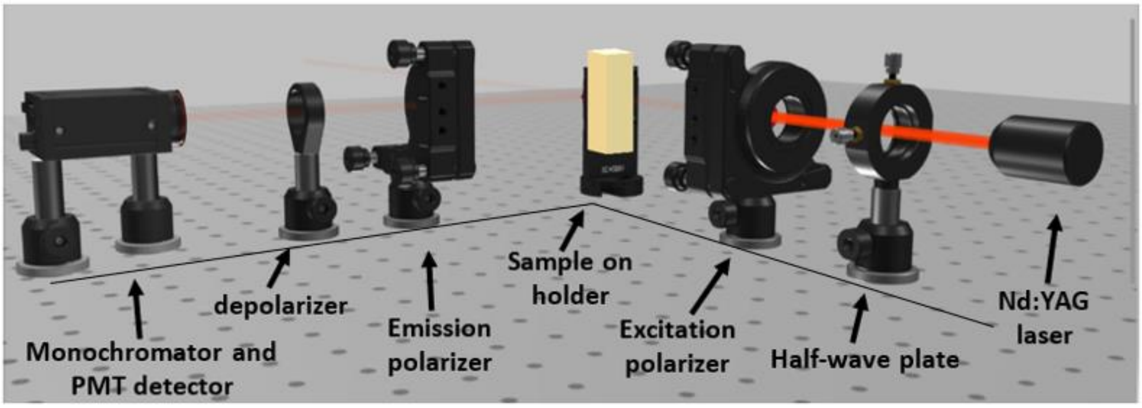

Figure 6.7 3D-Diagram of the alignment of the developed spectrofluorometer used in this work to perform FP/FA measurements.

The alignment of the excitation polarizer was performed in a similar manner to that for the emission polarizer. Here, the emission polarizer was mounted in the vertical position, and the intensity of scattered light was recording while rotating the excitation polarizer between different degree angles. The horizontal and vertical orientations of the excitation polarizer are assigned at minimum and maximum intensities of scattered light, respectively, as displayed in figure 6.8.

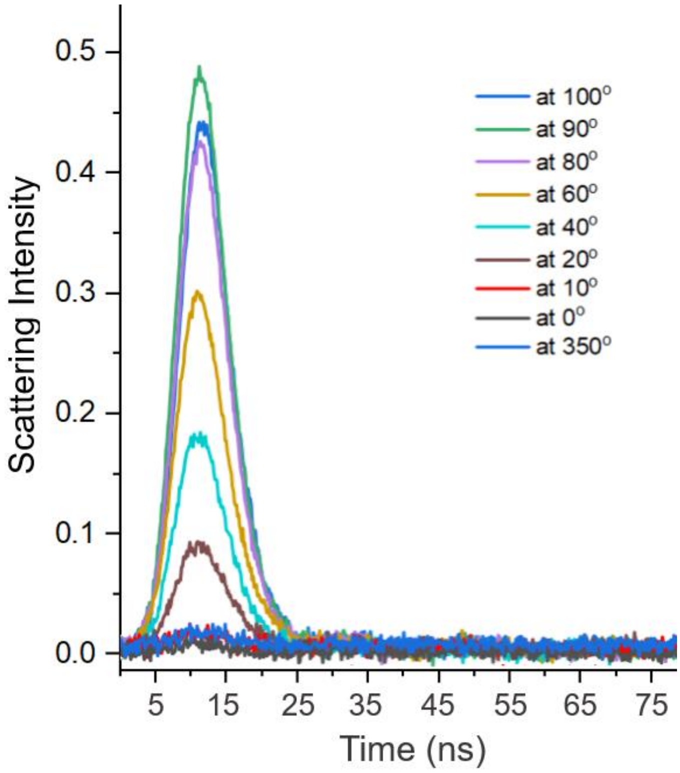

Figure 6.8 Kinetic traces of LUDOX 10% using vertically polarized light passing through the excitation polarizer. The emission intensities were recorded while the emission polarizer was mounted at different polarization angles.

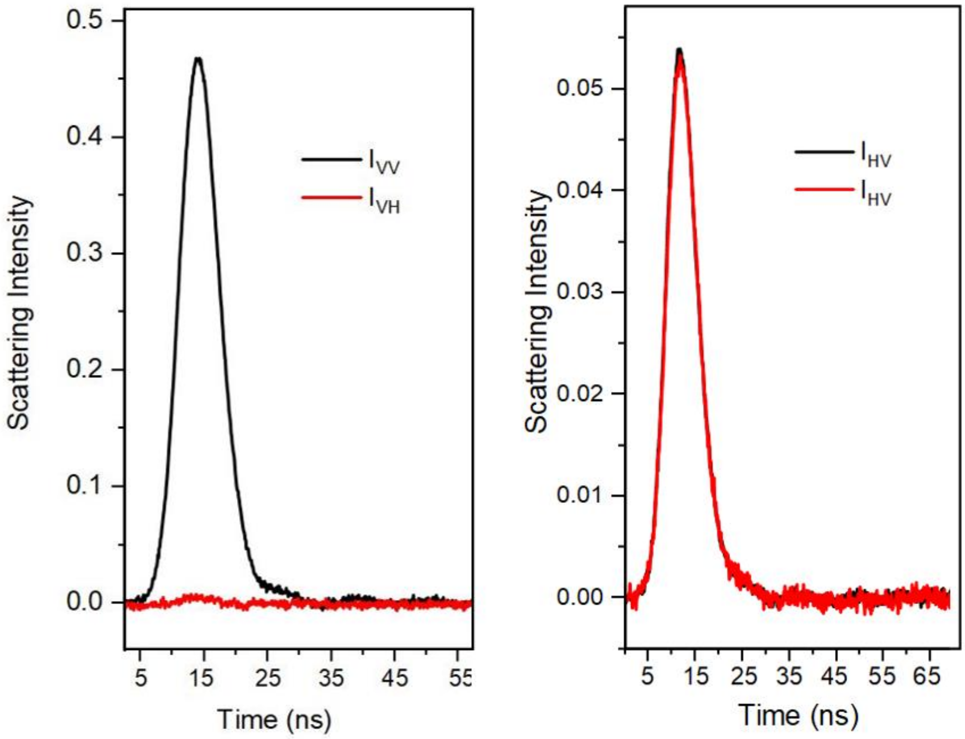

Figure 6.9 Kinetic traces of LUDOX 10% (recorder in the presence of the excitation polarizer) using vertically polarized light (left) and horizontally polarized light (right). In both cases, the scattering intensities were recorded while the emission polarizer was mounted parallel and perpendicular to the incident light.

The above figures show that by adding the excitation polarizer to the measuring system, the intensity of scattered light at the horizontal orientation of emission polarizer I_{VH} is notably decreased (almost extinct). Following the determination of horizontal and vertical angles for the excitation polarizer, 90^{o} and 0^{o} respectively, the fluorescence polarization and anisotropy values were calculated using the new setup for LUDOX and they were found to be 0.983 and 0.975 respectively. These values are high enough to conduct highly precise polarization measurements. However, another attempt for even more accurate polarization values was made by replacing the manual half-wave plate with an electronically driven liquid crystal variable wave plate to ensure the precise polarization rotation of the laser source. The aim of this procedure was to reduce any human error resulting from the mechanical movement of the half-wave plate. Nonetheless, the improvement in the polarization values was negligible over several measurements at less than 0.002 change in the polarization.

The same procedure was used for the alignment of laser source at 355 nm. The measured polarization and anisotropy values at this wavelength were 0.977 and 0.967, respectively.

6.3 Fluorescence Polarization/ Anisotropy Measurements

6.3.1 Fluorescence Polarization/ Anisotropy of common dyes

Before using the modified spectrofluorometer to study the binding in biological systems, the sensitivity of the system to changes in polarization was further evaluated by measuring the polarization and anisotropy of extensively studied fluorescent dyes (rhodamine 6G and fluorescein) in solvents with different viscosities. The polarization measurements of rhodamine 6G and fluorescein were carried out in methanol and in the highly viscous Tween 20 solvent, and the results are displayed in figures 6.10 and 6.11. Unlike the previous measurements which were recorded with the spectrofluorometer probing laser scatter, these measurements are now recorded at wavelengths consistent with the dye fluorescence and are deliberately chosen to avoid any interference from laser scatter, ca. 600 nm and 565 nm for rhodamine 6G and fluorescein, respectively. Again, the fluorescence lifetimes of these dyes are shorter than the laser pulse width. Thus, the emission intensities were recorded as a function of time, and the data were analysed using the same procedure applied to LUDOX.

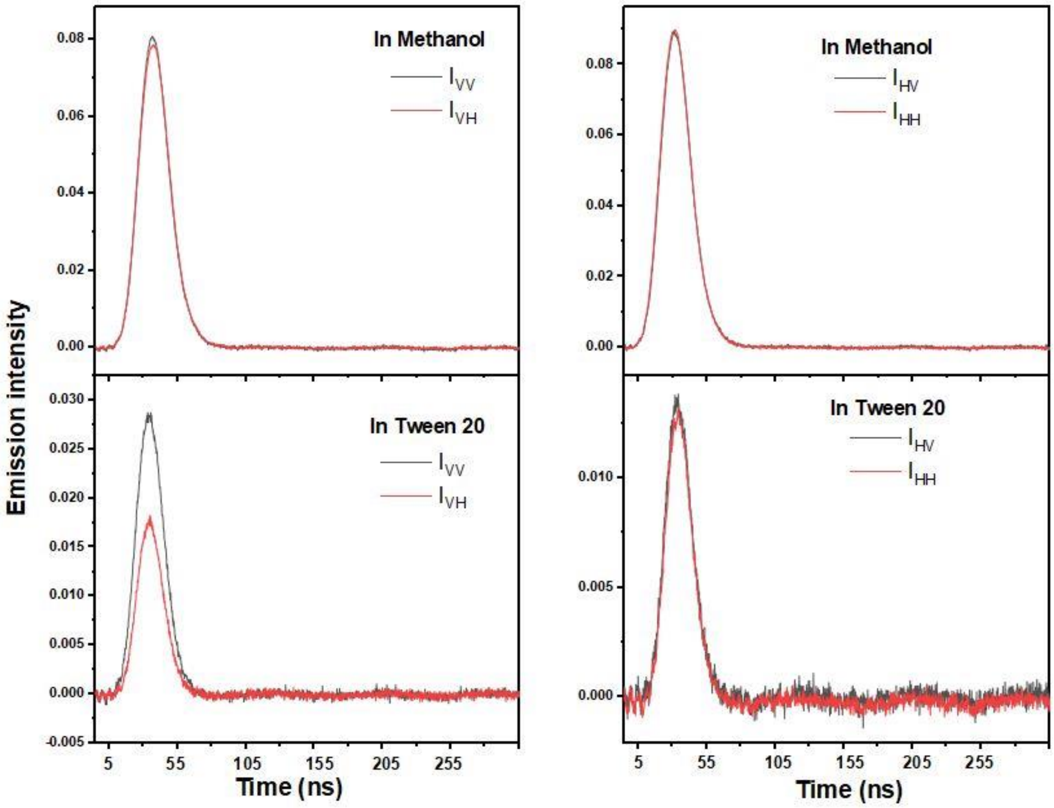

Figure 6.10 Kinetic traces of Fluorescein in methanol and tween20, using vertically polarized light (right) and horizontally polarized light (left). In all cases, the emission intensities were recorded while the emission polarizer was mounted parallel and perpendicular to the incident light

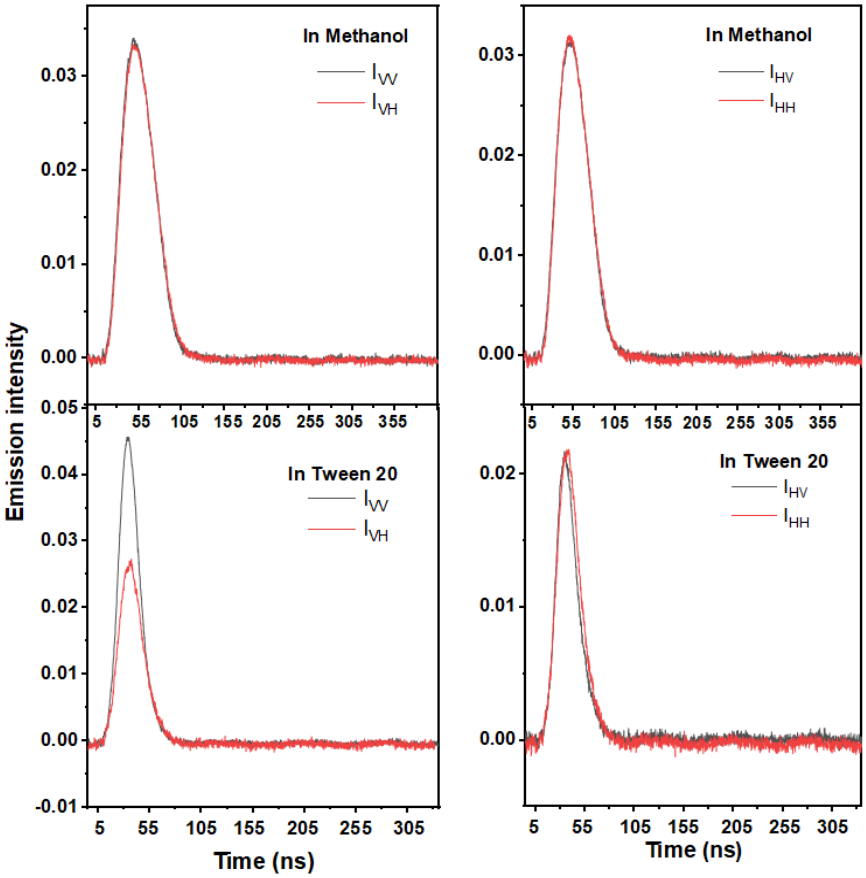

Figure 6.11 Kinetic traces of Rhodamine 6G in methanol and Tween20, using vertically polarized light (right) and horizontally polarized light (left). In all cases, the emission intensities were recorded while the emission polarizer was mounted parallel and perpendicular to the incident light.

Table 6.1 Polarization and anisotropy values of fluorescent dyes in methanol and Tween 20 solvents

	solvent	**p**	**r**
Fluorescein	Methanol	0.015	0.010
Fluorescein	Tween 20	0.270	0.198
Rhodamine 6G	Methanol	0.016	0.011
Rhodamine 6G	Tween 20	0.293	0.216

As shown in the above figures (Figs 6.10 and 6.11), upon excitation of both dyes using vertically polarized light, the emission intensities recorded in methanol in both parallel and perpendicular polarization planes are similar, indicating small polarization values (close to zero). In contrast, in the highly viscous solvent Tween 20, the emission intensity of each dye is substantially larger in the parallel orientation compared with the perpendicular direction, due to the reduction in the rate of molecular rotation in the viscous solvent. Therefore, polarization and anisotropy values are significantly increased in Tween 20 solvent, as shown in table 6.1. The anisotropy values for both dyes are in good agreement with previously published measurements. For example, the polarization values of Rhodamine 6G (using our system) were 0.016 and 0.293 in methanol and Tween 20, respectively, whilst the values found in the literature were 0.015 in methanol and 0.3 in viscous solvent ethylene glycol. This is indicative of the high sensitivity of the developed spectrofluorometer to the change in polarization. (Chen and Bowman 1965; Chen 1972; Fixler et al. 2005; Ameloot et al. 2013)

The same technique was applied to study Alexa fluor 594 by measuring polarization and anisotropy in DMSO (3 ml, 8 μM) and monitoring the change in these values after adding small volumes of Tween 20 (0.5 ml) and recording emission intensities with each additional aliquot. The polarizations and anisotropies of the dye are directly proportional to the increasing Tween 20 volume, as displayed in figure 6.12 and table 6.2.

Table 6.2 Polarization and anisotropy values of Alexa fluor 594 dye in DMSO and upon the addition of different volumes of tween 20 solvent

Volume of Tween 20 (ml)	*p*	*r*
0 (in DMSO)	0.063	0.043
0.5	0.138	0.097
1	0.247	0.180

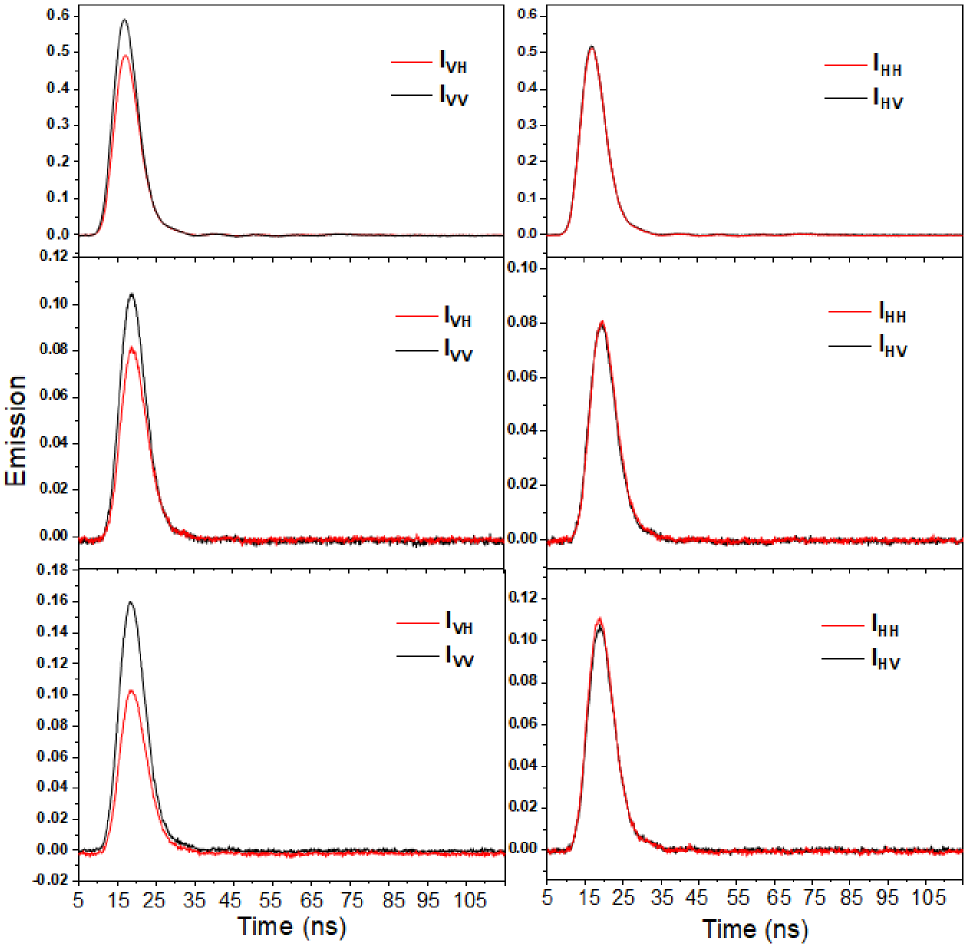

Figure 6.12 Kinetic traces of Alexa fluor 594 dye in DMSO (top) and after adding 0.5 ml (middle) and 1 ml (below) of tween20, using vertically polarized light (right) and horizontally polarized light (left). In all cases, the emission intensities were recorded while the emission polarizer was mounted parallel and perpendicular to the incident light.

6.3.2 Fluorescence Polarization/ Anisotropy of dye-doped polymer

Dye-doped polymers are a class of advanced materials that have garnered attention in recent years due to their unique optical properties and potential applications in a wide range of fields including electronics, optics, and energy. The basic idea behind dye-doped polymers is to incorporate a small amount of organic or inorganic dye into a polymer matrix to create a coloured material with enhanced optical properties. This approach has proven to be an effective way of creating highly efficient and low-cost materials that can be used in a variety of applications in diverse fields such as optoelectronic devices (e.g., OLED and LCD displays), sensors (e.g., chemical and biological sensors), solid-state dye laser, and biomedical applications (e.g., bioimaging, and photodynamic therapy).(Tan et al. 1995; Peng et al. 1996; Peng et al. 1998; Kuriki et al. 2000; Santra et al. 2004; Borisov et al. 2010; Zhang et al. 2016; Huh et al. 2017; Ibarra et al. 2018; Won et al. 2021) One of the most important features of dye-doped polymers is their ability to absorb and emit light in the visible and near-infrared spectral regions. The high absorption coefficients of the dyes allow dye-doped polymers to effectively convert light into electrical energy, making them well-suited for use in photovoltaic applications. (Ishchenko 2008) Similarly, the strong emission of light from the dyes makes them suitable for use in optical devices such as laser diodes, solar cells, and light-emitting diodes, where they can be used to generate light in a highly efficient manner. These dyes can also improve the sensing properties of the polymer, making it useful in applications such as chemical sensors, where the colour change of the polymer is indicative of the presence of a chemical target, or as physical sensors for detecting parameters such as temperature, pressure, and pH. (Hong and Kawano 2004; Haldar et al. 2009; Wolf et al. 2015; Resta et al. 2017; Tang et al. 2017; Li et al. 2018)

Dye-doped polymers can be engineered to have tailored optical properties for commercial applications (just like the phosphors in previous chapters), such as tuning absorption and emission spectra, scattering magnitudes, emission lifetimes, and emission polarizations. All of this can be achieved by selecting appropriate dyes with which to dope the polymer and controlling the doping concentration and distribution. Studying the fluorescence polarization of such a synthesized polymer is quite important since the emission of polarized light can often be a requirement for a particular application, for example in organic light-emitting diodes (OLEDs), liquid-crystal displays and some sensing applications.

Here, the modified fluorescence polarization/ anisotropy system was used to monitor the change in emission polarization values upon doping a novel polymer system with different fluorescent dyes. These experiments were carried out as a part of a study performed in cooperation with Taylor Young and Dr Ward’s group at Cardiff University to characterize a novel recyclable fluorescent polymer. The polymer was prepared by incorporating a luminescent dye, namely aminoanthraquinone (Mwt = 222.23 g/mol) or 4-piperidinyl-1,8-naphthalimide (Mwt = 303.43 g/mol), into copolymers of phthalic anhydride and cyclohexene oxide, abbreviated to AAQ-PA-CHO and Nap-PA-CHO (scheme 6.1).

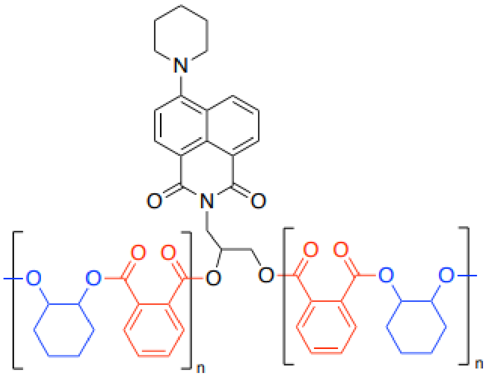

Scheme 6.1 the chemical structure of Nap-PA-CHO polymer

The emission polarization was measured for all un-doped and dye-doped polymers using the excitation wavelength 355 nm and following the same procedure described above. The samples were excited by vertically polarized light and the emission intensity was then recorded in parallel and perpendicular axis to the incident light. The horizontally polarized excitation source was used to calculate the G factor. The un-doped polymer does not display any absorption of the light at 355 nm, so all incident light is reflected giving high polarization and anisotropy values at this wavelength, 0.966 and 0.950, respectively, which is reminiscent of the behaviour seen early in LUDOX solutions. The results are shown in figure 6.13 and table 6.3.

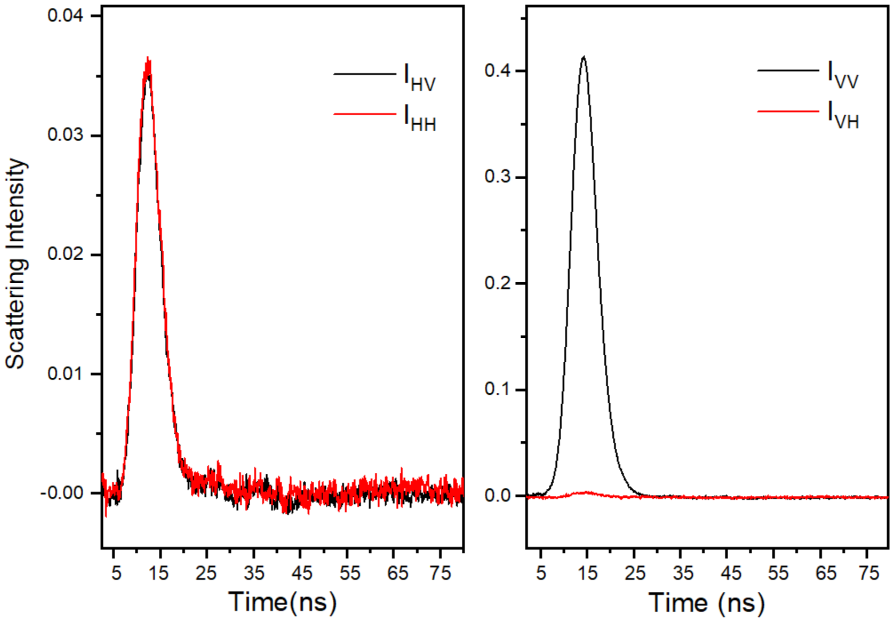

Figure 6.13 Scattering intensity of un-doped polymer after the excitation by using vertically polarized light (right) and horizontally polarized light (left). In both cases, the scattering intensities were recorded while the emission polarizer was mounted parallel and perpendicular to the incident light.

For each dye-doped polymer, AAQ-PA-CHO or Nap-PA-CHO, the emission intensity in the parallel polarization plane $I_{||}$ (I_{VV}) is greater than that at perpendicular axis $I_{\perp}$ (I_{VH}) indicating that doped polymers emit partially polarized light. However, the AAQ-PA-CHO polymer (doped with the dye with lower molecular weight) displays a notably higher polarization value than Nap-PA-CHO, with values of 0.255 and 0.193, respectively (figure 6.14 and table 6.3). This is likely due to varying the fluorescence lifetime of the dyes. As mentioned earlier in this chapter the degree of polarization observed in the emission from a sample depends on the molecular rotation of a fluorophore compared to the lifetime of the excited state (equation 6.1). It follows that the shorter the fluorescence lifetime, the less the fluorophore will rotate between the absorption and emission events, resulting in a higher polarization of the emitted light. The fluorescence lifetimes of the polymers were recorded by the Pope group and found to be < 1ns for AAQ-PA-CHO while Nap-PA-CHO displays an emission lifetime of ~ 9 ns. Therefore, the changes in polarization observed here show this discrepancy in lifetime: the emission from AAQ-PA-CHO is rapid, taking place prior to rotation. In the case of Nap-PA-CHO the longer fluorescence lifetime begins to compete with the rotational period, such that the observed anisotropy is reduced. (Vavilov and Levshin 1923; Jameson and Ross 2010) The consistency between FP measurements and emission lifetime indicates that the developed polarization spectrofluorometer is accurate and sensitive to the change in polarization.

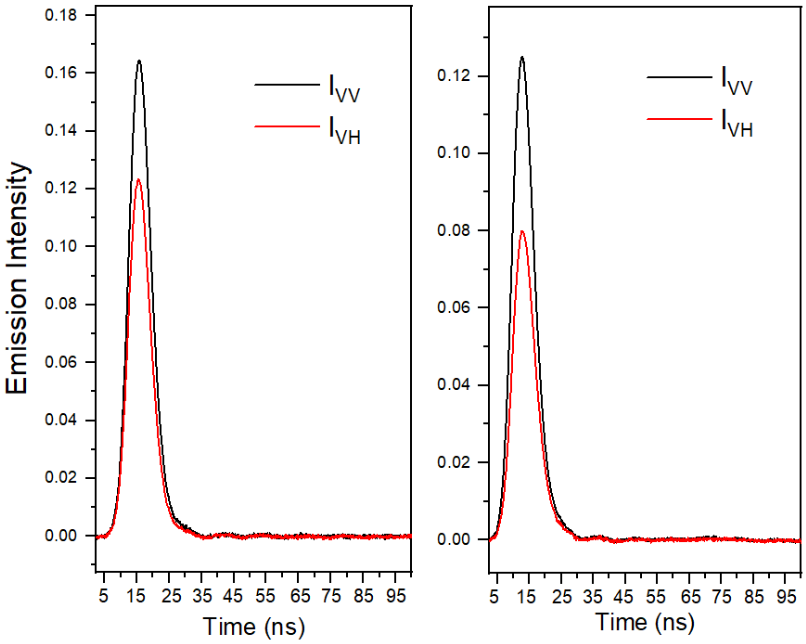

Figure 6.14 Emission intensities of Nap-PA-CHO (left) AAQ-PA-CHO (right) polymers, at parallel $I_{//}$ (black line) and perpendicular $I_{\perp}$ (red line) polarization plans. In all cases, samples were excited using vertically polarized light the emission intensities were recorded while the emission polarizer was mounted parallel and perpendicular to the incident light.

Table 6.3 Polarization and anisotropy values for un-doped and dye-doped polymer

	λ_{Em}	p	r
Un Doped	357	0.966	0.95
Nap-PA-CHO	560	0.139	0.097
AAQ-PA-CHO	600	0.255	0.186

6.3.3 Fluorescence Polarization/ Anisotropy Measurements for Studying the Binding Interaction between Colistin and the Bacterial Membrane Escherichia Coli.

Colistin, or polymyxin E, is an antibiotic peptide used as a last-line treatment for infections caused by multidrug-resistant Gram-negative organisms, such as Escherichia coli, Pneumoniae and Pseudomonas aeruginosa. It was first introduced in 1949 and used to treat Gram-negative bacteria but in the 1980s its use was abandoned due to the nephrotoxicity and neurotoxicity it caused. However, because of the rise in multidrug-resistant Gram-negative bacteria in the last two decades, it was necessary to use colistin again when all other antibiotic treatments failed due to its effectiveness in treating infections caused by these bacteria. (Bergan and Fuglesang 1981; Evans et al. 1999; Bialvaei and Samadi Kafil 2015; Pogue et al. 2017)

Generally, antibiotic peptides target the outer membrane of Gram-negative bacteria which has many lipopolysaccharide (LPS) units and then disrupt the membrane by preventing the further synthesis of this lipid. Colistin is polycationic and acts through two-step mechanisms that involves initial binding to the anionic lipid, the LPS anchor, subsequently inducing changes in cell membrane permeability. This then destabilizes the cytoplasmic membrane leading to cell death. Colistin can also interact with bacteria by ribosome binding, causing structural injuries, changing bacterial respiration, and generating reactive or toxic oxygen species. Nonetheless, the mechanisms of interactions between colistin and bacteria are not yet fully understood. (Trimble et al. 2016; Sierra et al. 2017; Armengol et al. 2019) Recently, an increasing number of colistin-resistant bacteria have emerged due to the modification of the phosphate groups of the lipid. This modification reduces the anionic charge of the cell surface, decreasing the electrostatic interactions between colistin and the membrane of Gram-negative bacteria.(Miller et al. 2011; Farizano et al. 2012; Gutu et al. 2013; Harris et al. 2014; Liu et al. 2016) The genes responsible for most of these modifications are the mobilized colistin resistance genes (mcr). mcr-1 was first reported in 2016 with 10 slightly different mcr genes (mcr-1 - mcr-10) now having been identified. (Liu et al. 2016; Ling et al. 2020; Wang et al. 2020; Hussein et al. 2021) The spread of mcr threatens to decrease the effectiveness of colistin, which is already considered a last-resort antibiotic. Therefore, understanding the mechanism of resistance to colistin and the effect of the mcr-gene on the bacterial membrane is greatly significant to develop new therapeutic strategies against colistin-resistant bacteria.

Fluorescence anisotropy measurements were performed in order to examine the binding between colistin drug and the bacterial membrane of Escherichia coli, as a part of a study performed in cooperation with Dr Pritchard's group at Cardiff University. This study was designed to investigate the effect of the mcr genes on the various surface properties of the bacterial membrane of Escherichia coli, and thus its ability to bind with colistin. For this aim, a colistin peptide was labelled with fluorescent dye Alexa fluor 594, and then added to two different strains of Escherichia coli: E. coli J53, E. coli and J53(pE30) mcr-1, as mcr-1 is resistant to colistin. The binding of colistin to the bacterial membrane was examined by monitoring the change in the fluorescence anisotropy of Alexa fluor 594, before and after the addition of the colistin solution to the bacteria strains.

6.4.1 Determination of the concentration of labelled fluorescent dye

For accurate anisotropy measurements, it is important to determine the concentration of tracer dye in the labelled peptide to avoid depolarization resulting from radiative energy transfer. At high concentrations, fluorescent dyes with significant overlap between their absorption and emission spectra, such as Alexa fluor 594, are more likely to display secondary emission due to reabsorption of the emitted radiation, which leads to low polarization and anisotropy values. (Weber 1956; Chen 1972; Lakowicz 2006) Therefore, the anisotropy values of free Alexa fluor 594 were recorded for four different concentrations, at ambient conditions and λ_{em} = 610 nm, and the results are displayed in table 6.4.

Table 6.4 Polarization and anisotropy values of different concentrations of Alexa fluor 594 in sodium phosphate buffer at λem = 610 nm.

Concentration (µg/ml)	***p***	***r***
0.068	0.062	0.042
0.14	0.063	0.043
1.08	0.017	0.012
2.02	0.009	0.006

The anisotropy values at concentrations higher than 1 µg/ml of Alexa fluor 594 are significantly reduced, but the FA values become almost identical at the lowest concentrations, 0.14 and 0.068 µg/ml. Because the sensitivity of the PMT detector to the fluorescence is high, the labelled colistin samples were prepared to contain a concentration of Alexa fluor 594 equivalent to 0.068 µg/ml. Following the determination of the tracer concentration, the fluorescence polarization and anisotropy were performed for the labelled colistin (Alexa-colistin conjugate), and they were found to be slightly increased to 0.066 and 0.045, respectively, which is attributed to the slight reduction in the dye rotational rate upon binding to the colistin. In addition, the polarization was also measured for the solution containing only Alexa fluor 594 and the bacteria cell (without colistin), in order to ensure that there is no direct binding between the cell and the dye. The ***p*** and ***r*** values were identical to those measured in the dye-only solutions, indicating that the fluorophore doesn't interact directly with the bacteria strain. Once the above measurements were verified, the polarization and anisotropy were recorded for four different concentrations of each bacteria strain, following the same procedure and using the excitation wavelength 532 nm. The results are displayed in table 6.5.

Table 6.5 Polarization and anisotropy values of both bacteria strains added at different concentration to Alexa-colistin conjugate .

Bactria strain	**Concentration CFU/ml***	***p***	***r***
J53	**3x10^8**	0.137	0.096
	3x10^7	0.085	0.058
	3x10^6	0.084	0.057
	3x10^5	0.070	0.048
MCR-1	**3x10^8**	0.066	0.045
	3x10^7	0.065	0.044
	3x10^6	0.066	0.045

*CFU, colony forming unit, is a unit of measurement used to determine the number of bacterial cells in a sample. CFU/ml is colony-forming unit per millilitre.

The above table shows a remarkable increase in ***p*** and ***r*** values upon the addition of Alexa 594-colistin conjugate to E. coli J53 strain. The increase in the ***p*** and ***r*** values is directly related to increasing the concentration of the bacteria cells, indicating that Alexa-labelled colistin is binding to the membrane of E. coli J53. In contrast, there is almost no change in the anisotropy values upon the addition of Alexa 594-colistin conjugate to the resistant E. coli (pE30) mcr-1 strain, suggesting that no binding interactions are occurring between colistin and the bacterial cell membrane contained resistant mcr-1 gene. These results nicely match the experimental results obtained by using Airyscanning Confocal laser scanning microscopy (CLSM) which was performed by Dr Pritchard's group in order to study the distribution of colistin (8 µg/ml) within bacterial cells (figure 6.15). This method demonstrated that colistin molecules were distributed within the bacterial membrane of E. coli J53, however, no colistin was detected in the outer membrane of the resistant E. coli (pE30) mcr-1 strain. These results highlight that the mcr-1 gene plays a critical role in protecting the integrity of the cell surface membrane of E. coli against colistin.

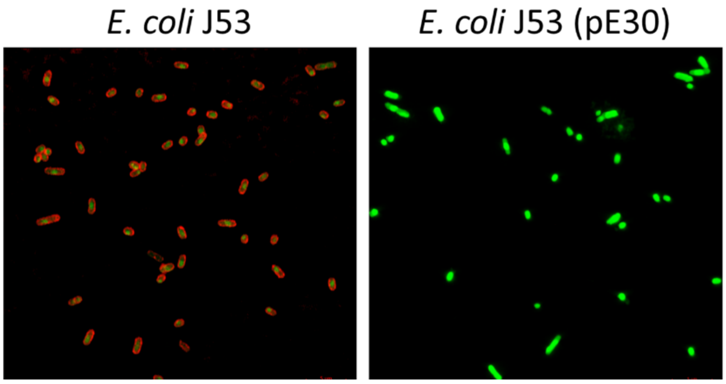

Figure 6.15 Airyscanning CLSM imaging of cell surface binding of Alexa 594-colistin conjugate with E.coli J53 (left) and E.coli J53 (right). Green indicates viable bacteria, and red colistin.

6.4 Conclusion and Future Work

The initial development of a spectrofluorometer was undertaken for the purpose of conducting highly sensitive fluorescence polarization/ anisotropy measurements for different materials. The instrument can be used to study samples that can be excited at wavelengths 355 nm or 532 nm, with commercial waveplates readily available at these wavelengths. The alignments of different mechanical and optical components were checked using a diluted LUDOX solution, resulting in fluorescence polarization values of 0.983 and 0.977 using excitation wavelengths 532 and 355 nm, respectively.

The developed spectrofluorometer was used to study the emission polarization of a new polymer doped with a fluorescent dye: aminoanthraquinone or 4-piperidinyl-1,8-naphthalimide naphthylamide. The fluorescence polarization was found to be higher for aminoanthraquinone-doped polymer due to the shorter lifetime of its excited state. The spectrofluorometer was also employed to examine the binding interactions between colistin and the bacterial membrane of two strains of Escherichia coli. The results demonstrate that Alexa-labelled colistin is able to bind to E. coli J53 strain, but not to the resistant E. coli (pE30) mcr-1 strain.

In conclusion, the spectrofluorometer developed in this study has proven to be a useful, accurate and cost-effective tool in the Beames lab that could be applied to studying fluorescence polarization and binding interactions in chemical and biological systems. For future work, it is recommended to diversify the excitation sources to expand the excitation wavelength range to include the entire visible region, so that the instrument can be used to analyse a wider range of samples and fluorescent dyes. Additionally, it would be useful to integrate a temperature control system to study temperature-dependent fluorescence polarization and anisotropy measurements. Furthermore, the integration of different detection techniques, such as ultrafast time-resolved fluorescence and steady-state fluorescence, will make the instrument even more versatile and valuable for a range of research applications.

7. Summary

This PhD thesis presents the development of analytical procedures that utilize a range of advanced spectroscopic techniques, supported by computational chemistry methods, to investigate a variety of novel luminescent organic and inorganic compounds.

In Chapters 3 and 4, a detailed analysis is presented for a series of Ir^{III} complexes with quinoxaline/quinoline cyclometallating ligands. These complexes exhibit variations in their main ligand structures, ancillary ligands, or attached substitution groups, providing valuable insights into the effects of structural modifications on their spectroscopic properties. The complexes demonstrate highly tunable optical properties in relation to ligand variation. In bidentate phenyl-quinoxaline iridium complexes, the nature and the position of substituents shift the photophysical properties, emission centre and lifetime, by different degrees. Substitution on the phenyl ring of cyclometalated ligands results in broader shifts in emission bands, while substitution on the quinoxaline moiety allows more precise tuning of emission properties, with fluorinated-phenyl complexes showing the most blue-shifted emission band and longest luminescent lifetime. The emission lifetimes demonstrate a significant increase under deoxygenated or low-temperature conditions, confirming that the emission arises from the triplet excited state, mixed ^{3}MLCT/^{3}ILCT. Additionally, replacing bidentate quinoxaline ligands with the tridentate ligands, with extended π-conjugation, increases emission lifetimes due to the increase of ^{3}ILCT character in the excited state. Similarly, quinoline Ir^{III} complexes display a clear correlation between ligands' structures and photophysical characterizations. For quinoline Ir^{III} complexes, it was found that the position of chelation at the naphthyl unit strongly influences the emission properties, more so than the role of the ligand substituent. This is attributed to the change in the degree of MLCT and ILCT characters in the emissive excited state. Increasing the degree of π-conjugation of the ancillary N^N ligand results in lowering its orbitals making it the main contributor to the emissive excited state. This leads to a red shift in the emission centres along with an increase in emission lifetime. This high tunability of Ir^{III} complexes diversifies their potential applications in different areas. Supporting computational calculations consistently predict the spectroscopic features of the entire range of complexes examined in this work, offering a comprehensive understanding of the role of each ligand on the photophysical properties of the complexes. The results of this analysis were used as a guide to design new iridium complexes that emit in the deep-red and near-IR regions with relatively long emission lifetimes. The analysis method applied in this work shows great promise in designing new iridium complexes with desirable properties for particular applications, which saves time and cost in the laboratory.

Chapter 5 outlines the analysis of organic dyads, N-substituted naphthalimide and three of its thionated variants, using the same methodology used to study iridium complexes. As for iridium complexes, the molecular geometries of the investigated naphthalimide dyads determine their photophysical characteristics. The N-PhPipNMI dyad displays different emission types in toluene, such as fluorescence, phosphorescence and TADF. However, in the more polar solvent, DCM, the phosphorescence was completely quenched while the TADF was significantly enhanced due to the stabilization of the charge transfer state. Thionation of the carbonyl group leads to a significant red shift in absorption bands due to a reduction of LUMO energy. A remarkable quenching of prompt fluorescence is also observed in the thionated dyads, indicating an increase in the rate of ISC and confirmation of the population of nearby triplet states. Chapter 6 presents the development of a cost-effective and accurate spectrofluorometer for highly sensitive fluorescence polarization measurements. This instrument has been successfully applied to investigate the emission polarization of a novel polymer and it was demonstrated that the polarization of the polymer depends on the lifetime of doped fluorescent dyes. The developed instrument was also used to study the binding interactions between colistin and two strains of E. coli. It was found that Alexa-labelled colistin is able to bind to E. coli J53 strain, but not to the resistant E. coli (pE30) mcr-1 strain.

8. Appendix

A. Transient Spectroscopic and Computational Analysis of poly-substituted Iridium (III) Quinoxaline Complexes

A.1 Bis-Quinoxaline Iridium (III) Complexes with Bipyridine Ancillary ligand

A.1.1 UV-Vis. Spectra

Table of absorbance data for $[Ir(L^{1\text{-}8})_2(bipy)]PF_6$ complexes.

Complex	**λ_{abs} ($\varepsilon \times 10^4$ M^{-1} cm^{-1}) / nm**
$[Ir(L^1)_2(bipy)]PF_6$	485 sh (0.4), 378 (1.7), 293 (3.1), 267 (3.5)
$[Ir(L^2)_2(bipy)]PF_6$	518 sh (0.4), 373 (2.1), 292 (3.1), 266 (3.6)
$[Ir(L^3)_2(bipy)]PF_6$	460 sh (0.2), 359 (0.7), 288 (2.4), 249 (2.7)
$[Ir(L^4)_2(bipy)]PF_6$	450 sh (0.7), 372 (2.4), 286 (4.9)
$[Ir(L^5)_2(bipy)]PF_6$	449 sh (0.4), 362 (1.6), 284 (2.5), 259 (2.9)
$[Ir(L^6)_2(bipy)]PF_6$	442 sh (0.2), 370 (1.8), 357 (1.1), 283 (1.9), 241 (1.8)
$[Ir(L^7)_2(bipy)]PF_6$	439 (0.7), 379 (2.9), 363 (2.2), 284 (4.6), 239 (4.3)
$[Ir(L^8)_2(bipy)]PF_6$	440 sh (0.2), 372 (1.0), 360 (1.0), 280 (1.6), 239 (1.8)

A.1.2 Kinetics Studies

Kinetic traces of the major features of the transient spectra of $[Ir(L^2)_2(bipy)]PF_6$ (left) and $[Ir(L^3)_2(bipy)]PF_6$ (right) complexes in acetonitrile at room temperature, aerated. Wavelengths and lifetimes of each trace are inset.

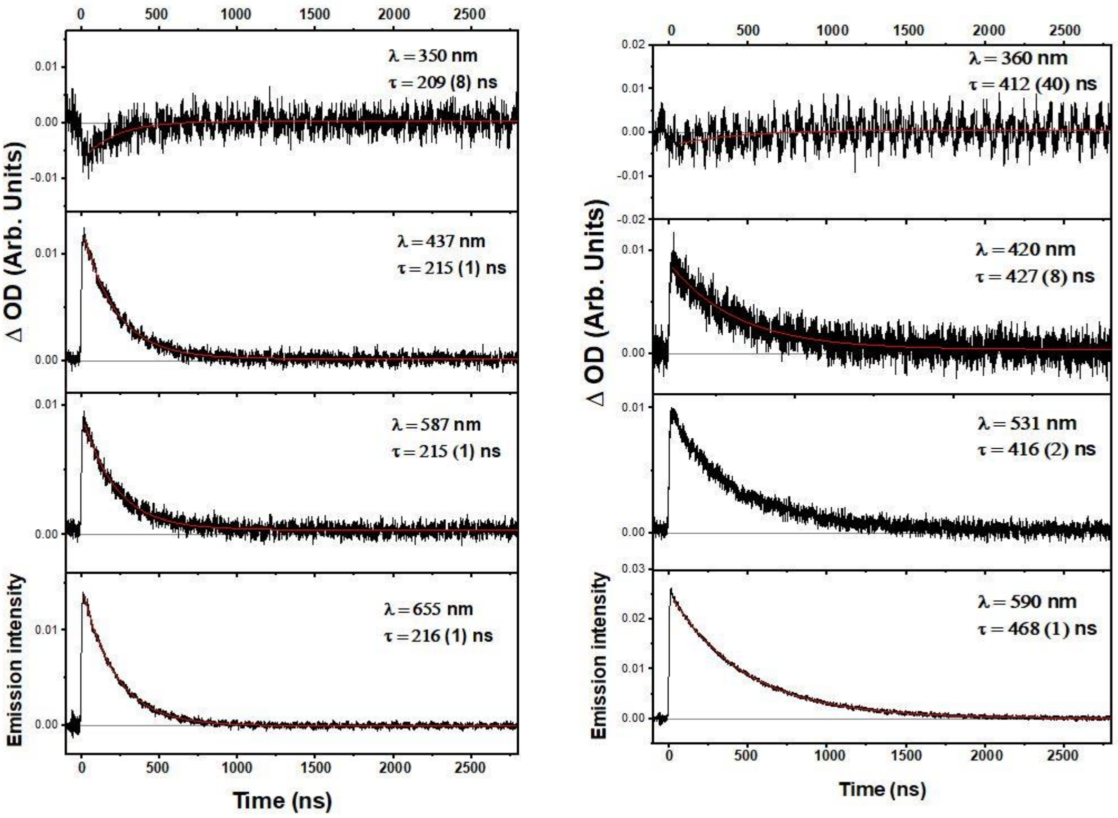

Kinetic traces of the major features of the transient spectra of $[Ir(L^4)_2(bipy)]PF_6$ (left) and $[Ir(L^5)_2(bipy)]PF_6$ (right) complexes in acetonitrile at room temperature, aerated. Wavelengths and lifetimes of each trace are inset.

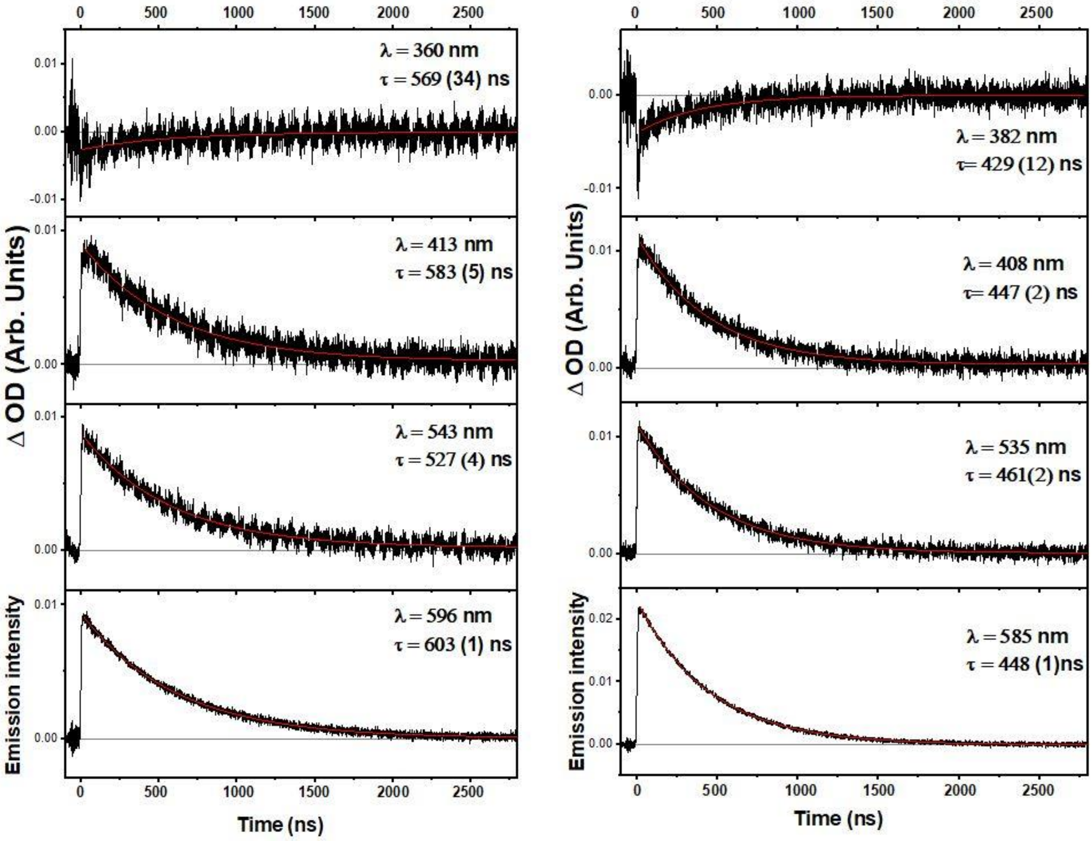

Kinetic traces of the major features of the transient spectra of $[Ir(L^7)_2(bipy)]PF_6$ (left) and $[Ir(L^8)_2(bipy)]PF_6$ (right) complexes in acetonitrile at room temperature, aerated. Wavelengths and lifetimes of each trace are inset.

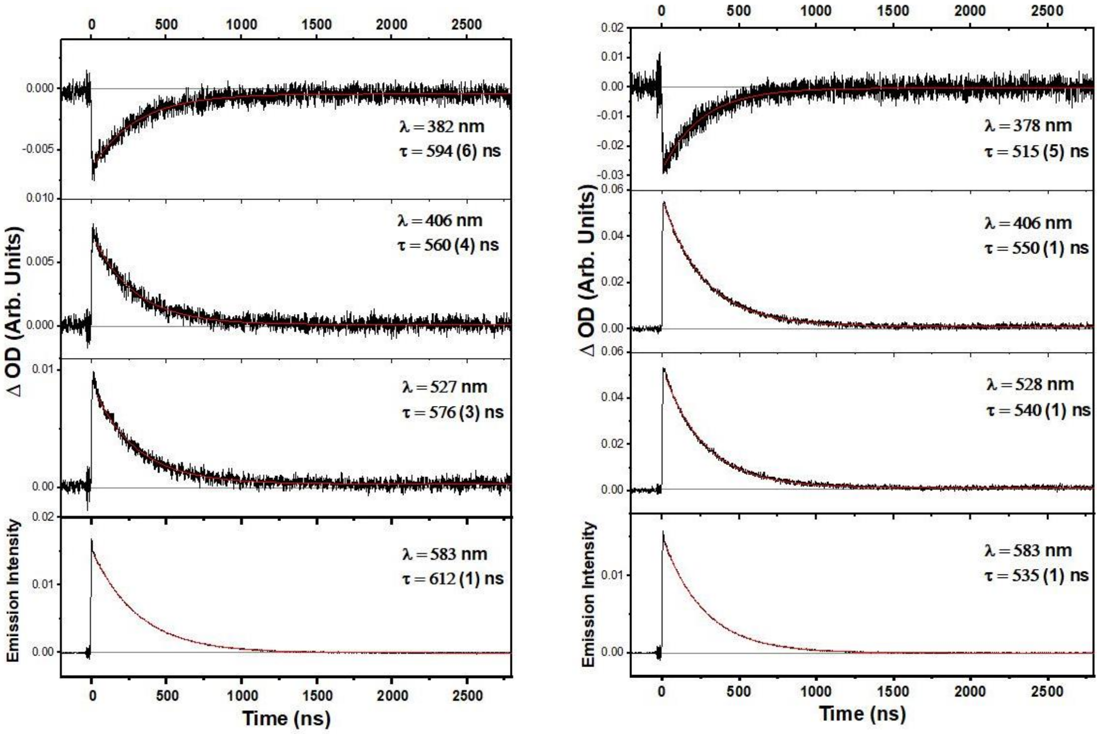

Emission traces of $[Ir(L^{1-8})_2(bipy)]PF_6$ complexes in acetonitrile at 77K, aerated. Wavelengths and lifetimes of each trace are inset.

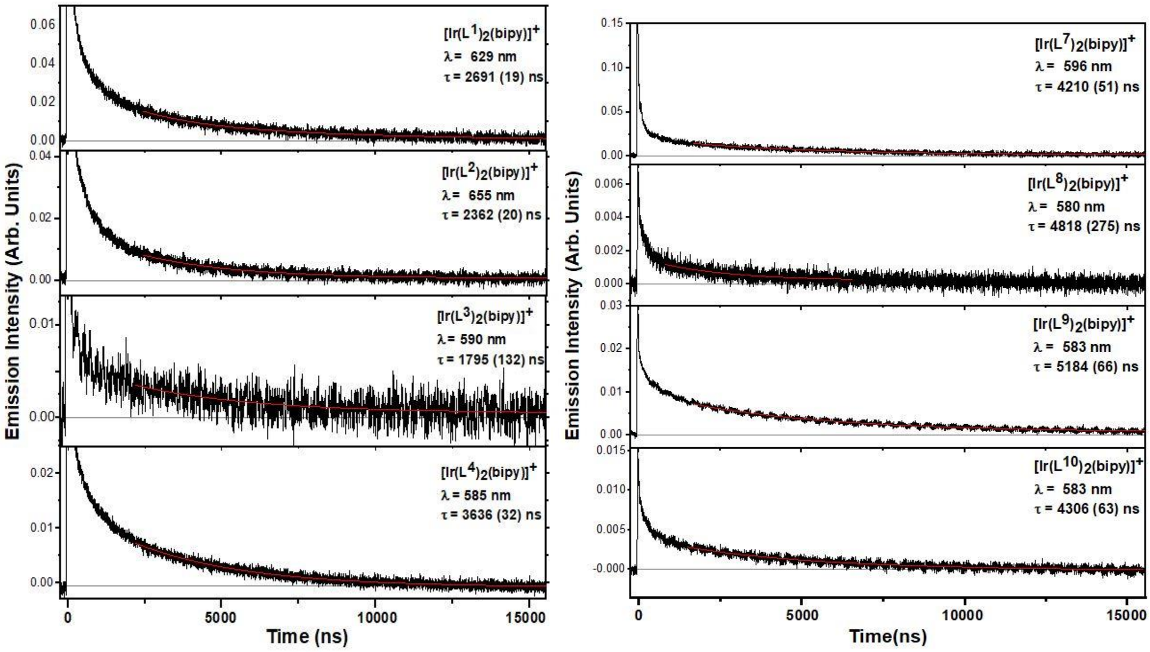

A.1.3 DFT

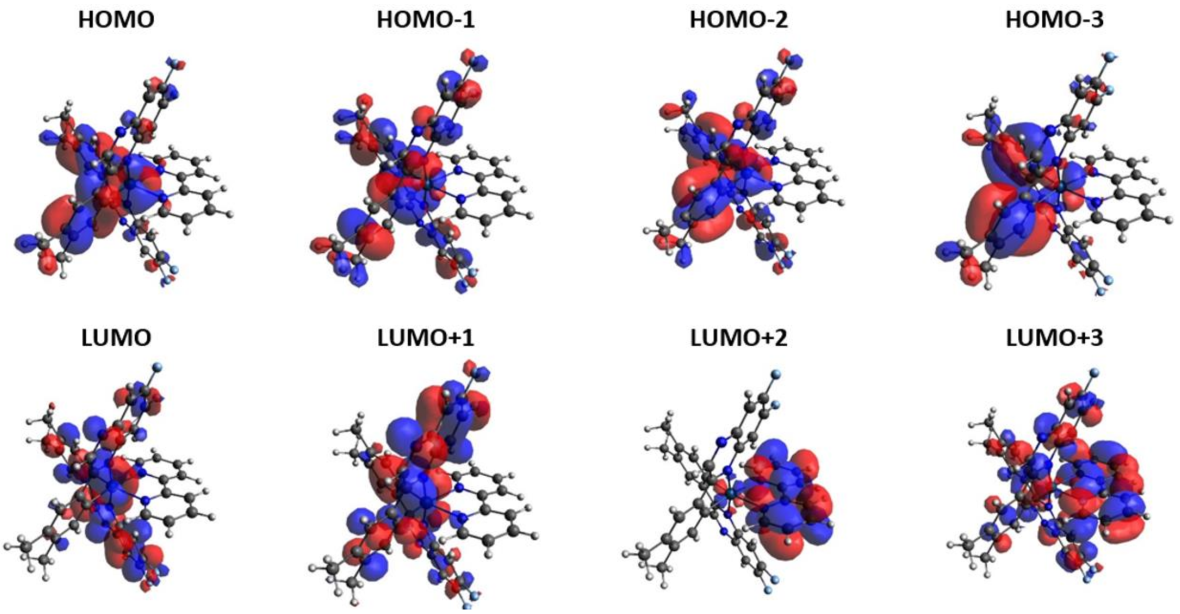

Calculated Kohn-Sham frontier molecular orbitals for [Ir(L^2)$_2$(bipy)]$^+$.

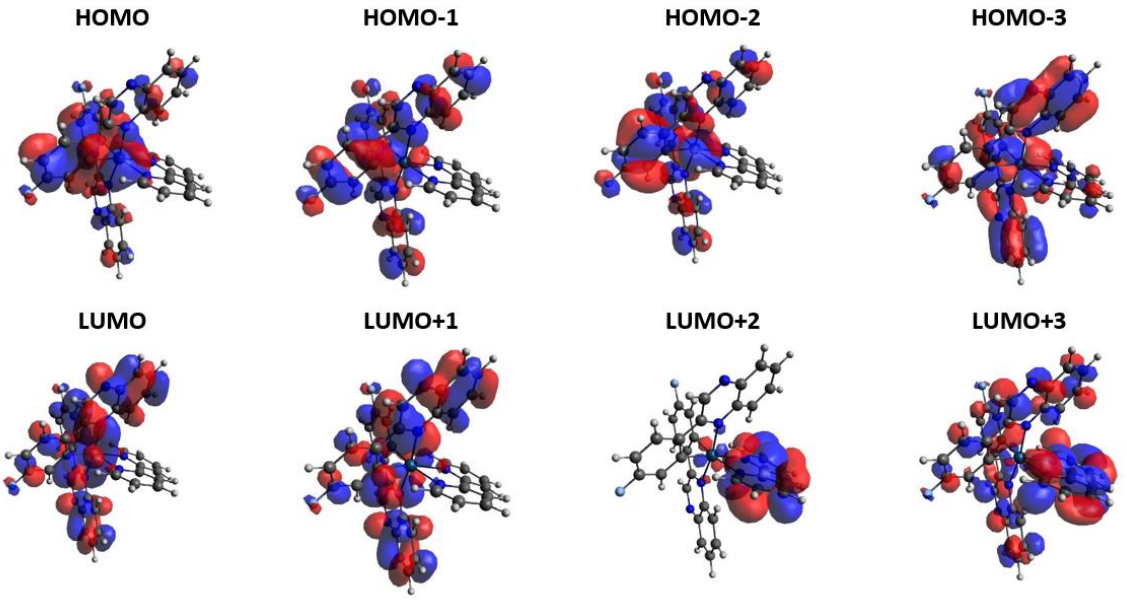

Calculated Kohn-Sham frontier molecular orbitals for [Ir(L^3)$_2$(bipy)]$^+$.

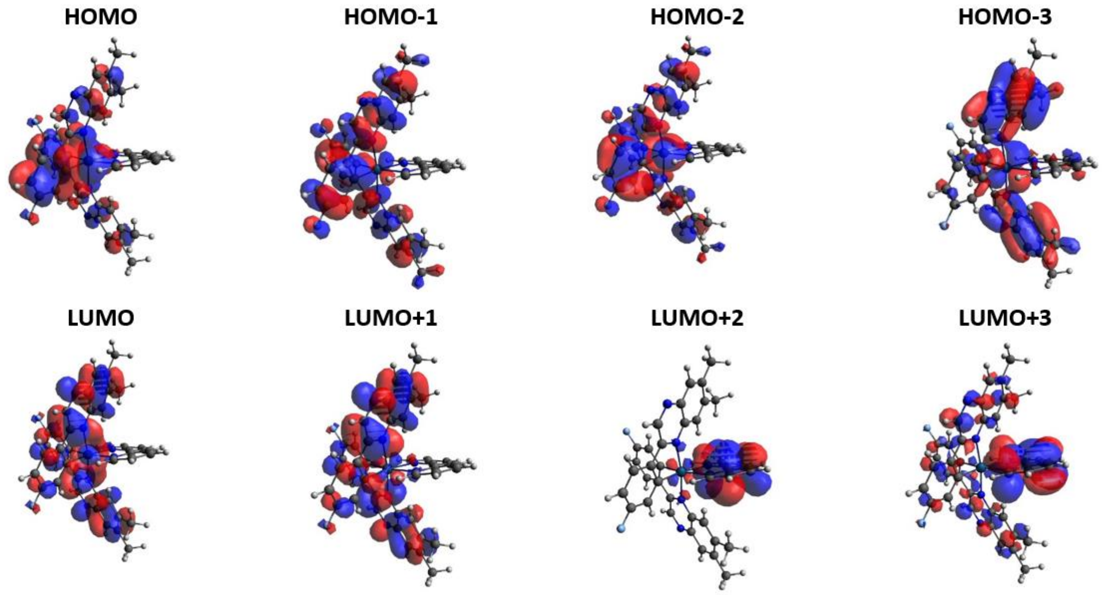

Calculated Kohn-Sham frontier molecular orbitals for [Ir(L^4)$_2$(bipy)]$^+$.

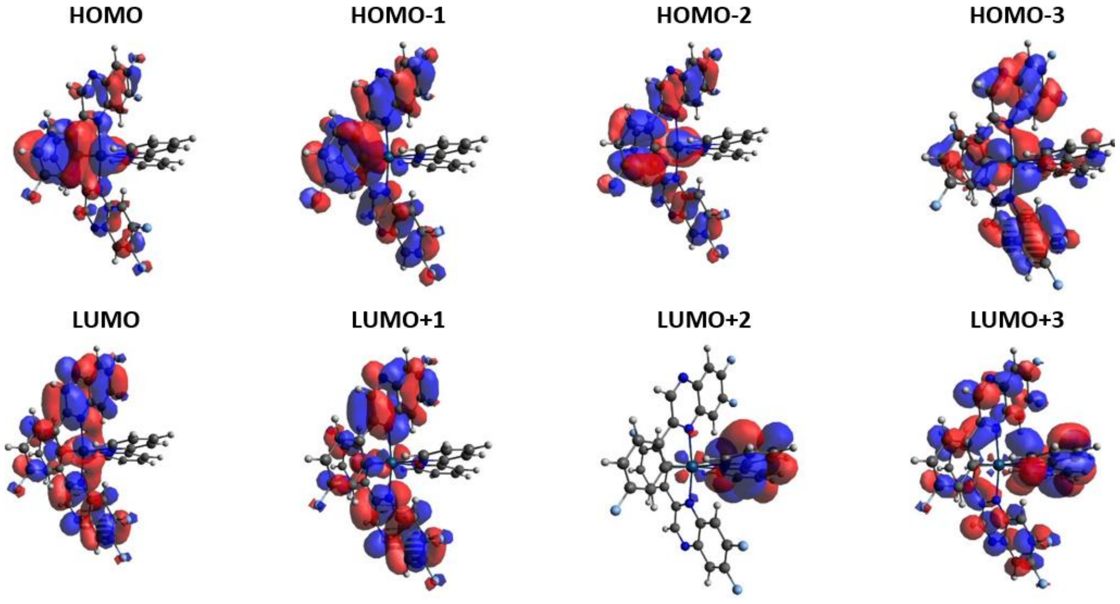

Calculated Kohn-Sham frontier molecular orbitals for [Ir(L^5)$_2$(bipy)]$^+$.

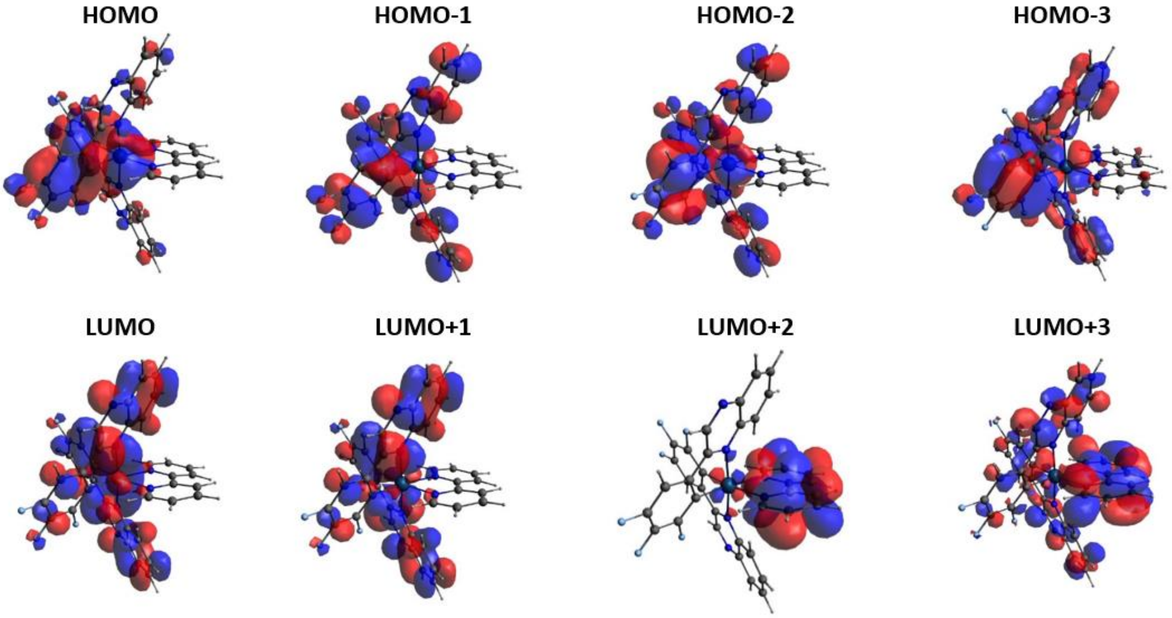

Calculated Kohn-Sham frontier molecular orbitals for $[Ir(L^6)_2(bipy)]^+$.

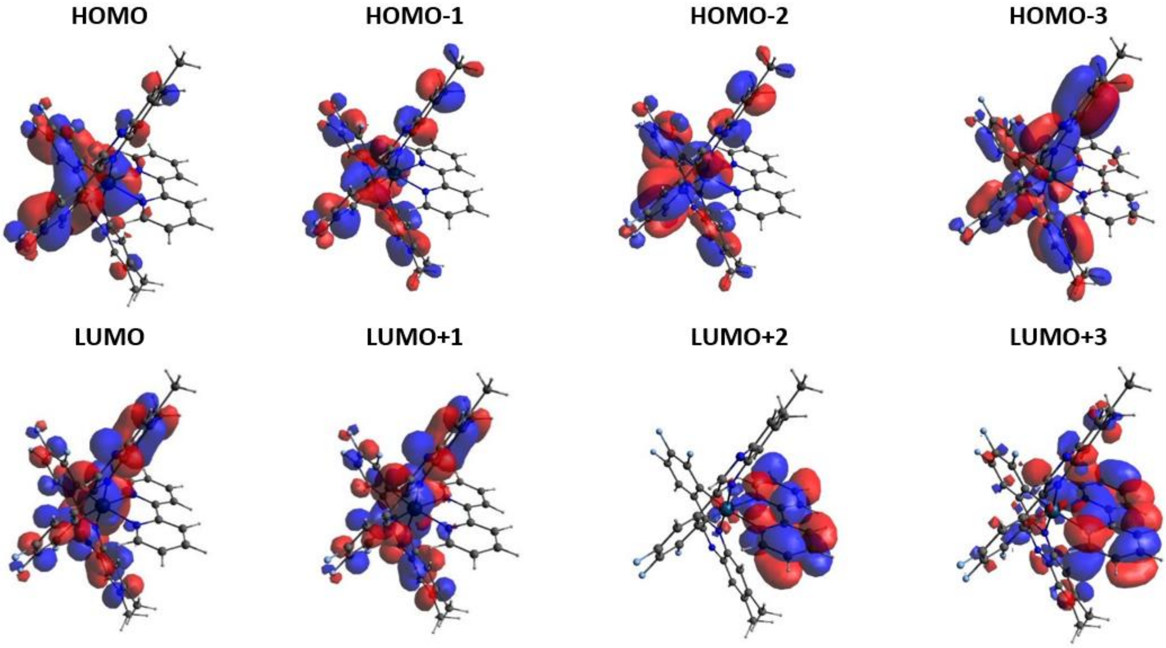

Calculated Kohn-Sham frontier molecular orbitals for $[Ir(L^7)_2(bipy)]^+$.

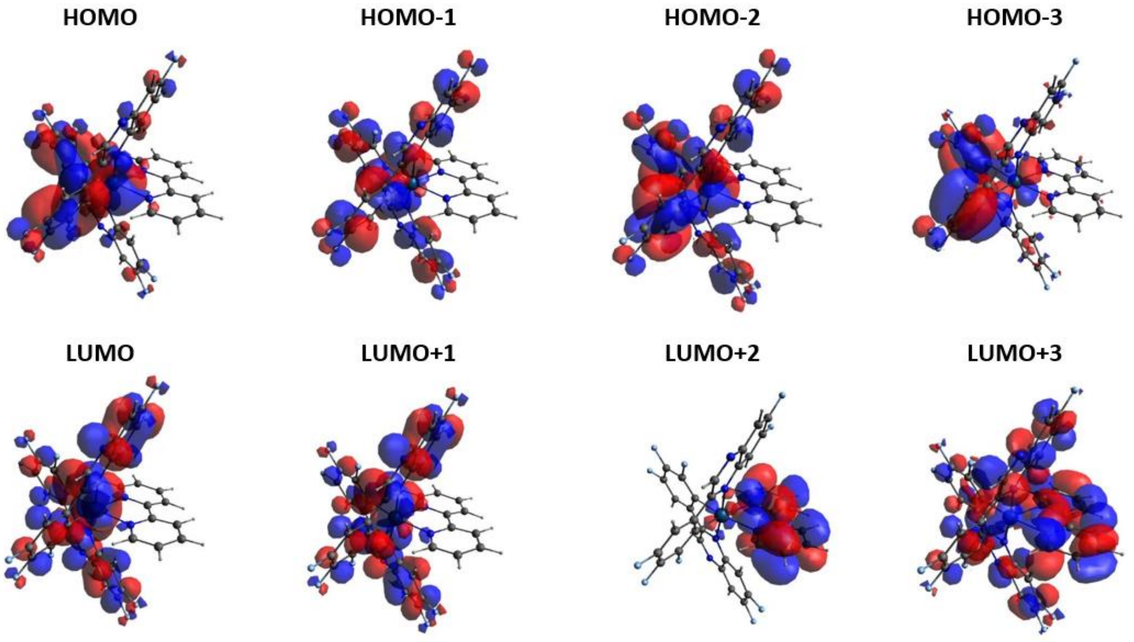

Calculated Kohn-Sham frontier molecular orbitals for [Ir(L^8)$_2$(bipy)]$^+$.

Table of a description of the calculated MO contributions, excited state descriptions and their associated transitions for [Ir(L^2)$_2$(bipy)]$^+$ complex (Q1 and Q2 are the different quinoxaline ligands; bipy = bipyridine).

	Moiety Contribution to Orbital (%)				**Orbital Contribution to Excited State**	
Orbital	**Ir (5d)**	**bipy**	**Q1**	**Q2**	**Excited State**	**Contributing Transitions (> 10%)**
LUMO +4	1	38	30	30	1 (419 nm f=0.1768)	HOMO → LUMO+1 (84%)
LUMO +3	2	60	19	19		
LUMO +2	2	96	1	1	2 (412 nm f=0.0456)	HOMO-1 → LUMO+1 (11%) HOMO → LUMO (84%)
LUMO +1	4	1	32	64		
LUMO	4	1	63	31		
HOMO	32	2	33	33	3 (341 nm f=0.0578)	HOMO → LUMO+2 (78%)
HOMO -1	4	1	47	47		
HOMO -2	8	1	45	46	4 (336 nm f=0.1809)	HOMO -2 → LUMO (24%) HOMO -1 → LUMO +1(59%)
HOMO -3	12	2	43	43		
HOMO -4	44	8	24	24	5 (334 nm f=0.2519)	HOMO -2 → LUMO+1 (21%) HOMO-1 → LUMO (49%) HOMO → LUMO+2 (13%)

Table of a description of the calculated MO contributions, excited state descriptions and their associated transitions for $[Ir(L^3)_2(bipy)]^+$ complex (Q1 and Q2 are the different quinoxaline ligands; bipy = bipyridine).

	Moiety Contribution to Orbital (%)				Orbital Contribution to Excited State	
Orbital	**Ir (5d)**	**bipy**	**L1**	**L2**	**Excited State**	**Contributing Transitions (> 10%)**
LUMO +4	1	44	28	27	1 (385 nm f=0.1896)	HOMO-1 → LUMO (12%) HOMO → LUMO+1 (81%)
LUMO +3	2	64	17	17		
LUMO +2	2	96	1	1	2 (380 nm f=0.0590)	HOMO-1 → LUMO+1 (14%) HOMO → LUMO (81%)
LUMO +1	4	1	48	48		
LUMO	4	1	48	47		
HOMO	35	2	32	32	3 (322 nm f=0.1107)	HOMO-2 → LUMO+1 (14%) HOMO-1 → LUMO (29%) HOMO → LUMO+2 (43%)
HOMO -1	8	1	46	46		
HOMO -2	14	1	43	42	4 (319 nm f=0.1216)	HOMO-2 → LUMO (25%) HOMO-1 → LUMO+1(53%)
HOMO -3	38	6	28	28		
HOMO -4	33	2	33	32	5 (318 nm f=0.0666)	HOMO -2 → LUMO+1 (10%) HOMO-1 → LUMO (24%) HOMO → LUMO+2 (45%)

Table of a description of the calculated MO contributions, excited state descriptions and their associated transitions for $[Ir(L^4)_2(bipy)]^+$ complex (Q1 and Q2 are the different quinoxaline ligands; bipy = bipyridine).

	Moiety Contribution to Orbital (%)				Orbital Contribution to Excited State	
Orbital	**Ir (5d)**	**bipy**	**Q1**	**Q2**	**Excited State**	**Contributing Transitions (> 10%)**
LUMO +4	1	70	14	14	1 (383 nm f=0.2536)	HOMO-1 → LUMO (14%) HOMO → LUMO+1 (78%)
LUMO +3	2	76	11	11		
LUMO +2	2	96	1	1	2 (379 nm f=0.0860)	HOMO-1 → LUMO+1 (17%) HOMO → LUMO (78%)
LUMO +1	4	2	45	50		
LUMO	4	2	50	45		
HOMO	32	2	33	33	3 (326 nm f=0.0653)	HOMO-1 → LUMO (11%) HOMO → LUMO+2 (68%)
HOMO -1	5	1	47	47		
HOMO -2	15	1	42	42	4 (320 nm f=0.1377)	HOMO -2 → LUMO (31%) HOMO -1 → LUMO+1(48%)
HOMO -3	29	4	33	34		
HOMO -4	22	1	39	38	5 (319 nm f=0.1153)	HOMO -2 → LUMO+1 (21%) HOMO-1 → LUMO (36%) HOMO → LUMO+2 (17%)

Table of description of the calculated MO contributions, excited state descriptions and their associated transitions for $[Ir(L^5)_2(bipy)]^+$ complex (Q1 and Q2 are the different quinoxaline ligands; bipy = bipyridine).

	Moiety Contribution to Orbital (%)				Orbital Contribution to Excited State	
Orbital	**Ir (5d)**	**bipy**	**Q1**	**Q2**	**Excited State**	**Contributing Transitions (> 10%)**
LUMO +4	1	29	35	35	1 (390 nm f=0.2120)	HOMO-1 → LUMO (12%) HOMO → LUMO+1 (80%)
LUMO +3	2	51	23	24		
LUMO +2	2	96	1	1	2 (385 nm f=0.0677)	HOMO-1 → LUMO+1 (15%) HOMO → LUMO (80%)
LUMO +1	4	1	54	41		
LUMO	4	1	41	54		
HOMO	33	2	32	32	3 (324 nm f=0.2233)	HOMO-2 → LUMO+1 (26%) HOMO-1 → LUMO (46%) HOMO → LUMO+2 (12%)
HOMO -1	6	1	47	47		
HOMO -2	12	1	44	43	4 (323 nm f=0.1541)	HOMO -2 → LUMO (29%) HOMO -1 → LUMO+1(52%)
HOMO -3	46	8	23	23		
HOMO -4	49	3	24	24	5 (317 nm f=0.0201)	HOMO → LUMO+2 (75%)

Table of description of the calculated MO contributions, excited state descriptions and their associated transitions for $[Ir(L^6)_2(bipy)]^+$ complex (Q1 and Q2 are the different quinoxaline ligands; bipy = bipyridine).

	Moiety Contribution to Orbital (%)				Orbital Contribution to Excited State	
Orbital	**Ir (5d)**	**bipy**	**Q1**	**Q2**	**Excited State**	**Contributing Transitions (> 10%)**
LUMO +4	1	15	42	42	1 (377 nm f=0.1679)	HOMO-1 → LUMO (11%) HOMO → LUMO+1 (81%)
LUMO +3	2	65	17	17		
LUMO +2	2	97	1	1	2 (377 nm f=0.0416)	HOMO → LUMO (84%)
LUMO +1	4	1	47	48		
LUMO	3	2	48	47		
HOMO	34	2	32	32	3 (318 nm f=0.1685)	HOMO-2 → LUMO+1 (28%) HOMO-1 → LUMO (35%) HOMO → LUMO+2 (21%)
HOMO -1	4	1	48	48		
HOMO -2	8	1	46	45	4 (316 nm f=0.1725)	HOMO-2 → LUMO (43%) HOMO-1 → LUMO+1(41%)
HOMO -3	20	4	38	38		
HOMO -4	17	0	42	41	5 (318 nm f=0.0666)	HOMO → LUMO+2 (64%)

Table of description of the calculated MO contributions, excited state descriptions and their associated transitions for $[Ir(L^7)_2(bipy)]^+$ complex (Q1 and Q2 are the different quinoxaline ligands; bipy = bipyridine).

	Moiety Contribution to Orbital (%)				**Orbital Contribution to Excited State**	
Orbital	**Ir (5d)**	**bipy**	**Q1**	**Q2**	**Excited State**	**Contributing Transitions (> 10%)**
LUMO +4	1	36	31	32	1 (375 nm f=0.2381)	HOMO-1 → LUMO (14%) HOMO → LUMO+1 (78%)
LUMO +3	2	77	11	11		
LUMO +2	2	97	1	1	2 (374 nm f=0.0665)	HOMO-1 → LUMO+1 (13%) HOMO → LUMO (82%)
LUMO +1	4	2	46	47		
LUMO	3	2	48	47		
HOMO	32	2	33	33	3 (322 nm f=0.1380)	HOMO-2 → LUMO+1 (22%) HOMO-1 → LUMO (24%) HOMO → LUMO+2 (39%)
HOMO -1	2	1	49	49		
HOMO -2	9	1	45	45	4 (319 nm f=0.1791)	HOMO-2 → LUMO (47%) HOMO-1 → LUMO+1(38%)
HOMO -3	20	3	38	38		
HOMO -4	11	0	45	44	5 (318 nm f=0.1056)	HOMO-4 → LUMO+1 (20%) HOMO-3 → LUMO (32%) HOMO → LUMO+2 (27%)

Table of description of the calculated MO contributions, excited state descriptions and their associated transitions for $[Ir(L^8)_2(bipy)]^+$ complex (Q1 and Q2 are the different quinoxaline ligands; bipy = bipyridine).

	Moiety Contribution to Orbital (%)				**Orbital Contribution to Excited State**	
Orbital	**Ir (5d)**	**bipy**	**Q1**	**Q2**	**Excited State**	**Contributing Transitions (> 10%)**
LUMO +4	1	11	45	44	1 (381 nm f=0.1896)	HOMO-1 → LUMO (11%) HOMO → LUMO+1 (81%)
LUMO +3	2	54	22	23		
LUMO +2	2	96	1	1	2 (380 nm f=0.0476)	HOMO-1 → LUMO+1 (11%) HOMO → LUMO (84%)
LUMO +1	4	1	48	48		
LUMO	3	2	47	48		
HOMO	33	2	33	33	3 (321 nm f=0.2982)	HOMO-2 → LUMO+1 (36%) HOMO-1 → LUMO (42%)
HOMO -1	2	1	49	49		
HOMO -2	6	1	47	46	4 (320 nm f=0.2145)	HOMO-2 → LUMO (44%) HOMO-1 → LUMO+1(40%)
HOMO -3	16	3	41	41		
HOMO -4	21	4	38	38	5 (312 nm f=0.0163)	HOMO → LUMO+2 (81%)

A. 2 Bis-Tridentate Quinoxaline Iridium (III) Complexes

Table of key bond lengths (Å) for of $[Ir(L^9)_2]^+$ (left) and $[Ir(L^{10})_2]^+$ (right).

		Exp.	**Calc.**			**Exp.**	**Calc.**
Ir(1)	N(1)	1.999(2)	2.037	Ir(1)	N(1)	2.009(5)	2.036
Ir(1)	N(31)	1.997(2)	2.037	Ir(1)	N(4)	2.191(5)	2.277
Ir(1)	N(2)	2.183(2)	2.279	Ir(1)	N(31)	2.017(5)	2.036
Ir(1)	N(32)	2.199(2)	2.279	Ir(1)	N(34)	2.198(5)	2.276
Ir(1)	C(45)	1.993(3)	2.019	Ir(1)	C(1)	1.999(6)	2.020
Ir(1)	C(15)	1.989(3)	2.019	Ir(1)	C(31)	2.005(7)	2.020

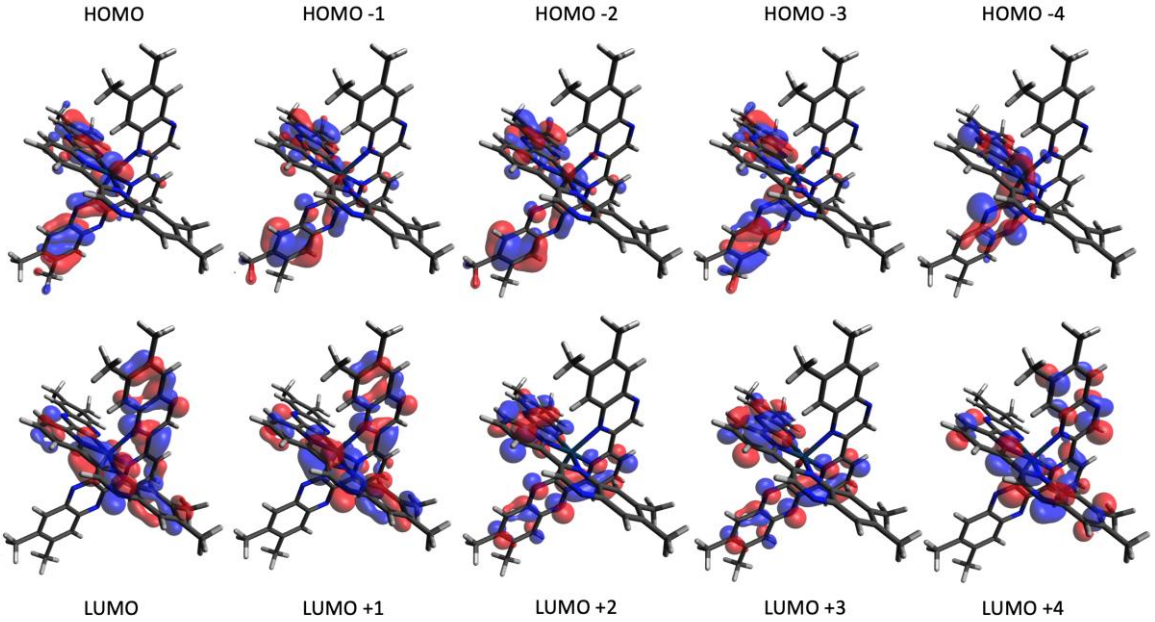

Calculated Kohn-Sham frontier molecular orbitals for $[Ir(L^{10})_2(bipy)]^+$.

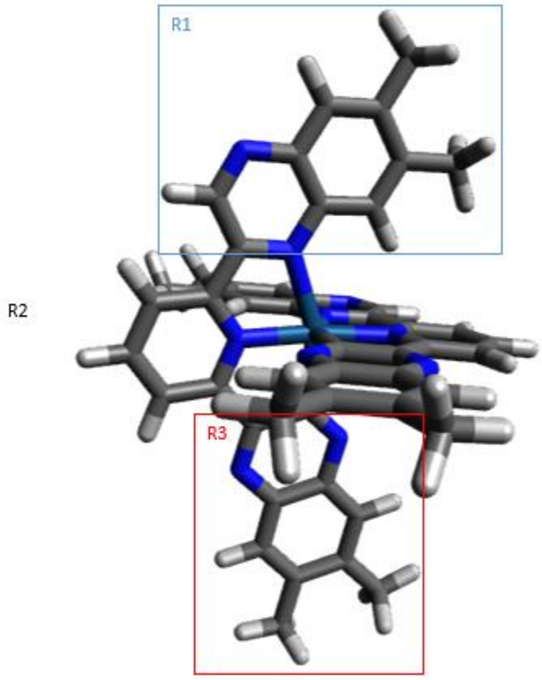

Table of description of the calculated MO contributions, excited state descriptions and their associated transitions for $[Ir(L^{10})_2(bipy)]^+$ complex.

Orbital	Moiety Contribution to Orbital (%)						
	Ir 5d	Q1			Q2		
		R1	R2	R3	R1	R2	R3
LUMO +4	1	34	16	0	33	15	0
LUMO +3	1	0	22	27	0	22	27
LUMO +2	1	1	20	29	1	20	29
LUMO +1	4	40	12	0	33	10	0
LUMO	4	31	11	1	39	14	1
HOMO	26	2	3	32	2	3	32
HOMO -1	4	2	4	40	2	5	43
HOMO -2	6	1	5	42	1	5	39
HOMO -3	2	2	4	42	2	4	42
HOMO -4	8	2	1	43	2	1	42

B. Transient Spectroscopic and Computational Analysis of poly-substituted Iridium (III) Quinoline Complexes

B.1 Cyclometallating Ligand Variation

B.1.1 UV-Vis. Spectra

Normalised UV-Vis spectra of Ir(**L**$^{11\text{-}16}$)$_2$(bipy)]PF$_6$ complexes in aerated acetonitrile

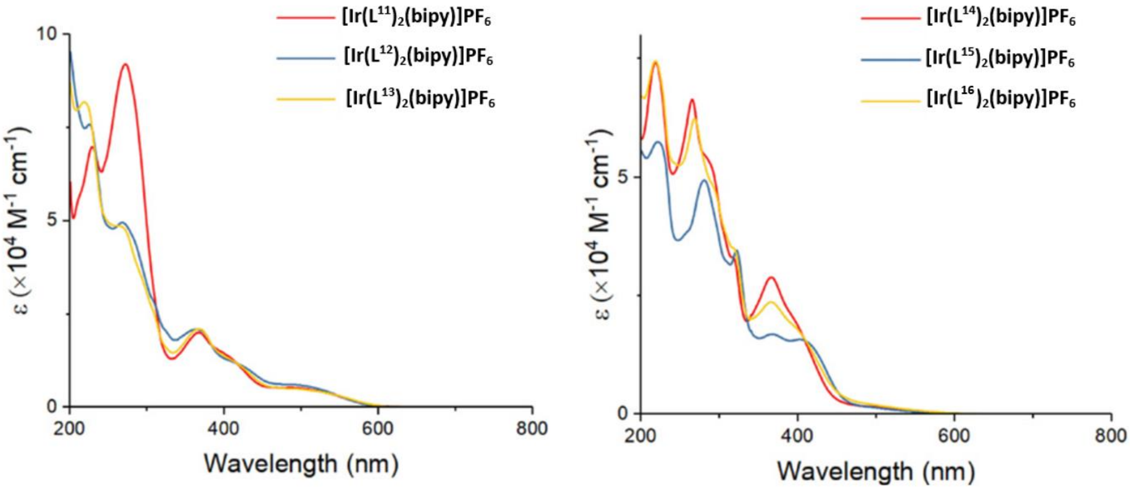

B.1.2 Emission Spectra

Normalised room temperature luminescence spectra of Ir(**L**$^{11\text{-}16}$)$_2$(bipy)]PF$_6$ complexes (aerated acetonitrile; λ_{ex}=510 nm).

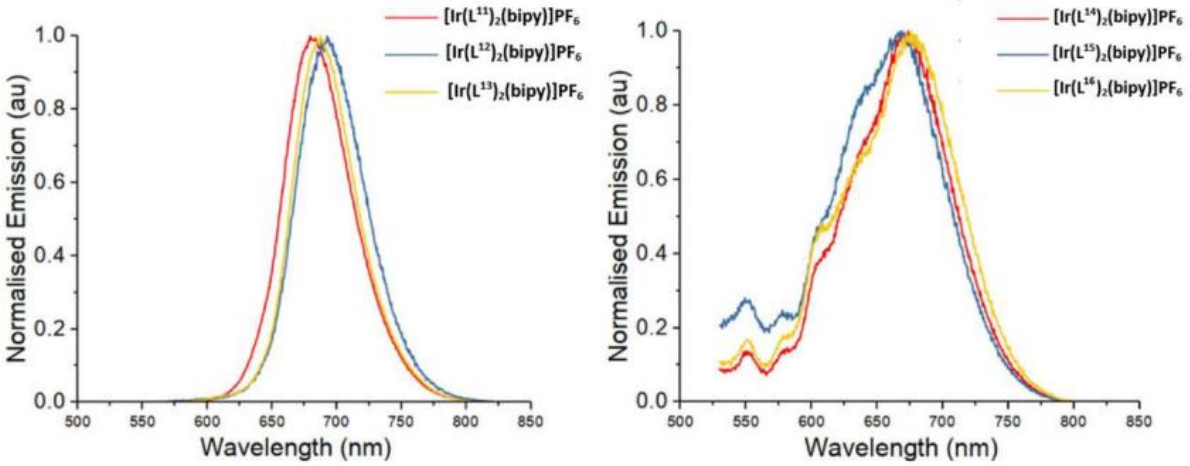

B.1.3 TA Spectra

Nanosecond time-resolved transient absorption spectra of $[\mathrm{Ir}(\mathbf{L}^{11})_2(\mathrm{bipy})]\mathrm{PF}_6$ upon pulsed laser excitation in deaerated acetonitrile (λ_{ex}=510 nm, c=5×10^{-5} M) and B) decay trace of $[\mathrm{Ir}(\mathbf{L}^{11})_2(\mathrm{bipy})]\mathrm{PF}_6$ at 625 nm in acetonitrile (c=5×10^{-5} M) under air and N_2, 20 °C

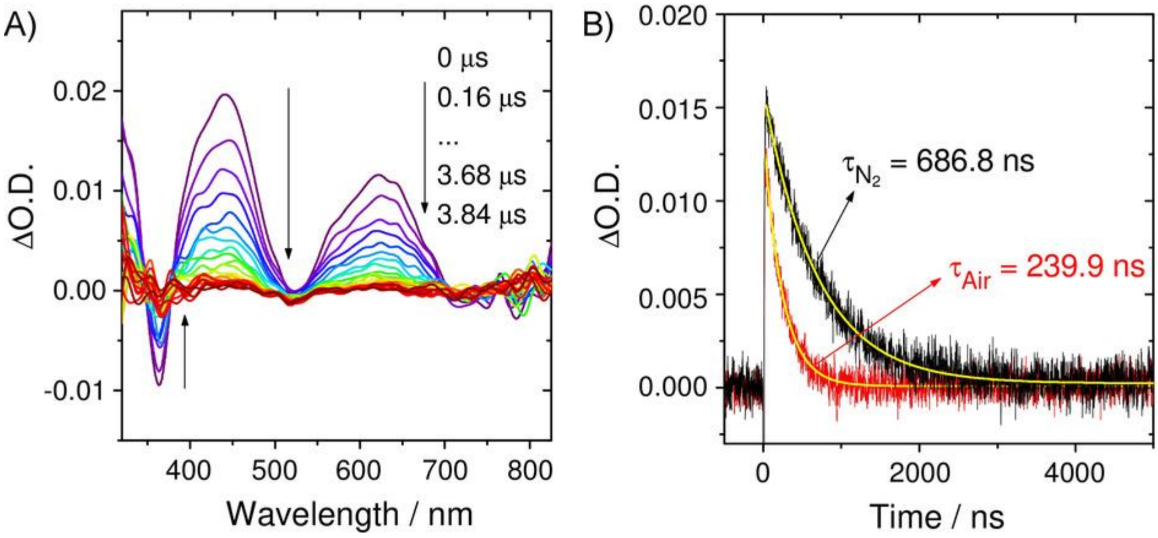

B.1.4 DFT

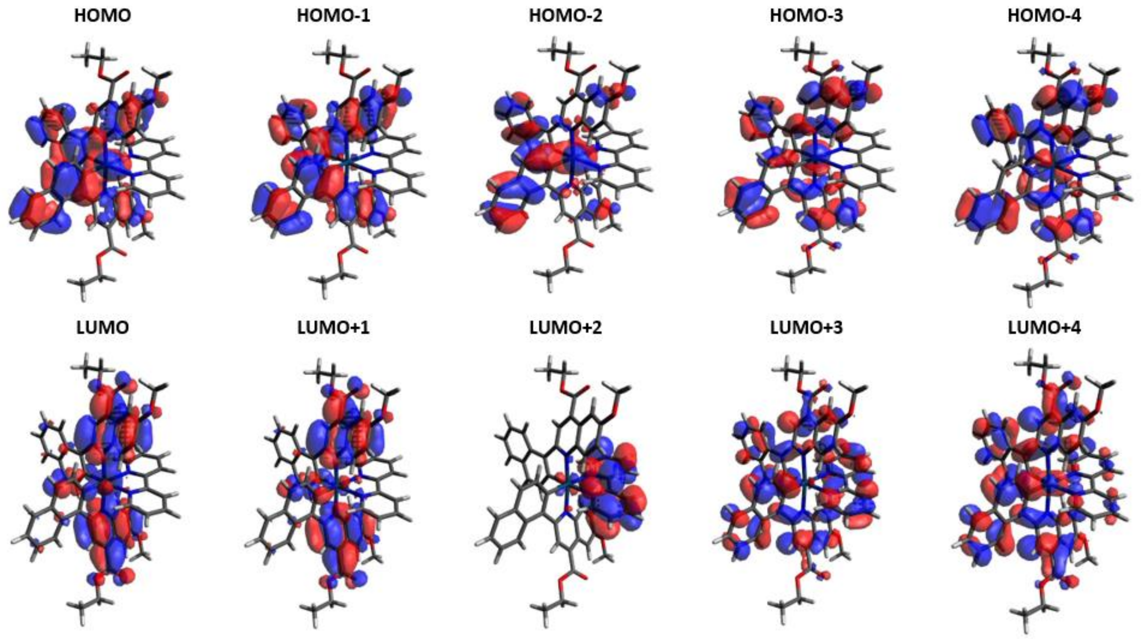

Calculated Kohn-Sham frontier molecular orbitals for $[\mathrm{Ir}(L^{11})_2(\mathrm{bipy})]^+$.

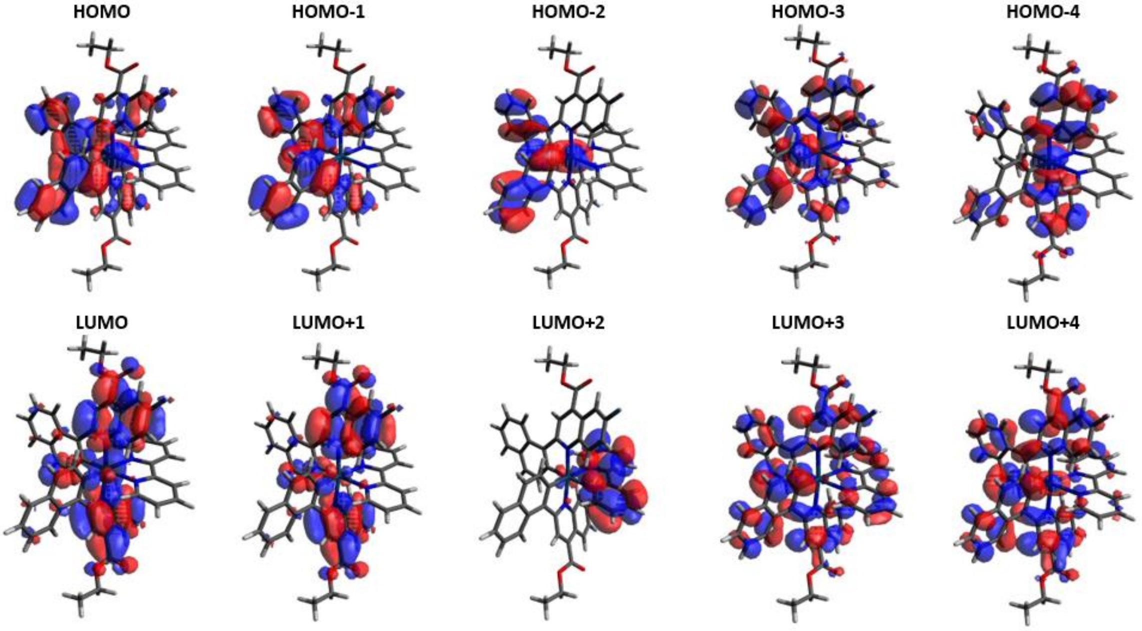

Calculated Kohn-Sham frontier molecular orbitals for $[Ir(L^{12})_2(bipy)]^+$.

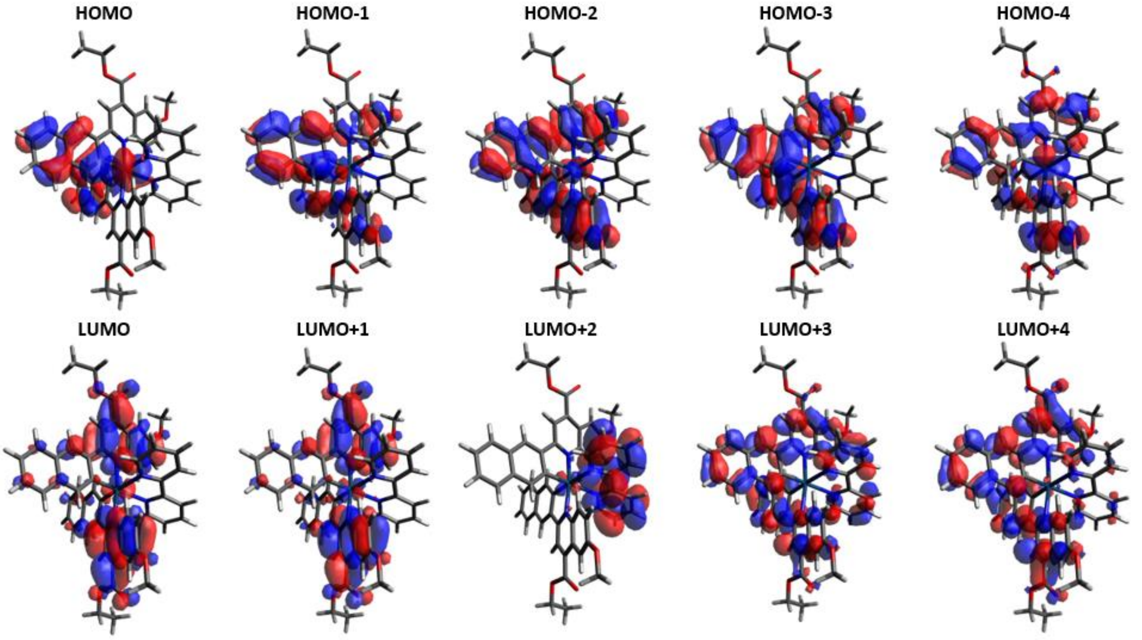

Calculated Kohn-Sham frontier molecular orbitals for $[Ir(L^{15})_2(bipy)]^+$.

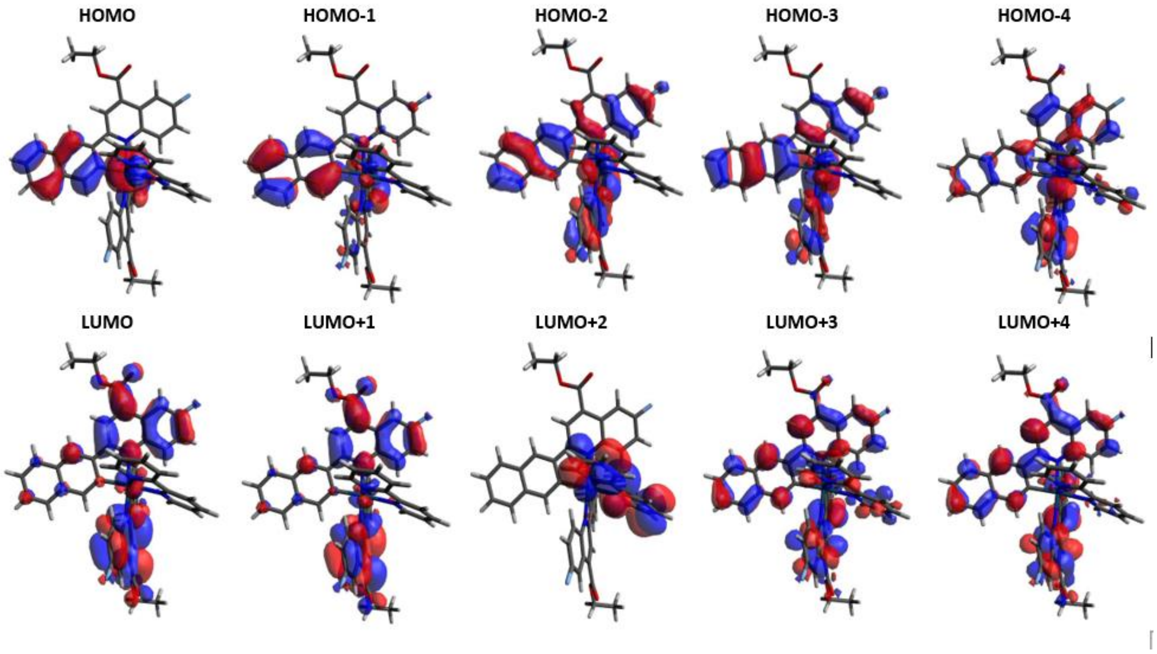

Calculated Kohn-Sham frontier molecular orbitals for [Ir(L^{16})$_2$(bipy)

Table of description of the calculated MO contributions, excited state descriptions and their associated transitions for [Ir(L^{12})$_2$(bipy)]$^+$ complex (Q1 and Q2 are the different quinoline ligands; bipy = bipyridine).

	Moiety Contribution to Orbital (%)				**Orbital Contribution to Excited State**	
Orbital	**Ir (5d)**	**Bipy**	**Q1**	**Q2**	**Excited State**	**Contributing Transitions**
LUMO +4	2	7	45	45	1 (442 nm f=0.1234)	HOMO-1 → LUMO +1 (19.37%) HOMO → LUMO (73.76%)
LUMO +3	2	26	35	36		
LUMO +2	2	96	1	1	2 (440 nm f=0.2356)	HOMO-1 → LUMO (21.61%) HOMO → LUMO +1 (70.67%)
LUMO +1	3	1	46	49		
LUMO	5	1	48	46		
HOMO	19	1	40	40	3 (358 nm f=0.1743)	HOMO -3 → LUMO (2.77%) HOMO -2 → LUMO+1 (16.33%) HOMO -1 → LUMO (44.84%) HOMO → LUMO +2 (16.41%)
HOMO -1	1	0	49	49		
HOMO -2	19	1	40	40		
HOMO -3	14	0	43	43	4 (356 nm f=0.0993)	HOMO -2 → LUMO (19.93%) HOMO -1 → LUMO+1 (56.16%) HOMO → LUMO (10.19%)
HOMO -4	20	2	39	39	5 (350 nm f=0.0101)	HOMO -1 → LUMO (10.75%) HOMO → LUMO+2 (70.75%)

Table of description of the calculated MO contributions, excited state descriptions and their associated transitions for $[\mathrm{Ir}(L^{13})_2(\mathrm{bipy})]^+$ complex (Q1 and Q2 are the different quinoline ligands; bipy = bipyridine).

	Moiety Contribution to Orbital (%)				**Orbital Contribution to Excited State**	
Orbital	**Ir (5d)**	**Bipy**	**Q1**	**Q2**	**Excited State**	**Contributing Transitions**
LUMO +4	2	5	47	46	1 (441 nm f=0.1209)	HOMO-1 → LUMO +1 (12.97%) HOMO → LUMO (62.47%) HOMO → LUMO +1 (12.67%)
LUMO +3	2	17	40	41		
LUMO +2	2	97	1	1	2 (440 nm f=0.1796)	HOMO-1 → LUMO (14.23%) HOMO → LUMO (13.20%) HOMO → LUMO +1 (60.47%)
LUMO +1	3	1	51	45		
LUMO	5	1	44	50		
HOMO	20	1	39	39	3 (356 nm f=0.1961)	HOMO -2 → LUMO+1 (16.38%) HOMO -1 → LUMO (57.46%)
HOMO -1	1	0	49	49		
HOMO -2	16	1	41	41		
HOMO -3	31	4	33	32	4 (355 nm f=0.1243)	HOMO -2 → LUMO (17.40%) HOMO -1 → LUMO+1 (60.85%)
HOMO -4	35	1	31	33	5 (342 nm f=0.0171)	HOMO → LUMO+2 (81.52%)

Table of description of the calculated MO contributions, excited state descriptions and their associated transitions for $[\mathrm{Ir}(L^{15})_2(\mathrm{bipy})]^+$ complex (Q1 and Q2 are the different quinoline ligands; bipy = bipyridine)

	Moiety Contribution to Orbital (%)				**Orbital Contribution to Excited State**	
Orbital	**Ir (5d)**	**bipy**	**Q1**	**Q2**	**Excited State**	**Contributing Transitions**
LUMO +4	1	5	47	47	1 (405 nm f=0.0144)	HOMO-2 → LUMO (10.62%) HOMO → LUMO (77.40%)
LUMO +3	1	16	42	42		
LUMO +2	2	97	1	1	2 (402 nm f=0.0610)	HOMO-2 → LUMO+1(10.29%) HOMO → LUMO+1 (75.43%)
LUMO +1	3	1	49	48		
LUMO	2	1	48	49		
HOMO	30	2	34	34	3 (370 nm f=4495)	HOMO-2 → LUMO +1 (31.57) HOMO-1 → LUMO (42.00%) HOMO → LUMO+1 (10.25%)
HOMO -1	3	1	48	48		
HOMO -2	5	0	47	47	4 (370 nm f=0.2992)	HOMO -2 → LUMO +1 (37.65%) HOMO -1 → LUMO (34.00%) HOMO → LUMO+1 (11.46%)
HOMO -3	2	1	49	49		
HOMO -4	30	2	49	19	5 (346 nm f=0.0013)	HOMO → LUMO+2 (83.69%)

Table of description of the calculated MO contributions, excited state descriptions and their associated transitions for $[\mathrm{Ir}(L^{16})_2(\mathrm{bipy})]^+$ complex (Q1 and Q2 are the different quinoline ligands; bipy = bipyridine)

	Moiety Contribution to Orbital (%)				**Orbital Contribution to Excited State**	
Orbital	**Ir (5d)**	**bipy**	**Q1**	**Q2**	**Excited State**	**Contributing Transitions**
LUMO +4	1	3	48	48	1 (414 nm f=0.0007)	HOMO → LUMO (84.00%)
LUMO +3	1	11	44	44		
LUMO +2	2	97	0	1	2 (402 nm f=0.0610)	HOMO → LUMO+1 (82.50%)
LUMO +1	3	0	49	48		
LUMO	2	1	48	49		
HOMO	29	2	34	35	3 (370 nm f=4495)	HOMO-2 → LUMO+1 (29.38)
HOMO -1	3	1	48	48		HOMO-1 → LUMO (50.60%)
HOMO -2	9	0	45	45	4 (370 nm f=0.2992)	HOMO -3 → LUMO (10.22%)
HOMO -3	8	1	45	45		HOMO -2 → LUMO +1 (38.45%) HOMO -1 → LUMO (38.22%)
HOMO -4	49	7	22	22	5 (346 nm f=0.0013)	HOMO → LUMO+2 (83.60%)

B.2 Ancillary Ligand Variation

Kinetic traces of the major features of the transient spectra of $[Ir(L^{11})_2(L^{17})]^+$ (left) and $[Ir(L^{11})_2(L^{19})]^+$ (right) complexes in acetonitrile at room temperature, aerated. Wavelengths and lifetimes of each trace are inset.

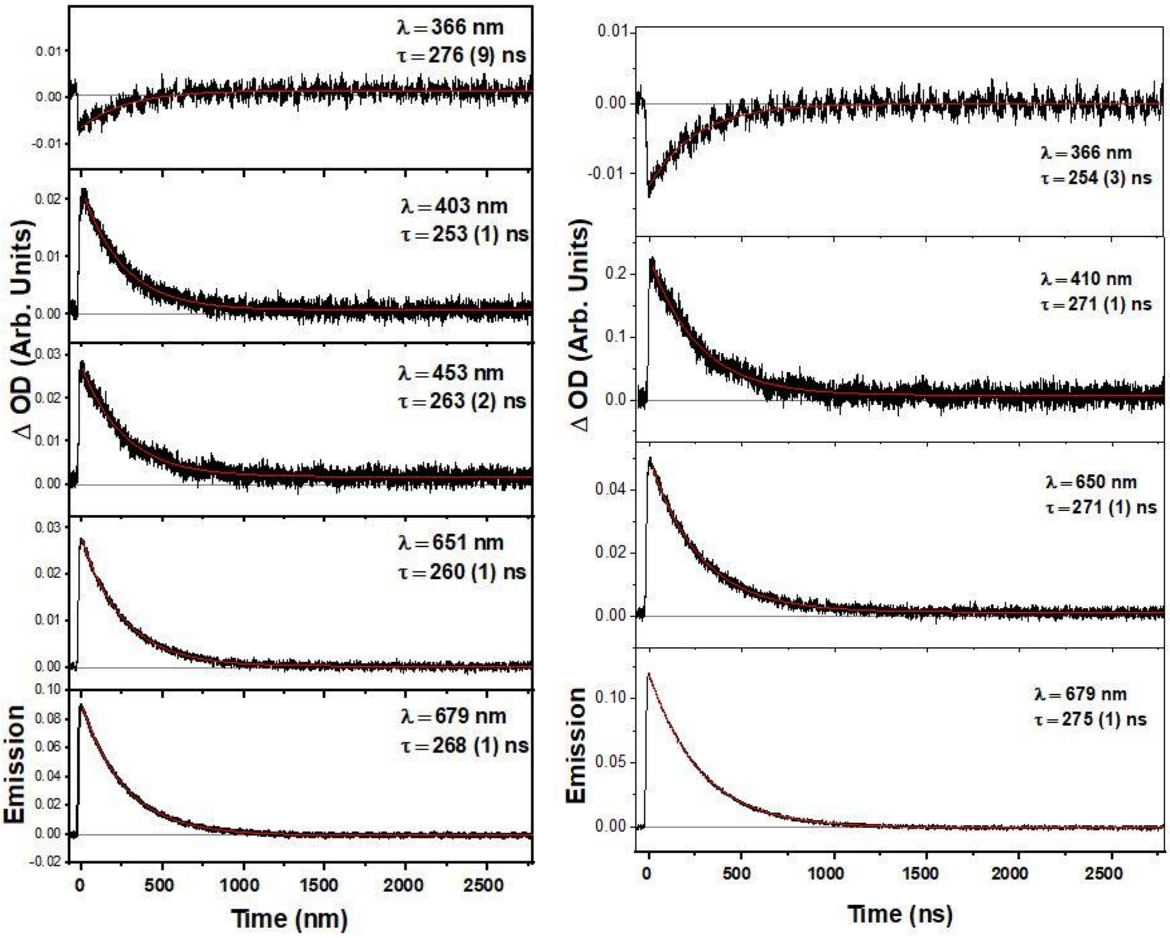

Kinetic traces of the major features of the transient spectra of $[\mathrm{Ir}(\mathrm{L}^{11})_2(\mathrm{L}^{20})]^+$ (left) and $[\mathrm{Ir}(\mathrm{L}^{11})_2(\mathrm{L}^{22})]^+$ (right) complexes in acetonitrile at room temperature, aerated. Wavelengths and lifetimes of each trace are inset.

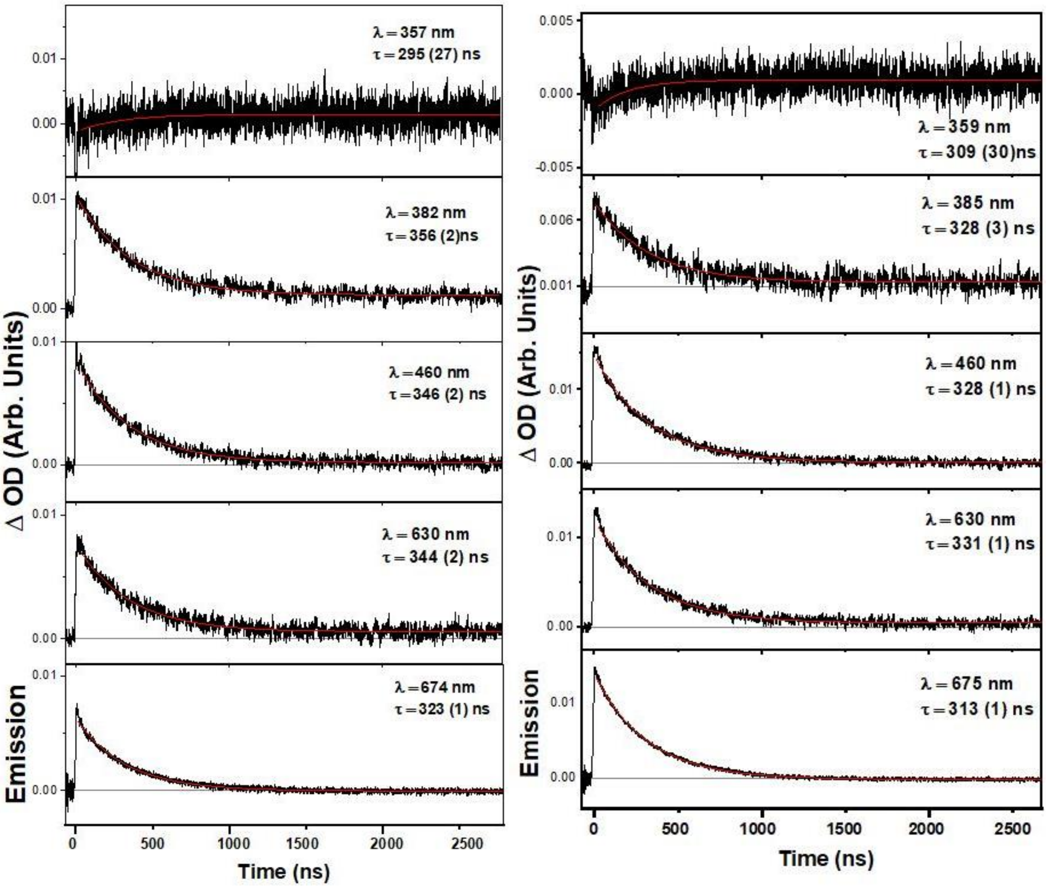

Kinetic traces of the major features of the transient spectra of $[Ir(L^{14})_2(L^{17})]^+$ (left) and $[Ir(L^{14})_2(L^{19})]^+$ (right) complexes in acetonitrile at room temperature, aerated. Wavelengths and lifetimes of each trace are inset.

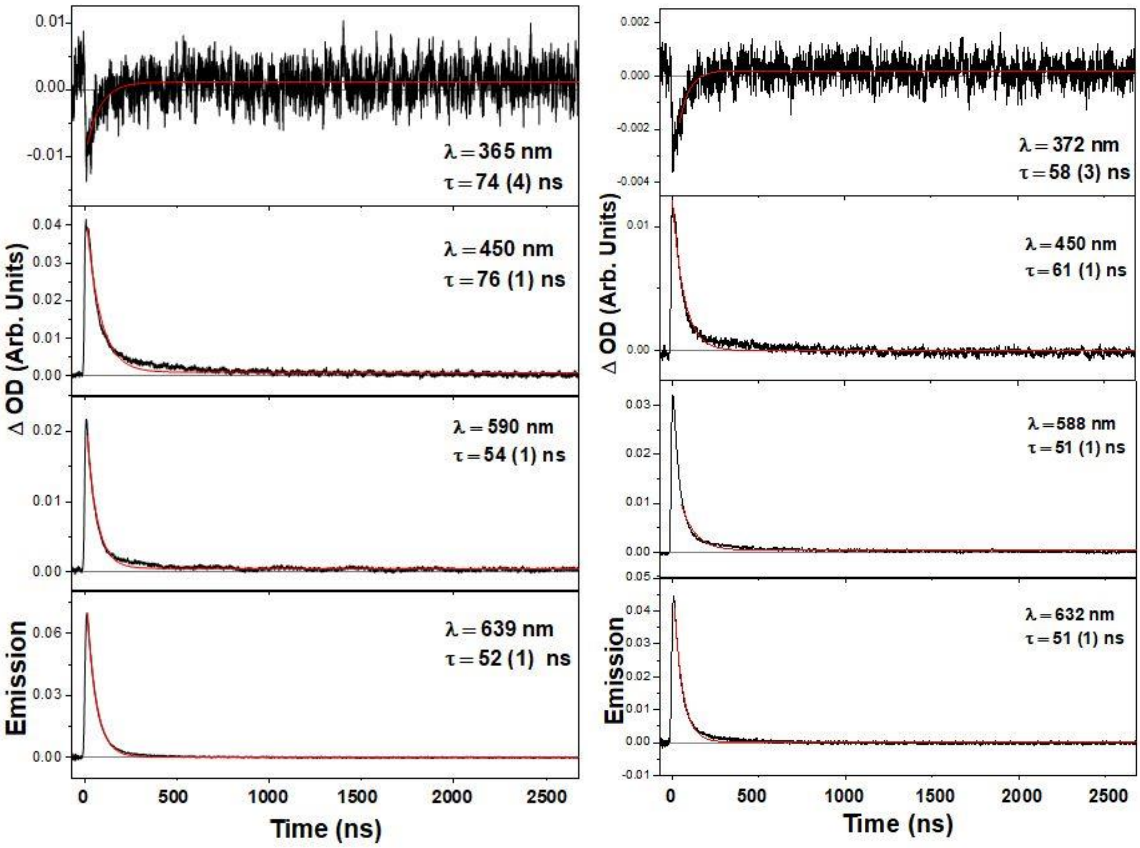

Kinetic traces of the major features of the transient spectra of $[Ir(L^{14})_2(L^{21})]^+$ (left) and $[Ir(L^{14})_2(L^{22})]^+$ (right) complexes in acetonitrile at room temperature, aerated. Wavelengths and lifetimes of each trace are inset.

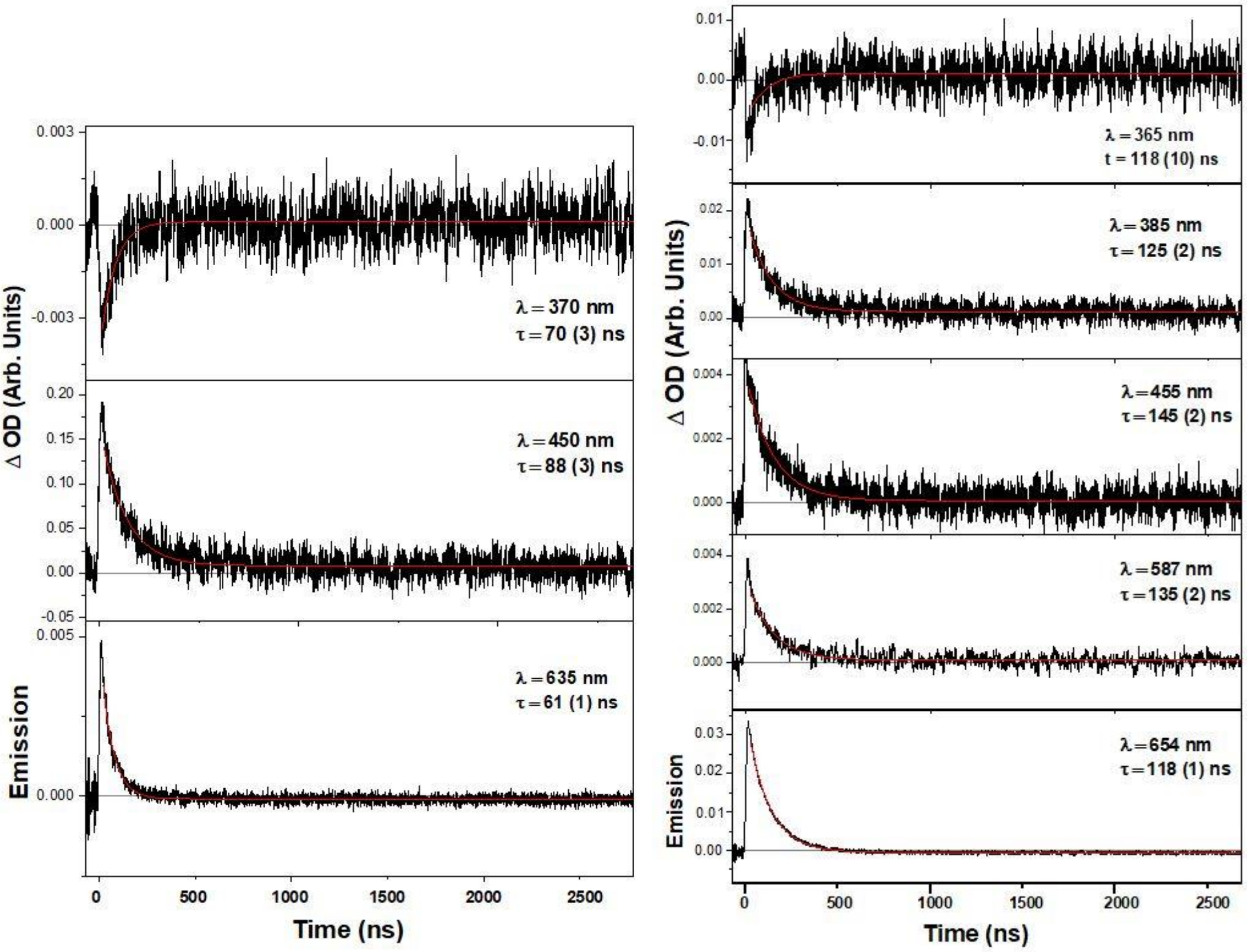

Table of description of the calculated MO contributions, excited state descriptions and their associated transitions for $[Ir(L^{11})_2(L^{18})]^+$ complex (Q1 and Q2 are the different quinoline ligands).

	Moiety Contribution to Orbital (%)				**Orbital Contribution to Excited State**	
Orbital	**Ir (5d)**	**L^n**	**Q1**	**Q2**	**Excited State**	**Contributing Transitions**
LUMO +4	2	28	11	54	1 (439.44nm f=0.1524)	HOMO → LUMO (31.07%) HOMO → LUMO+1 (34.39%) HOMO → LUMO+2 (12.12%)
LUMO +3	1	98	1	0		
LUMO +2	4	6	50	40		
LUMO +1	4	2	39	55	2 (421.87 nm f=0.1453)	HOMO-1 → LUMO+1 (23.10%) HOMO → LUMO+1 (30.57%) HOMO → LUMO+2 (27.64%)
LUMO	3	91	5	1	3 (393.98nm f=0.0370)	HOMO → LUMO (46.20%) HOMO → LUMO+2 (28.53%)
HOMO	19	1	48	32		
HOMO -1	2	1	43	54	4 (376.66 nm f=0.1715)	HOMO-3 → LUMO (17.32%) HOMO-2 → LUMO+2 (69.41%)
HOMO -2	14	25	29	32		
HOMO -3	7	68	17	8		
HOMO -4	15	6	28	50	5 (356.07 nm f=0.0814)	HOMO-1 → LUMO (46.67%) HOMO-1 → LUMO+2 (11.72%)

Table of description of the calculated MO contributions, excited state descriptions and their associated transitions for $[Ir(L^{11})_2(L^{19})]^+$ complex (Q1 and Q2 are the different quinoline ligands).

	Moiety Contribution to Orbital (%)				**Orbital Contribution to Excited State**	
Orbital	**Ir (5d)**	**L^n**	**Q1**	**Q2**	**Excited State**	**Contributing Transitions**
LUMO +4	2	43	7	47	1 (441.10 nm f=0.1466)	HOMO → LUMO (34.35 %) HOMO → LUMO+1 (33.66%) HOMO → LUMO+2 (10.20%)
LUMO +3	1	98	1	1		
LUMO +2	4	4	46	46		
LUMO +1	4	2	46	46	2 (421.80 nm f=0.1548)	HOMO-1 → LUMO+1 (20.73%) HOMO → LUMO+1 (30.03%) HOMO → LUMO+2 (28.52%)
LUMO	2	93	3	1	3 (400.87 nm f=0.0344)	HOMO → LUMO (44.17%) HOMO → LUMO+2 (28.49%)
HOMO	18	1	49	31		
HOMO -1	2	1	42	55	4 (360.16 nm f=0.0619)	HOMO-1 → LUMO (68.49%)
HOMO -2	12	2	43	39		
HOMO -3	22	7	39	32	5 (346.84 nm f=0.1501)	HOMO-1 → LUMO+1 (45.20%) HOMO-1 → LUMO+2 (10.00%)
HOMO -4	27	1	48	24		

Table of description of the calculated MO contributions, excited state descriptions and their associated transitions for $[Ir(L^{11})_2(L^{21})]^+$ complex (Q1 and Q2 are the different quinoline ligands).

	Moiety Contribution to Orbital (%)				**Orbital Contribution to Excited State**	
Orbital	**Ir (5d)**	**L^n**	**Q1**	**Q2**	**Excited State**	**Contributing Transitions**
LUMO +4	1	92	2	5	1 (439.34 nm f=0.1399)	HOMO → LUMO (36.74%) HOMO → LUMO+1 (35.50%)
LUMO +3	1	94	4	1	2 (419.84 nm f=0.1661)	HOMO-1 → LUMO+1 (18.30%) HOMO → LUMO+1 (25.10%) HOMO→ LUMO+2 (30.18%)
LUMO +2	4	4	12	80		
LUMO +1	4	5	78	14	3 (410.67 nm f=0.0345)	HOMO → LUMO (39.39%) HOMO → LUMO+1 (11.28%) HOMO → LUMO+2 (29.24%)
LUMO	3	94	3	1		
HOMO	17	1	49	33	4 (363.12 nm f=0.0265)	HOMO-1 → LUMO (81.60%)
HOMO -1	2	1	42	55	5 (346.14 nm f=0.1325)	HOMO-6→ LUMO (23.07%) HOMO-4→ LUMO (23.06%) HOMO-3→ LUMO (22.87%)
HOMO -2	16	5	39	39		
HOMO -3	6	80	12	2		
HOMO -4	5	4	38	52		

Table of description of the calculated MO contributions, excited state descriptions and their associated transitions for $[Ir(L^{11})_2(L^{22})]^+$ complex (Q1 and Q2 are the different quinoline ligands).

	Moiety Contribution to Orbital (%)				**Orbital Contribution to Excited State**	
Orbital	**Ir (5d)**	**L^n**	**Q1**	**Q2**	**Excited State**	**Contributing Transitions**
LUMO +4	1	90	3	6	1 (443.19nm f=0.1045)	HOMO → LUMO (51.82%) HOMO → LUMO+1 (25.23%)
LUMO +3	1	94	4	1	2 (420.77nm f=0.1795)	HOMO-1 → LUMO+1 (13.18%) HOMO → LUMO (18.75%) HOMO → LUMO+1 (42.53%)
LUMO +2	4	4	29	63	3 (415.03 nm f=0.0570)	HOMO-1 → LUMO+1 (17.33%) HOMO → LUMO (15.17%) HOMO → LUMO+2 (51.75%)
LUMO +1	4	3	61	32		
LUMO	3	94	2	1	4 (370.67 nm f=0.0186)	HOMO-1 → LUMO (83.07%)
HOMO	18	1	48	33	5 (347.07 nm f=0.0910)	HOMO-2 → LUMO+1 (13.13%) HOMO-1 → LUMO+1 (24.04%) HOMO-1 → LUMO+2 (32.75%)
HOMO -1	2	1	43	54		
HOMO -2	17	2	41	40		
HOMO -3	28	7	54	11		
HOMO -4	21	1	29	49		

Table of description of the calculated MO contributions, excited state descriptions and their associated transitions for $[Ir(L^{14})_2(L^{18})]^+$ complex (Q1 and Q2 are the different quinoline ligands).

	Moiety Contribution to Orbital (%)				**Orbital Contribution to Excited State**	
Orbital	**Ir (5d)**	**L^n**	**Q1**	**Q2**	**Excited State**	**Contributing Transitions**
LUMO +4	1	6	37	56	1 (412.46 nm f=0.0194)	HOMO → LUMO (59.88%) HOMO → LUMO+2 (12.40%)
LUMO +3	1	97	2	1	2 (396.64 nm f=0.0134)	HOMO → LUMO+1 (69.12%)
LUMO +2	2	10	62	26	3 (382.28 nm f=0.0171)	HOMO → LUMO (17.71%) HOMO → LUMO +2(58.02%)
LUMO +1	2	2	25	70		
LUMO	3	87	10	1	4 (362.62 nm f=0.0185)	HOMO-4 → LUMO (41.52%) HOMO-2 → LUMO+2 (10.68%)
HOMO	28	2	37	33		
HOMO -1	2	1	49	48	5 (356.44 nm f=0.5120)	HOMO-4 → LUMO (39.16%) HOMO-1 → LUMO+2(14.43%)
HOMO -2	11	1	48	39		
HOMO -3	12	5	35	48		
HOMO -4	1	90	7	2		

Table of description of the calculated MO contributions, excited state descriptions and their associated transitions for $[Ir(L^{14})_2(L^{19})]^+$ complex (Q1 and Q2 are the different quinoline ligands).

	Moiety Contribution to Orbital (%)				**Orbital Contribution to Excited State**	
Orbital	**Ir (5d)**	**L^n**	**Q1**	**Q2**	**Excited State**	**Contributing Transitions**
LUMO +4	1	7	38	54	1 (419.18 nm f=0.0109)	HOMO → LUMO (86.63%)
LUMO +3	1	97	1	1		
LUMO +2	2	3	28	67	2 (395.68 nm f=0.0169)	HOMO → LUMO +1 (65.37%) HOMO → LUMO +2 (13.64%)
LUMO +1	2	3	65	30	3 (387.48 nm f=0.0122)	HOMO → LUMO (12.27%) HOMO → LUMO +2 (59.92%)
LUMO	2	92	4	1		
HOMO	28	2	37	33	4 (360.80 nm f=2800)	HOMO-2 → LUMO (12.04%) HOMO-2 → LUMO+2 (16.53%) HOMO-1 → LUMO (16.48%) HOMO -1 → LUMO +2 (23.65%)
HOMO -1	2	1	49	48		
HOMO -2	11	1	48	40		
HOMO -3	11	2	39	49	5 (351.89 nm f=0.4298)	HOMO -3→ LUMO +1 (13.01%) HOMO -2→ LUMO +1 (26.49%) HOMO -1→ LUMO +1 (37.47%)
HOMO -4	31	18	33	18		

Table of description of the calculated MO contributions, excited state descriptions and their associated transitions for $[Ir(L^{14})_2(L^{21})]^+$ complex (Q1 and Q2 are the different quinoline ligands).

	Moiety Contribution to Orbital (%)				**Orbital Contribution to Excited State**	
Orbital	**Ir (5d)**	**L^n**	**Q1**	**Q2**	**Excited State**	**Contributing Transitions**
LUMO +4	1	75	8	15	1 (419.55 nm f=0.0118)	HOMO → LUMO (72.92%)
LUMO +3	1	95	2	1		
LUMO +2	2	1	5	92	2 (393.71nm f=0.0072)	HOMO → LUMO+1 (76.39%)
LUMO +1	2	6	87	5	3 (390.40 nm f=0.0217)	HOMO → LUMO+2 (68.83%)
LUMO	3	93	3	1		
HOMO	27	2	38	33	4 (366.87 nm f=0.0303)	HOMO-4 → LUMO (69.42%)
HOMO -1	2	1	48	49	5 (358.59 nm f=0.5052)	HOMO-4 → LUMO (17.03%) HOMO-2 → LUMO +2 (16.79%) HOMO-1 → LUMO +1 (11.93%) HOMO-1 → LUMO +2 (11.71%)
HOMO -2	11	1	50	39		
HOMO -3	8	3	37	52		
HOMO -4	2	93	5	1		

Table of description of the calculated MO contributions, excited state descriptions and their associated transitions for $[Ir(L^{14})_2(L^{22})]^+$ complex (Q1 and Q2 are the different quinoline ligands).

	Moiety Contribution to Orbital (%)				**Orbital Contribution to Excited State**	
Orbital	**Ir (5d)**	**L^n**	**Q1**	**Q2**	**Excited State**	**Contributing Transitions**
LUMO +4	1	86	5	8	1 (430.68 nm f=0.0046)	HOMO → LUMO (77.86%)
LUMO +3	1	95	3	1		
LUMO +2	2	1	4	93	2 (392.79 nm f=0.0043)	HOMO → LUMO +1(66.58%) HOMO → LUMO +2(12.96%)
LUMO +1	2	5	89	3	3 (391.46 nm f=0.0284)	HOMO → LUMO+1 (12.45%) HOMO→ LUMO+2 (63.09%)
LUMO	3	94	2	1		
HOMO	26	2	38	34	4 (362.65nm f=0.2288)	HOMO -2→ LUMO (12.43%) HOMO -2→ LUMO+2 (10.29%) HOMO-1 → LUMO (21.99%) HOMO -1 → LUMO+1 (17.47%)
HOMO -1	2	1	49	49	5 (352.42 nm f=0.0427)	HOMO -2→ LUMO (12.43%) HOMO -2→ LUMO+2 (10.29%) HOMO-1 → LUMO (21.99%) HOMO -1 → LUMO+1 (17.47%)
HOMO -2	11	1	50	39		
HOMO -3	7	2	39	52		
HOMO -4	30	11	54	4		

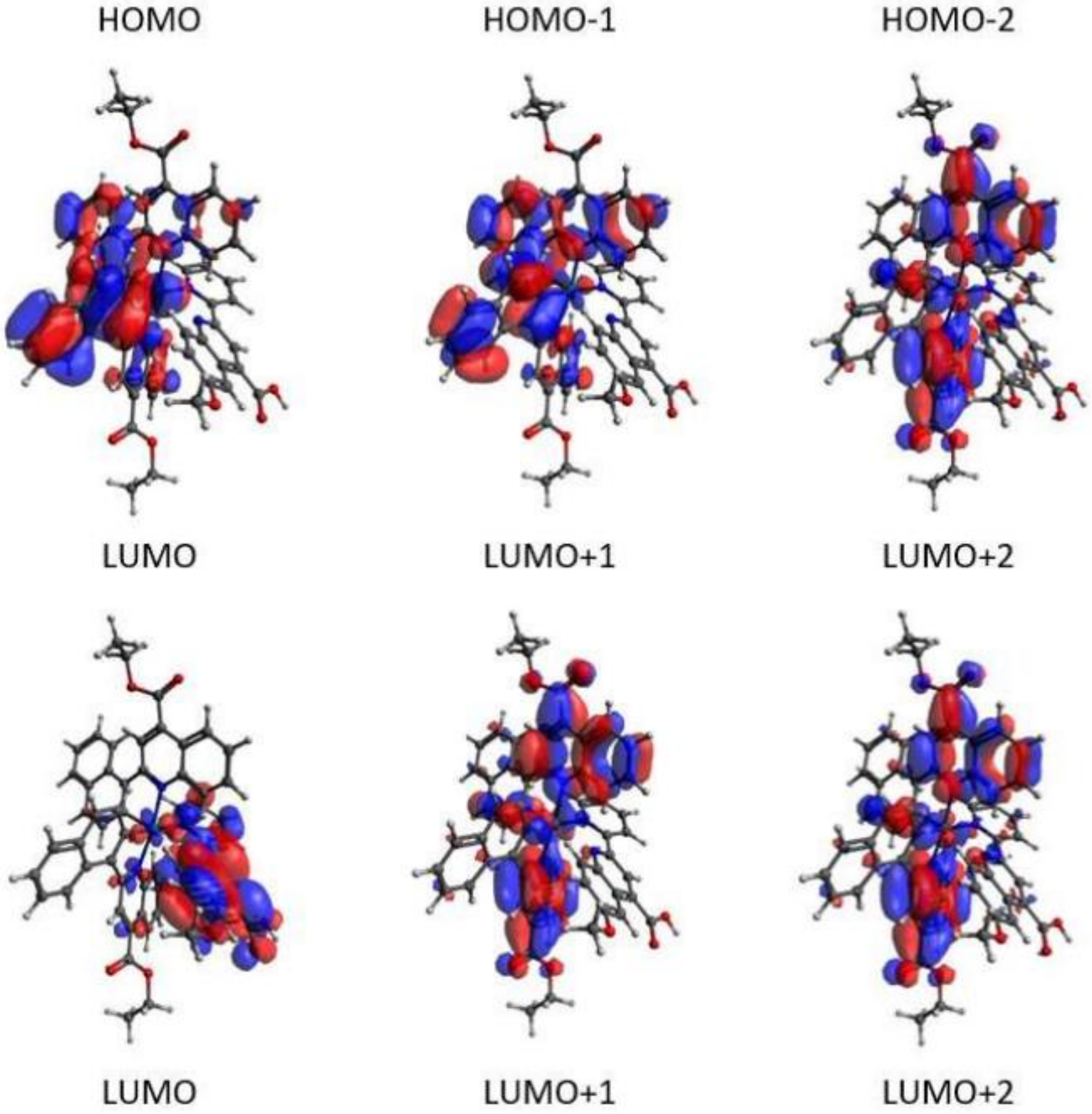

Calculated Kohn-Sham frontier molecular orbitals for $[Ir(L^{11})_2(L^{18})]^+$

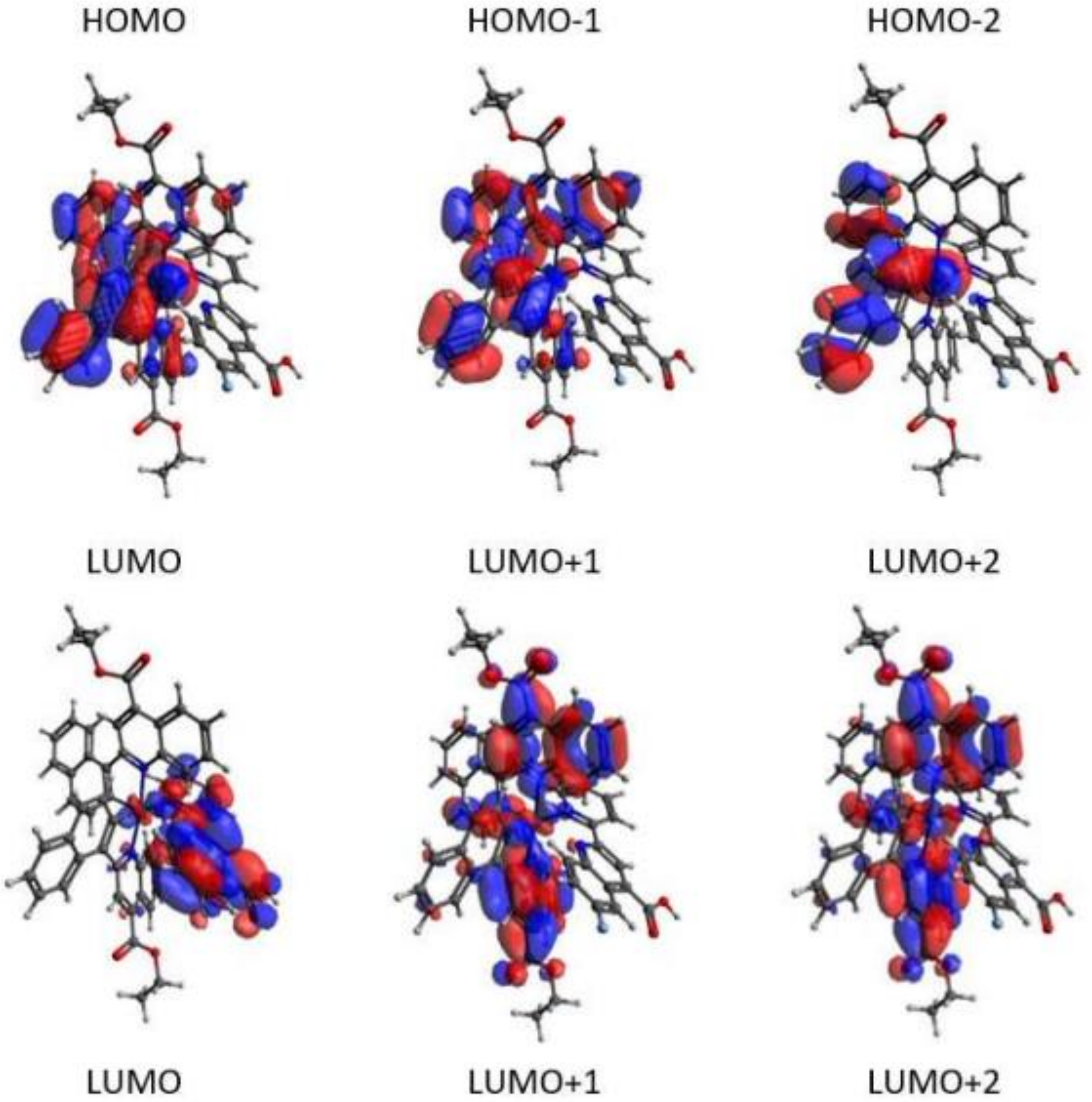

Calculated Kohn-Sham frontier molecular orbitals for $[Ir(L^{11})_2(L^{19})]^+$

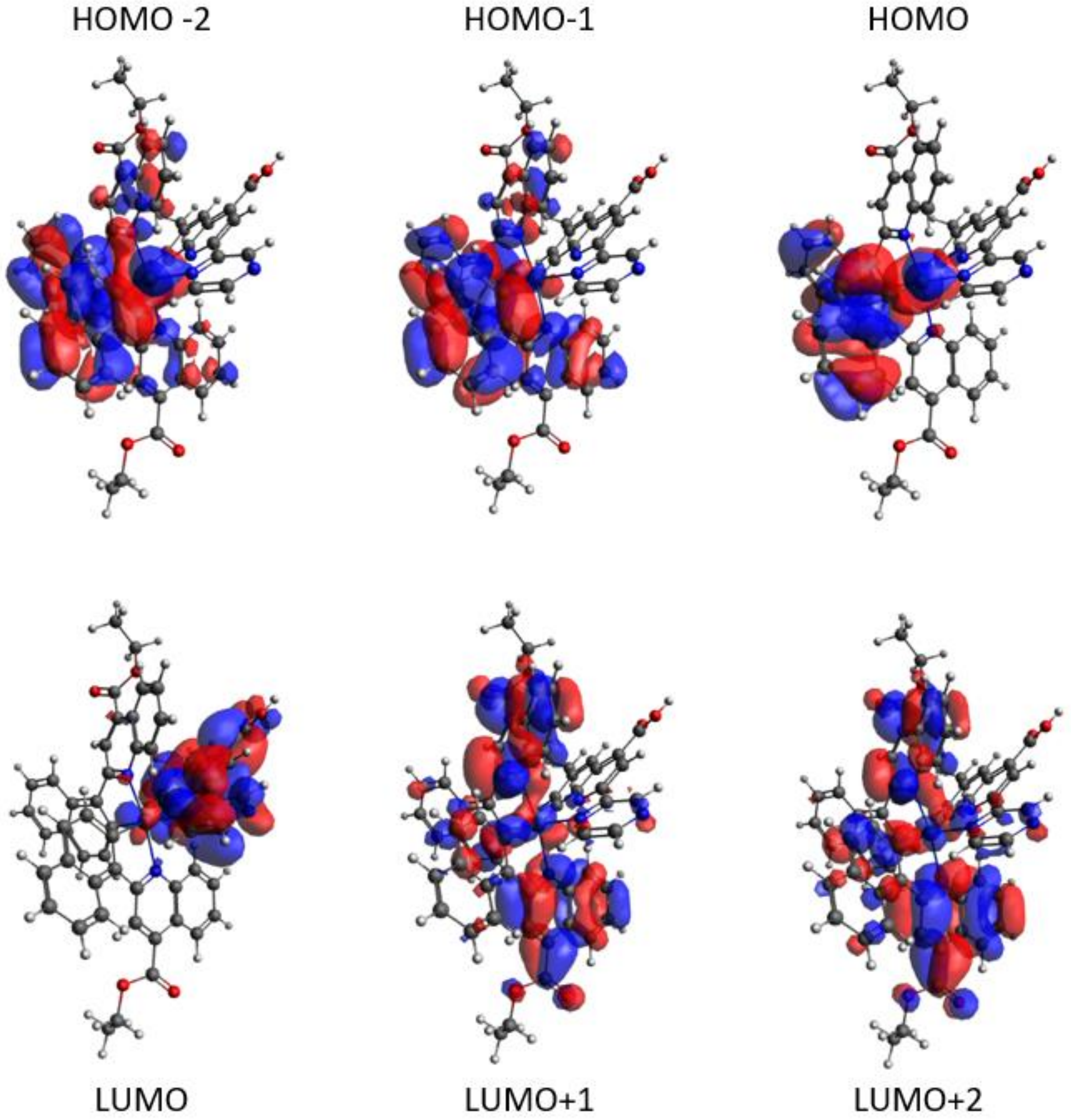

Calculated Kohn-Sham frontier molecular orbitals for $[Ir(L^{11})_2(L^{21})]^+$

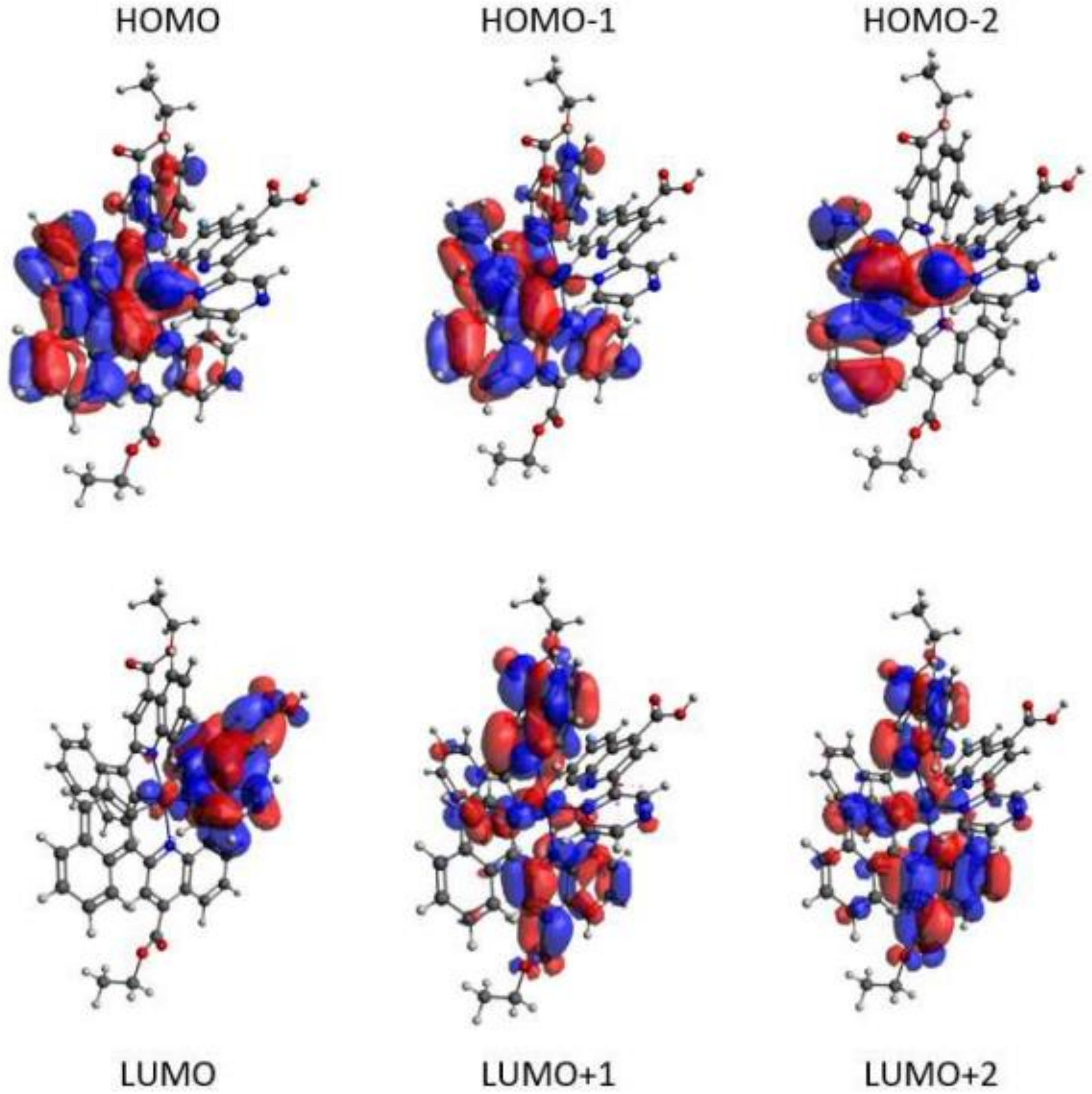

Calculated Kohn-Sham frontier molecular orbitals for $[Ir(L^{11})_2(L^{22})]^+$

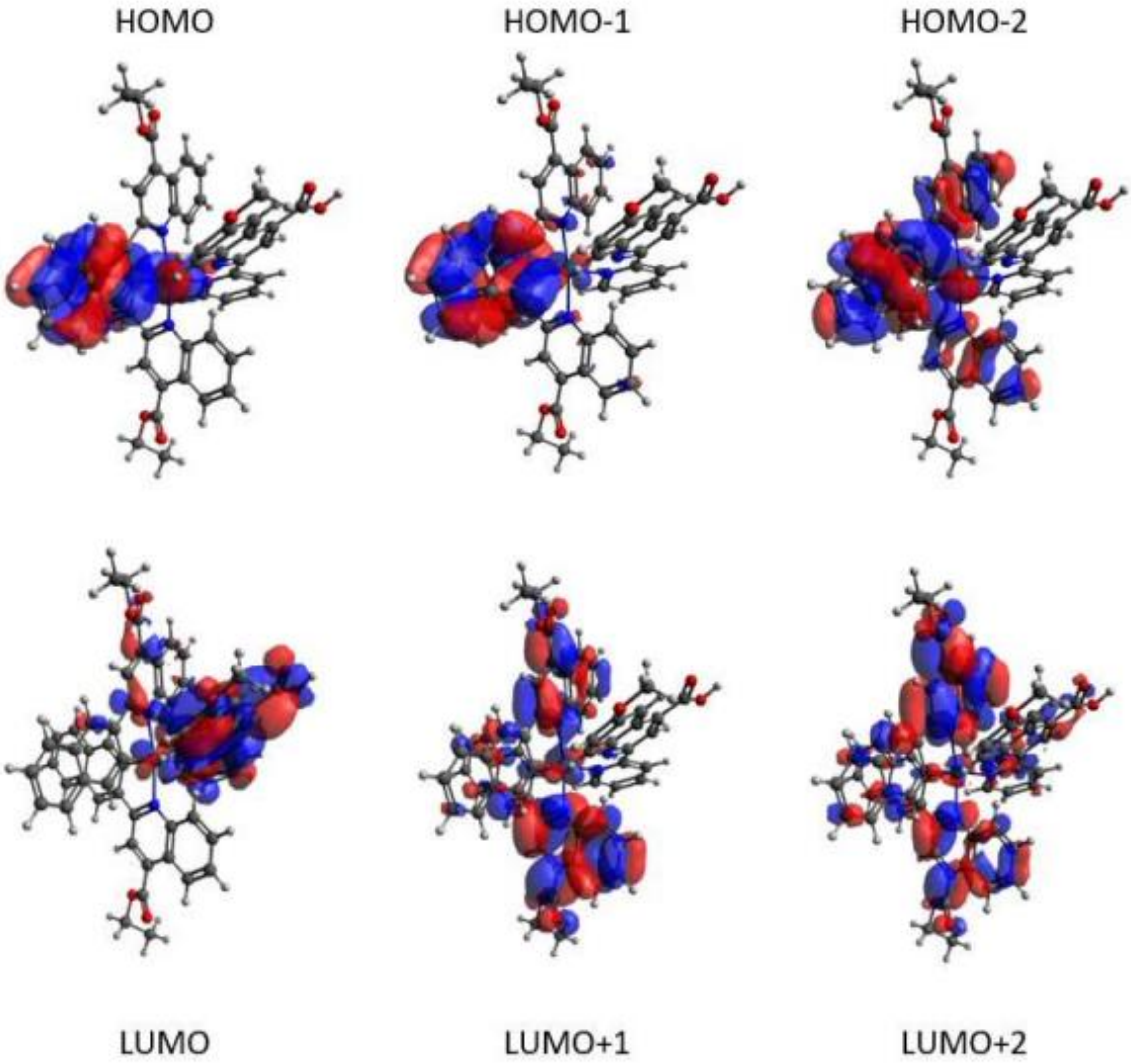

Calculated Kohn-Sham frontier molecular orbitals for $[Ir(L^{14})_2(L^{18})]^+$

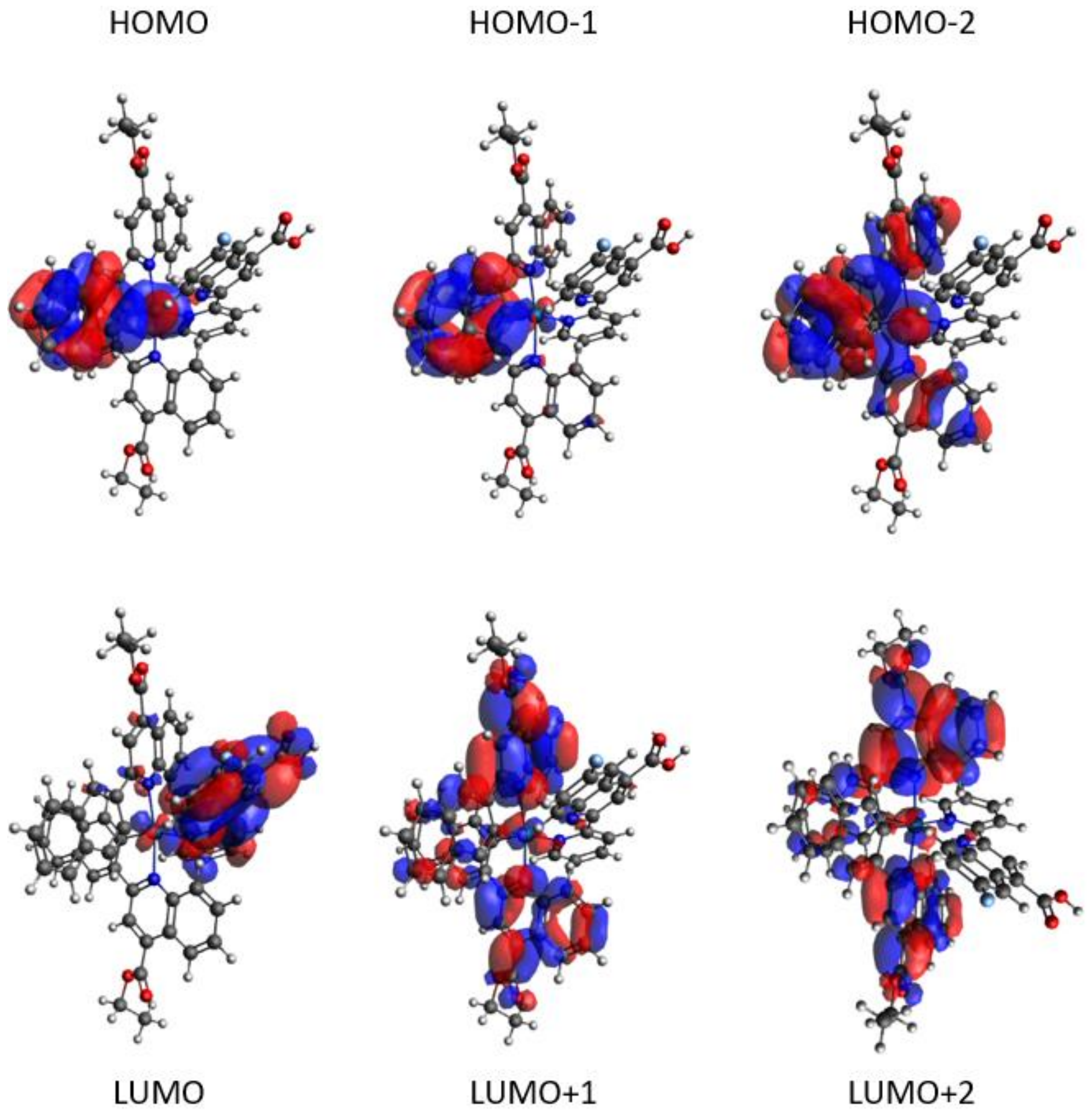

Calculated Kohn-Sham frontier molecular orbitals for $[Ir(L^{14})_2(L^{19})]^+$

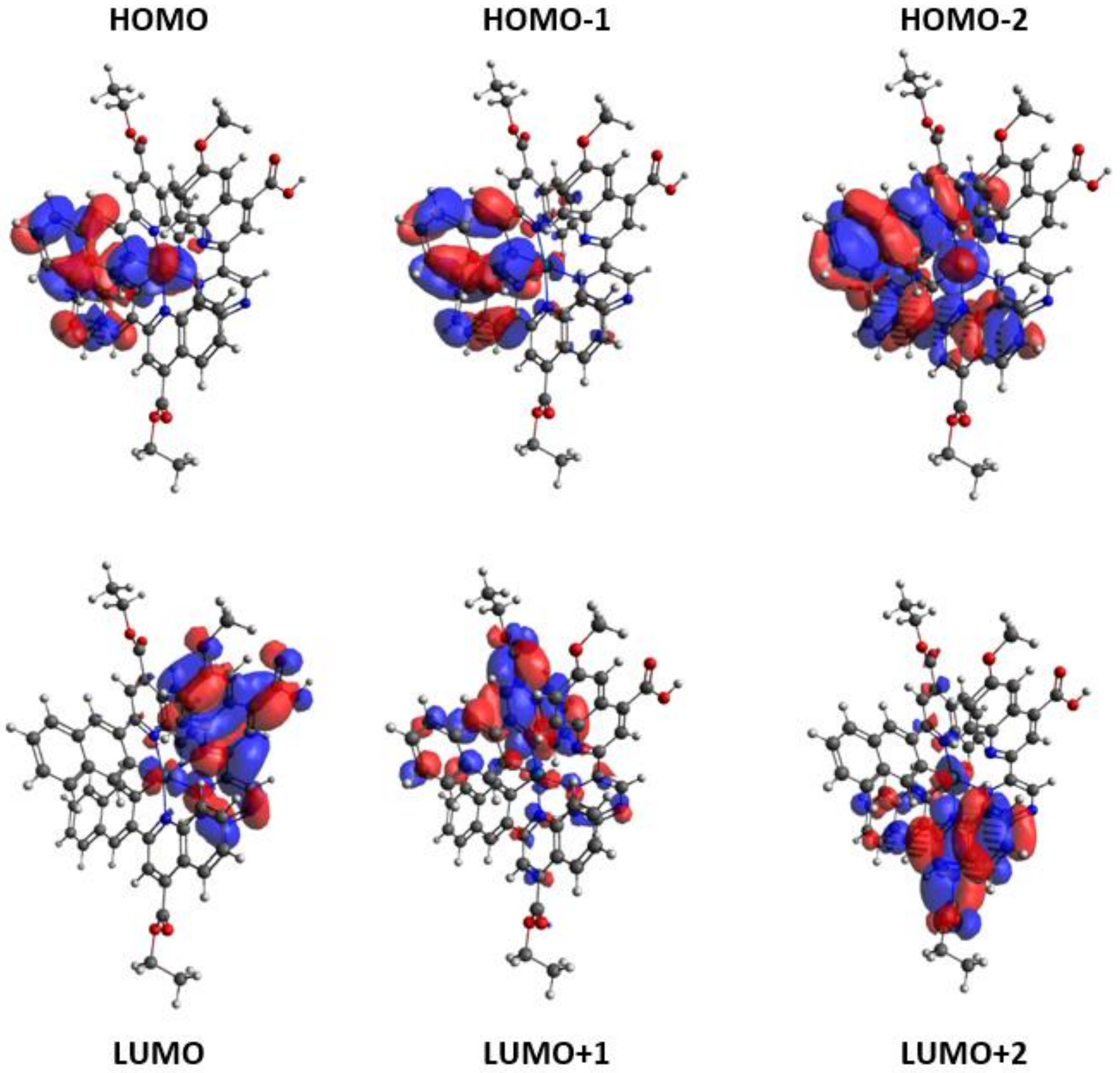

Calculated Kohn-Sham frontier molecular orbitals for $[Ir(L^{14})_2(L^{21})]^+$

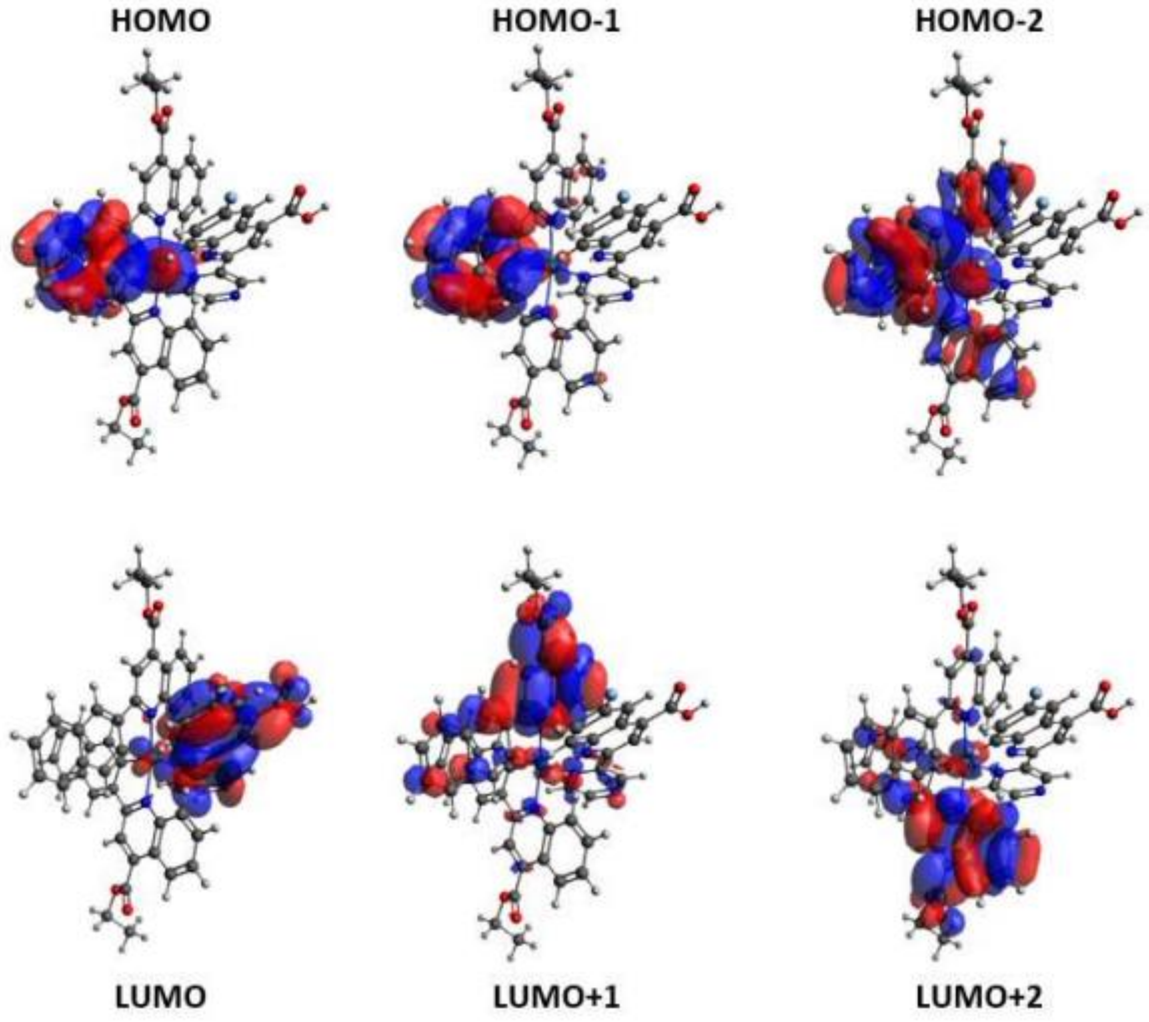

Calculated Kohn-Sham frontier molecular orbitals for $[Ir(L^{14})_2(L^{22})]^+$

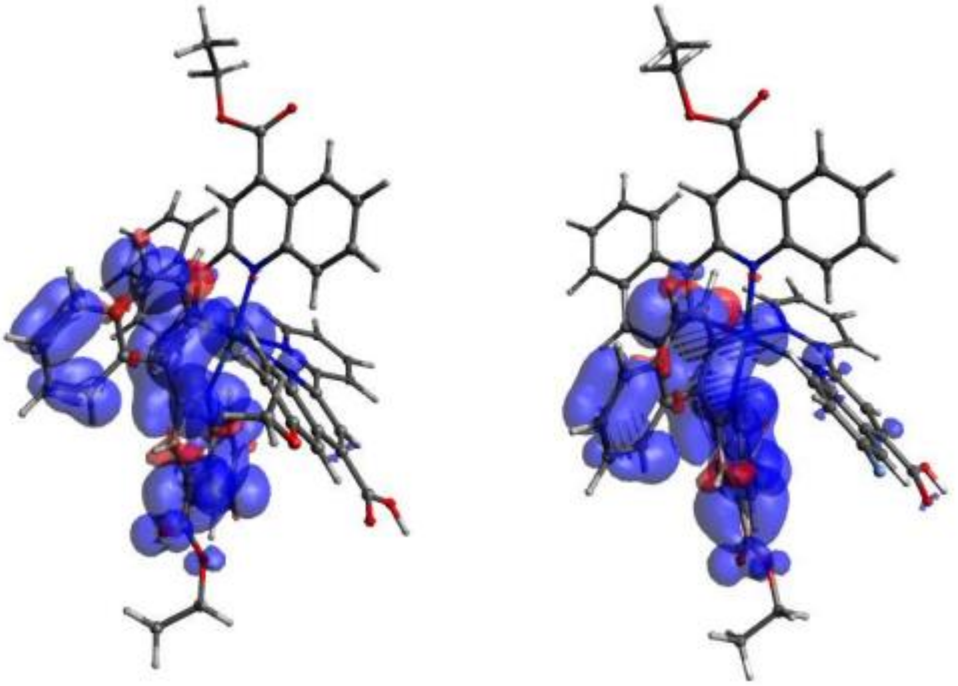

Calculated spin densities of $[Ir(L^{11})_2(L^{18})]^+$ ***(left)*** *$[Ir(L^{11})_2(L^{19})]^+$* ***(right)*** *complexes*

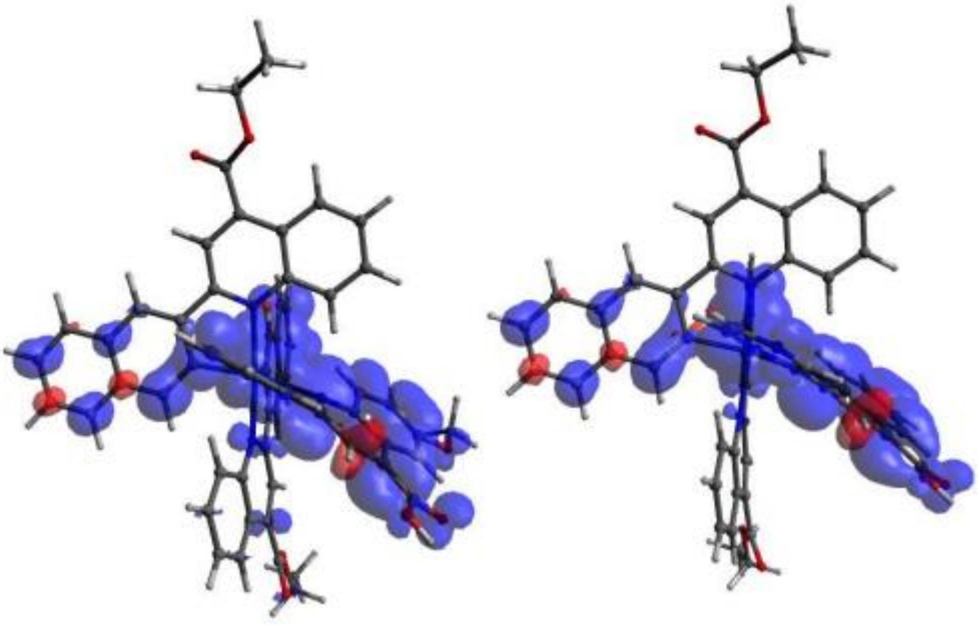

Calculated spin densities of $[Ir(L^{14})_2(L^{18})]^+$ ***(left)*** *$[Ir(L^{14})_2(L^{22})]^+$* ***(right)*** *complexes*

Table of description of the calculated MO contributions, excited state descriptions and their associated transitions for D2 complex (Q1 and Q2 are the different quinoline ligands).

D2	**Moiety Contribution to Orbital (%)**				**Orbital Contribution to Excited State**	
Orbital	**Ir (5d)**	**N^N**	**Q1**	**Q2**	**Excited State**	**Contributing Transitions (> 10 %)**
LUMO +4	3	1	53	43	1 (415 nm f=0.0502)	HOMO → LUMO+1 (80%)
LUMO +3	6	5	46	43		
LUMO +2	1	66	11	21	2 (407 nm f=0.1931)	HOMO → LUMO (15%)
LUMO +1	2	33	36	29		HOMO → LUMO+2 (42%) HOMO → LUMO+3 (24%)
LUMO	1	94	2	2	3 (377 nm f=0082)	HOMO → LUMO (25%)
HOMO	18	1	40	41		HOMO → LUMO+2 (78%)
HOMO -1	1	1	49	49	4 (335 nm f=0.0077)	HOMO → LUMO+1 (10%)
HOMO -2	22	2	37	39		HOMO → LUMO+2 (29%)
HOMO -3	12	1	44	43		HOMO → LUMO+3 (46%)
HOMO -4	10	4	40	47	5 (327 nm f=0.1733)	HOMO-1→ LUMO+1 (73%)

Table of description of the calculated MO contributions, excited state descriptions and their associated transitions for D3 complex (Q1 and Q2 are the different quinoline ligands).

D3	**Moiety Contribution to Orbital (%)**				**Orbital Contribution to Excited State**	
Orbital	**Ir (5d)**	**N^N**	**Q1**	**Q2**	**Excited State**	**Contributing Transitions (> 10 %)**
LUMO +4	3	1	54	42	1 (421 nm f=0.0595)	HOMO → LUMO+1 (76%)
LUMO +3	6	4	45	44		
LUMO +2	2	54	19	26	2 (413 nm f=0.1998)	HOMO → LUMO (14%)
LUMO +1	2	46	29	23		HOMO → LUMO+2 (10%) HOMO → LUMO+3 (54%)
LUMO	1	95	2	2	3 (384 nm f=0105)	HOMO → LUMO+2 (78%)
HOMO	17	1	41	41		HOMO → LUMO+3 (11%)
HOMO -1	1	1	49	49	4 (342 nm f=0.0099)	HOMO -1 → LUMO+1 (14%)
HOMO -2	12	1	43	43		HOMO → LUMO+2 (60%)
HOMO -3	4	0	49	47		HOMO → LUMO+3 (10%)
HOMO -4	21	4	36	39	5 (333 nm f=0.1765)	HOMO-1→ LUMO+1 (71%)

Table of description of the calculated MO contributions, excited state descriptions and their associated transitions for D5 complex (Q1 and Q2 are the different quinoline ligands).

D5	**Moiety Contribution to Orbital (%)**				**Orbital Contribution to Excited State**	
Orbital	**Ir (5d)**	**N^N**	**Q1**	**Q2**	**Excited State**	**Contributing Transitions (> 10 %)**
LUMO +4	0	93	4	3	1 (423 nm f=0.0533)	HOMO → LUMO (16%)
LUMO +3	1	89	5	5		HOMO → LUMO+2 (84%)
LUMO +2	4	3	45	47	2 (408 nm f=0.0486)	HOMO → LUMO+1 (84%)
LUMO +1	3	10	44	42		
LUMO	2	95	1	1	3 (384 nm f=1548)	HOMO → LUMO (21%)
HOMO	19	1	40	40		HOMO → LUMO+2 (60%)
HOMO -1	2	2	48	48	4 (338 nm f=0.0511)	HOMO -1 → LUMO (77%)
HOMO -2	25	4	36	35		
HOMO -3	17	2	40	41		
HOMO -4	9	12	43	36	5 (327 nm f=0.1367)	HOMO-1→ LUMO+1(75%) HOMO → LUMO+2 (11%)

Table of description of the calculated MO contributions, excited state descriptions and their associated transitions for D6 complex (Q1 and Q2 are the different quinoline ligands).

D6	**Moiety Contribution to Orbital (%)**				**Orbital Contribution to Excited State**	
Orbital	**Ir (5d)**	**N^N**	**Q1**	**Q2**	**Excited State**	**Contributing Transitions (> 10 %)**
LUMO +4	0	80	11	9	1 (429 nm f=0.0795)	HOMO → LUMO (64%)
LUMO +3	1	91	4	4		HOMO → LUMO+2 (19%)
LUMO +2	4	4	45	48	2 (418 nm f=0.0633)	HOMO → LUMO+1 (84%)
LUMO +1	3	9	46	43		
LUMO	2	95	1	2	3 (391 nm f=0.1599)	HOMO → LUMO (26%)
HOMO	17	1	41	41		HOMO → LUMO+2 (55%)
HOMO -1	1	2	48	48	4 (343 nm f=0.0540)	HOMO -1 → LUMO (79%)
HOMO -2	7	1	48	45		
HOMO -3	3	3	45	48		
HOMO -4	31	24	23	22	5 (336 nm f=0.1256)	HOMO-1→ LUMO+1 (77%) HOMO → LUMO+2 (13%)

Table of description of the calculated MO contributions, excited state descriptions and their associated transitions for D7 complex (Q1 and Q2 are the different quinoline ligands).

D7	Moiety Contribution to Orbital (%)				Orbital Contribution to Excited State	
Orbital	**Ir (5d)**	**N^N**	**Q1**	**Q2**	**Excited State**	**Contributing Transitions (> 10 %)**
LUMO +4	0	91	4	4	1 (431 nm f=0.0742)	HOMO → LUMO (65%)
LUMO +3	1	90	5	5		HOMO → LUMO+2 (19%)
LUMO +2	4	4	44	48	2 (318 nm f=0.0633)	HOMO → LUMO+1 (84%)
LUMO +1	3	9	46	42		
LUMO	2	95	1	2	3 (392 nm f=0.1610)	HOMO → LUMO (26%)
HOMO	17	1	41	41		HOMO → LUMO+2 (56%)
HOMO -1	1	2	49	48	4 (344 nm f=0.0492)	HOMO -1 → LUMO (80%)
HOMO -2	7	1	47	46		
HOMO -3	3	3	47	48		
HOMO -4	32	19	25	24	5 (337 nm f=0.1294)	HOMO-1→ LUMO+1 (77%)
						HOMO → LUMO+2 (12%)

Table of description of the calculated MO contributions, excited state descriptions and their associated transitions for D8 complex (Q1 and Q2 are the different quinoline ligands).

D8	Moiety Contribution to Orbital (%)				Orbital Contribution to Excited State	
Orbital	**Ir (5d)**	**N^N**	**Q1**	**Q2**	**Excited State**	**Contributing Transitions (> 10 %)**
LUMO +4	0	89	6	5	1 (438 nm f=0.0508)	HOMO → LUMO (73%)
LUMO +3	1	88	5	5		HOMO → LUMO+2 (13%)
LUMO +2	4	3	45	48	2 (318 nm f=0.0616)	HOMO → LUMO+1 (83%)
LUMO +1	3	11	45	41		
LUMO	2	95	1	1	3 (395 nm f=0.1815)	HOMO → LUMO (18%)
HOMO	17	1	41	41		HOMO → LUMO+2 (62%)
HOMO -1	1	2	48	48	4 (350 nm f=0.0292)	HOMO -1 → LUMO (84%)
HOMO -2	6	1	45	48		
HOMO -3	3	2	49	46		
HOMO -4	33	14	27	27	5 (336 nm f=0.1281)	HOMO-1→ LUMO+1 (77%)
						HOMO → LUMO+2 (12%)

Table of description of the calculated MO contributions, excited state descriptions and their associated transitions for D9 complex (Q1 and Q2 are the different quinoline ligands).

D9	**Moiety Contribution to Orbital (%)**				**Orbital Contribution to Excited State**	
Orbital	**Ir (5d)**	**N^N**	**Q1**	**Q2**	**Excited State**	**Contributing Transitions (> 10 %)**
LUMO +4	0	92	4	3	1 (460 nm f=0.0098)	HOMO → LUMO (87%)
LUMO +3	1	81	6	12		
LUMO +2	4	2	55	39	2 (408 nm f=0.0507)	HOMO → LUMO+1 (82%)
LUMO +1	3	19	34	44		
LUMO	2	96	1	1	3 (392 nm f=0.1902)	HOMO → LUMO+2 (72%)
HOMO	19	1	40	41		
HOMO -1	2	2	49	48	4 (364 nm f=0.0220)	HOMO -1 → LUMO (81%)
HOMO -2	22	3	39	37		
HOMO -3	16	2	40	43		
HOMO -4	13	16	16	55	5 (343 nm f=0.0216)	HOMO-4→ LUMO (29%) HOMO-2→ LUMO (48%)

Table of description of the calculated MO contributions, excited state descriptions and their associated transitions for D10 complex (Q1 and Q2 are the different quinoline ligands).

D10	**Moiety Contribution to Orbital (%)**				**Orbital Contribution to Excited State**	
Orbital	**Ir (5d)**	**N^N**	**Q1**	**Q2**	**Excited State**	**Contributing Transitions (> 10 %)**
LUMO +4	0	96	2	2	1 (500 nm f=0.0032)	HOMO → LUMO (90%)
LUMO +3	2	46	26	26		
LUMO +2	5	2	46	47	2 (411 nm f=0.0482)	HOMO → LUMO+1 (72%)
LUMO +1	2	54	22	22		
LUMO	2	96	1	1	3 (395 nm f=0.1943)	HOMO → LUMO+2 (75%)
HOMO	18	1	40	40		
HOMO -1	1	2	48	48	4 (388 nm f=0.0049)	HOMO -1 → LUMO (81%)
HOMO -2	18	2	40	40		
HOMO -3	14	1	43	42		
HOMO -4	10	6	42	42	5 (363 nm f=0.0198)	HOMO-4→ LUMO (33%) HOMO-2→ LUMO (50%)

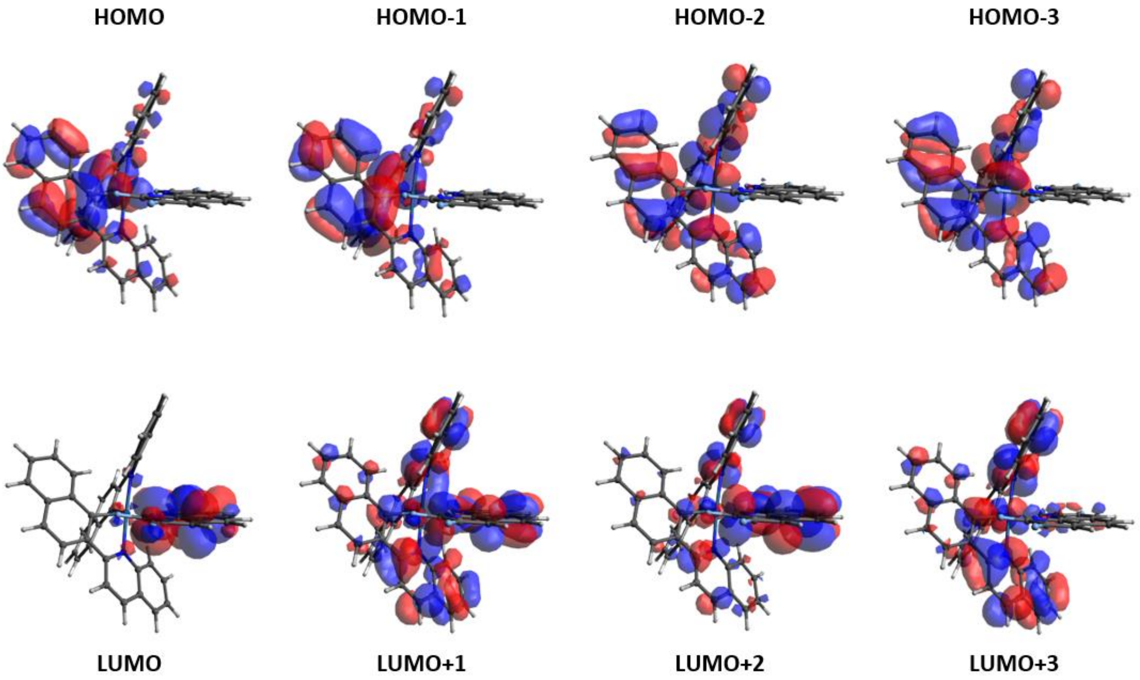

Calculated Kohn-Sham frontier molecular orbitals for D2 complex

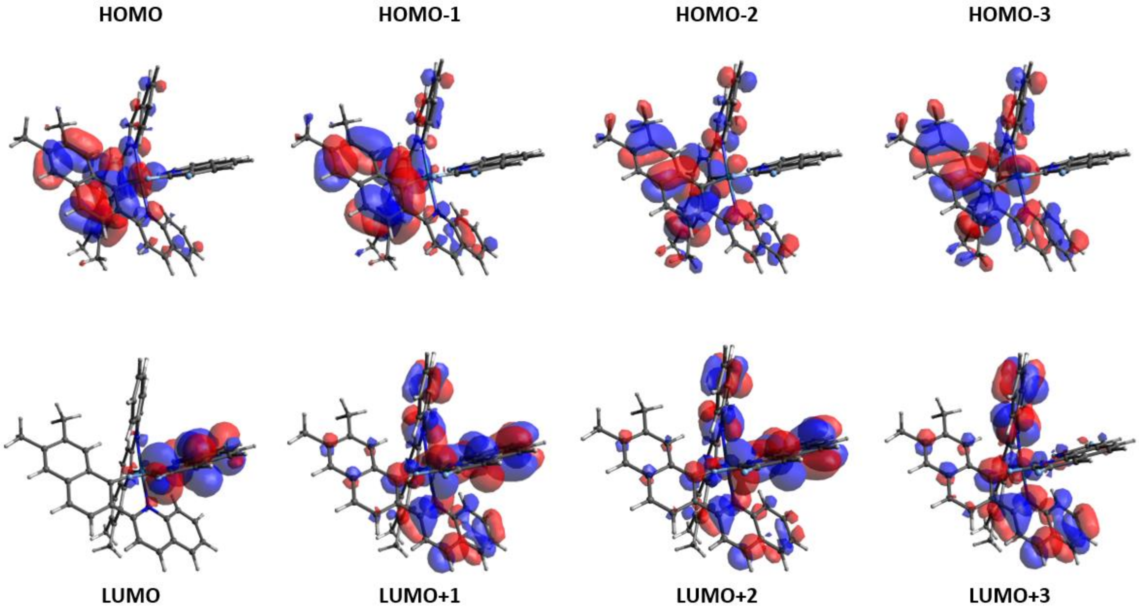

Calculated Kohn-Sham frontier molecular orbitals for D3 complex

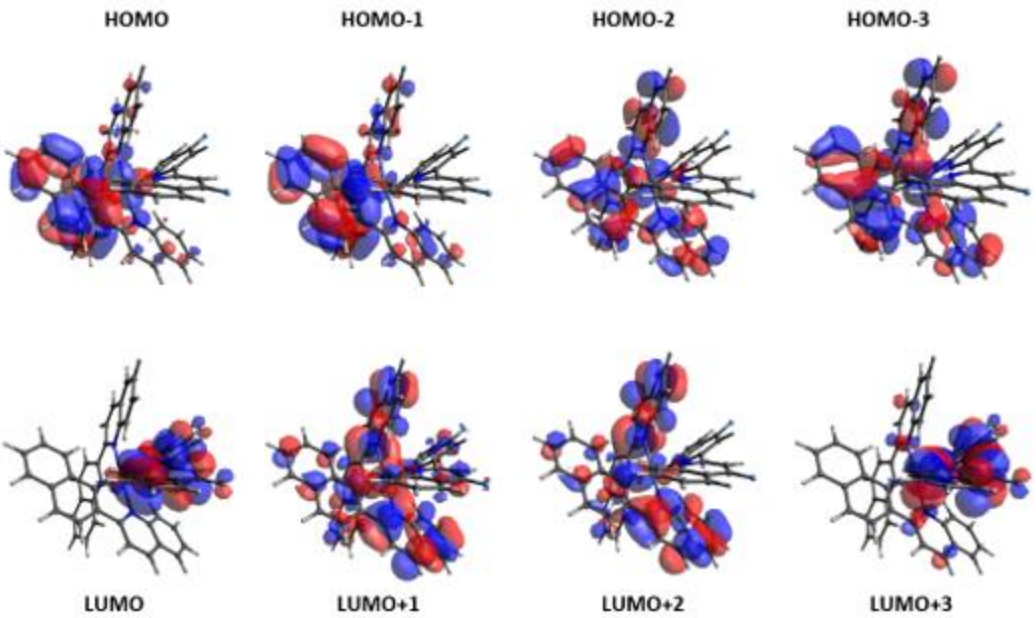

Calculated Kohn-Sham frontier molecular orbitals for D5 complex

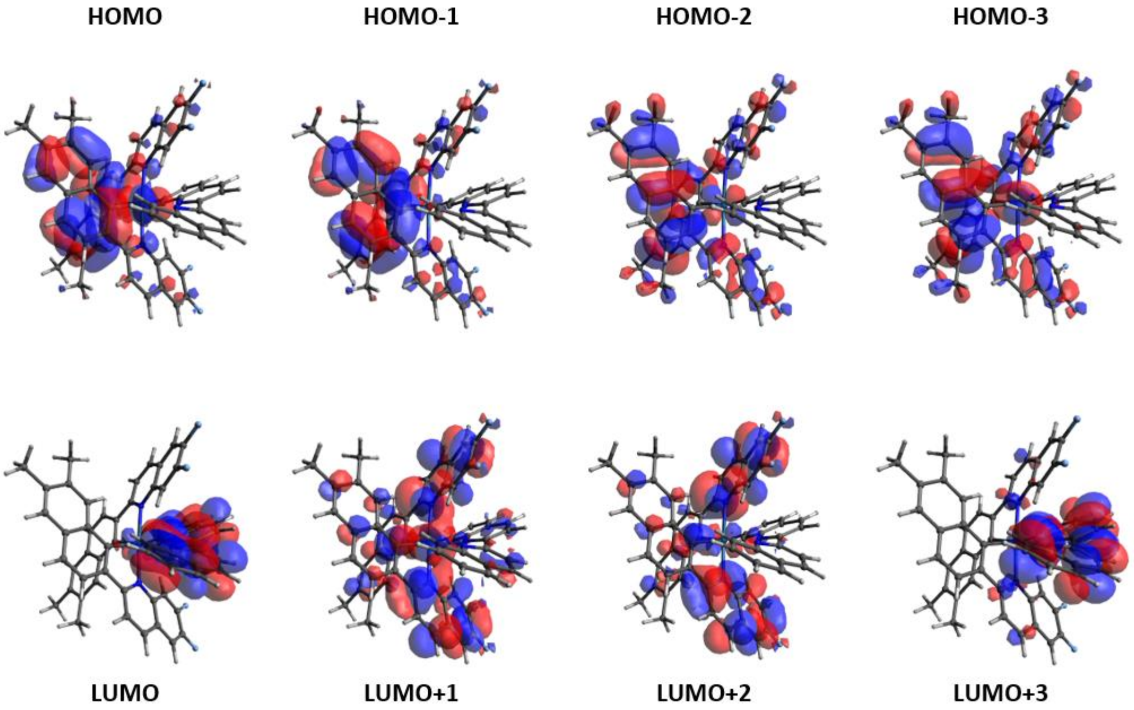

Calculated Kohn-Sham frontier molecular orbitals for D6 complex

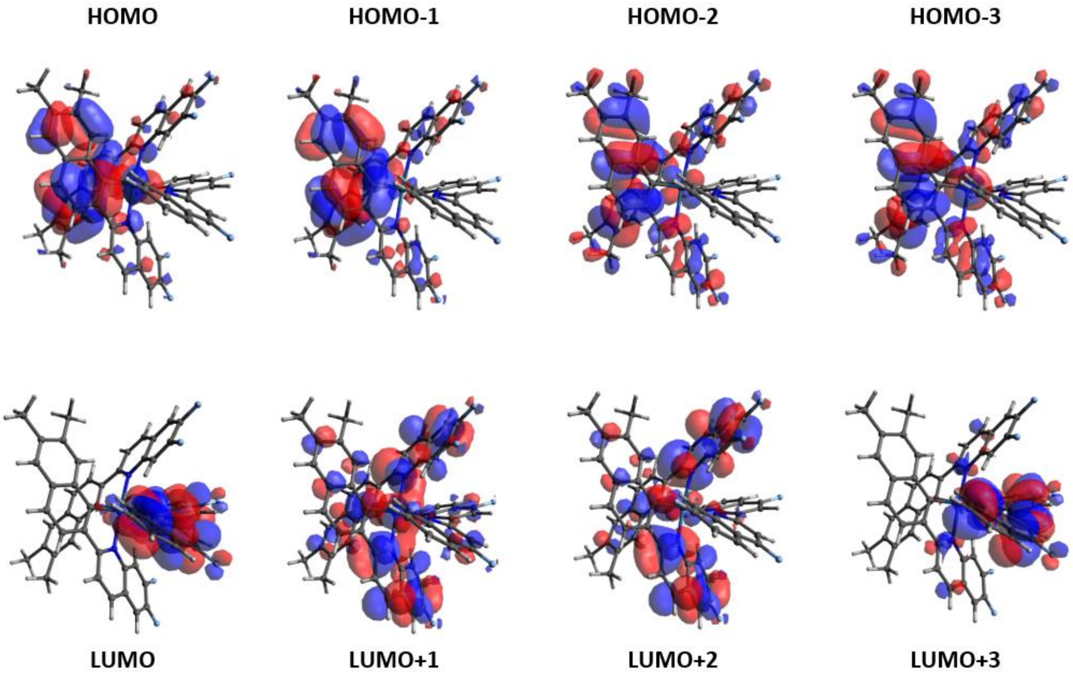
HOMO HOMO-1 HOMO-2 HOMO-3

LUMO LUMO+1 LUMO+2 LUMO+3

Calculated Kohn-Sham frontier molecular orbitals for D7 complex

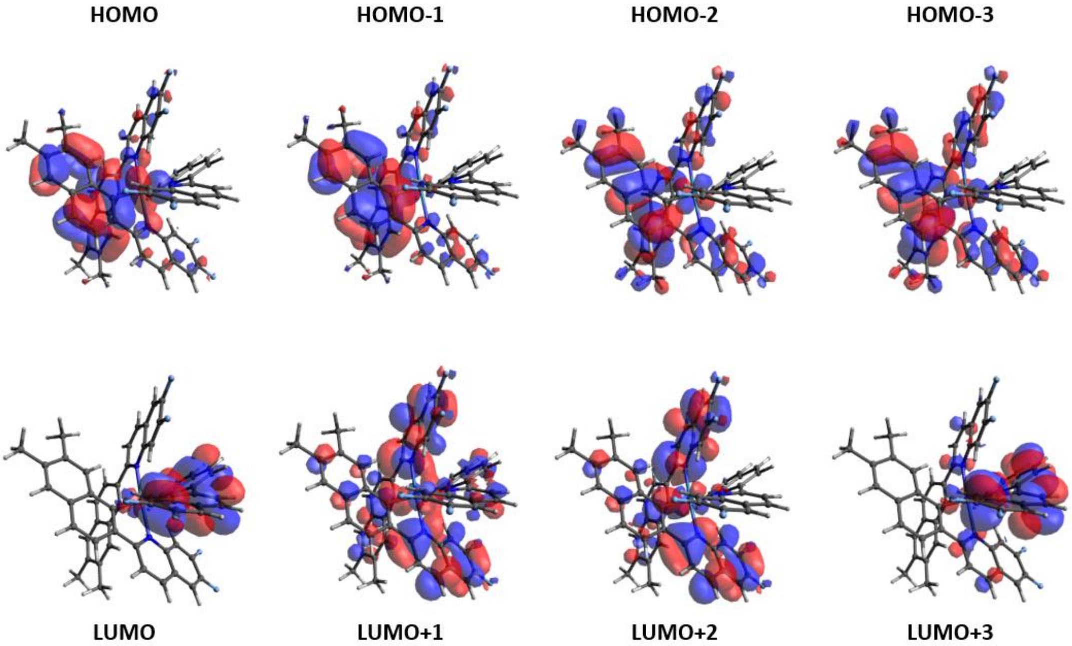
HOMO HOMO-1 HOMO-2 HOMO-3

LUMO LUMO+1 LUMO+2 LUMO+3

Calculated Kohn-Sham frontier molecular orbitals for D8 complex

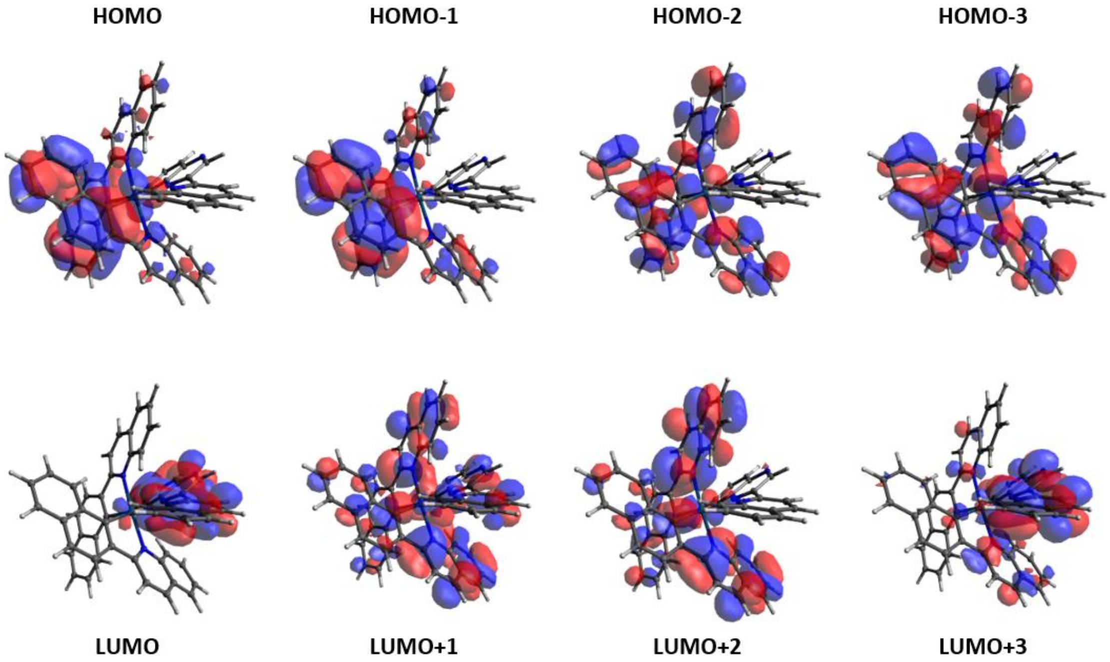

Calculated Kohn-Sham frontier molecular orbitals for D9 complex

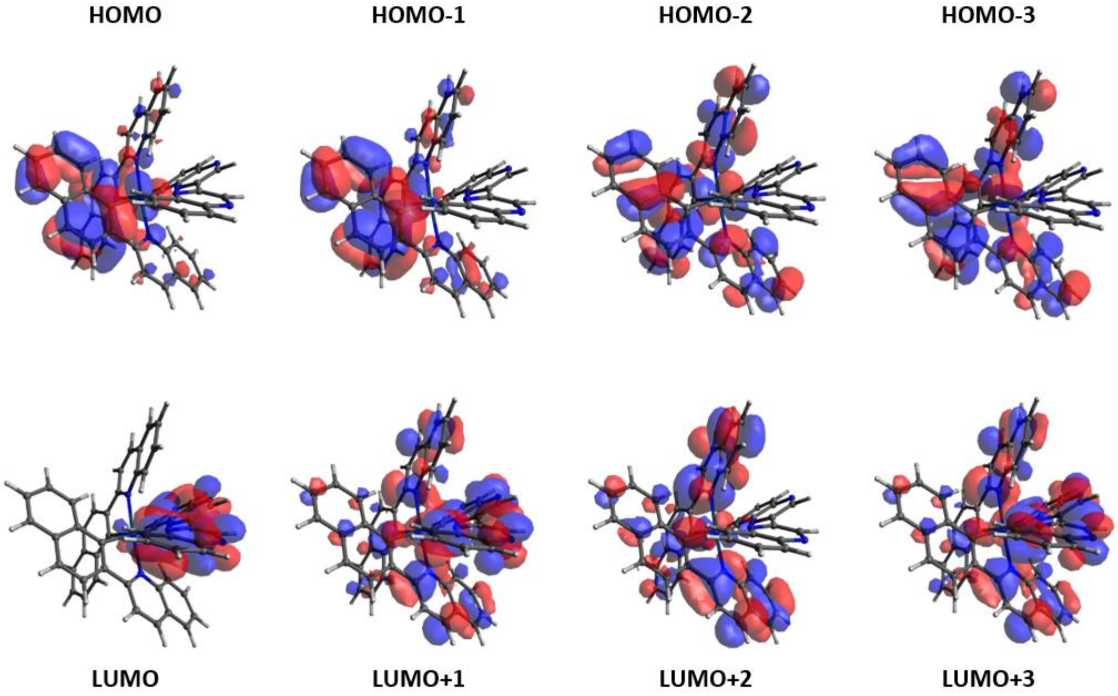

Calculated Kohn-Sham frontier molecular orbitals for D10 complex

C. Spectroscopic and Computational Analysis of the Excited-state Dynamics of Organic N-substituted Naphthalimide Dyads

Emission of N-PhPipNMI in degassed DCM at room temperature.

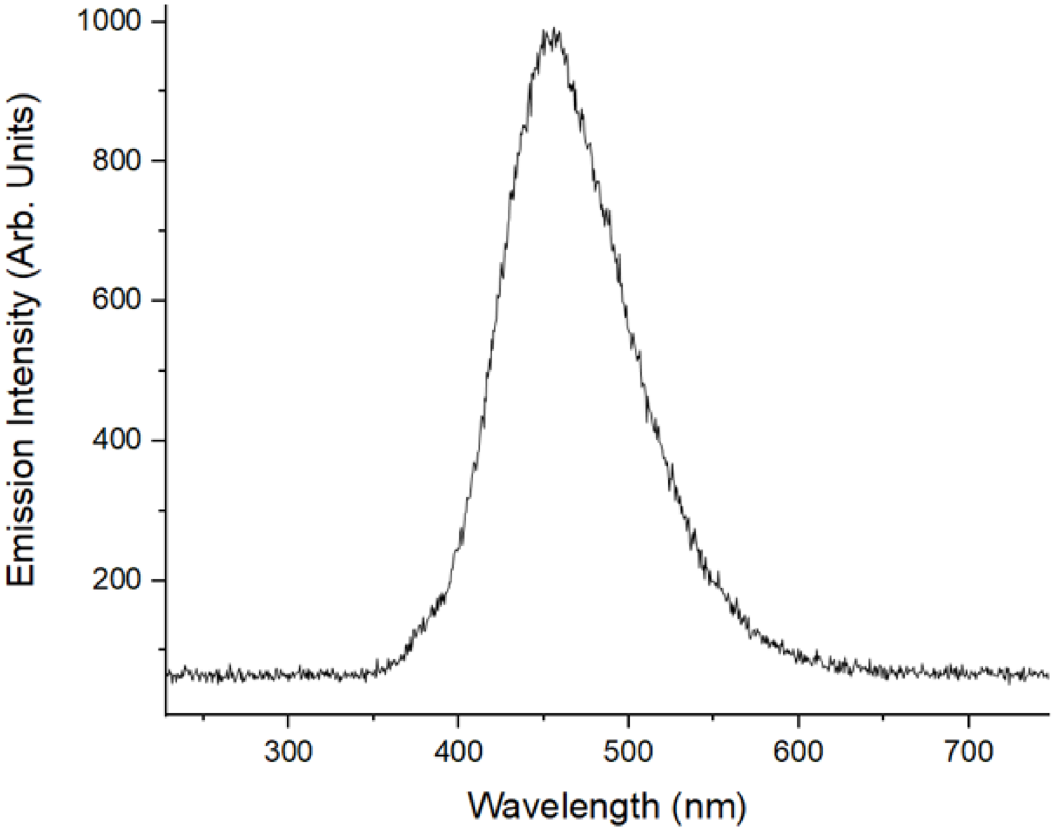

D. The Development of a Fluorescence Polarization Spectrophotometer

Emission intensities of Alexa fluor 594 at different concentrations. In all cases, samples were excited using vertically polarized light (right) and horizontally polarized light (right). The emission intensities were recorded while the emission polarizer was mounted vertically (red lines) and horizontally (black lines).

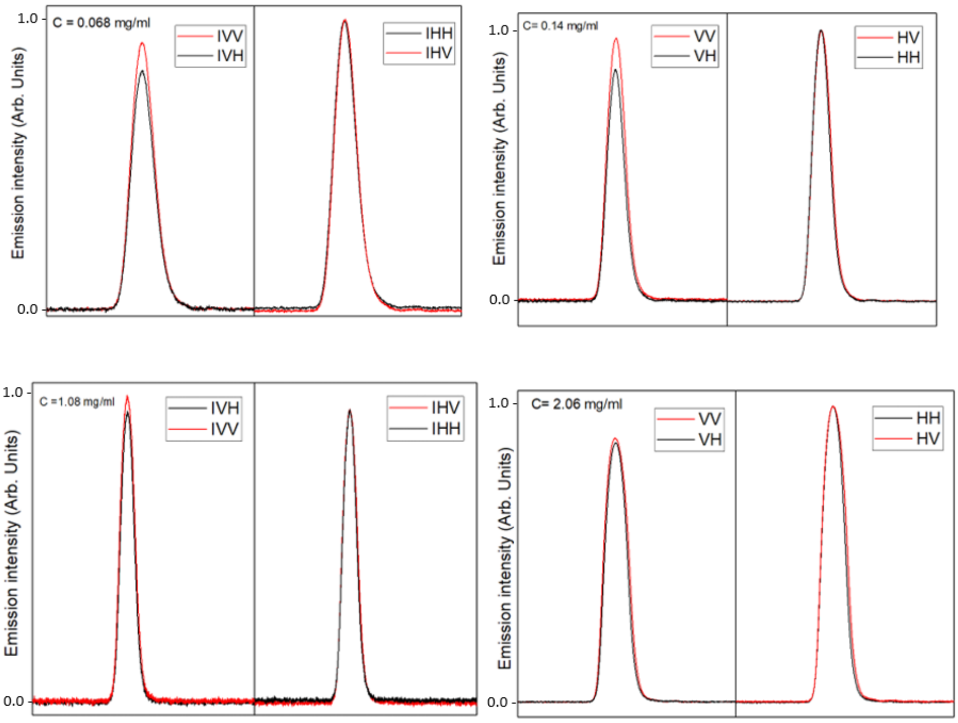

Emission intensities of Alexa fluor with colistin after the excitation by using vertically polarized light (right) and horizontally polarized light (left). In both cases, the emission intensities were recorded while the emission polarizer was mounted parallel and perpendicular to the incident light.

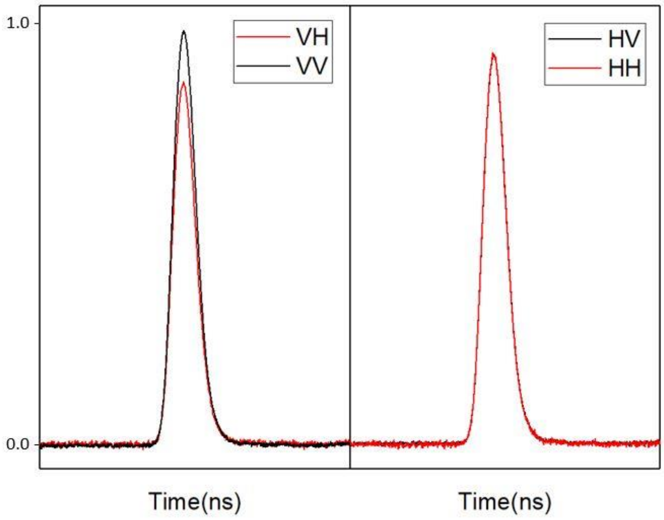

9. Bibliography

1. Abbas, S., Din, I. u. D., Raheel, A. and Tameez ud Din, A. 2020. Cyclometalated Iridium (III) complexes: Recent advances in phosphorescence bioimaging and sensing applications. *Applied Organometallic Chemistry* 34(3), p. e5413.
2. Adachi, C. and Sandanayaka, A. S. 2020. The leap from organic light-emitting diodes to organic semiconductor laser diodes. *CCS Chemistry* 2(4), pp. 1203-1216.
3. Alexiou, M., Tychopoulos, V., Ghorbanian, S., TYMAN, J. P., Brown, R. and Brittain, P. 1990. The UV-visible absorption and fluorescence of some substituted 1, 8-naphthalimides and naphthalic anhydrides. *Perkin transactions. 2* (5), pp. 837-842.
4. Alia, J. D. and Flack, J. A. 2020. Unspecified verticality of Franck–Condon transitions, absorption and emission spectra of cyanine dyes, and a classically inspired approximation. *RSC advances* 10(70), pp. 43153-43167.
5. Ameloot, M., Acuña, A. U. and Valeur, B. 2013. Fluorescence anisotropy measurements in solution: Methods and reference materials (IUPAC Technical Report). *Pure and Applied Chemistry* 85(3), pp. 589-608.
6. An, Z. et al. 2015. Stabilizing triplet excited states for ultralong organic phosphorescence. *Nature Materials* 14(7), pp. 685-690.
7. Arkin, M. R., Glicksman, M. A., Fu, H., Havel, J. J. and Du, Y. 2012. Inhibition of protein-protein interactions: non-cellular assay formats. *Assay Guidance Manual [Internet]*,
8. Armengol, E., Domenech, O., Fusté, E., Pérez-Guillén, I., Borrell, J., Sierra, J. and Vinas, M. 2019. Efficacy of combinations of colistin with other antimicrobials involves membrane fluidity and efflux machinery. *Infection and drug resistance* 12, p. 2031.
9. Arunchai, R., Sudyoadsuk, T., Prachumrak, N., Namuangruk, S., Promarak, V., Sukwattanasinitt, M. and Rashatasakhon, P. 2015. Synthesis and characterization of new triphenylamino-1, 8-naphthalimides for organic light-emitting diode applications. New Journal of Chemistry 39(4), pp. 2807-2814.
10. Aveline, B. M., Matsugo, S. and Redmond, R. W. 1997. Photochemical mechanisms responsible for the versatile application of naphthalimides and naphthaldiimides in biological systems. *Journal of the American Chemical Society* 119(49), pp. 11785-11795.
11. Avouris, P., Gelbart, W.M. and El-Sayed, M.A. 1977. Nonradiative electronic relaxation under collision-free conditions. *Chemical Reviews* 77(6), pp. 793–833. doi: 10.1021/cr60310a002.
12. Baer, M. and Englman, R. 1997. A modified Born-Oppenheimer equation: application to conical intersections and other types of singularities. *Chemical Physics Letters* 265(1–2), pp. 105–108. doi: 10.1016/S0009-2614(96)01411-X.
13. Balzani, V., Ceroni, P. and Juris, A. 2014. *Photochemistry and photophysics : concepts, research, applications*. Weinheim, Germany: Wiley-VCH Verlag GmbH & Co. KGaA.
14. Baranoff, E., Yum, J.-H., Graetzel, M. and Nazeeruddin, M. K. 2009. Cyclometallated iridium complexes for conversion of light into electricity and electricity into light. *Journal of Organometallic Chemistry* 694(17), pp. 2661-2670.
15. Barros, T., Berci Filho, P., Toscano, V. and Politi, M. J. 1995. Intramolecular excimer formation from 1, 8-N-alkyldinaphthalimides. *Journal of Photochemistry and Photobiology A: Chemistry* 89(2), pp. 141-146.
16. Bassan, E., Gualandi, A., Cozzi, P. G. and Ceroni, P. 2021. Design of BODIPY dyes as triplet photosensitizers: electronic properties tailored for solar energy conversion, photoredox catalysis and photodynamic therapy. *Chemical Science* 12(19), pp. 6607-6628.
17. Becke, A.D. 1988. Density-functional exchange-energy approximation with correct asymptotic behavior. *Physical Review A* 38(6), pp. 3098–3100. doi: 10.1103/PhysRevA.38.3098.
18. Bejoymohandas, K., Kumar, A., Varughese, S., Varathan, E., Subramanian, V. and Reddy, M. 2015. Photophysical and electroluminescence properties of bis (2′, 6′-difluoro-2, 3′-bipyridinato-N, C 4′) iridium (picolinate) complexes: effect of electron-withdrawing and electron-donating group substituents at the 4′ position of the pyridyl moiety of the cyclometalated ligand. *Journal of Materials Chemistry C* 3(28), pp. 7405-7420.
19. Berera, R., van Grondelle, R. and Kennis, J. 2009. Ultrafast transient absorption spectroscopy: principles and application to photosynthetic systems. *Photosynthesis research* 101(2), pp. 105-118.

20. Bergan, T. and Fuglesang, J. 1981. Polymyxin antibiotics. *Pharmacokinetics II* 31, pp. 119-144.

21. Bhosale, S. V., Al Kobaisi, M., Jadhav, R. W., Morajkar, P. P., Jones, L. A. and George, S. 2021. Naphthalene diimides: perspectives and promise. Chemical Society Reviews 50(17), pp. 9845-9998.

22. Bialvaei, A. Z. and Samadi Kafil, H. 2015. Colistin, mechanisms and prevalence of resistance. *Current medical research and opinion* 31(4), pp. 707-721.

23. Bixon, M. and Jortner, J. 1968. Intramolecular Radiationless Transitions. *The Journal of Chemical Physics* 48(2), pp. 715–726. doi: 10.1063/1.1668703.

24. Bondybey, V.E. 1984. Relaxation and Vibrational Energy Redistribution Processes in Polyatomic Molecules. *Annual Review of Physical Chemistry* 35(1), pp. 591–612. doi: 10.1146/annurev.pc.35.100184.003111.

25. Borisov, S. M., Mayr, T., Mistlberger, G. and Klimant, I. 2010. Dye-doped polymeric particles for sensing and imaging. Advanced fluorescence reporters in chemistry and biology II: Molecular constructions, polymers and nanoparticles, pp. 193-228.

26. Born, M. and Oppenheimer, R. 1927. Zur Quantentheorie der Molekeln. *Annalen der Physik* 389(20), pp. 457–484. doi: 10.1002/andp.19273892002.

27. Bowen, E.J. and Sahu, J. 1959. The Effect of Temperature on Fluorescence of Solutions. *The Journal of Physical Chemistry* 63(1), pp. 4–7. doi: 10.1021/j150571a003.

28. Braslavsky, S.E. 2007. Glossary of terms used in photochemistry, 3rd edition (IUPAC Recommendations 2006). *Pure and Applied Chemistry* 79(3), pp. 293–465. doi: 10.1351/pac200779030293.

29. Bröring, M. et al. 2008. Bis (BF2)-2, 2′-Bidipyrrins (BisBODIPYs): Highly Fluorescent BODIPY Dimers with Large Stokes Shifts. *Chemistry–A European Journal* 14(10), pp. 2976-2983.

30. Buckle, T., van der Wal, S., van Willigen, D. M., Aalderink, G., KleinJan, G. H. and van Leeuwen, F. W. 2020. Fluorescence background quenching as a means to increase Signal to Background ratio-a proof of concept during Nerve Imaging. *Theranostics* 10(21), p. 9890.

31. Bui, T.-T., Goubard, F., Ibrahim-Ouali, M., Gigmes, D. and Dumur, F. 2018. Recent advances on organic blue thermally activated delayed fluorescence (TADF) emitters for organic light-emitting diodes (OLEDs). *Beilstein journal of organic chemistry* 14(1), pp. 282-308.

32. Burgess, C. and Jones, D. 1995. *Spectrophotometry, luminescence and colour : science & compliance*. Amsterdam: Elsevier.

33. Burke, K. and Wagner, L.O. 2013. DFT in a nutshell. *International Journal of Quantum Chemistry* 113(2), pp. 96–101. doi: 10.1002/qua.24259.

34. Cakmak, Y. et al. 2011. Designing excited states: Theory-guided access to efficient photosensitizers for photodynamic action. *Angewandte Chemie International Edition* 50(50), pp. 11937-11941.

35. Caporale, C. and Massi, M. 2018. Cyclometalated iridium (III) complexes for life science. *Coordination Chemistry Reviews* 363, pp. 71-91.

36. Caspar, J. V., Sullivan, B. P., Kober, E. M. and Meyer, T. J. 1982. Application of the energy gap law to the decay of charge transfer excited states, solvent effects. *Chemical Physics Letters* 91(2), pp. 91-95.

37. Chatterjee, S., Pramanik, S., Hossain, S. U., Bhattacharya, S. and Bhattacharya, S. C. 2007. Synthesis and photoinduced intramolecular charge transfer of N-substituted 1, 8-naphthalimide derivatives in homogeneous solvents and in presence of reduced glutathione. *Journal of Photochemistry and Photobiology A: Chemistry* 187(1), pp. 64-71.

38. Chatterjee, S., Pramanik, S., Hossain, S. U., Bhattacharya, S. and Bhattacharya, S. C. 2007. Synthesis and photoinduced intramolecular charge transfer of N-substituted 1, 8-naphthalimide derivatives in homogeneous solvents and in presence of reduced glutathione. *Journal of Photochemistry and Photobiology A: Chemistry* 187(1), pp. 64-71.

39. Chen, K. et al. 2017. Triplet excited state of BODIPY accessed by charge recombination and its application in triplet–triplet annihilation upconversion. *The Journal of Physical Chemistry A* 121(40), pp. 7550-7564.

40. Chen, R. F. 1972. Measurements of absolute values in biochemical fluorescence spectroscopy. *Journal of Research of the National Bureau of Standards. Section A, Physics and Chemistry* 76(6), p. 593.

41. Chen, S. et al. 2012. An AIE-active hemicyanine fluorogen with stimuli-responsive red/blue emission: extending the pH sensing range by “switch+ knob” effect. Chemical Science 3(6), pp. 1804-1809.

42. Chen, X. et al. 2016. Versatile room-temperature-phosphorescent materials prepared from N-substituted naphthalimides: emission enhancement and chemical conjugation. *Angewandte Chemie International Edition* 55(34), pp. 9872-9876.

43. Chen, X., Xiao, X. and Zhao, J. 2022. Application of time-resolved electron paramagnetic resonance spectroscopy in the mechanistic study of thermally activated delayed fluorescence (TADF) materials. *Journal of Materials Chemistry C* 10(12), pp. 4546-4557.

44. Chen, Z. q., Bian, Z. q. and Huang, C. h. 2010. Functional IrIII complexes and their applications. *Advanced Materials* 22(13), pp. 1534-1539.

45. Cheng, L., Deng, L., Guo, R., Leng, Y. and Wu, J. 2022. Synthesis and Characterization of Heteroleptic Bis-Cyclometalated Iridium(III) Complexes. *Journal of Organometallic Chemistry* 972, p. 122375.

46. Chi, Y. and Chou, P.-T. 2010. Transition-metal phosphors with cyclometalating ligands: fundamentals and applications. *Chemical Society Reviews* 39(2), pp. 638-655.

47. Cho, D. W. 2014. Excimer and exciplex emissions of 1, 8-naphthalimides caused by aggregation in extremely polar or nonpolar solvents. *New Journal of Chemistry* 38(6), pp. 2233-2236.

48. Cho, D. W., Fujitsuka, M., Choi, K. H., Park, M. J., Yoon, U. C. and Majima, T. 2006. Intramolecular exciplex and intermolecular excimer formation of 1, 8-naphthalimide− linker− phenothiazine dyads. *The Journal of Physical Chemistry B* 110(10), pp. 4576-4582.

49. Choi, J.-W., Kang, D.-K., Park, H., deMello, A. J. and Chang, S.-I. 2012. High-throughput analysis of protein–protein interactions in picoliter-volume droplets using fluorescence polarization. *Analytical Chemistry* 84(8), pp. 3849-3854.

50. Chou, P. T. and Chi, Y. 2007. Phosphorescent dyes for organic light-emitting diodes. Chemistry–A European Journal 13(2), pp. 380-395.

51. Chou, P.-T., Chi, Y., Chung, M.-W. and Lin, C.-C. 2011. Harvesting luminescence via harnessing the photophysical properties of transition metal complexes. *Coordination Chemistry Reviews* 255(21-22), pp. 2653-2665.

52. Cichos, F., Willert, A., Rempel, U. and Von Borczyskowski, C. 1997. Solvation dynamics in mixtures of polar and nonpolar solvents. *The Journal of Physical Chemistry A* 101(44), pp. 8179-8185.

53. Collin, J.-P., Dixon, I. M., Sauvage, J.-P., Williams, J. G., Barigelletti, F. and Flamigni, L. 1999. Synthesis and photophysical properties of iridium (III) bisterpyridine and its homologues: a family of complexes with a long-lived excited state. *Journal of the American Chemical Society* 121(21), pp. 5009-5016.

54. Colombo, M. G., Hauser, A. and Güdel, H. U. 1994. Competition between ligand centered and charge transfer lowest excited states in bis cyclometalated Rh 3+ and Ir 3+ complexes.*Electronic and Vibronic Spectra of Transition Metal Complexes I*. Springer, pp. 143-171.

55. Condon, E. 1926. A Theory of Intensity Distribution in Band Systems. *Physical Review* 28(6), pp. 1182–1201. doi: 10.1103/PhysRev.28.1182.

56. Condon, E.U. 1928. Nuclear Motions Associated with Electron Transitions in Diatomic Molecules. *Physical Review* 32(6), pp. 858–872. doi: 10.1103/PhysRev.32.858.

57. Correia, J. J. and Detrich III, H. W. 2009. *Biophysical Tools for Biologists: In Vivo Techniques*. Academic Press.

58. Cotton, F. A., Wilkinson, G. and Gaus, P. L. 1995. Basic inorganic chemistry. John Wiley & Sons.

59. Crabtree, R. H. 2009. *The organometallic chemistry of the transition metals*. John Wiley & Sons.

60. Cramer, C.J. 2004. *Essentials of Computational Chemistry: Theories and Models*. 2nd ed. Wiley.

61. D'Agostino, S. et al. 2013. Exciton coupling in molecular salts of 2-(1, 8-naphthalimido) ethanoic acid and cyclic amines: modulation of the solid-state luminescence. *CrystEngComm* 15(48), pp. 10470-10480.

62. Das, A. et al. 2021. Dynamics of Anthracene Excimer Formation within a Water-Soluble Nanocavity at Room Temperature. *Journal of the American Chemical Society* 143(4), pp. 2025-2036.

63. Data, P. and Takeda, Y. 2019. Recent advancements in and the future of organic emitters: TADF-and RTP-active multifunctional organic materials. *Chemistry–An Asian Journal* 14(10), pp. 1613-1636.

64. Day, P. P. 1955. Electromagnetic spectrum of Am 241. Physical Review 97(3), p. 689.

65. Dedeian, K., Djurovich, P., Garces, F., Carlson, G. and Watts, R. 1991. A new synthetic route to the preparation of a series of strong photoreducing agents: fac-tris-ortho-metalated complexes of iridium (III) with substituted 2-phenylpyridines. *Inorganic chemistry* 30(8), pp. 1685-1687.

66. Deiana, M. et al. 2022. Site-selected thionated benzothioxanthene chromophores as heavy-atom-free small-molecule photosensitizers for photodynamic therapy. *Communications Chemistry* 5(1), pp. 1-11.

67. Demas, J. N. and DeGraff, B. 1997. Applications of luminescent transition metal complexes to sensor technology and molecular probes. ACS Publications.

68. Demas, J. N. and DeGraff, B. A. 1991. Design and applications of highly luminescent transition metal complexes. *Analytical Chemistry* 63(17), pp. 829A-837A. doi: 10.1021/ac00017a001

69. Demeter, A., Biczok, L., Berces, T., Wintgens, V., Valat, P. and Kossanyi, J. 1993. Laser photolysis studies of transient processes in the photoreduction of naphthalimides by aliphatic amines. *The Journal of Physical Chemistry* 97(13), pp. 3217-3224.

70. Deželić, G. and Kratohvil, J. 1960. Determination of size of small particles by light scattering. Experiments on ludox colloidal silica. *Kolloid-Zeitschrift* 173(1), pp. 38-48.

71. Dias, F. B., Penfold, T. J. and Monkman, A. P. 2017. Photophysics of thermally activated delayed fluorescence molecules. *Methods and applications in fluorescence* 5(1), p. 012001.

72. DiLuzio, S., Mdluli, V., Connell, T. U., Lewis, J., VanBenschoten, V. and Bernhard, S. 2021. High-throughput screening and automated data-driven analysis of the triplet photophysical properties of structurally diverse, heteroleptic iridium (III) complexes. *Journal of the American Chemical Society* 143(2), pp. 1179-1194.

73. Duan, J.-P., Sun, P.-P. and Cheng, C.-H. 2003. New iridium complexes as highly efficient orange–red emitters in organic light-emitting diodes. Advanced Materials 15(3), pp. 224-228.

74. Duan, Y.-C. et al. 2018. Fluorescence, phosphorescence, or delayed fluorescence?—A theoretical exploration on the reason why a series of similar organic molecules exhibit different luminescence types. *The Journal of Physical Chemistry C* 122(40), pp. 23091-23101.

75. Duman, S., Cakmak, Y., Kolemen, S., Akkaya, E. U. and Dede, Y. 2012. Heavy atom free singlet oxygen generation: doubly substituted configurations dominate S1 states of bis-BODIPYs. *The Journal of Organic Chemistry* 77(10), pp. 4516-4527.

76. Drummond, B. H. et al. 2021. Electron spin resonance resolves intermediate triplet states in delayed fluorescence. Nature communications 12(1), p. 4532.

77. Elgar, C.E. et al. 2021. Iridium(III) Sensitisers and Energy Upconversion: The Influence of Ligand Structure upon TTA-UC Performance. *Chemistry – A European Journal* 27(10), pp. 3427–3439

78. Elsaesser, T. and Kaiser, W. 1991. Vibrational and Vibronic Relaxation of Large Polyatomic Molecules in Liquids. *Annual Review of Physical Chemistry* 42(1), pp. 83–107. doi: 10.1146/annurev.pc.42.100191.000503.

79. Englman, R. and Jortner, J. 1970. The energy gap law for radiationless transitions in large molecules. *Molecular Physics* 18(2), pp. 145–164. doi: 10.1080/00268977000100171.

80. Etherington, M. K., Gibson, J., Higginbotham, H. F., Penfold, T. J. and Monkman, A. P. 2016. Revealing the spin–vibronic coupling mechanism of thermally activated delayed fluorescence. *Nature communications* 7(1), pp. 1-7.

81. Evans, M. E., Feola, D. J. and Rapp, R. P. 1999. Polymyxin B sulfate and colistin: old antibiotics for emerging multiresistant gram-negative bacteria. *Annals of Pharmacotherapy* 33(9), pp. 960-967.

82. Farizano, J. V., de las Mercedes Pescaretti, M., López, F. E., Hsu, F.-F. and Delgado, M. A. 2012. The PmrAB system-inducing conditions control both lipid A remodeling and O-antigen length distribution, influencing the Salmonella Typhimurium-host interactions. *Journal of Biological Chemistry* 287(46), pp. 38778-38789.

83. Farr, E.P., Quintana, J.C., Reynoso, V., Ruberry, J.D., Shin, W.R. and Swartz, K.R. 2018. Introduction to Time-Resolved Spectroscopy: Nanosecond Transient Absorption and Time-Resolved Fluorescence of Eosin B. *Journal of Chemical Education* 95(5), pp. 864–871. doi: 10.1021/acs.jchemed.7b00941.

84. Felip-León, C., Galindo, F. and Miravet, J. F. 2018. Insights into the aggregation-induced emission of 1, 8-naphthalimide-based supramolecular hydrogels. *Nanoscale* 10(36), pp. 17060-17069.

85. Ferraudi, G. 2010. Flash Photolysis and Chemistry of Transients and Excited States. In: *Physical Inorganic Chemistry*. Hoboken, NJ, USA: John Wiley & Sons, Inc., pp. 199–267. doi: 10.1002/9780470602539.ch6.

86. Ferreira, R., Baleizao, C., Munoz-Molina, J., Berberan-Santos, M. and Pischel, U. 2011. Photophysical Study of Bis (naphthalimide)− Amine Conjugates: Toward Molecular Design of Excimer Emission Switching. *The Journal of Physical Chemistry A* 115(6), pp. 1092-1099.

87. Ferrer, F. J. A. and Santoro, F. 2012. Comparison of vertical and adiabatic harmonic approaches for the calculation of the vibrational structure of electronic spectra. *Physical Chemistry Chemical Physics* 14(39), pp. 13549-13563.

88. Filatov, M. A. 2020. Heavy-atom-free BODIPY photosensitizers with intersystem crossing mediated by intramolecular photoinduced electron transfer. *Organic & Biomolecular Chemistry* 18(1), pp. 10-27.

89. Finikova, O. S. et al. 2008. Oxygen microscopy by two-photon-excited phosphorescence. *ChemPhysChem* 9(12), pp. 1673-1679.

90. Fixler, D., Tirosh, R., Zurgil, N. and Deutsch, M. 2005. Tracing apoptosis and stimulation in individual cells by fluorescence intensity and anisotropy decay. *Journal of biomedical optics* 10(3), p. 034007.

91. Flamigni, L., Barbieri, A., Sabatini, C., Ventura, B. and Barigelletti, F. 2007. Photochemistry and photophysics of coordination compounds: iridium.*Photochemistry and Photophysics of Coordination Compounds II*. Springer, pp. 143-203.

92. Förster, T. 1969. Excimers. *Angewandte Chemie International Edition in English* 8(5), pp. 333-343.

93. Franca, L. G., Long, Y., Li, C., Danos, A. and Monkman, A. 2021. The Critical Role of nπ* States in the Photophysics and Thermally Activated Delayed Fluorescence of Spiro Acridine-Anthracenone. *The journal of physical chemistry letters* 12(5), pp. 1490-1500.

94. Franck, J. and Dymond, E.G. 1926. Elementary processes of photochemical reactions. *Transactions of the Faraday Society* 21(February), p. 536. doi: 10.1039/tf9262100536.

95. Frank, I. 2022. Classical Nuclear Motion: Comparison to Approaches with Quantum Mechanical Nuclear Motion. *Hydrogen* 4(1), pp. 11–21. doi: 10.3390/hydrogen4010002.

96. Fu, X., Wang, X. and Rao, X. 2017. An LED-based spectrally tuneable light source for visible and near-infrared spectroscopy analysis: A case study for sugar content estimation of citrus. Biosystems engineering 163, pp. 87-93.

97. Gao, F., Du, R., Han, C., Zhang, J., Wei, Y., Lu, G. and Xu, H. 2019. High-efficiency blue thermally activated delayed fluorescence from donor–acceptor–donor systems via the through-space conjugation effect. *Chemical Science* 10(21), pp. 5556-5567.

98. Gao, R., Mei, X., Yan, D., Liang, R. and Wei, M. 2018. Nano-photosensitizer based on layered double hydroxide and isophthalic acid for singlet oxygenation and photodynamic therapy. *Nature communications* 9(1), p. 2798.

99. Ghosh, A., Strandell, D.P. and Kambhampati, P. 2023. A spectroscopic overview of the differences between the absorbing states and the emitting states in semiconductor perovskite nanocrystals. *Nanoscale* . doi: 10.1039/D2NR05698D.

100. Gibson, J., Monkman, A. P. and Penfold, T. J. 2016. The importance of vibronic coupling for efficient reverse intersystem crossing in thermally activated delayed fluorescence molecules. *ChemPhysChem* 17(19), pp. 2956-2961.

101. Gispert, J.R. 2008. *Coordination Chemistry*. Wiley.

102. Goldsmith, J. I., Hudson, W. R., Lowry, M. S., Anderson, T. H. and Bernhard, S. 2005. Discovery and high-throughput screening of heteroleptic iridium complexes for photoinduced hydrogen production. *Journal of the American Chemical Society* 127(20), pp. 7502-7510.

103. Goring, D. 1953. Construction and use of a semimicro light-scattering apparatus. *Canadian Journal of Chemistry* 31(11), pp. 1078-1092.

104. Greenwood, N. N. and Earnshaw, A. 1997. 26 - Cobalt, Rhodium and Iridium.*Chemistry of the Elements (Second Edition)*. Oxford: Butterworth-Heinemann, pp. 1113-1143.

105. Guo, K., Righetto, M., Minotto, A., Zampetti, A. and Cacialli, F. 2021. Non-toxic near-infrared light-emitting diodes. iScience 24(6), p. 102545.

106. Guo, X., Liu, Y., Chen, Q., Zhao, D. and Ma, Y. 2018. New bichromophoric triplet photosensitizer designs and their application in triplet–triplet annihilation upconversion. *Advanced Optical Materials* 6(4), p. 1700981.

107. Gutu, A. D. et al. 2013. Polymyxin resistance of Pseudomonas aeruginosa phoQ mutants is dependent on additional two-component regulatory systems. *Antimicrobial agents and chemotherapy* 57(5), pp. 2204-2215.

108. Haghighatbin, M. A., Laird, S. E. and Hogan, C. F. 2018. Electrochemiluminescence of cyclometalated iridium (III) complexes. *Current Opinion in Electrochemistry* 7, pp. 216-223.

109. Haldar, A., Maity, S. and Manik, N. 2009. Electrical and photovoltaic characterisations of methyl red dye doped solid-state photoelectrochemical cell. *Ionics* 15, pp. 79-83.

110. Hall, M. D., Yasgar, A., Peryea, T., Braisted, J. C., Jadhav, A., Simeonov, A. and Coussens, N. P. 2016. Fluorescence polarization assays in high-throughput screening and drug discovery: a review. *Methods and applications in fluorescence* 4(2), p. 022001.

111. Han, F.-Q., Han, C.-M. and Xu, H. 2016. Recent progress in functionalized electrophosphorescent iridium (III) complexes. *Chinese Chemical Letters* 27(8), pp. 1193-1200.

112. Han, L., Zhang, D., Wang, J., Lan, Z. and Yang, R. 2015. Efficiency phosphorescent OLEDs with a low roll-off based on a hetero-triplet iridium complex. Dyes and Pigments 113, pp. 649-654.

113. Hansen, N. 2010. *Multiscale modeling of reaction and diffusion in zeolites.* Technische Universität Hamburg.

114. Hari, D. P. and Koenig, B. 2013. The photocatalyzed meerwein arylation: classic reaction of aryl diazonium salts in a new light. *Angewandte Chemie International Edition* 52(18), pp. 4734-4743.

115. Harris, T. L., Worthington, R. J., Hittle, L. E., Zurawski, D. V., Ernst, R. K. and Melander, C. 2014. Small molecule downregulation of PmrAB reverses lipid A modification and breaks colistin resistance. *ACS chemical biology* 9(1), pp. 122-127.

116. Heine, V. 2007. Group theory in quantum mechanics: an introduction to its present usage. Courier Corporation.

117. Herd, R. M., Dover, J. S. and Arndt, K. A. 1997. Basic laser principles. Dermatologic clinics 15(3), pp. 355-372.

118. Hong, B.-C. and Kawano, K. 2004. Organic dye-doped thin films for wavelength conversion and their effects on the photovoltaic characteristics of CdS/CdTe solar cell. *Japanese Journal of Applied Physics* 43(4R), p. 1421.

119. Hong, G., Gan, X., Leonhardt, C., Zhang, Z., Seibert, J., Busch, J. M. and Bräse, S. 2021. A brief history of OLEDs—emitter development and industry milestones. Advanced Materials 33(9), p. 2005630.

120. Horrocks, D. L. 1971. Techniques for the study of excimers.*Organic Scintillators and Scintillation Counting*. Elsevier, pp. 75-90.

121. Hou, Y. et al. 2019. Charge separation, charge recombination, long-lived charge transfer state formation and intersystem crossing in organic electron donor/acceptor dyads. *Journal of Materials Chemistry C* 7(39), pp. 12048-12074.

122. Housecroft, C. E. and Sharpe, A. G. 2008. Inorganic chemistry. Pearson Education.

123. Hu, Y.-X., Xia, X., He, W.-Z., Tang, Z.-J., Lv, Y.-L., Li, X. and Zhang, D.-Y. 2019. Recent developments in benzothiazole-based iridium (Ⅲ) complexes for application in OLEDs as electrophosphorescent emitters. *Organic Electronics* 66, pp. 126-135.

124. Huh, J.-W., Yu, B.-H., Heo, J., Ji, S.-M. and Yoon, T.-H. 2017. Technologies for display application of liquid crystal light shutters. Molecular Crystals and Liquid Crystals 644(1), pp. 120-129.

125. Hussain, M. et al. 2017. Intersystem crossing and triplet excited state properties of thionated naphthalenediimide derivatives. *Journal of Luminescence* 192, pp. 211-217.

126. Hussain, M., El-Zohry, A. M., Hou, Y., Toffoletti, A., Zhao, J., Barbon, A. and Mohammed, O. F. 2021. Spin–Orbit Charge-Transfer Intersystem Crossing of Compact Naphthalenediimide-Carbazole Electron-Donor–Acceptor Triads. The Journal of Physical Chemistry B 125(38), pp. 10813-10831.

127. Hussein, N. H., Al-Kadmy, I. M., Taha, B. M. and Hussein, J. D. 2021. Mobilized colistin resistance (mcr) genes from 1 to 10: a comprehensive review. *Molecular biology reports* 48, pp. 2897-2907.

128. Ibarra, L. E. et al. 2018. Metallated porphyrin-doped conjugated polymer nanoparticles for efficient photodynamic therapy of brain and colorectal tumor cells. Nanomedicine 13(6), pp. 605-624.

129. Ishchenko, A. A. 2008. Photonics and molecular design of dye-doped polymers for modern light-sensitive materials. *Pure and Applied Chemistry* 80(7), pp. 1525-1538.

130. Jablonski, A. 1933. Efficiency of Anti-Stokes Fluorescence in Dyes. *Nature* 131(3319), pp. 839–840. doi: 10.1038/131839b0.

131. Jabłoński, A. 1935. Über den Mechanismus der Photolumineszenz von Farbstoffphosphoren. *Zeitschrift für Physik* 94(1–2), pp. 38–46. doi: 10.1007/BF01330795.

132. Jacko, A., Powell, B. and McKenzie, R. H. 2010. Sensitivity of the photophysical properties of organometallic complexes to small chemical changes. The Journal of Chemical Physics 133(12), p. 124314.

133. Jaffé, H. H. and Miller, A. L. 1966. The fates of electronic excitation energy. *Journal of chemical education* 43(9), p. 469.

134. Jameson, D. M. and Ross, J. A. 2010. Fluorescence polarization/anisotropy in diagnostics and imaging. *Chemical reviews* 110(5), pp. 2685-2708.

135. Jameson, D. M. and Ross, J. A. 2010. Fluorescence polarization/anisotropy in diagnostics and imaging. *Chemical reviews* 110(5), pp. 2685-2708.

136. Jameson, D.M. and Ross, J.A. 2010. Fluorescence Polarization/Anisotropy in Diagnostics and Imaging. *Chemical Reviews* 110(5), pp. 2685–2708. doi: 10.1021/cr900267p.

137. Jena, S., Dhanalakshmi, P., Bano, G. and Thilagar, P. 2020. Delayed fluorescence, room temperature phosphorescence, and mechanofluorochromic naphthalimides: Differential imaging of normoxia and hypoxia live cancer cells. *The Journal of Physical Chemistry B* 124(26), pp. 5393-5406.

138. Jiang, J.-Y., Xu, Z.-H., Li, T., Cai, D.-H., Zhou, H. and Chen, Z.-J. 2021. Deep NIR-I Emissive Iridium (III) Complex Bearing DA Ligand: Synthesis, Photophysical Properties and DFT/TDDFT Calculation. *Crystals* 11(9), p. 1038.

139. Jin, R. and Tang, S. 2013. Theoretical investigation into optical and electronic properties of 1, 8-naphthalimide derivatives. *Journal of molecular modeling* 19(4), pp. 1685-1693.

140. Jolley, M. 1981. Fluorescence polarization immunoassay for the determination of therapeutic drug levels in human plasma. *Journal of analytical toxicology* 5(5), pp. 236-240.

141. Jones, J. W., Greene, T. A., Grygon, C. A., Doranz, B. J. and Brown, M. P. 2008. Cell-free assay of G-protein-coupled receptors using fluorescence polarization. *SLAS Discovery* 13(5), pp. 424-429.

142. Juris, A., Balzani, V., Barigelletti, F., Campagna, S., Belser, P. and von Zelewsky, A. v. 1988. Ru (II) polypyridine complexes: photophysics, photochemistry, eletrochemistry, and chemiluminescence. *Coordination Chemistry Reviews* 84, pp. 85-277.

143. Kafle, B.P. 2020. *Chemical Analysis and Material Characterization by Spectrophotometry*. Amsterdam: Elsevier.

144. Kamkaew, A., Lim, S. H., Lee, H. B., Kiew, L. V., Chung, L. Y. and Burgess, K. 2013. BODIPY dyes in photodynamic therapy. *Chemical Society Reviews* 42(1), pp. 77-88.

145. Kasha, M. 1950. Characterization of electronic transitions in complex molecules. *Discussions of the Faraday Society* 9, p. 14. doi: 10.1039/df9500900014.

146. Kasha, Michael. 1947. Phosphorescence and the R⊚le of the Triplet State in the Electronic Excitation of Complex Molecules. *Chemical Reviews* 41(2), pp. 401–419. doi: 10.1021/cr60129a015.

147. Kautsky, H. 1939. Quenching of luminescence by oxygen. Transactions of the Faraday Society 35, pp. 216-219.

148. Kim, H. U. et al. 2018. Substituents engineered deep-red to near-infrared phosphorescence from tris-heteroleptic iridium (III) complexes for solution processable red-NIR organic light-emitting diodes. *Journal of Materials Chemistry C* 6(39), pp. 10640-10658.

149. Kim, S.-Y., Kim, J.-H., Lee, S., Yun, B.-S., Son, H.-J. and Kang, S. O. 2022. Tuning the photophysical properties of homoleptic tris-cyclometalated Ir (III) complexes by facile modification of the imidazo-phenanthridine and their application to phosphorescent organic light-emitting diodes. *ACS omega* 7(20), pp. 17234-17244.

150. Kitai, A. 2016. Principles of Solid State. Materials for Solid State Lighting and Displays, p. 1.

151. Kitai, A. 2018. *Principles of solar cells, LEDs and related devices: the role of the PN junction*. John Wiley & Sons.

152. Kober, E. M., Caspar, J. V., Lumpkin, R. S. and Meyer, T. J. 1986. Application of the energy gap law to excited-state decay of osmium (II)-polypyridine complexes: calculation of relative nonradiative decay rates from emission spectral profiles. *The Journal of Physical Chemistry* 90(16), pp. 3722-3734.

153. Kolosov, D., Adamovich, V., Djurovich, P., Thompson, M. E. and Adachi, C. 2002. 1, 8-naphthalimides in phosphorescent organic LEDs: the interplay between dopant, exciplex, and host emission. *Journal of the American Chemical Society* 124(33), pp. 9945-9954.

154. Kosower, E. M. 1982. Intramolecular donor-acceptor systems. 9. Photophysics of (phenylamino) naphthalenesulfonates: a paradigm for excited-state intramolecular charge transfer. *Accounts of Chemical Research* 15(8), pp. 259-266.

155. Kucheryavy, P., Li, G., Vyas, S., Hadad, C. and Glusac, K. D. 2009. Electronic properties of 4-substituted naphthalimides. *The Journal of Physical Chemistry A* 113(23), pp. 6453-6461.

156. Kumke, M. U., Shu, L., McGown, L. B., Walker, G. T., Pitner, J. B. and Linn, C. P. 1997. Temperature and quenching studies of fluorescence polarization detection of DNA hybridization. *Analytical Chemistry* 69(3), pp. 500-506.

157. Kuo, H. H. et al. 2017. Bis-tridentate Ir (III) metal phosphors for efficient deep-blue organic light-emitting diodes. *Advanced Materials* 29(33), p. 1702464.

158. Kuriki, K., Kobayashi, T., Imai, N., Tamura, T., Koike, Y. and Okamoto, Y. 2000. Organic dye-doped polymer optical fiber laser. Polymers for Advanced Technologies 11(8-12), pp. 612-616.

159. Ladouceur, S., Swanick, K. N., Gallagher-Duval, S., Ding, Z. and Zysman-Colman, E. 2013. Strongly blue luminescent cationic iridium (III) complexes with an electron-rich ancillary ligand: Evaluation of their optoelectronic and electrochemiluminescence properties. European Journal of Inorganic Chemistry 2013(30), pp. 5329-5343.

160. Lakowicz, J. R. 1999. Introduction to fluorescence.*Principles of fluorescence spectroscopy*. Springer, pp. 1-23.

161. Lakowicz, J. R. 2006. *Principles of fluorescence spectroscopy*. Springer.

162. Lamansky, S. et al. 2001. Highly phosphorescent bis-cyclometalated iridium complexes: Synthesis, photophysical characterization, and use in organic light emitting diodes. *Journal of the American Chemical Society* 123(18), pp. 4304-4312. doi: 10.1021/ja003693s

163. Lea, W. A. and Simeonov, A. 2011. Fluorescence polarization assays in small molecule screening. *Expert opinion on drug discovery* 6(1), pp. 17-32.

164. Lee, C., Yang, W. and Parr, R.G. 1988. Development of the Colle-Salvetti correlation-energy formula into a functional of the electron density. *Physical Review B* 37(2), pp. 785–789. doi: 10.1103/PhysRevB.37.785.

165. Lee, E. D., Werner, T. C. and Seitz, W. R. 1987. Luminescence ratio indicators for oxygen. Analytical Chemistry 59(2), pp. 279-283.

166. Lee, J., Park, H., Park, K.-M., Kim, J., Lee, J.-Y. and Kang, Y. 2015. Deep-blue phosphorescent iridium (III) dyes based on fluorine-functionalized bis (2, 3′-bipyridyl) ligand for efficient organic light-emitting diodes. *Dyes and Pigments* 123, pp. 235-241.

167. Leung, C. W. T., Hong, Y., Chen, S., Zhao, E., Lam, J. W. Y. and Tang, B. Z. 2013. A photostable AIE luminogen for specific mitochondrial imaging and tracking. Journal of the American Chemical Society 135(1), pp. 62-65.

168. Li, F. et al. 2022. Singlet and triplet to doublet energy transfer: improving organic light-emitting diodes with radicals. *Nature communications* 13(1), p. 2744.

169. Li, G., Congrave, D. G., Zhu, D., Su, Z. and Bryce, M. R. 2018. Recent advances in luminescent dinuclear iridium (III) complexes and their application in organic electroluminescent devices. Polyhedron 140, pp. 146-157.

170. Li, K., Yu, R.-H., Shi, C.-M., Tao, F.-R., Li, T.-D. and Cui, Y.-Z. 2018. Electrospun nanofibrous membrane based on AIE-active compound for detecting picric acid in aqueous solution. *Sensors and Actuators B: Chemical* 262, pp. 637-645.

171. Ling, Z., Yin, W., Shen, Z., Wang, Y., Shen, J. and Walsh, T. R. 2020. Epidemiology of mobile colistin resistance genes mcr-1 to mcr-9. *Journal of Antimicrobial Chemotherapy* 75(11), pp. 3087-3095.

172. Liu, R. et al. 2014. Influence of different diimine (N∧ N) ligands on the photophysics and reverse saturable absorption of heteroleptic cationic iridium (III) complexes bearing cyclometalating 2-(Liu et al.) pyridine (C∧ N) ligands. *The Journal of Physical Chemistry C* 118(40), pp. 23233-23246.

173. Liu, Y.-Y. et al. 2016. Emergence of plasmid-mediated colistin resistance mechanism MCR-1 in animals and human beings in China: a microbiological and molecular biological study. *The Lancet infectious diseases* 16(2), pp. 161-168.

174. Lowry, M. S. and Bernhard, S. 2006. Synthetically tailored excited states: phosphorescent, cyclometalated iridium (III) complexes and their applications. *Chemistry–A European Journal* 12(31), pp. 7970-7977.

175. Luo, S. et al. 2015. Novel 1, 8-naphthalimide derivatives for standard-red organic light-emitting device applications. Journal of Materials Chemistry C 3(20), pp. 5259-5267.

176. Luo, X., Yang, Y. and Qian, X. 2020. Recent progresses on the development of thioxo-naphthalimides. *Chinese Chemical Letters* 31(11), pp. 2877-2883.

177. Ma, D., Tsuboi, T., Qiu, Y. and Duan, L. 2017. Recent progress in ionic iridium (III) complexes for organic electronic devices. *Advanced Materials* 29(3), p. 1603253.

178. Ma, D.-L., Lin, S., Wang, W., Yang, C. and Leung, C.-H. 2017. Luminescent chemosensors by using cyclometalated iridium (III) complexes and their applications. Chemical Science 8(2), pp. 878-889.

179. Ma, D.-L., Ng, H. P., Wong, S.-Y., Vellaisamy, K., Wu, K.-J. and Leung, C.-H. 2018. Iridium (iii) complexes as reaction based chemosensors for medical diagnostics. Dalton Transactions 47(43), pp. 15278-15282.

180. Majumdar, P. et al. 2014. Cyclometalated Ir (III) complexes with styryl-BODIPY ligands showing near IR absorption/emission: preparation, study of photophysical properties and application as photodynamic/luminescence imaging materials. *Journal of Materials Chemistry B* 2(19), pp. 2838-2854.

181. Majumdar, P., Nomula, R. and Zhao, J. 2014. Activatable triplet photosensitizers: magic bullets for targeted photodynamic therapy. *Journal of Materials Chemistry C* 2(30), pp. 5982-5997.

182. Manna, A. and Chakravorti, S. 2010. Charge Transfer in 1, 8-Naphthalimide: A Combined Theoretical and Experimental Approach. *Photochemistry and photobiology* 86(1), pp. 47-54.

183. Marini, A., Muñoz-Losa, A., Biancardi, A. and Mennucci, B. 2010. What is Solvatochromism? *The Journal of Physical Chemistry B* 114(51), pp. 17128–17135. doi: 10.1021/jp1097487.

184. Martell, A., Hancock, R. D. and Motekaitis, R. 1994. Factors affecting stabilities of chelate, macrocyclic and macrobicyclic complexes in solution. Coordination Chemistry Reviews 133, pp. 39-65

185. Middelhoek, E., Van der Meulen, P., Verhoeven, J. and Glasbeek, M. 1995. Picosecond time-dependent Stokes shift studies of fluoroprobe in liquid solution. Chemical physics 198(3), pp. 373-380.

186. Miller, A. K. et al. 2011. PhoQ mutations promote lipid A modification and polymyxin resistance of Pseudomonas aeruginosa found in colistin-treated cystic fibrosis patients. *Antimicrobial agents and chemotherapy* 55(12), pp. 5761-5769.

187. Morello, G. R. 2017. Accurate prediction of emission energies with TD-DFT methods for platinum and iridium OLED materials. *Journal of molecular modeling* 23(6), pp. 1-10.

188. Musser, A. et al. 2017. Intermolecular states in organic dye dispersions: excimers vs. aggregates. *Journal of Materials Chemistry C* 5(33), pp. 8380-8389.

189. Na, H., Wen, Z., Judy, I., Wu, C. and Teets, T. S. 2019. Mixed-carbene cyclometalated iridium complexes with saturated blue luminescence. *Chemical Science* 10(25), pp. 6254-6260.

190. Nakanotani, H., Tsuchiya, Y. and Adachi, C. 2021. Thermally-activated delayed fluorescence for light-emitting devices. *Chemistry Letters* 50(5), pp. 938-948.

191. Nazeeruddin, M. K., Humphry-Baker, R., Berner, D., Rivier, S., Zuppiroli, L. and Graetzel, M. 2003. Highly phosphorescence iridium complexes and their application in organic light-emitting devices. Journal of the American Chemical Society 125(29), pp. 8790-8797.

192. Nielsen, O. and Martin, R. M. 1985. Quantum-mechanical theory of stress and force. Physical Review B 32(6), p. 3780.

193. Ott, I., Xu, Y., Liu, J., Kokoschka, M., Harlos, M., Sheldrick, W. S. and Qian, X. 2008. Sulfur-substituted naphthalimides as photoactivatable anticancer agents: DNA interaction, fluorescence imaging, and phototoxic effects in cultured tumor cells. *Bioorganic & medicinal chemistry* 16(15), pp. 7107-7116.

194. Palmer, J. R., Wells, K. A., Yarnell, J. E., Favale, J. M. and Castellano, F. N. 2020. Visible-Light-Driven Triplet Sensitization of Polycyclic Aromatic Hydrocarbons Using Thionated Perinones. *The journal of physical chemistry letters* 11(13), pp. 5092-5099.

195. Parikh, J., Mohan, B., Bhatt, K., Patel, N., Patel, S., Vyas, A. and Modi, K. 2023. Effect of temperature on metal-organic frameworks chemical sensors detection properties. *Microchemical Journal* 184, p. 108156. doi: 10.1016/j.microc.2022.108156.

196. Patsenker, L. D. and Artyukhova, Y. Y. 2003. Molecular structure and spectral properties of thionaphthalimides. *Journal of molecular structure* 655(2), pp. 311-320.

197. Pavia, D., Lampman, G., Kriz, G. and Vyvyan, J. 2009. *Introduction to spectroscopy*. 4th ed. Belmont, CA : Brooks/Cole, Cengage Learning.

198. Pearce, N. et al. 2018. Thionated naphthalene diimides: tuneable chromophores for applications in photoactive dyads. *Physical Chemistry Chemical Physics* 20(2), pp. 752-764.

199. Peng, G. D., Chu, P., Xiong, Z., Whitbread, T. W. and Chaplin, R. P. 1996. Dye-doped step-index polymer optical fiber for broadband optical amplification. Journal of lightwave technology 14(10), pp. 2215-2223.

200. Peng, G. D., Xiong, Z. and Chu, P. L. 1998. Fluorescence decay and recovery in organic dye-doped polymer optical fibers. Journal of lightwave technology 16(12), p. 2365.

201. Perrin, F. 1926. The polarisation of flourescence light. Average life of molecules in their excited state. *Journal De Physique Et Le Radium* 7, pp. 390-401.

202. Phillips, K. A. et al. 2018. Ligand-Tuneable, Red-Emitting Iridium (III) Complexes for Efficient Triplet–Triplet Annihilation Upconversion Performance. *Chemistry–A European Journal* 24(34), pp. 8577-8588.

203. Picollo, M., Aceto, M. and Vitorino, T. 2018. UV-Vis spectroscopy. Physical sciences reviews 4(4), p. 20180008.

204. Piet, J. J., Schuddeboom, W., Wegewijs, B. R., Grozema, F. C. and Warman, J. M. 2001. Symmetry breaking in the relaxed S1 excited state of bianthryl derivatives in weakly polar solvents. *Journal of the American Chemical Society* 123(22), pp. 5337-5347.

205. Poddar, M., Sharma, V., Mobin, S. M. and Misra, R. 2018. 1, 8-Naphthalimide-Substituted BODIPY Dyads: Synthesis, Structure, Properties, and Live-Cell Imaging. *Chemistry–An Asian Journal* 13(19), pp. 2881-2890.

206. Pogue, J., Ortwine, J. and Kaye, K. 2017. Clinical considerations for optimal use of the polymyxins: a focus on agent selection and dosing. *Clinical Microbiology and Infection* 23(4), pp. 229-233.

207. Porter, G.B. 1983. Introduction to inorganic photochemistry: Principles and methods. *Journal of Chemical Education* 60(10), p. 785. doi: 10.1021/ed060p785.

208. Priestley, E. and Haug, A. 1968. Phosphorescence spectrum of pure crystalline naphthalene. *The Journal of Chemical Physics* 49(2), pp. 622-629.

209. Ramasamy, S. and Hurtubise, R. J. 1996. Energy-gap law and room-temperature phosphorescence of polycyclic aromatic hydrocarbons adsorbed on cyclodextrin/sodium chloride solid matrices. *Applied spectroscopy* 50(1), pp. 115-118.

210. Ramsden, C. A. 1994. Non-bonding molecular orbitals and the chemistry of non-classical organic molecules. Chemical Society Reviews 23(2), pp. 111-118.

211. Reddy, M. and Bejoymohandas, K. 2016. Evolution of 2, 3′-bipyridine class of cyclometalating ligands as efficient phosphorescent iridium (III) emitters for applications in organic light emitting diodes. *Journal of Photochemistry and Photobiology C: Photochemistry Reviews* 29, pp. 29-47.

212. Reineke, S. and Baldo, M. A. 2014. Room temperature triplet state spectroscopy of organic semiconductors. *Scientific reports* 4(1), pp. 1-8.

213. Reineke, S., Thomschke, M., Lüssem, B. and Leo, K. 2013. White organic light-emitting diodes: Status and perspective. Reviews of Modern Physics 85(3), p. 1245.

214. Renger, T., Grundkötter, B., Madjet, M.E.-A. and Müh, F. 2008. Theory of solvatochromic shifts in nonpolar solvents reveals a new spectroscopic rule. *Proceedings of the National Academy of Sciences* 105(36), pp. 13235–13240. doi: 10.1073/pnas.0801025105.

215. Resta, V. et al. 2017. Nanoparticle-doped electrospun fiber random lasers with spatially extended light modes. *Optics Express* 25(20), pp. 24604-24614.

216. Rezende, M. C., Dominguez, M., Aracena, A. and Millán, D. 2011. Solvatochromism and electrophilicity. Chemical Physics Letters 514(4-6), pp. 267-273.

217. Roundhill, D.M. 1994. *Photochemistry and photophysics of metal complexes*. New York: Plenum Press.

218. Ruta, J., Perrier, S., Ravelet, C., Fize, J. and Peyrin, E. 2009. Noncompetitive fluorescence polarization aptamer-based assay for small molecule detection. *Analytical Chemistry* 81(17), pp. 7468-7473.

219. Santra, S., Xu, J., Wang, K. and Tand, W. 2004. Luminescent nanoparticle probes for bioimaging. Journal of nanoscience and nanotechnology 4(6), pp. 590-599.

220. Sathyanarayana, D. 2001. *Electronic absorption spectroscopy and related techniques*. Universities Press.

221. Schneider, G. E. 2013. *Ionic transition metal complexes containing iridium (III) for lighting applications.* University_of_Basel.

222. Schrödinger, E. 1926. The Schrödinger equation. Phys Rev 28(6), pp. 1049-1070.

223. Sebők-Nagy, K. and Biczók, L. 2004. Effect of protonation and hydrogen bonding on the fluorescent properties and exciplex formation of N-(4-pyridyl)-1, 2-naphthalimide. *Photochemical & Photobiological Sciences* 3(4), pp. 389-395.

224. Serdiuk, I. E., Mońka, M., Kozakiewicz, K., Liberek, B., Bojarski, P. and Park, S. Y. 2021. Vibrationally Assisted Direct Intersystem Crossing between the Same Charge-Transfer States for Thermally Activated Delayed Fluorescence: Analysis by Marcus–Hush Theory Including Reorganization Energy. *The Journal of Physical Chemistry B* 125(10), pp. 2696-2706.

225. Shi, H., Yao, W., Ye, W., Ma, H., Huang, W. and An, Z. 2022. Ultralong Organic Phosphorescence: From Material Design to Applications. *Accounts of Chemical Research* 55(23), pp. 3445–3459. doi: 10.1021/acs.accounts.2c00514.

226. Shi, L. and Xia, W. 2012. Photoredox functionalization of C–H bonds adjacent to a nitrogen atom. *Chemical Society Reviews* 41(23), pp. 7687-7697.

227. Shinde, G., Godage, R.K., Jadhav, R.S., Manoj, B. and Aniket, B. 2020. A Review on Advances in UV Spectroscopy. *Research Journal of Science and Technology* 12(1), p. 47. doi: 10.5958/2349-2988.2020.00005.4.

228. Shokri, S. et al. 2017. A naphtho-p-quinodimethane exhibiting baird's (anti) aromaticity, broken symmetry, and attractive photoluminescence. *The Journal of Organic Chemistry* 82(19), pp. 10167-10173.

229. Sierra, J. M., Fusté, E., Rabanal, F., Vinuesa, T. and Viñas, M. 2017. An overview of antimicrobial peptides and the latest advances in their development. *Expert Opinion on Biological Therapy* 17(6), pp. 663-676.

230. Silberberg, M. S., Amateis, P., Venkateswaran, R. and Chen, L. 2006. Chemistry: The molecular nature of matter and change. McGraw-Hill New York.

231. Singh-Rachford, T. N. and Castellano, F. N. 2010. Photon upconversion based on sensitized triplet–triplet annihilation. *Coordination Chemistry Reviews* 254(21-22), pp. 2560-2573.

232. Sinopoli, A., Wood, C. J., Gibson, E. A. and Elliott, P. I. 2017. New cyclometalated iridium (III) dye chromophore complexes for p-type dye-sensitised solar cells. Dyes and Pigments 140, pp. 269-277.

233. Slonczewski, J. 1999. Excitation of spin waves by an electric current. Journal of Magnetism and Magnetic Materials 195(2), pp. L261-L268.

234. Smith, D. S. and Eremin, S. A. 2008. Fluorescence polarization immunoassays and related methods for simple, high-throughput screening of small molecules. *Analytical and bioanalytical chemistry* 391(5), pp. 1499-1507.

235. Song, H., Wang, K., Kuang, Z., Zhao, Y. S., Guo, Q. and Xia, A. 2019. Solvent modulated excited state processes of push–pull molecule with hybridized local excitation and intramolecular charge transfer character. *Physical Chemistry Chemical Physics* 21(7), pp. 3894-3902.

236. Song, M. X., Hao, Z. M., Wu, Z. J., Song, S. Y., Zhou, L., Deng, R. P. and Zhang, H. J. 2013. Density functional theory and time-dependent density functional theory study on a series of iridium complexes with tetraphenylimidodiphosphinate ligand. *Journal of Physical Organic Chemistry* 26(10), pp. 840-848.

237. Song, M.-X., Wang, G.-F., Wang, J., Wang, Y.-H., Bai, F.-Q. and Qin, Z.-K. 2015. Theoretical study on a series of iridium complexes with low efficiency roll-off property. *Spectrochimica Acta Part A: Molecular and Biomolecular Spectroscopy* 134, pp. 406-412.

238. Stasicka, Z. and Marchaj, A. 1977. Flash photolysis of coordination compounds. *Coordination Chemistry Reviews* 23(2), pp. 131–181. doi: 10.1016/S0010-8545(00)80333-1.

239. Stokes, G.G. 1852. XXX. On the change of refrangibility of light. *Philosophical Transactions of the Royal Society of London* 142, pp. 463–562. doi: 10.1098/rstl.1852.0022.

240. Stonelake, T. M. et al. 2020. Spectroscopic and theoretical investigation of color tuning in deep-red luminescent iridium (III) complexes. *Inorganic chemistry* 59(4), pp. 2266-2277.

241. Strickler, S. and Berg, R. A. 1962. Relationship between absorption intensity and fluorescence lifetime of molecules. The Journal of Chemical Physics 37(4), pp. 814-822.

242. Sun, M. and Song, P. S. 1977. Solvent effects on the fluorescent states of indole derivatives-dipole moments. Photochemistry and photobiology 25(1), pp. 3-9.

243. Suppan, P. 1990. Invited review solvatochromic shifts: The influence of the medium on the energy of electronic states. *Journal of Photochemistry and Photobiology A: Chemistry* 50(3), pp. 293–330. doi: 10.1016/1010-6030(90)87021-3.

244. Sutton, J. J. et al. 2021. Excited-State Switching in Rhenium (I) Bipyridyl Complexes with Donor–Donor and Donor–Acceptor Substituents. *Journal of the American Chemical Society* 143(24), pp. 9082-9093.

245. Symons, H. E., Hagemann, M. J., Harniman, R. L. and Faul, C. F. 2022. Thionated PDI supramolecular polymers: controlling aggregation mechanisms, morphology and function. *Journal of Materials Chemistry C* 10(7), pp. 2828-2837.

246. Tamayo, A. B., Garon, S., Sajoto, T., Djurovich, P. I., Tsyba, I. M., Bau, R. and Thompson, M. E. 2005. Cationic bis-cyclometalated iridium (III) diimine complexes and their use in efficient blue, green, and red electroluminescent devices. *Inorganic chemistry* 44(24), pp. 8723-8732.

247. Tan, W., Shi, Z.-Y. and Kopelman, R. 1995. Miniaturized fiber-optic chemical sensors with fluorescent dye-doped polymers. Sensors and Actuators B: Chemical 28(2), pp. 157-163.

248. Tang, G. et al. 2019. Red thermally activated delayed fluorescence and the intersystem crossing mechanisms in compact naphthalimide–phenothiazine electron donor/acceptor dyads. *The Journal of Physical Chemistry C* 123(50), pp. 30171-30186.

249. Tang, G., Yang, W. and Zhao, J. 2022. Naphthalimide–Carbazole Compact Electron Donor–Acceptor Dyads: Effect of Molecular Geometry and Electron-Donating Capacity on the Spin-Orbit Charge Transfer Intersystem Crossing. *The Journal of Physical Chemistry A*,

250. Tang, Y., Liang, G., Chen, J., Yu, S., Li, Z., Rao, L. and Yu, B. 2017. Highly reflective nanofiber films based on electrospinning and their application on color uniformity and luminous efficacy improvement of white light-emitting diodes. *Optics Express* 25(17), pp. 20598-20611.

251. Tao, P. et al. 2017. Highly efficient blue phosphorescent iridium (III) complexes with various ancillary ligands for partially solution-processed organic light-emitting diodes. *Journal of Materials Chemistry C* 5(36), pp. 9306-9314.

252. Tilley, A. J., Pensack, R. D., Lee, T. S., Djukic, B., Scholes, G. D. and Seferos, D. S. 2014. Ultrafast triplet formation in thionated perylene diimides. *The Journal of Physical Chemistry C* 118(19), pp. 9996-10004.

253. Titos-Padilla, S., Colacio, E., Pope, S. J., Delgado, J. J., Melgosa, M. and Herrera, J. M. 2013. Photophysical properties of [Ir (tpy) 2] 3+-doped silica nanoparticles and synthesis of a colour-tunable material based on an Ir (core)–Eu (shell) derivative. *Journal of Materials Chemistry C* 1(24), pp. 3808-3815.

254. Trimble, M. J., Mlynárčik, P., Kolář, M. and Hancock, R. E. 2016. Polymyxin: alternative mechanisms of action and resistance. *Cold Spring Harbor perspectives in medicine* 6(10), p. a025288.

255. Tritton, D. N. et al. 2022. Development and advancement of iridium (III)-based complexes for photocatalytic hydrogen evolution. Coordination Chemistry Reviews 459, p. 214390.

256. Turro, N. J., Ramamurthy, V. and Scaiano, J. C. 2010. *Modern molecular photochemistry of organic molecules*. University Science Books Sausalito, CA.

257. Vandergriff, L. J. and McLean, V. 2008. Nature and properties of light. Fundamentals of Photonics, pp. 1-38.

258. Vavilov, S. and Levshin, W. 1923. Beiträge zur Frage über polarisiertes fluorescenzlicht von Farbstofflösungen. *Zeitschrift für Physik* 16, pp. 135-154.

259. Ventura, B., Bertocco, A., Braga, D., Catalano, L., d'Agostino, S., Grepioni, F. and Taddei, P. 2014. Luminescence properties of 1, 8-naphthalimide derivatives in solution, in their crystals, and in co-crystals: toward room-temperature phosphorescence from organic materials. *The Journal of Physical Chemistry C* 118(32), pp. 18646-18658.

260. Wang, C., Feng, Y., Liu, L., Wei, L., Kang, M. and Zong, Z. 2020. Identification of novel mobile colistin resistance gene mcr-10. *Emerging microbes & infections* 9(1), pp. 508-516.

261. Wang, L., Cui, P., Kilina, S. and Sun, W. 2017. Toward broadband reverse saturable absorption: investigating the impact of cyclometalating ligand π-conjugation on the photophysics and reverse saturable absorption of cationic heteroleptic iridium complexes. *The Journal of Physical Chemistry C* 121(10), pp. 5719-5730.

262. Wang, Y. et al. 2010. The synthesis and photoluminescence characteristics of novel blue light-emitting naphthalimide derivatives. Dyes and Pigments 86(2), pp. 190-196.

263. Wang, Y., Zhu, M., Deng, J., Xie, G. and Baranoff, E. 2017. Iridium-based emitters containing pendant triphenylene moieties for bluish-green OLEDs with improved efficiency upon thermal annealing. *New Journal of Chemistry* 41(4), pp. 1773-1780.

264. Ward, J. S. et al. 2019. Impact of methoxy substituents on thermally activated delayed fluorescence and room-temperature phosphorescence in all-organic donor–acceptor systems. *The Journal of Organic Chemistry* 84(7), pp. 3801-3816.

265. Ward, J. S., Danos, A., Stachelek, P., Fox, M. A., Batsanov, A. S., Monkman, A. P. and Bryce, M. R. 2020. Exploiting trifluoromethyl substituents for tuning orbital character of singlet and triplet states to increase the rate of thermally activated delayed fluorescence. *Materials Chemistry Frontiers* 4(12), pp. 3602-3615.

266. Ward, J. S., Nobuyasu, R. S., Batsanov, A. S., Data, P., Monkman, A. P., Dias, F. B. and Bryce, M. R. 2016. The interplay of thermally activated delayed fluorescence (TADF) and room temperature organic phosphorescence in sterically-constrained donor–acceptor charge-transfer molecules. *Chemical Communications* 52(12), pp. 2612-2615.

267. Ware, W.R. and Baldwin, B.A. 1965. Effect of Temperature on Fluorescence Quantum Yields in Solution. *The Journal of Chemical Physics* 43(4), pp. 1194–1197. doi: 10.1063/1.1696903.

268. Warner, J. and Berry, R. S. 1985. Hund's rule. Nature 313, pp. 160-160.

269. Weber, G. 1956. Photoelectric method for the measurement of the polarization of the fluorescence of solutions. *JOSA* 46(11), pp. 962-970.

270. Wei, S., Sun, Y., Guo, P., Hu, X. and Fan, J. 2012. A novel 4-(tetrahydro-2-furanmethoxy)-N-octadecyl-1, 8-naphthalimide based blue emitting probe: Solvent effect on the photophysical properties and protein detection. *Russian Journal of Bioorganic Chemistry* 38(5), pp. 469-478.

271. Wilde, A. and Watts, R. J. 1991. Solvent effects on metal-to-ligand charge-transfer bands in ortho-metalated complexes of iridium (III): estimates of transition dipole moments. The Journal of Physical Chemistry 95(2), pp. 622-629.

272. Wintgens, V., Valat, P., Kossanyi, J., Biczok, L., Demeter, A. and Bérces, T. 1994. Spectroscopic properties of aromatic dicarboximides. Part1.—N—H and N-methyl-substituted naphthalimides. *Journal of the Chemical Society, Faraday Transactions* 90(3), pp. 411-421.

273. Wolf, C., Tscherner, M. and Köstler, S. 2015. Ultra-fast opto-chemical sensors by using electrospun nanofibers as sensing layers. *Sensors and Actuators B: Chemical* 209, pp. 1064-1069.

274. Won, Y., Shin, H. S., Jo, M., Lim, Y. J., Manda, R. and Lee, S. H. 2021. An electrically switchable dye-doped liquid crystal polarizer for organic light emitting-diode displays. Journal of Molecular Liquids 333, p. 115922.

275. Xiao, X. and Zhen, S. 2022. Recent advances in fluorescence anisotropy/polarization signal amplification. *RSC Advances* 12(11), pp. 6364–6376. doi: 10.1039/D2RA00058J.

276. Xu, Q.-L. et al. 2015. Efficient OLEDs with low efficiency roll-off using iridium complexes possessing good electron mobility. *Journal of Materials Chemistry C* 3(15), pp. 3694-3701.

277. Xu, Z., Yoon, J. and Spring, D. R. 2010. A selective and ratiometric Cu2+ fluorescent probe based on naphthalimide excimer–monomer switching. Chemical Communications 46(15), pp. 2563-2565.

278. Yamanaka, K. et al. 2023. Ultrafast charge-transfer dynamics in a visible-light-excited iridium(III) terpyridine 2-phenylpyridine complex studied by femtosecond X-ray absorption spectroscopy. *Journal of Photochemistry and Photobiology A: Chemistry* 435, p. 114267. doi: 10.1016/j.jphotochem.2022.114267.

279. Yanai, T., Tew, D.P. and Handy, N.C. 2004. A new hybrid exchange–correlation functional using the Coulomb-attenuating method (CAM-B3LYP). *Chemical Physics Letters* 393(1–3), pp. 51–57. doi: 10.1016/j.cplett.2004.06.011.

280. Ye, C., Zhou, L., Wang, X. and Liang, Z. 2016. Photon upconversion: from two-photon absorption (TPA) to triplet–triplet annihilation (TTA). *Physical Chemistry Chemical Physics* 18(16), pp. 10818-10835.

281. Ye, K., Cao, L., van Raamsdonk, D. M., Wang, Z., Zhao, J., Escudero, D. and Jacquemin, D. 2022. Naphthalimide-phenothiazine dyads: effect of conformational flexibility and matching of the energy of the charge-transfer state and the localized triplet excited state on the thermally activated delayed fluorescence. Beilstein journal of organic chemistry 18(1), pp. 1435-1453.

282. Yoshihara, T. et al. 2015. Intracellular and in vivo oxygen sensing using phosphorescent Ir (III) complexes with a modified acetylacetonato ligand. *Analytical Chemistry* 87(5), pp. 2710-2717.

283. You, Y., Cho, S. and Nam, W. 2014. Cyclometalated iridium (III) complexes for phosphorescence sensing of biological metal ions. *Inorganic chemistry* 53(4), pp. 1804-1815.

284. You, Y., Seo, J., Kim, S. H., Kim, K. S., Ahn, T. K., Kim, D. and Park, S. Y. 2008. Highly phosphorescent iridium complexes with chromophoric 2-(2-hydroxyphenyl) oxazole-based ancillary ligands: interligand energy-harvesting phosphorescence. *Inorganic chemistry* 47(5), pp. 1476-1487.

285. Zeitler, K. 2009. Photoredox catalysis with visible light. *Angewandte Chemie International Edition* 48(52), pp. 9785-9789.

286. Zeng, D. et al. 2019. Cyclometalated Iridium (III) Complexes Incorporating Aromatic Phosphonate Ligands: Syntheses, Structures, and Tunable Optical Properties. *ACS omega* 4(15), pp. 16543-16550.

287. Zeng, D. et al. 2019. Cyclometalated Iridium (III) Complexes Incorporating Aromatic Phosphonate Ligands: Syntheses, Structures, and Tunable Optical Properties. ACS omega 4(15), pp. 16543-16550.

288. Zeng, L., Huang, L., Han, J. and Han, G. 2022. Enhancing Triplet–Triplet Annihilation Upconversion: From Molecular Design to Present Applications. *Accounts of Chemical Research* 55(18), pp. 2604–2615. doi: 10.1021/acs.accounts.2c00307.

289. Zhang, H. et al. 2019. Fluorescence polarization assays for chemical contaminants in food and environmental analyses. *TrAC Trends in Analytical Chemistry* 114, pp. 293–313. doi: 10.1016/j.trac.2019.03.013.

290. Zhang, J.-P., Wang, Y., Ma, J.-B., Jin, L., Liu, F.-T. and Bai, F.-Q. 2018. Density functional theory investigation on iridium (III) complexes for efficient blue electrophosphorescence. *RSC advances* 8(35), pp. 19437-19448.

291. Zhang, W.-H., Hu, X.-X. and Zhang, X.-B. 2016. Dye-doped fluorescent silica nanoparticles for live cell and in vivo bioimaging. Nanomaterials 6(5), p. 81.

292. Zhang, X. et al. 2022. Red Light-Emitting Thermally-Activated Delayed Fluorescence of Naphthalimide-Phenoxazine Electron Donor-Acceptor Dyad: Time-Resolved Optical and Magnetic Spectroscopic Studies. *Chemistry–A European Journal*, p. e202200510.

293. Zhang, Y. and Qiao, J. 2021. Near-infrared emitting iridium complexes: Molecular design, photophysical properties, and related applications. iScience 24(8), p. 102858.

294. Zhang, Y.-Y. and Zhou, C.-H. 2011. Synthesis and activities of naphthalimide azoles as a new type of antibacterial and antifungal agents. Bioorganic & medicinal chemistry letters 21(14), pp. 4349-4352.

295. Zhao, Q., Li, F., Liu, S., Yu, M., Liu, Z., Yi, T. and Huang, C. 2008. Highly selective phosphorescent chemosensor for fluoride based on an iridium (III) complex containing arylborane units. *Inorganic chemistry* 47(20), pp. 9256-9264.

296. Zhou, G. et al. 2008. Manipulating charge-transfer character with electron-withdrawing main-group moieties for the color tuning of iridium electrophosphors. *Advanced functional materials* 18(3), pp. 499-511.

297. Zimnyakov, D., Zdrajevsky, R., Yuvchenko, S., Ushakova, O., Angelsky, O. and Yermolenko, S. 2015. Enhancement of light depolarization by random ensembles of titania-based low-dimensional nanoparticles. *Journal of Quantitative Spectroscopy and Radiative Transfer* 152, pp. 37-44.